Institutional Repository - Research Portal
Dépôt Institutionnel - Portail de la Recherche
researchportal.unamur.be
University of Namur

THESIS / THÈSE

DOCTOR OF SCIENCES

Hydrodynamics of solute transport in karst conduits with contrasted geometries

Karstogenesis description and tracer test modelling in the Waulsortian mudmounds (Furfooz, Belgium)

Dewaide, Lorraine

Award date:
2018

Awarding institution:
University of Namur

Link to publication

General rights
Copyright and moral rights for the publications made accessible in the public portal are retained by the authors and/or other copyright owners and it is a condition of accessing publications that users recognise and abide by the legal requirements associated with these rights.

- Users may download and print one copy of any publication from the public portal for the purpose of private study or research.
- You may not further distribute the material or use it for any profit-making activity or commercial gain
- You may freely distribute the URL identifying the publication in the public portal ?

Take down policy
If you believe that this document breaches copyright please contact us providing details, and we will remove access to the work immediately and investigate your claim.

Download date: 02. May. 2026

Hydrodynamics of solute transport in karst conduits with contrasted geometries:

Karstogenesis description and tracer test modelling in the Waulsortian mudmounds (Furfooz, Belgium)

Lorraine DEWAIDE, December 2018

Thesis dissertation submitted in fulfillment of the requirements for the degree of Doctor of Sciences

Department of Geology – Faculty of Sciences

University of Namur, Belgium

Cover Graphic Design : © Presses universitaires de Namur
Cover Picture : the lake of the « Trou Qui Fume » cave, Furfooz Natural Reserve (G. Rochez)

© Presses universitaires de Namur & Lorraine Dewaide
Rempart de la Vierge, 13
B - 5000 Namur (Belgique)

Any reproduction of any extract from this book, outside the restrictive limits provided for by law, by any process whatsoever, and in particular by photocopying or scanning, is strictly prohibited for all countries.
Printed in Belgium
ISBN : 978-2-39029-030-8
Legal deposit: D/2018/1881/32

Dissertation Committee:

Prof. Dr. V. Hallet - Thesis advisor

Department of Geology – Faculty of Sciences

University of Namur, Belgium

Prof. Dr. P. Collon – Thesis co-advisor

GeoRessources

RING - Research for Integrative Numerical Geology

Ecole Nationale Supérieure de Géologie

University of Lorraine, France

Prof. Dr. J. Yans – Committee President

Department of Geology – Faculty of Sciences

University of Namur, Belgium

Prof. Dr. J-M. Baele – Committee member

Department of Geology and Applied Geology

University of Mons, Belgium

Dr. N. Dörfliger – Committee member

Division of Water, Environment & Ecotechnologies

Bureau de Recherches Géologiques et Minières, France

Dr. M. S. Field – Committee member

Office of Research and Development

US Environmental Protection Agency, United States of America

Remerciements

En préparant ces remerciements, je suis tombée sur un extrait de « l'art de la thèse » de Michel Beaud (2006) qui nous dit : «… Sachez trouver le ton juste : ni emphase, ni circonvolutions ; soyez sobre et concis …». Rassurez-vous, je ferai tout le contraire !

Sept années de thèse, passées à ruminer sur les mêmes problématiques, avec toujours plus de données qui s'amoncellent, c'est autant d'occasions de passer une tranche de vie « le nez dans le guidon ». Et c'est là toute la responsabilité d'un thésard de comprendre que s'ouvrir aux autres, et les laisser rentrer dans son aventure de recherche, ça fait aussi partie de la thèse. Au-delà des découvertes scientifiques qui structurent la thèse, la convergence des réflexions, les échanges d'idées et les nombreuses interactions humaines sont partie intégrante de l'évolution de la recherche…mais aussi du chercheur. Je tiens donc à intégrer à ce manuscrit tous ceux qui, de près ou de loin, ont contribué à l'aboutissement de mon doctorat.

En tout premier lieu, je voudrais chaleureusement remercier le promoteur de cette thèse, le Professeur Vincent Hallet. J'ai eu une chance incroyable de bénéficier de votre encadrement ; il est rare, je pense, d'avoir un promoteur aussi attentif, disponible et à l'écoute. Nos discussions ont souvent débloqué des situations difficiles et m'ont permis d'aller de l'avant. Merci pour votre implication et vos suggestions toujours très perspicaces. Je profite aussi de l'occasion pour exprimer ma gratitude pour la formation que j'ai reçue de votre part alors que j'étais étudiante, en recherche de mon avenir. Vous avez un don pour transmettre votre passion de la géologie et des générations entières d'étudiants se joindraient certainement à moi pour vous dire merci.

Ensuite, je tiens à saluer du fond du cœur notre superman du département, Gaëtan Rochez ! Technicien d'exception, spéléologue chevronné, photographe hors pair, et j'en passe… ;) Quel plaisir d'avoir travaillé avec toi toutes ces années. Merci pour ton implication, toujours passionnée, sur le terrain et aussi dans nos discussions sur ce p… de double pic ! Ta présence et tes qualités ont ouvert des possibilités d'investigations qu'on n'aurait pas osées sans toi… Merci pour tout, et je te jure, cette fois-ci, c'est le dernier traçage ! Quand tu veux pour une Chinette.

Merci à Pauline Collon, co-promotrice attentive de cette thèse. Merci pour toutes tes corrections pointilleuses (des articles, du manuscrit de thèse). Tu as clairement contribué à élever le niveau et la rigueur scientifique de mes recherches! Merci d'avoir lancé le projet OM-MADE. Merci pour ton soutien et tes encouragements. Merci de m'avoir accueillie à Nancy à plusieurs reprises dans une équipe si sympathique – au passage, je remercie d'ailleurs toute l'équipe RING de l'époque (François, Pablo, Jonathan, Guillaume R., Guillaume C., Jeanne, Julie, Gautier,…) pour avoir rendu mes séjours chez vous si agréables !

Un énorme merci à Jean-Marc Baele, catapulté sur ce sujet de thèse au détour de quelques carbonates suspects! Merci d'avoir accepté de faire partie de l'aventure sans savoir à priori qui, quoi, où, comment… Grâce à toi, l'intérêt karstogénétique de Furfooz a trouvé tout son

sens! Merci pour ta disponibilité et tes explications pédagogiques et pointilleuses… J'espère pouvoir encore faire de belles découvertes scientifiques à tes côtés !

Merci à Yves Quinif et Sarah Vandycke pour avoir fait partie du comité d'accompagnement. Merci pour vos avis et vos regards critiques et passionés, merci pour votre intérêt, merci pour votre sympathie!

Merci aux autres membres du Jury pour avoir accepté d'évaluer le travail présenté dans ce manuscrit: Dr. Nathalie Dörfliger, Dr. Malcolm Field, Pr. Johan Yans. Merci pour vos conseils et critiques avisées, merci pour le regard neuf apporté à cette thèse. Thank you, Malcolm, for having overcome your flight fright and being an "oversea" committee member. Thank you for your constant interest in our research.

Merci au Professeur Rudy Swennen et à ses étudiants de la KUL, Stefanie Van Offenwert et Gert-Jan De Ridder, pour leurs excellents travaux de fin de bachelier réalisés à Furfooz.

Merci à Anne-Julie Tinet, de l'Université de Lorraine, pour la création et le suivi d'OM-MADE.

Merci à l'asbl Ardennes et Gaume et au gestionnaire du Parc de Furfooz, Monsieur Goffin, pour nous avoir donné accès sans restriction à cette superbe Réserve Naturelle.

Merci à Michel Pauwels pour ses nombreuses plongées à Furfooz. Merci de ta sérénité et de la confiance que tu nous as accordée !

Merci à tous les spéléo qui, un jour ou l'autre, sont passés à Furfooz et ont contribué à la connaissance de ses réseaux karstiques. Merci tout particulièrement à Bibiche, Rudy, Jean-Benoit et Jean-Christophe pour leurs fouilles permanentes ! Bravo pour la découverte de La Sépulture ! Merci à Jean Godissart pour nous avoir fourni ses chroniques sur les sources de la Galerie des Sources.

Merci à la Cwepps pour leur inventaire minutieux des cavités karstiques de Wallonie.

Merci à Amaël Poulain pour avoir si bien rempli la chaise de bureau à côté de la mienne ;) Merci d'avoir été le premier investigateur du double pic, merci pour les échanges d'idées toujours enrichissants, merci pour les bons petits délires en colloques, merci pour le soutien et l'ambiance ! Et merci d'avoir été le témoin de mon plongeon dans la Lesse… ;o

Monsieur Augu Dekoninck, merci pour ta bonne humeur permanente ! Avec toi, on a toujours la banane ! J'ai été heureuse de partager mes années d'assistanat avec toi !

L'impétrante remercie Monsieur le président – dit Johan – pour ses chaleureuses salutations de couloir ! Merci pour la bonne ambiance et les discussions diverses et variées à propos de la recherche ou autre. Merci de m'avoir emmenée au Maroc, merci pour la bouteille de champagne que je n'ai jamais bue ;o

Merci à tous mes collègues du département Geo^2. Il y a une ambiance exceptionnelle qui règne ici et c'est grâce à vous tous !

Merci à Isabelle pour m'avoir transmis tous ses trucs et astuces d'assistante ! Et merci de ne pas m'avoir laissé tomber dans la Lesse ;)

Merci à tous les étudiants dont j'ai eu le plaisir d'être l'assistante. J'espère sincèrement avoir pu vous transmettre un maximum. Merci de m'avoir accordé votre confiance. Merci à Caroline Thomas pour son travail de fin de bachelier à Furfooz. Merci à Corentin Gervais pour s'être en premier cassé la tête sur la maquette de terrain.

Merci à ma famille et belle famille pour votre soutien! Maman, Papa, merci pour votre gentillesse, pour votre aide quotidienne et l'appui logistique dont on abuse ! Merci de m'avoir soutenue dans mon choix d'étude et de m'avoir permis d'aller au bout ! Merci Alex pour ta gentillesse, tes corrections d'anglais et ton crément d'Alsace ;) Merci Thérèse pour ton aide avec les enfants.

Merci à mes amis pour votre intérêt et vos encouragements ces derniers mois ! Désolée d'avoir été moins présente ; ne vous inquiétez pas, je vais me rattraper ;)

Et enfin, merci à ceux qui me soutiennent quotidiennement: Jean-François et nos deux adorables petites boules d'amour, Florent et Aline. Merci pour vos sourires, vos rires et vos pleurs. Vous êtes mon moteur de tous les jours !

« La moindre chose qui se forme au monde est toujours le produit d'une formidable coïncidence »

P. Teilhard de Chardin

Abstract

This manuscript presents the research led in the context of a Doctorate in Geology and Hydrogeology. The study focuses on the specific case study of the Furfooz karst system, located in a Carboniferous mudmound of Tournaisian-Visean Age (Waulsort Formation), in Southern Belgium. This massif supported a heterogeneous dolomitization that takes the form of dolomite patches. An intensive karstification occurs through the massif. Within the saturated zone of the massif, an underground river infiltrates, from the surface Lesse River, through a swallow hole called “Le Chantoir des Nutons”. From there, the underground river flows on about 1.2 km to a diffuse resurgence (“Trou de la Loutre”), and crosses two meanders of the surface river on its path. The underground river flows through contrasted geometries: small conduits vs. underground voluminous lakes (the “Trou Qui Fume” lake and the “Puits des Vaux” lake). Several cave networks give access to the river. The Furfooz karst is investigated, in the present work, through two main approaches: the hydrogeological functioning of the karst system, and the karstogenesis of the massif.

The hydrogeological approach concentrates on the study of the underground river that drains the conduit system. A complete monitoring of the river (water-level data, physico-chemical data, gauging of flow-rates) was set up for several years to characterize the functioning of the river. The study is then focused on solute transport issues. Fifteen tracer tests were conducted on the site, in various discharge conditions, and from different injection points. They highlighted a complex functioning of the Furfooz system, mainly due to the presence of the lakes on the tracer path. Double-peaked breakthrough curves (BTC) appear downstream the lakes. These results are very sensitive to the discharge conditions. The double-peaked BTCs are interpreted, in a conceptual model, as the result of a double advection-dispersion phenomena through two exchanging flow zones that takes place within the lake. This conceptual model ought to be nuanced, as single-peaked BTCs are observed downstream the lakes at very low discharge conditions. The conceptual model, based on field information, is then confronted to physical and numerical modelling. The simulations show that the conceptual model is relevant to explain the double-peaked BTCs observed on the field. The dimensioning achieved through the modelling is constrained by some strong field hypotheses.

To a smaller extent, this manuscript develops theories about the karstogeneis of the Furfooz massif. Some specific geochemical processes of dedolomitization and calcite cementation are revealed. These processes are geometrically related to karst cavities in the dolomitized zones of the mudmound. Analyses (cathodoluminescence, isotopic analyses, fluid inclusions measurements, and Laser Induced Breakdown Spectroscopy imaging) tend to show that these geochemical changes could also be related in time with the ongoing karstification process. This first set of observations open doors to further investigations.

Contents

Chapter 1 Introduction **3**
1.1 Karst: general considerations 3
1.2 Motivation and objectives of the doctoral research 5
1.3 A case study: site choice 5
1.4 Dissertation content 7
1.5 References 8

Chapitre 2 Geographical and Geological Setting **11**
2.1 Geographical setting and geomorphology 11
2.2 Geological setting 11
2.2.1 Regional features 11
2.2.2 Local setting 14
2.2.2.1 Lithological description 14
2.2.2.2 The Waulsortian buildups 18
2.2.2.3 Local structures 22
2.2.2.4 Karstification 24
2.2.2.4.a Field observations 25
2.2.2.4.b Laboratory investigations 28
2.2.2.4.b.1 Material and methods 28
2.2.2.4.b.2 Petrography 29
a. Dolomite (Figure 20 A) 29
b. Calcite in cavities (Figure 20 B, C) 30
c. Dedolomite (Figure 21) 30
d. Relationships between the fabrics and interpretation 31
2.2.2.4.c Discussion and perspectives 33
2.2.2.4.d New data 35
2.2.2.4.d.1 Isotopic and fluid inclusions data 36
2.2.2.4.d.2 LIBS data 36

a. Material and method 38
b. Results 40
c. Discussion 43
2.2.2.4.d.3 Conclusion 45
2.3 References 47

Chapitre 3 Hydrogeological setting 55
3.1 Regional setting 55
3.1.1 Hydrogeological units 55
3.1.2 The flow scheme at a mid- to local-scale 57
3.2 The Furfooz karst system 58
3.2.1 Description 59
3.2.1.1 The Chantoir des Nutons swallow hole (CN) and the Trou Qui Fume cave (TQF) 59
3.2.1.2 The Puits des Vaux cave and lake (PDV) 62
3.2.1.3 The Sepulture cave (SEP) 64
3.2.1.4 The Galerie des Sources cave (GDS) 64
3.2.1.5 The Trou de la Loutre cave (TDL) and the Abri de la Source (ASO) 66
3.2.2 Characterization of the system hydrodynamic 68
3.2.2.1 Methodology 68
3.2.2.2 Monitoring results 69
3.2.2.2.a Hydrometry 69
3.2.2.2.a.1 Hydrological context 69
3.2.2.2.a.2 Water-level data 70
3.2.2.2.a.3 Flow-rate data 74
3.2.2.2.b Physico-chemical variability 76
3.2.2.2.b.1 Probes data
3.2.2.2.b.2 Chemical analyses 80
3.3 References 82

Chapitre 4 The dye-tracing system of Furfooz **85**
4.1 Introduction 85
4.2 Tracer tests in the karst conduit system of Furfooz 87
4.2.1 Methodology 87
4.2.2 Historical data 91
4.2.3 Injections at the CN swallow hole 94
4.2.3.1 Tracer test 1 94
4.2.3.2 Tracer-test 2 98
4.2.3.3 Tracer test 3 100
4.2.3.4 Tracer test 4 102
4.2.3.4.a Observations at the TQF lake 103
4.2.3.4.b Observations at the PDV lake 105
4.2.3.4.c Observations at the GDS 107
4.2.3.5 Tracer test 5 108
4.2.3.6 Tracer test 6 110
4.2.3.7 Tracer test 7 111
4.2.3.8 Tracer test 8 112
4.2.3.9 Brief summary 114
4.2.4 Injections at the TQF river 116
4.2.4.1 Tracer test 9 116
4.2.4.2 Tracer test 10 117
4.2.5 Injections at the PDV lake 118
4.2.5.1 Tracer tests 11 and 12 118
4.2.6 Injections at the GDS site 119
4.2.6.1 Tracer tests 13 and 14 119
4.2.7 Injection at the Sebia (tracer test 15) 121
4.3 Discussion 122
4.4 References 131

Chapter 5 Physical modelling **137**
5.1 Introduction 137
5.2 Scaling operation 138
5.3 Tracer tests 140
5.3.1 Testing of the conceptual model 140

5.3.2 Discharge influence 141
5.4 Discussion 143
5.5 References 145

Chapter 6 Numerical modelling 149

6.1 Introduction 149
6.2 The modelling tool 151
6.2.1 A new model: OM-MADE 153
6.3 Modelling of the Furfooz conceptual system 155
6.3.1 The Furfooz conceptual system 155
6.3.1.1 Discretization of the conceptual system 156
6.3.1.2 OM-MADE simulations 157
6.3.1.3 Calibration and final fitting 159
6.3.1.4 Sensitivity tests 163
6.3.2 The Furfooz conceptual model at very low discharge conditions 167
6.4 Conclusion 172
6.5 References 174

Chapter 7 Conclusions and Perspectives 179

7.1 Summary and main outcomes 179
7.1.1 Karstification 179
7.1.2 The karst conduit system of Furfooz 180
7.1.2.1 Monitoring 180
7.1.2.2 Tracer tests 180
7.1.2.3 Modelling 181
7.2 Perspectives 182
7.2.1 Karstogenesis 182
7.2.2 Solute transport issue 183
7.3 Final comment : karstogenesis vs. solute transport 184
7.4 References 185

Appendices 187

Chapter 1

Introduction

Chapter 1 Introduction

Karst is a fascinating world that constitutes a playground for inquiring minds. From amateur speleologists to professional scientists, from painters to writers, from children to grown-up, no one can be left unmoved in a karst environment. The beauty of the unknown has led many disciplines to give interest to this medium. Numerous research studies have been conducted on karst areas all over the world keeping in mind one single line: the underworld follows its own rules.

1.1 Karst: general considerations

The word "karst" refers to a carbonate plateau in the Balkans (named "*Kras*" in Slovene, "*Carso*" in Italian and "*Karst"* in German) where an extended multi-disciplinary work about biology, hydrogeology, and geomorphology of the karst was first settled in the 19th century (Gams, 1993; Kranjc, 2011). Karst points out every shape in nature that results from erosion and weathering of carbonate rock formations. In the soil air, CO_2 is mainly the result of organic activity. When this CO_2 dissolves in water, it becomes carbonic acid (H_2CO_3). The chemical reaction of carbonic acid-enriched water with carbonate rocks is responsible for **carbonate dissolution** (Dreybrodt, 1988; White, 2016). This weathering can be expressed through specific shapes in the landscape but also (and mainly) through unseen subterraneous developments.

If mechanical erosion should also be considered in the extended karstification process, the chemical weathering is really the engine of karstification. It is responsible for the development of secondary **porosity** that originates mainly from the enlargement of a primary porosity (Ford & Williams, 2007). However, several conditions are necessary to allow this secondary porosity to develop into a karst network with conduits and drains. The massif must be made of a thick, mechanically resistant, and prone to dissolution carbonate rocks. They should have an intense developement of joints to allow **circulation of groundwater**. The availability of groundwater must be high and, furthermore, the groundwater should be able to enter and penetrate the massif through very local pathways driven by the hydraulic head (Dörfliger, 2010; Quinif, 1983). Time is a very important parameter that constraints karst development. Indeed, karstification is a dynamic process that leads the karst system to evolve through time (Ford & Williams, 2007). The controlling arguments of this evolution consist mainly in **kinetic considerations**. Dreybrodt (Dreybrodt, 1990) has highlighted, through geochemical modelling, that the development of conduit permeability through time is constraint by three determinant parameters : the width of the initial aperture, the hydraulic gradient and the path length. It is indeed necessary for the initial aperture to be large enough in order to avoid a too quick sur-saturation of the circulating groundwater, which would lead to a dissolutional enlargement near the surface only. A sufficient aperture width will allow, depending of the kinetics threshold, under-saturated waters to travel from the recharge to the (future) discharge

area(s), dissolving the encountered carbonates. Karstification is thus selective. Of course, this minimum width also depends on the **hydraulic gradient** (defining the velocities) and on the length of the permeable path (White, 2002; Worthington & Ford, 2009). Thanks to a solutional enlargement, the secondary porosity evolves in tertiary porosity (conduits) in which the flow becomes turbulent and dependent on the hydraulic difference between input and output (Ford & Williams, 2007).

The development of a high inter-connected porosity allows circulation of groundwater, which turns karst areas into underground environments that should be seen as potential groundwater reservoirs. A karst aquifer is defined by different levels of porosity hydraulically connected: open fractures, conduits and caves where the flow is driven by a regional hydraulic gradient. Given the constant evolution mentioned above, karst aquifers can be defined as "self-organized, high permeability channel networks formed by a positive feed-back between dissolution and flow" (Worthington & Ford, 2009) (Figure 1). The **temporal variability** of a karst aquifer, along with **the spatial heterogeneity** of its porosity development, makes its study very specific compared to other aquifers.

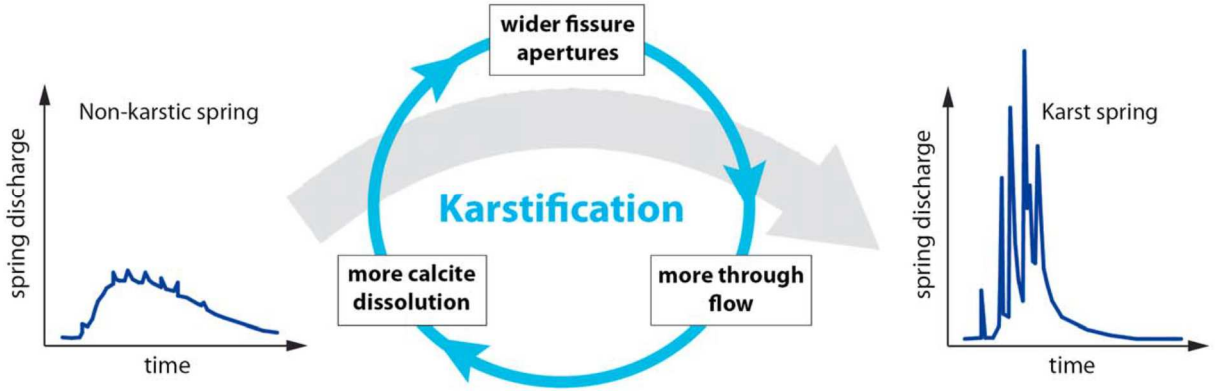

Figure 1. Schematic representation of the constant evolution of karst aquifer. The process of karstification is self-organized : dissolution of initial apertures allow more flow to enter, which itself creates more dissolution and so on (Hartmann, Goldscheider, Wagener, Lange, & Weiler, 2014).

The study of karst aquifers is indeed an essential research field. Karst regions cover a large surface of the Earth's continental area (10 to 15 %), and about 20 to 25 % of the world's population depends of the karst aquifers as groundwater resources (Ford & Williams, 2007). Protection of karst areas is obviously a major issue in the preservation of groundwater resources. This is particularly true given the high vulnerability of karst environments. A **vulnerability** that is difficult to deal with because of the important **heterogeneity** encountered in karst aquifers in regards to the distribution of hydraulic conductivities and the geometries of karst conduits (Drew & Hötzl, 1999).

1.2 Motivation and objectives of the doctoral research

For this PhD thesis, a karst area has been chosen as the object of study. This common object is investigated through two major aspects: the hydrogeological functioning of the karst system, and the geologic evolution and karstogenesis of the massif. These two approaches have in common a better understanding of the heterogeneities that characterize the karst development in general, but tackle this issue at different observation scales. On the one hand, the study focuses on a micro- to outcrop- scale method that aims to define the petrological and geochemical processes leading to the creation of porosity and the development of karst conduits. On the other hand, the characterization of the flow dynamics in these conduits considers a wider scale (massif scale). The multi-scale approach proposed in this work aims to improve the knowledge of karst aquifers and to therefore help in improving the management of water resources contained in those reservoirs.

The two approaches of the study do not however have the same weight in this thesis. The karstogenesis study is limited to a first set of observations, using different techniques, that open doors for further investigations. These observations and the conclusions that could be drawn, appertain to the Chapter 2 of the dissertation on the geological settings of the study area.

The hydrogeological approach is more widely developed in the present work. The study of a karst aquifer in its whole is a complex matter that must deal with the slow and diffusive flow existing in the matrix and the fast and concentrate flow running in the conduits and cave network. This doctoral research has not considered the global behavior and functioning of a karst aquifer but mainly focuses on the saturated zone, and more specifically, on the flow that drains the conduits system of the studied massif.

1.3 A case study: site choice

The issues tackled in this PhD dissertation are related to natural processes. The philosophy of the research is to base the scientific debate on field observations. Its methodology is resolutely practical in order to demonstrate and quantify natural processes. A case study was then to be chosen. The Carboniferous aquifer of Southern Belgium represents a major source of drinking water. It is widely exploited by water distribution companies, but is also constituted by geologic formations that are particularly prone to karstification (Nogarède et al., 2003). For this reason, this aquifer is highly vulnerable and specific protection strategies should be taken into account for its management, as it should be the case for karst aquifers in general. A better understanding of the object is, of course, the base of an integrated strategy.

The site of Furfooz, which lies on the Southern edge of this Carboniferous aquifer, was selected because the karst development in this massif is particularly heterogeneous. Furfooz is located in the South of Belgium (Figure 2) along the *Lesse* valley where Carboniferous limestones outcrop massively.

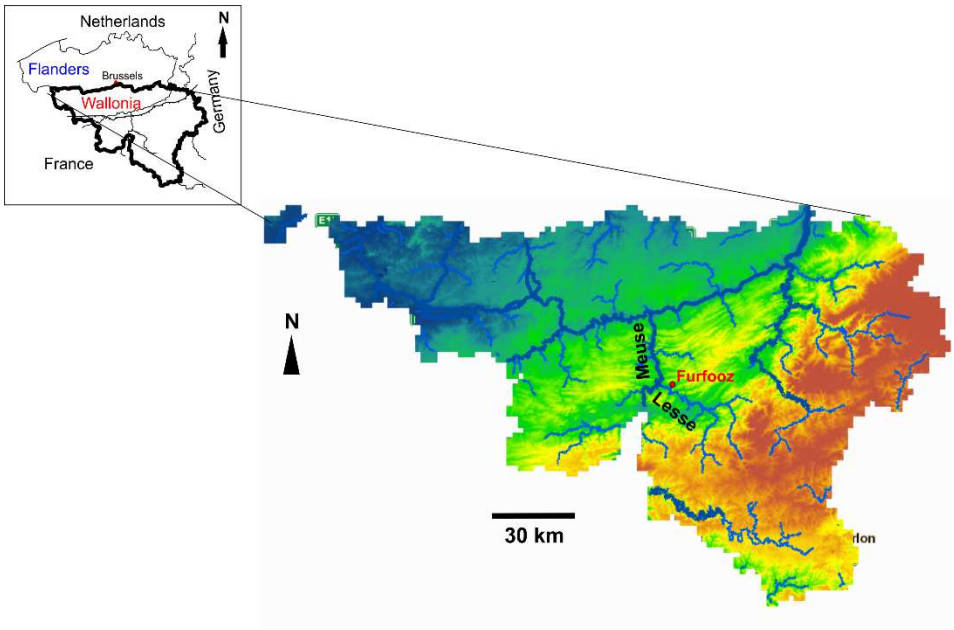

Figure 2. Map of the Walloon Region (Southern part of Belgium) and location of the Furfooz case study.

More precisely, the studied karst system has developed mainly in carbonates of the Waulsort and Leffe Formations (Late Tournaisian to Early Visean, Low Carboniferous). The karst development of the Furfooz massif is particularly intensive in comparison to the other surrounding limestones, at least regarding the frequency of karst cavities (

Figure 3). Though, the Waulsortian rocks of Furfooz are known to be partially dolomitized (Brodkom, 1994; Lees, 1982) . It is usually a priori considered that dolomite is less soluble than calcite (Liu & Dreybrodt, 1997); and so a first question that arises in this work is: "Why are those partially dolomitized rocks more prone to karstification than the limestones nearby?" Obviously the question relates to heterogeneity issues within the massif: difference in relative solubility and mechanical properties of limestone and dolostone, structural heterogeneities and their influences on karst development, differential evolution of the massif related to specific paleo-conditions, etc.

The geometrical heterogeneity of the active karst conduits is the second issue that has motivated the selection of Furfooz. Amongst the numerous karstic development of the Furfooz massif, some have developed into interconnected conduits in which flows an underground river today. The underground river in Furfooz has been known for a long time (Van den Broeck & Rahir, 1903). It constitutes a rare example of a double meander crossing in Belgium. One major feature of this system is the existence of voluminous underground lakes (several thousands of cubic meters) along the river flow. These volumes contrast with the secluded underground river (0.05 to 1 m^2) that flows into and out of the lakes. The influence of contrasted flow sections on solute transport represents in this context an interesting aspect to characterize.

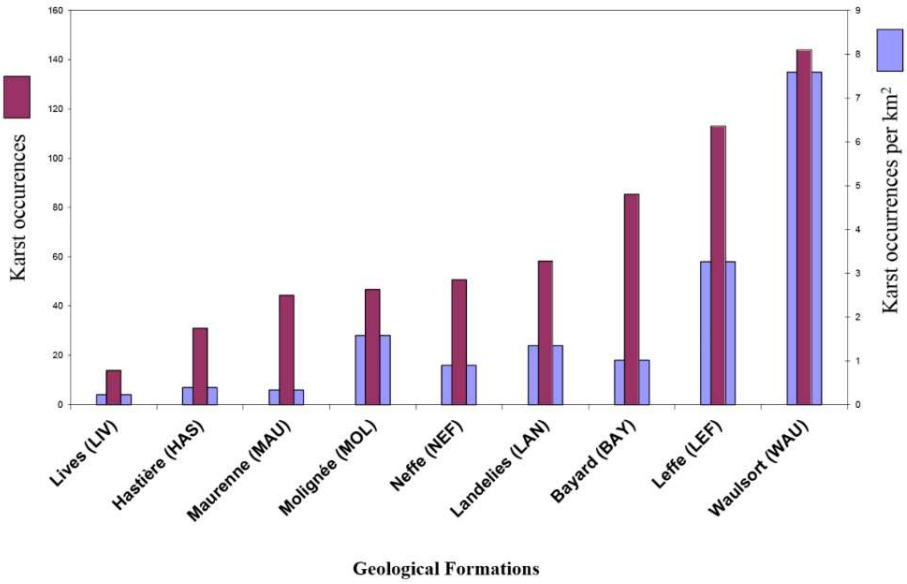

Figure 3. Frequency of karst in the Tournaisian-Visean carbonate formations of the Furfooz area (raw data retrieved from Thys and Michel, 2014).

1.4 Dissertation content

This manuscript will first describe the geographical and geological settings of the Furfooz karst system (Chapter 2). Special attention is given to the sedimentology of the Waulsortian mud-mounds. In this chapter, the specific karstification of the Furfooz massif is detailed. The main results of the analyses performed on rock materials are given and their interpretation is exposed.

Chapter 3 summarizes the hydrogeological setting of the Furfooz karst system. The chapter starts with general considerations over the regional hydrogeology and then focuses on the Furfooz karst system. After a complete description of the different cave networks of this system, Chapter 3 exposes the results of the hydrogeological monitoring conducted in the karst system.

Once the hydrogeological functioning of the Furfooz conduit system has been defined, numerous tracer tests will be detailed in Chapter 4. This chapter starts with the methodology applied for the production and interpretation of these tests, continues with the description of each test, and ends with a synthesis on the dye-tracing system of Furfooz and the establishment of a conceptual model.

Chapter 5 and 6 respectively propose a physical and a numerical modelling of the Furfooz conceptual system. Both chapters start with theoretical considerations before exposing the modelling postulates. The results and interpretation of the simulations are then detailed.

Finally, this dissertation concludes with the main outcomes and perspectives to this doctoral research (Chapter 7).

1.5 References

Brodkom, F. (1994). *Les roles et comportements tectoniques de mudmounds waulsortiens au sein de séries calcaro-schisteuses dinantiennes lors des déformations varisques.* Univeristé Catholique de Louvain.

Dörfliger, N. (2010). *Guide méthodologique : Les outils de l'hydrogéologie karstique pour la caractérisation de la structure et du fonctionnement des systèmes karstiques et l'évaluation de leur ressource*. Avec la collaboration de Ph. Crochet, R. Guerin, N. Jozja, B. Marsaud, P-H. Mondain, Ph. Muet, V. Plagnes ; BRGM RP- 58237-FR, 246 pp., 82 ill., 5 ann.

Drew, D., & Hötzl, H. (1999). Karst hydrogeology and human activities : impacts, consequences and implications. In D. Drew & H. Höltz (Eds.), *International contributions to hydrogeology* (p. 338). Rotterdam: AA. BALKEMA.

Dreybrodt, W. (1988). *Processes in Karst systems : physics, chemistry, and geology*. Springer-Verlag.

Dreybrodt, W. (1990). The role of dissolution kinetics in the development of karst aquifers in limestone: a model simulation of karst evolution. *Journal of Geology*, *98*, 639–655.

Ford, D., & Williams, P. (2007). *Speleogenesis: The development of cave systems*. *Karst Hydrogeology and Geomorphology*. John Wiley & Sons Ltd. 562 p. https://doi.org/10.1002/9781118684986

Gams, I. (1993). Origin of the term "karst", and the transformation of the classical karst (kras). *Environmental Geology*, *21*(3), 110–114. https://doi.org/10.1007/BF00775293

Hartmann, A., Goldscheider, N., Wagener, T., Lange, J., & Weiler, M. (2014). Karst water resources in a changing world: Review of hydrological modeling approaches. *Review of Geophysics*, *52*(3), 218–242. https://doi.org/10.1002/2013RG000443

Kranjc, A. (2011). The Origin and evolution of the term "Karst"; *Procedia - Social and Behavioral Sciences*, *19*, 567–570. https://doi.org/10.1016/j.sbspro.2011.05.170

Lees, A. (1982). The paleoenvironmental setting and distribution of the Waulsortian facies of Belgium and southern Britain. In K. Bolton, H. R. Lane, & D. V. LeMone (Eds.), *Symposium on the Environmental Setting and Distribution of the Waulsortian Facies* (pp. 1–16). El Paso Geological Society and University of Texas at El Paso.

Liu, Z., & Dreybrodt, W. (1997). Dissolution kinetics of calcium carbonate minerals in H2O-CO2 solutions in turbulent flow: the role of the diffusion boundary layer and the slow reaction H2O+CO2↔H+ + HCO3-. *Geochemica and Cosmochemica Acta*, *61*, 2879–2889.

Nogarède, P., Vanbrabant, Y., Rekk, S., & Hallet, V. (2003). *Notice explicative de la carte hydrogéologique Hastière-Dinant (53/7-8)*. Facultés Notre-Dame de la Paix, Namur, Service Public de Wallonie, DGO 3.

Quinif, Y. (1983). Éléments d'une approche énergétique du karst. Application à quelques exemples réels de karsts. *Karstologia : Revue de Karstologie et de Spéléologie Physique*, *1*(1), 47–54. https://doi.org/10.3406/karst.1983.2039

Thys, G., & Michel, G. (2014). Atlas du karst wallon : Bassin de La Basse Lesse. Commission Wallonne d'Etudes et de Protection des Sites Souterrains (CWEPSS), SPW Editions, 400p.

Van den Broeck, E., & Rahir, E. (1903). *La Lesse souterraine et la traversée des deux boucles de la rivière à* Furfooz *démontrée au moyen de la fluorescéine* (Hayez-im). Bruxelles.

White, W. (2015). Chemistry and karst. *Acta Carsologica*, *44*(3). https://doi.org/10.3986/ac.v44i3.1896

White, W. (2002). Karst hydrology: Recent developments and open questions. *Engineering Geology*, *65*(2–3), 85–105. https://doi.org/10.1016/S0013-7952(01)00116-8

Worthington, S. R. H., & Ford, D. C. (2009). Self-organized permeability in carbonate aquifers. *Ground Water*, *47*(3), 326–336. https://doi.org/10.1111/j.1745-6584.2009.00551.x

Chapter 2

Geographical and Geological Settings

Chapitre 2 Geographical and Geological Settings

In brief, in this chapter:

- Geographical and geological settings of The Furfooz Natural Reserve are defined at a regional and local scale;
- Sedimentological and structural considerations of the Waulsortian mud-mounds are exposed;
- Focus is given to the karstification of the Furfooz massif, with at first a description of field observations;
- Analysis results (cathodoluminescence, isotopes and fluid inclusions, LIBS (Laser-Induced Breakdown Spectroscopy) images) are presented and interpreted.

2.1 Geographical setting and geomorphology

The site of Furfooz is located in the south of Belgium, about 5 km SE from the city of Dinant (Figure 1). It sits on the southern border of a geomorphological unit called “Le Condroz”. The landscape of this unit is characterized by an alternation of ridges (locally called “tiges”) trending SW-NE and parallel depressions (locally called “chavées”), shaping the landscape as an undulating plateau. This plateau is cut by numerous rivers that are most of the time organized in a rectangular network. The main rivers are The Meuse flowing up north, and The Lesse flowing from east to west.

The Furfooz site lies along the meandering river Lesse which has three tributaries in the studied zone: The Saint-Hadelin and The Sebia on the right bank; The Ri des Vesses on the left bank (Figure 2). The altitudes vary around 90 m in the valleys and rise to 280 m on the plateau. About the land use, the plateaus are mainly dedicated to farmland while woods remain in the valleys. South of the Furfooz village, a Natural Reserve of about 4 km^2 has been created and is managed by the “Ardenne et Gaume non-profit organization”.

2.2 Geological setting

2.2.1 Regional features

The Condroz is located in the front of a structural unit called the Ardenne Allochton (Belanger et al., 2012). The latter represents the front part of a fold-and-thrust belt of Southern Belgium aged from Variscan time and part of the Western European Variscan Belt. The Ardenne Allochton is limited to the north by the Midi Fault and consists of fold-and-thrust structures

thrusting NNW (Figure 3). Those structures are oriented ENE – WSW except in some corridors where the trend changes to W – E (Lacquement et al., 2005; Averbuch et al., 2006).

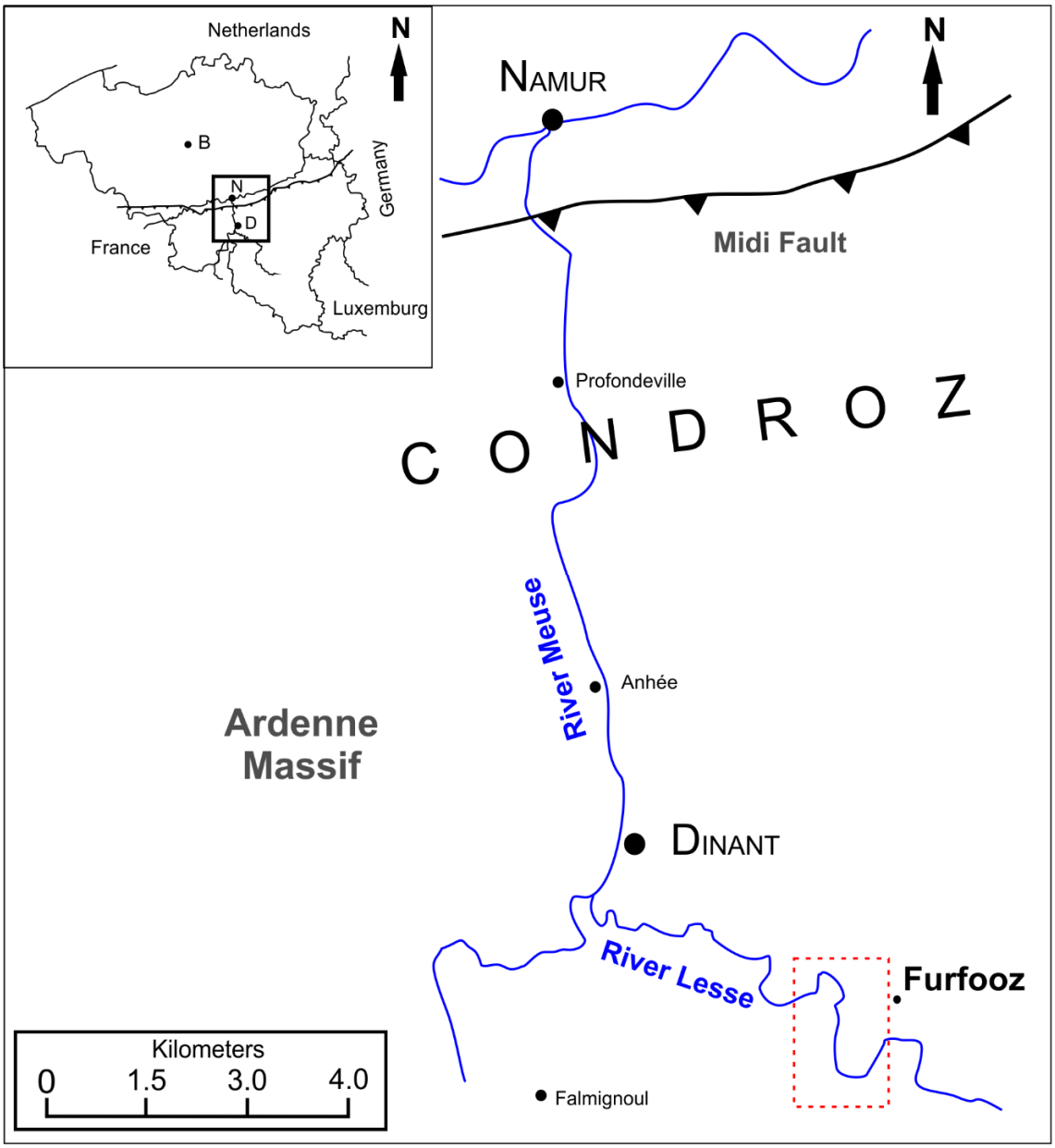

Figure 1. Geographical and geological settings of Furfooz. The main study site lies within the dashed-line box.

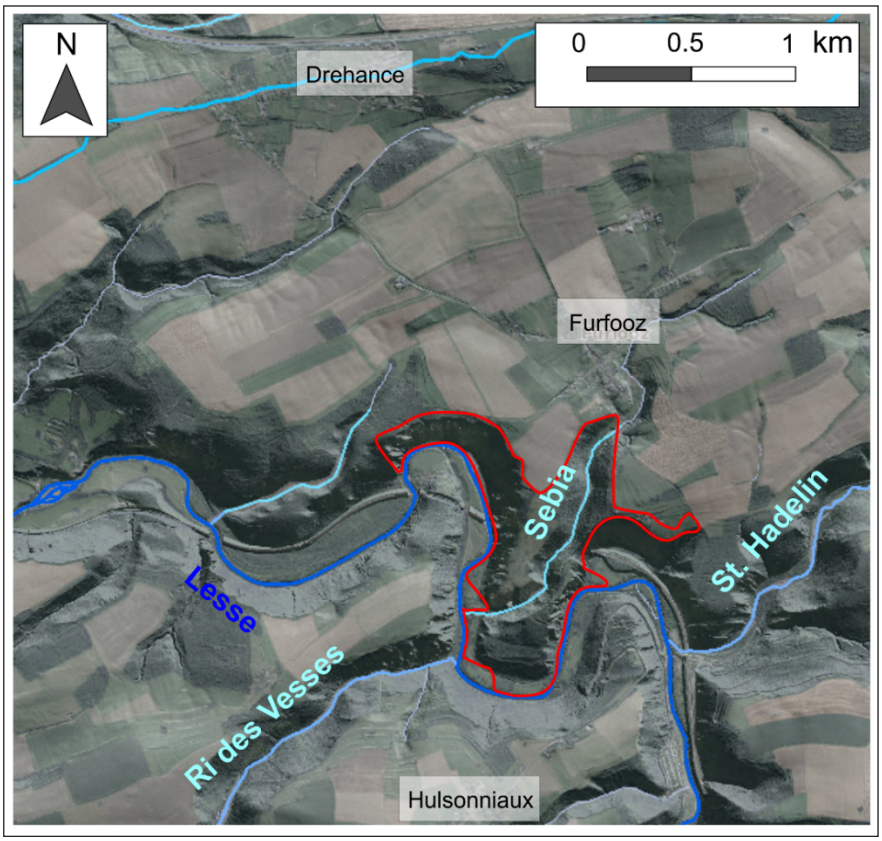

Figure 2. Landscape, land occupation and hydrography of the Furfooz Natural Reserve (limits in red) and its surroundings.

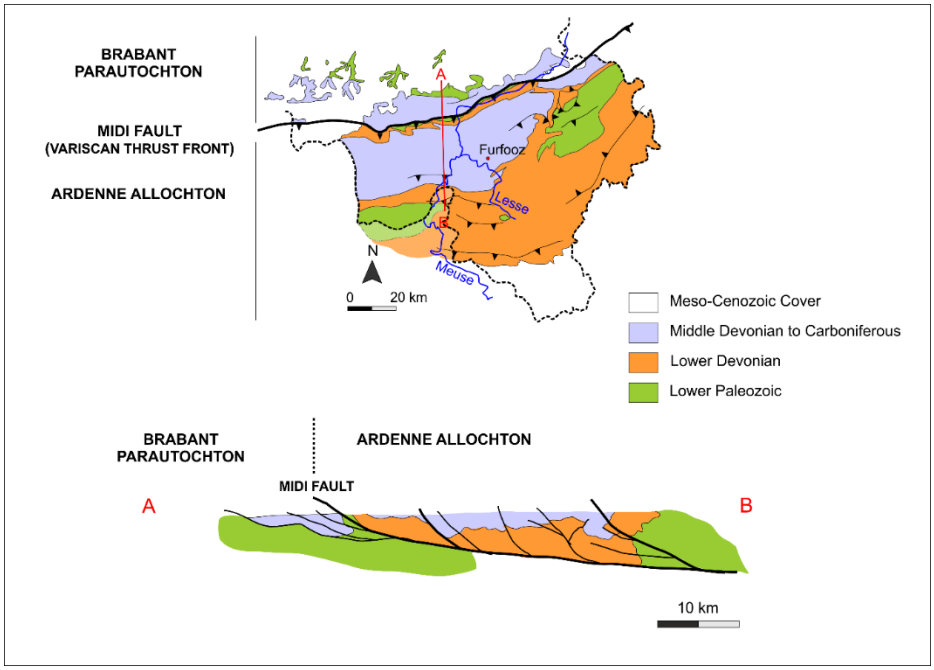

Figure 3. Regional geologic features of Southern Belgium (mofified from Averbuch et al., 2006). Furfooz lies on the south of the Variscan thrust front.

Furfooz is located in a unit composed of middle Devonian to Carboniferous rocks (Figure 4). More precisely, in this area, early Carboniferous limestones synclines alternate with late Devonian sandstones anticlines. The differential erosion affecting those rocks gives way to a series of depressions (in limestones) and hills (in sandstones) that shape the characteristic landscape of “Le Condroz”. Along with these highly folded rocks, longitudinal thrust faults are present. Karst occurences are frequent in the Carboniferous limestones and particularly in the Tournaisian Waulsort Formation as it can be seen on the regional geological map (Figure 4).

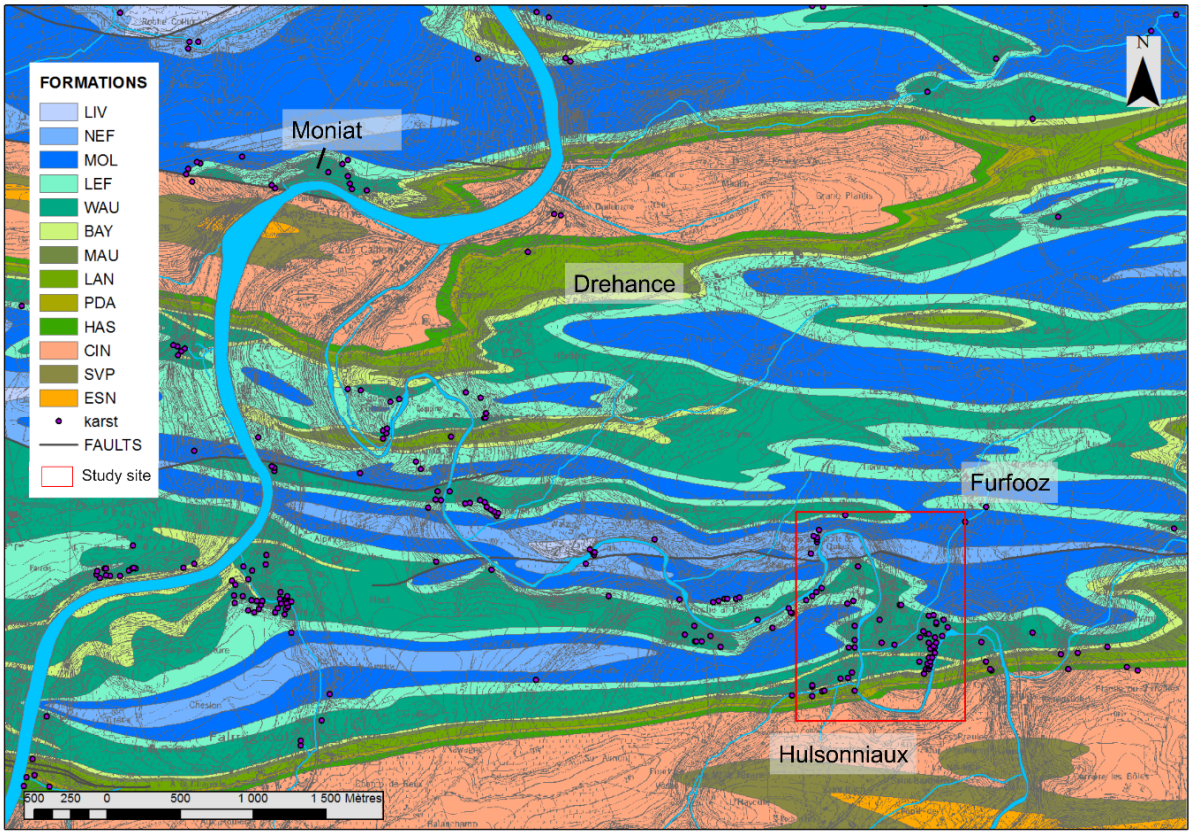

Figure 4. Regional geological map (scale 1:20 000). The Furfooz site stands on the southern edge of a large syncline that stretches from Drehance to Hulsonniaux (modified from Delcambre and Pingot, 1993).

2.2.2 Local setting

The following chapter gives first a lithological description of the official Formations defined on the geological map of the Furfooz area. In a second step, a review over the literature regarding the Waulsortian buildups is proposed. Then, it ends with an overview of the local structures and tectonic specificities in Furfooz.

2.2.2.1 Lithological description

The rock formations outcropping in the studied zone date from Late Devonian to Early Visean. The following descriptions, starting from the oldest formation to the youngest one, are

summarized from Delcambre & Pingot (1993), Bultynck & Dejonghe (2001), Poty et al. (2001). The log is presented in Figure 5.

The Ciney Formation (CIN) – Late Famennian (Strunian)

This Formation is constituted by fine-grained micaceous sandstones and siltstones. Nodular limestones are found at the base of the Formation. Thin shale beds appear upward. At the top, sandstones show a lime cement and some interbedded limestone can appear. The Formation thickness varies from 250 to 300 m.

The Hastière Formation (HAS) – Hastarian

The Formation consists of thin to thick-bedded crinoidal packstones with shale beds. The thickness varies from 20 to 35 m.

The Pont d'Arcole Formation (PDA) – Hastarian

It is constituted mainly by greenish shale with a few crinoïds. Some beds of crinoidal limestone are found at the top. A maximum thickness of 20 m has been recorded for this formation.

The Landelies Formation (LAN) – Hastarian

The Formation is formed by argillaceous crinoidal packstones interbedded with shales at the base of the formation. Brachiopods and corals can be abundant. The thickness is variable but is about 35 m in the studied area.

The Maurenne Formation (MAU) – Hastarian

It consists in argillaceous limestones and calcareous shales. Small clasts of brachiopods and corals are present in the limestone beds. It is about 20 m thick.

The Bayard Formation (BAY) – Ivorian

Well bedded crinoidal limestones constitute this Formation. Black cherts can be found locally. Some beds can be partially or totally dolomitised. This formation represents a basal lateral equivalent of the Waulsortian buildups or can be found as the sole of the buildups and sometimes as intercalations. The thickness depends of its proximity to the Waulsortian buildups; it varies from 5 to 30 m.

The Waulsort Formation (WAU) – Ivorian

This formation constitutes the main part of the Waulsortian buildups that are local lenticular mud-mounds (see chap. 2.2.2). It consists in massive wackstones and packstones, mainly made of crinoids and bryozoans. Three distinct facies are usually described: at the base, a

crinoidal and fenestellid packstone; in the middle, a spar-rich wackstone (the “veines bleues” facies); and a biomicrite at the top. Cherts are non-existent and secondary dolomitisation can be strong in some areas. The thickness is highly variable from 0 and up to 300 m.

The Leffe Formation (LEF) – Ivorian

It consists of well-bedded violet wackstones to packstones, locally cherty and poor in macrofauna. Diagenetic dolomitisation can occur. It represents the lateral equivalent of the upper part of the Waulsortian buildups or can be found in intercalations with the buildups or as their cap. It has a variable thickness, that is about 20 m in the studied area.

The Molignée Formation (MOL) – Moliniacian

This formation is composed of finely bedded black fine-grained limestones alternating with thick beds of dark grey limestone. It is locally cherty mainly in the upper part of the formation. The base of this formation can be locally contemporaneous with the upper part of the Waulsortian buildups as a lateral equivalent or it can directly overlie the buildups. The distribution and thickness of the Molignée Formation is linked to the buildups. Its thickness varies from a few meters up to more than 100 m.

The Neffe Formation (NEF) – Moliniacian

The base of the formation consists in thick beds (several meters large) of light grey packstones while the upper part is made of darker thin-bedded limestones with stromatholites. Abundant macrofauna is found (brachiopods, crinoids). Dolomitisation can occur, mainly at the base. It has a highly variable thickness, from 90 to 160 m.

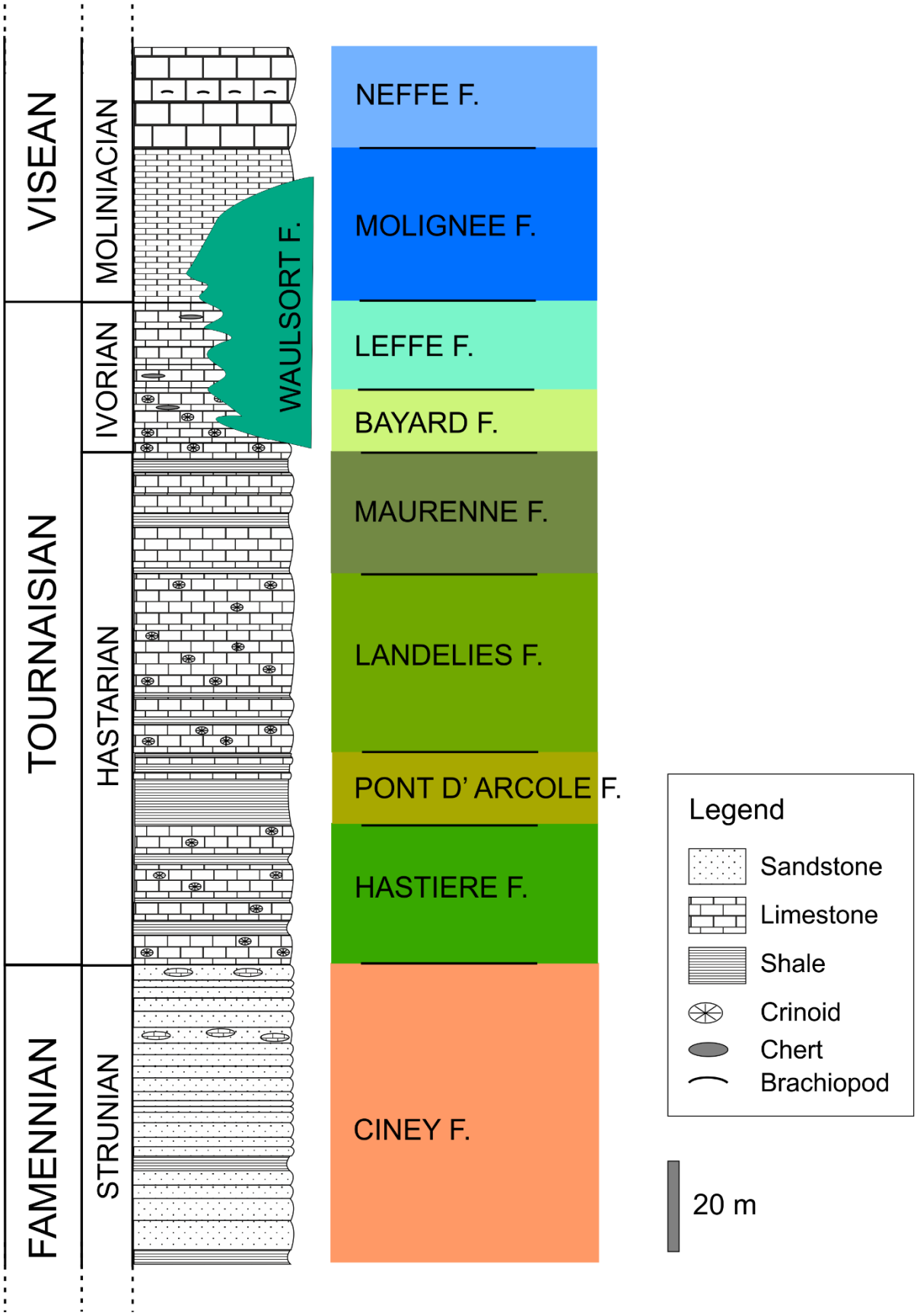

Figure 5. Lithostratigraphic log (modified from Delcambre and Pingot, 1993).

2.2.2.2 The Waulsortian buildups

The flooded karst system in Furfooz is mainly developed in the Waulsort Formation. The origin of the buildups has been debated for a long time. They were first described in the literature by Dupont (Dupont, 1883) as reef formations because he interpreted the sparry cavity fillings as stromatoporoids. He named those "reefs" from Waulsort, the village where it was first observed. The term "Wauslortian" was officially used by de Dorlodot (de Dorlodot, 1895) to refer to the massive "reefs" and their lateral bedded equivalents (the Leffe and Bayard Formations). From there, the Waulsortian "reefs" were recognized and described in several places in the world as Late Tournaisian occurences. The diagenesis of the buildups were soon questioned and through the extended work of Lees and his collaborators from the 50's to the 90's, the term "reef" was abandoned to the benefit of the word "mud-mound". Lees (Lees, 1961) stated that the Waulsortian buildups of Ireland did not have any rigid skeletal framework and that the spar cavities were not stromatoporoids. The main composant of the buildups was recognized as carbonate mud, having probably a microbial origin and with a complex diagenetic and compaction story creating the sparry cemented cavities (Lees & Miller, 1995). Today Waulsortian refers to the Waulsort Formation that composes the mud-mounds, while the lateral equivalents are recognized as peri-Waulsortian facies.

The Waulsortian buildups developed in several places all over the world (Figure 6) mainly during Late Tournaisian to Early Visean. The described lithofacies are rather characteristics and three "end-member" facies are recognized: bryzoan (fenesteliid) buried in micrite, wackstones with sparry masses, crinoid-rich packstones (Lees and Miller, 1995). The geometry of these buildups is, however, variable and they are therefore referred to as "Waulsortian banks" in some literature. As the Waulsortian buildups of Belgium present clearly a "mound" shape and are mainly carbonate mud accumulation, the term "mud-mounds" is used through this manuscript. The mud-mounds of Belgium are large lenticular formations that can extend on several kilometers across and a few hundred meters thick. They all lie within the Sedimentation area of Dinant (Figure 7) and are therefore linked to specific sedimentation conditions of this basin during Late Tournaisian times (Hance et al., 2001).

Lithofacies studies of the Waulsortian mud-mounds and their lateral equivalents allowed to construct a regional model setting the mud-mounds in a ramp environment development during Late Tournaisian (Lees, 1982). Petrographical analyses were led in several sections of the buildups and their proximal lateral equivalents (Lees et al., 1985). While some allochems, like ostracods and bivalve debris, are too widespread through the samples to give any clues for interpretation, other components were recognized to have a specific distribution through the Waulsortian and peri-Waulsortian rocks. Four assemblages of grain types are defined, from bottom to top:

(A) fenestrate bryozoans + crinoids + ostracods
(B) as (A) but + hyalosteliid sponge spicules
(C) as (B) + plurilocular foraminifera
(D) as (C) + cryptalgal coating, various micritization features and calcareous algae.

Figure 6. Distribution of the known Waulsortian banks through the world(modified from Lees and Miller, 1995). 1: Belgium; 2: France (Avesnois and Brittany); 3: England (southwest, central and northern) and South Wales; 4: Ireland; 5: Poland; 6: Afghanistan; 7: Algeria (possibly); 8: Canada (Alberta); 9 to 15: United States, 9 (North Dakota), 10 (Montana), 11 (California), 12 (New Mexico), 13 (Texas), 14 (Kentucky), 15 (Oklahoma and Missouri).

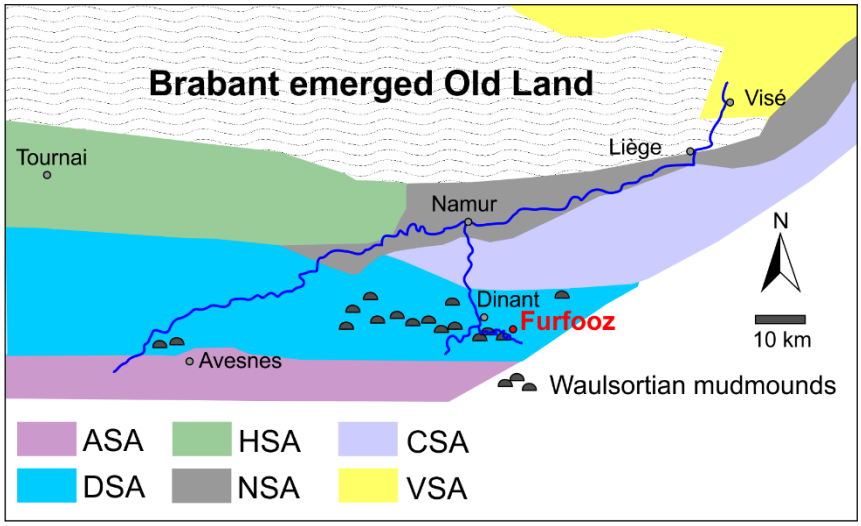

Figure 7. Sedimentation areas in the Namur-Dinant Basin (modified from Hance, Poty and Devuyst, 2001). ASA: Southern Avesnois Sedimentation Area, DSA : Dinant Sedimentation Area, HSA: Hainaut Sedimentation Area, NSA: Namur Sedimentation Area, CSA: Condroz Sedimentation Area, VSA : Visé Sedimentation Area.

Environmental interpretation of these assemblages provided evidences of the wide range of water depth over which the sediments have formed. Each assemblage is related to a bathymetry phase starting from 300 m deep (phase A) to rather shallow photic zone (phase D) (Figure 8). Some phases can be absent in mud-mounds, depending on the depth at which the growth of the buildup started. This initial depth evolved in time due to the late Tournaisian regression that could even have provoked downslope diachronism of the grain-type assemblages.

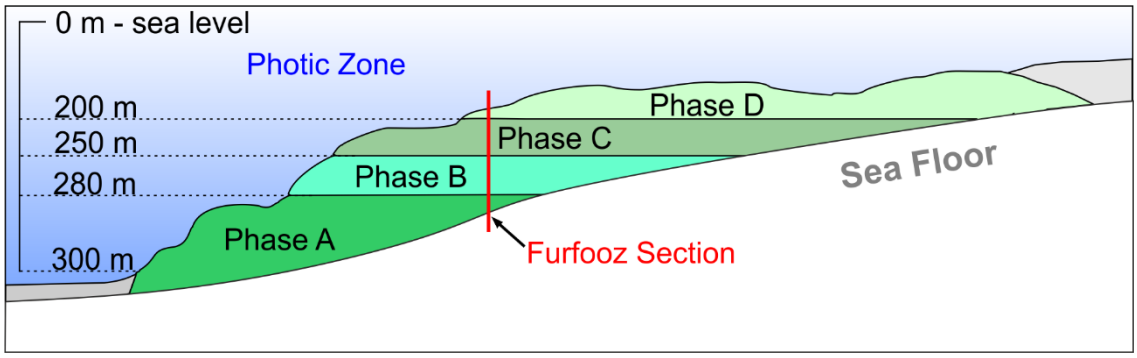

Figure 8. Phases A to D distribution pattern along a ramp setting (modified from Lees, Hallet et Hibo 1985).

The origin of the mud-mounds is not clearly established. Lees and Miller (Lees & Miller, 1995) proposed a genetic model starting with a mud-maker factory probably due to some microbial agents. The production of an active surface biofilm (by combinate action of bacterial agents and any fungal or cyanobacterial filaments) contributed to the binding of the mud grains as a "self-sealing mat". This biofilm could have been a "repellant" for other organisms at the beginning until some mud-tolerant colonizers (as bryozoans) became abundant and started to modify the substrate. In this new environment, epifaunas as crinoïds and shell organisms could appear. Dolomitisation of the mud-mounds has never been thoroughly studied, but is known to come at a later stage (post-Waulsortian) depending on regional factors. In the Irish examples, dolomitisation has been documented as polyphase and resulting from different modes of replacement (Lees & Hennebert, 1982; Lees & Miller, 1995). In any case, dolomitisation in the mud-mounds seems a complex process that is peculiar to each setting.

The massif of Furfooz offers the most complete sections within a Waulsortian mud-mound. This buildup is about 2 km long and 300 m thick. The exposed section of the massif gives the opportunity to observe both the Waulsortian and the peri-Waulsortian facies from the Bayard crinoidal sole to the Leffe Formation cap (Figure 9).

The four grain-type assemblages (A to D) are present in the Furfooz section (Figure 10). Dolomitisation occur throughout the Furfooz mud-mound but is very heterogeneous. Dolostone appears as patches through the massif, on the contrary of the bedded peri-Waulsortian facies where the dolomitisation follows the bedding. The dolomitisation rate is furthermore variable (from 10 % to total replacement).

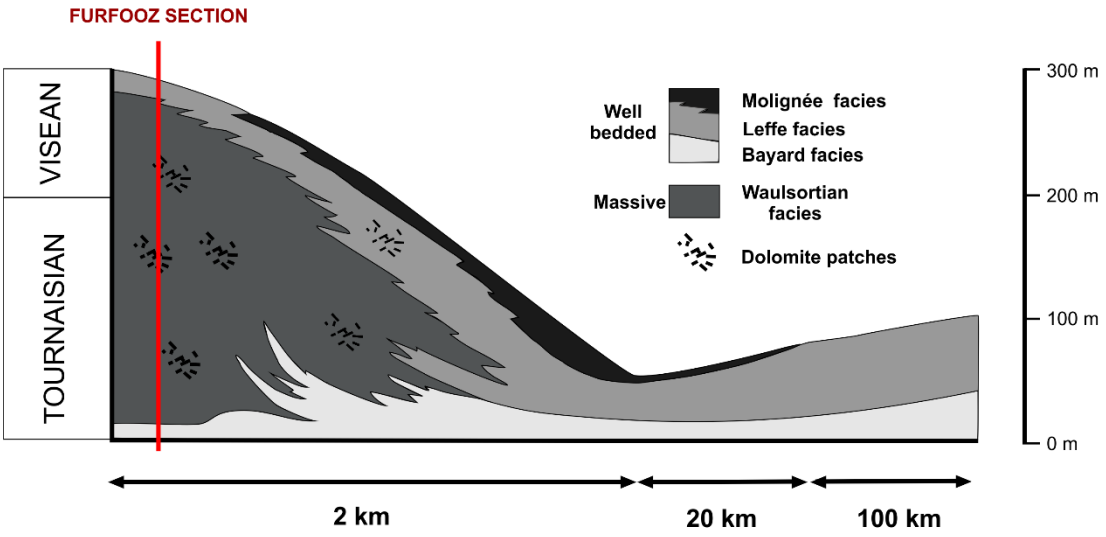

Figure 9. Conceptual model of the Furfooz buildup (modified from Lees, Hallet and Hibo, 1985).

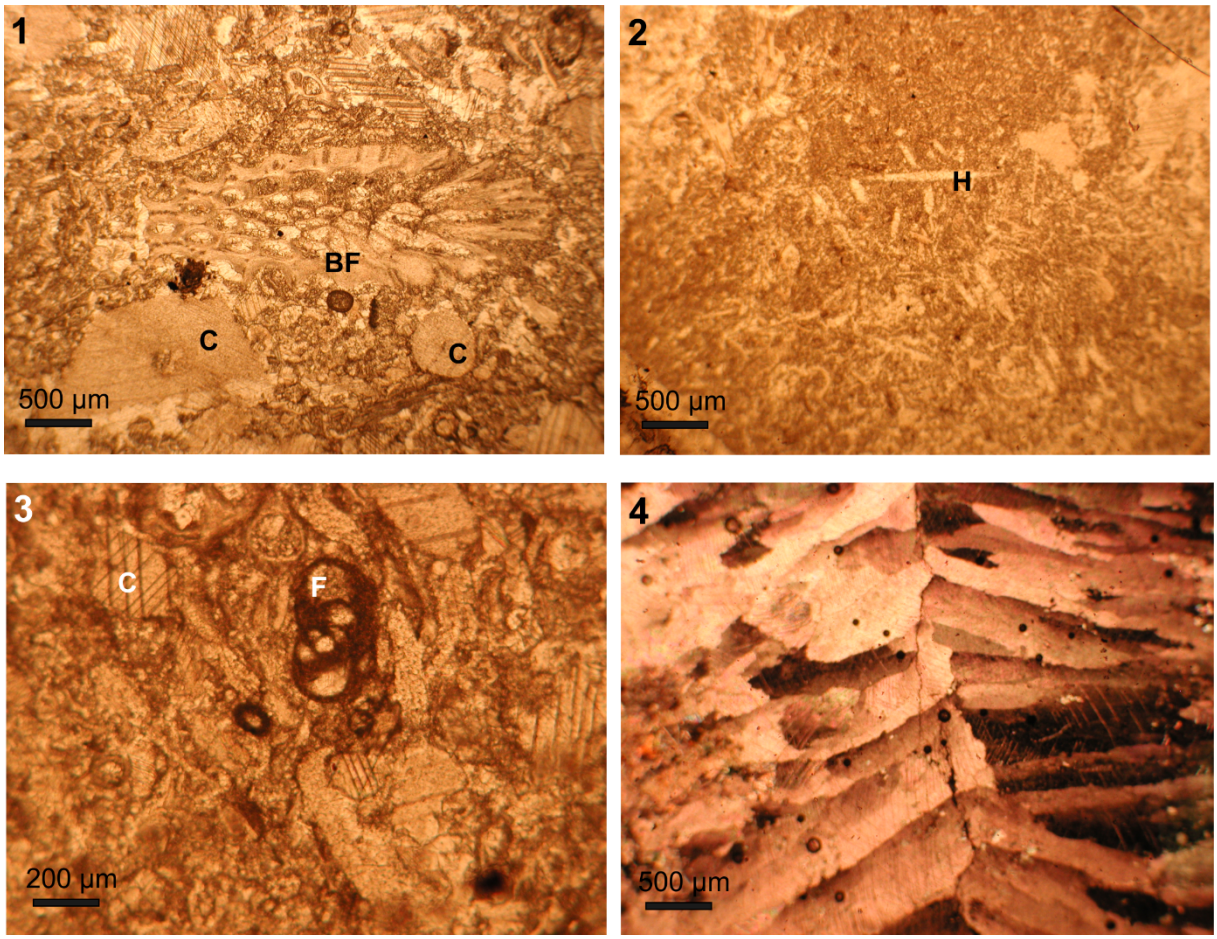

Figure 10. Microphotographs of some facies of the Waulsortian buildups found in the Furfooz section. 1) Facies A: wackstone to packstone with crinoids [C] and bryozoans fenestellid [BF], 2) facies B: appearance of the hyalosteliid sponges [H], 3) Facies C: appearance of the plurilocular foraminifera [F], 4) spar-filled cavity called "veine bleue".

2.2.2.3 Local structures

As said before, Furfooz lies on the south border of a large fold-and-thrust structure (locally called “synclinorium de Dinant”). More precisely, the Furfooz massif lies on the southern edge of a large Carboniferous syncline that stretches from Drehance in the north to Hulsonniaux in the south, pinched between two sandstones anticlines (Figure 4). The general trend of those structures is roughly W – E. Some major longitudinal thrust faults dipping south have developed, most of them being reverse faults. Numerous secondary folds appear within the syncline, most of them being plunged in opposite directions.

In Furfooz the beds tend to be subvertical (dip varying from 75 to 90 °) or even slightly overturned to the north. The mean trend varies from N70°E to N90°E. Starting from Chaleux, where a reverse longitudinal fault stands, and going to the south to the Lieu-dit “Haute Recène”, two major folds are recognized in the Waulsortian massif of Furfooz. The anticline axis A1 is plunged to the east. It extends widely to the west where its fold axis shows variation in its plunge and in the orientation of its axial plane. The syncline axis S2 is, in the east, slightly thrust to the north and plunged to the east, while in the west this same S2 is upright and plunged to the west (Brodkom, 1994). Two small secondary folds (A3 and S4) are also visible only on the western peri-Wauslortian envelope (Figure 11, Figure 12).

The tectonic behavior of the mud-mounds is a complex matter. This is mainly due to the contrasted lithofacies of the massive mud-mound and its “bedded envelope”(Brodkom, 1994; Delcambre & Pingot, 1993). A complete survey of the Furfooz tectonic structures was completed by Brodkom in his PhD Thesis in 1994. He defined six structural lithofacies that have singular reaction to the deformation: (i) the alternate series (the bedded shale and lime of the Maurenne Formation), (ii) the bedded series (Leffe and Molignée Formations), (iii) the crinoidal intercalations (Bayard Formation and the crinoidal facies at the base of the mud-mounds), (iv) the lenticular aggregates (the massif wauslortian facies of the mud-mounds), (v) the isolated banks (isolated Waulsortian beds), and finally (vi) the dolomitized patches in the other lithofacies. The lenticular aggregate is the mud-mound s.s. that represent a rigid and competent aggregate but with heterogeneity elements that influence the deformation. Those elements are the crinoidal intercalations and the dolomite patches mainly. Specific deformation structures are found in the aggregate and these are orthogonal diaclases and shear zones. The shear zones can be the consequence of the interactions between the aggregate and the bedded envelope (compensation of the deformation in a less ductile formation) but they can also correspond to extreme deformation zones due to the interaction with the dolomite patches that have been clearly established as pre-tectonic (Brodkom, 1994). Dolomite can have dual tectonic behavior: if it is spread in micro-agregates, dolomitization can actually favor the ductility of the host rock; but when it takes the form of patches within limestones it implies a brittle behavior. Finally, specific deformation structures are also found in the crinoidal intercalations: diaclases and diagenetic stylolithes (parallel to the bedding).

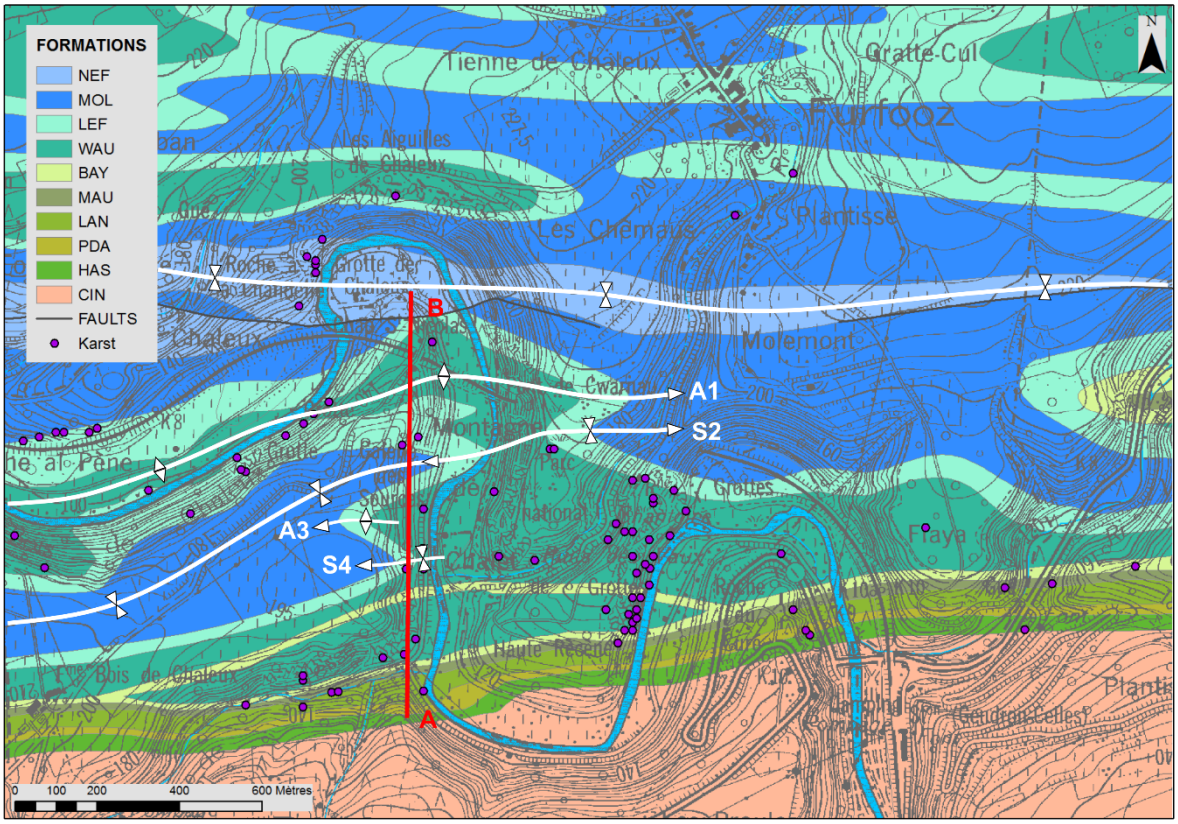

Figure 11. Local geological map and geologic structure (scale 1:7000). Modified from Delcambre & Pingot, 1993.

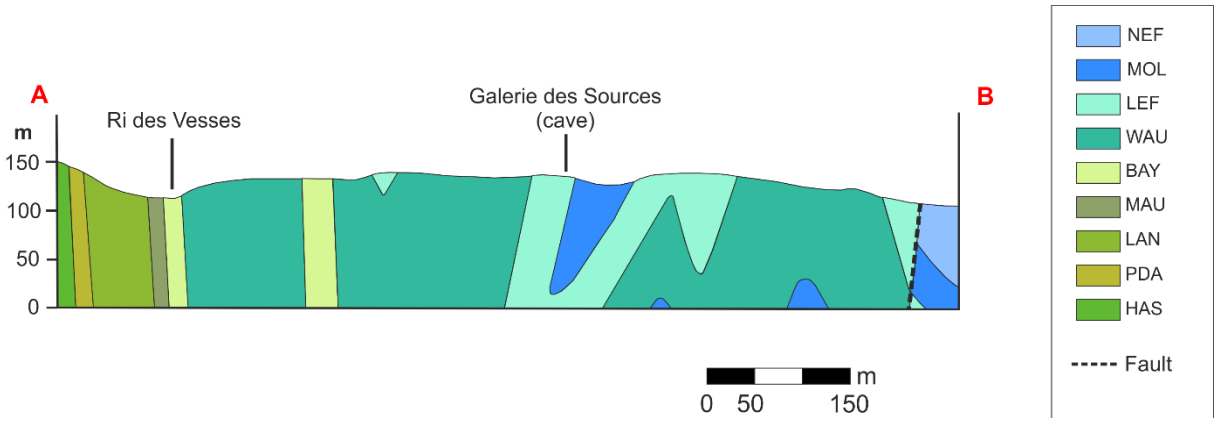

Figure 12. Cross- section of the Furfooz massif. The location of the cross-section A-B is shown in Figure 11. The bedding is sub-vertical, but not visible in the massive Waulsort Formation. While the bedded envelope of the mud-moud is folded, the waulsortian aggregate s.s. is mainly fractured.

2.2.2.4 Karstification

The geological maps of Figure 4 and, at a more local scale, Figure 11 show very clearly that the Waulsort Formation is particularly prone to karstification. The purple dots plotted on the maps correspond to any surface or subterraneous event related to karstification. They point out to cavity, swallow hole, sinkhole, collapse, spring, etc. observed on the field. The data are retrieved from a recent inventory exposed in the "Atlas du Karst Wallon" (Thys & Michel, 2014). These data will be, from now on, referred to as "karst occurences". Quantification of these data on a regional scale indicates that there is about 4 times more karst in the Waulsort Formation than in the surrounding pure limestone of the Neffe or the Molignée Formations (Figure 13). A general idea is that pure dolomites are less soluble than limestones and that, in limestones, the dissolution rate increases with the purity of the rock (Ford & Williams, 2007). Exceptions exist and are related to numerous factors that need to be defined. The Waulsort Formation, being partially dolomitized, represents an interesting case study deserving to be investigated. A specific study on this topic was led and the main results published in an article released in *Geologica Belgica* named "Karstification in dolomitized Waulsortian mud-mounds (Belgium)" (Dewaide et al., 2014). This article is, first, based on field observations that have highlighted the preferential development of the karst in the dolomitized sections of the mud-mounds. Second, cathodoluminescence investigations brought to light a close relationship between the karst and complex geochemical processes implying dedolomitization of the initial dolomite. A global karstogenesis model is proposed at the end of the article and included in a discussion that raises several questions, namely about the paleo-environmental setting of such phenomena. The following chapters are based on this published article. New, unpublished, data have been gathered since the release of this article; they are detailed in section 2.2.2.4.d.

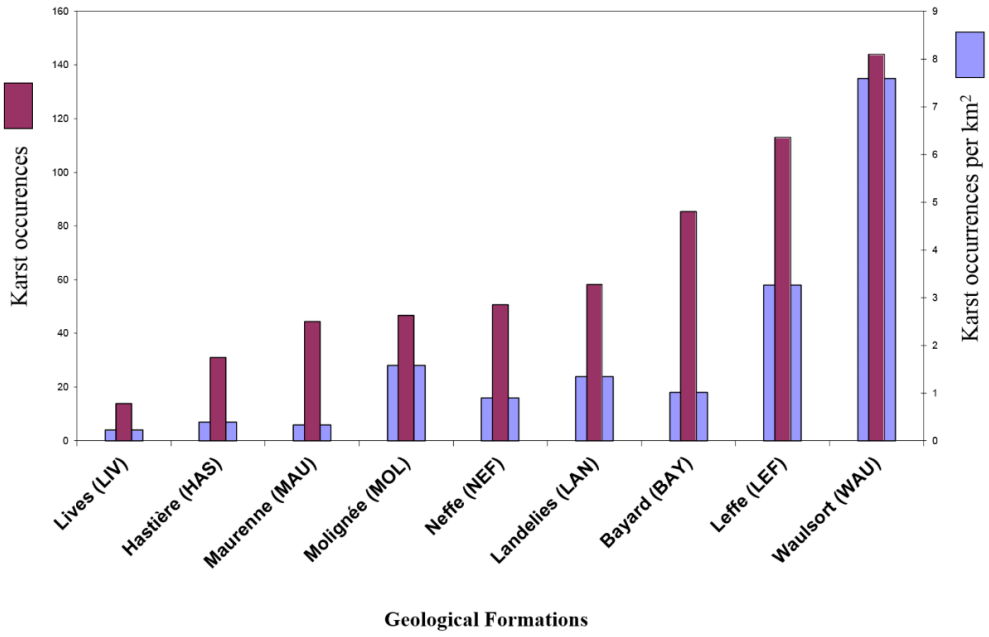

Figure 13. Statistical analyze of the karstification in the carbonates of the Dinant area (raw data retrieved from Thys & Michel, 2014).

2.2.2.4.a Field observations

Large scale observations were performed on two Waulsortian sites: the Furfooz site and the Moniat site that is located along the Meuse valley, west of Dinant (Figure 4). Field observations of the karst development in the Waulsortian buildups allow distinguishing two types of karst features (Figure 14). First, a subordinate karst occurrences correspond to structurally-controlled, classical caves with large conduits developed along a preferential direction. Secondly, rather small (centimeters to a few meters long) and very frequent cavities are developed preferentially in the dolomitized parts of the mud-mounds. This study focuses on this last type of cavities, which is named “the dolostone cavity type”.

The observation of numerous occurrences of “dolostone cavity type” on the field (Figure 15) allowed unraveling the controlling lithological features associated with these cavities. Two major characteristics were observed. First, karstification is preferentially developed along one or several fractures. Second, although the “dolostone cavity type” is found within dolomitized rocks, a calcitic transition zone outlines almost systematically the boundary of the cavities. This transition zone has an elongated lenticular outer shape with its major axis oriented parallel to the fracture. It consists of coarse crystalline calcite as well as microcrystalline reddish calcite. The coarse crystalline calcite can take the form of large calcite rhombohedra that can reach a decimeter in size and that preferentially line the walls of the cavity and fracture axes.

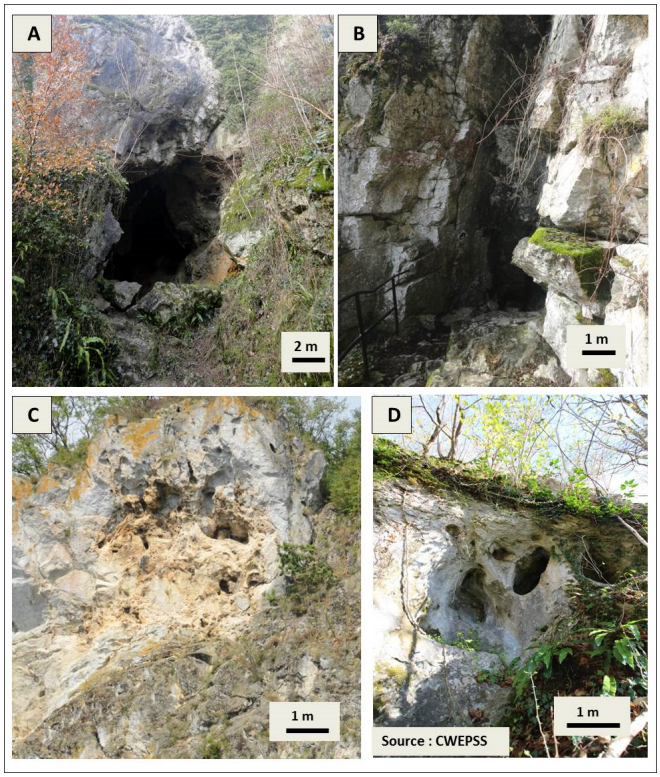

Figure 14. Illustration of the two types of karst found in the Waulsortian mud-mounds. (A) “Trou des Nutons” and (B) “Trou qui fume” are entrances of large caves representing a classical structurally-controlled karst. (C) and (D) show typical cavities of the “dolostone cavity type”.

Figure 16 is a sketch of “the dolostone cavity type” that shows the features associated to its development: fractures geometrically related to the cavities, rhombohedra lining the cavities, calcitic zone surrounding the cavities. Structural features of the fractures associated with the “dolostone cavity type” are presented in the stereogram in Figure 17. Two main fracture groups are visible: a first family, represented by strongly dipping planes (60° to 80°) with a roughly E-W strike, is actually parallel to regional stratification. The second family of fractures can be identified as subvertical diaclases their direction varies around N170E which is roughly perpendicular to the stratification. Brodkom (1994) recognized the same fracture groups and added a third one defined also as diaclase planes with a similar direction (N170E) but a weaker dip (10° to 35°). The plots in the center of the stereogram in Figure 17 could correspond to this third group. According to Brodkom, these groups of fractures are related to the Variscan orogeny.

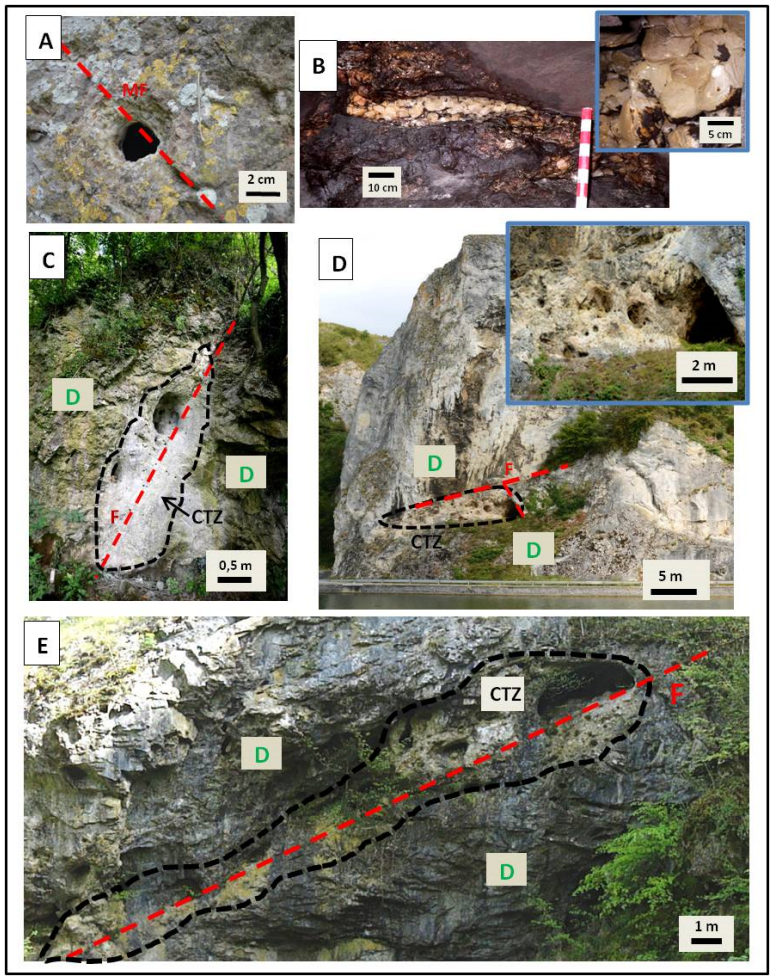

Figure 15. Field occurences of the “dolostone cavity type” at various scales. (A) Centimetric cavity developed on a microfracture [MF]. Calcite crystals are visible on the walls of the cavity. (B) Metric cavity partially filled with large rhombohedra, the inset on the right shows a zoom on the rhombohedra. (C) Metric cavity related to a fracture [F]. A calcitic transition zone [CTZ] is developed between the cavity and the host dolostone [D]. (D) Moniat site with the inset zooming on the cavities and (E) “Puits des Vaux” in Furfooz are metric to plurimetric cavities showing fracture axis [F] and calcitic transition zone [CTZ].

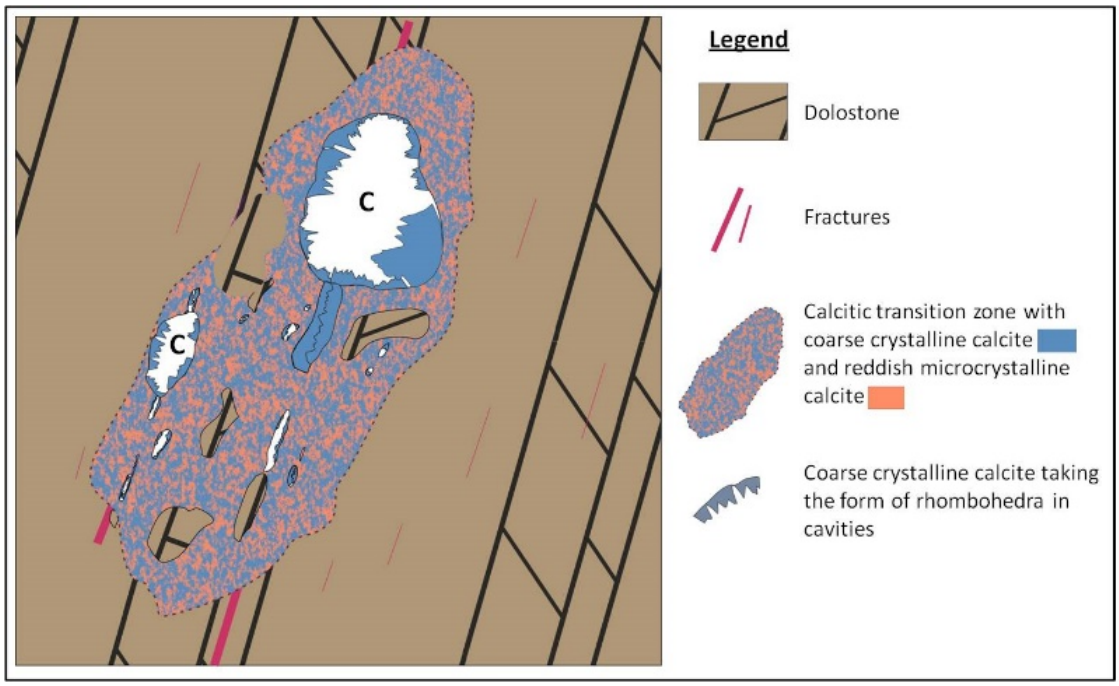

Figure 16. Sketch of a "dolostone cavity type", here hosted in a crudely subverticaly stratified dolomitic interval of the mud-mounds. The development of cavities [C] is related to fracturation. Calcite rhombohedra are mainly concentrated on the walls of the cavities and in open fractures. A lenticular transition zone made of micro- to macro-crystalline calcite exists between the cavities and the host dolostone.

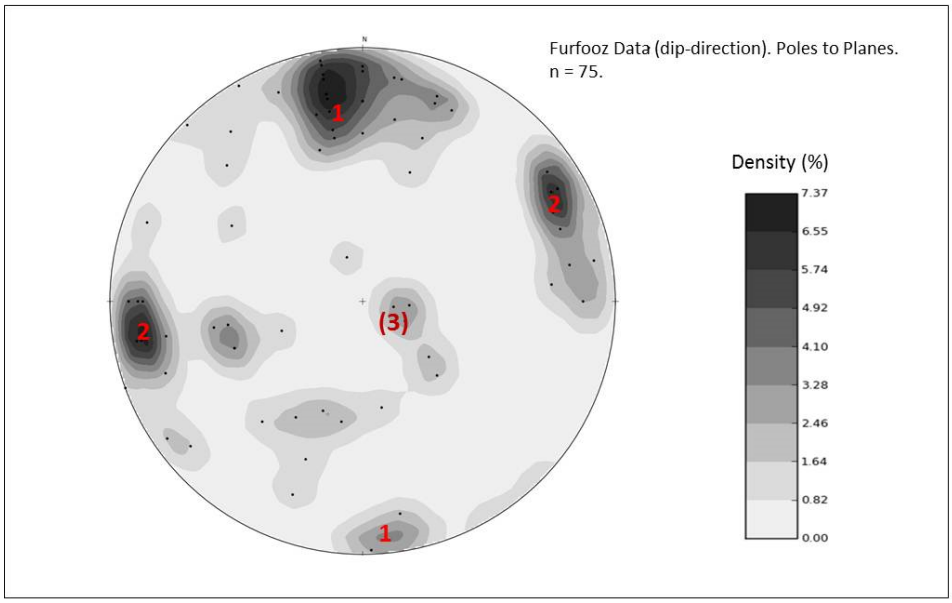

Figure 17. Fracturing land survey results. Measurements were made on fractures affecting the Waulsortian rocks in the Furfooz site. Π-pole method: Family [1] close to the poles has a strong dip (between 60 and 80 °) and a N80E –N90E strike; family [2] are diaclase planes with a N170E direction and a subvertical dip; family [3], less frequent, is also a diaclase group with a N170E direction but a low dip.

2.2.2.4.b Laboratory investigations

2.2.2.4.b.1 Material and methods

One well developed occurrence of the "dolostone cavity type" was chosen based on representativeness, exposure and access conditions. The chosen outcrop is similar to the sketch shown in Figure 16. Samples were collected along various transects with a coring machine (Figure 18). Sampling density was usually 2 samples per meter along transects, except near the cavity where it was increased to 4 samples/m.

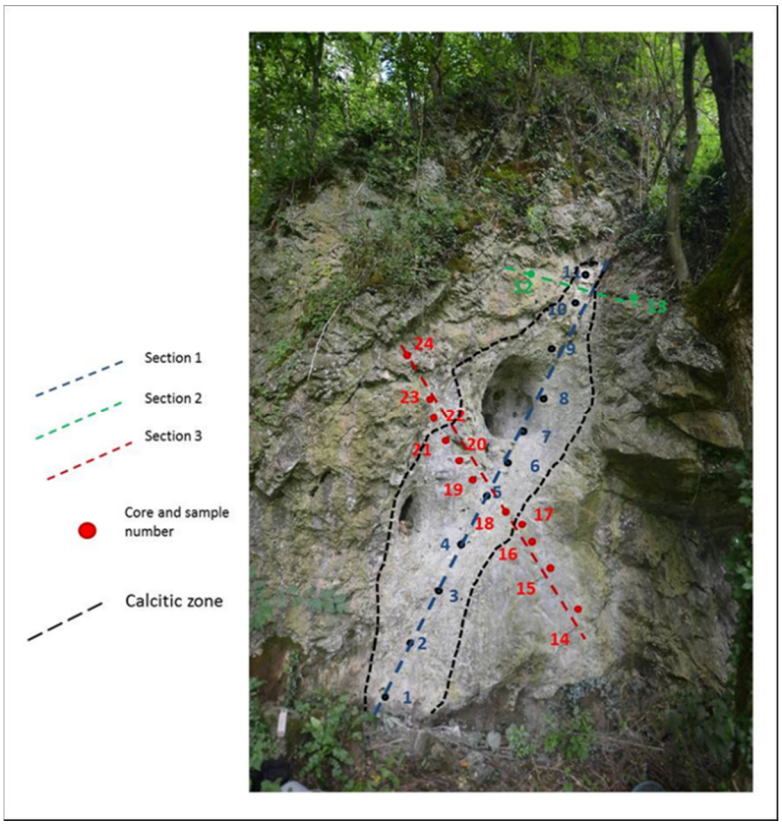

Figure 18. Sampling map of one occurrence of the "dolostone cavity type". Sampling line 1 roughly follows the fracture axis while lines 2 and 3 are roughly perpendicular.

X-ray fluorescence analyses (XRF) were performed at the Central laboratory of Lhoist industry (Lhoist West Europe Division). However, these analyses were realized randomly and only the basic chemical elements were analyzed (Ca, Mg, Fe, Al, Mn and Si). As the bulk chemical composition of the samples didn't reveal any useful conclusions within the framework of this paper, the results are not presented here.

Thin sections were made from each drilled core. Prior to sawing, the samples were impregnated in epoxy resin for a few days. After mounting on glass slides, the sections were thinned to 40 µm and left uncovered. The thin sections were first studied with a Leica polarizing microscope. They were then diamond-polished for cathodoluminescence (CL) analysis at the University of Mons, Department of Geology and Applied Geology, using a CITL

Mk5 unit operated at 15 kV and 500 µA beam voltage and current, respectively. The distinction between calcite and dolomite under CL, which may be ambiguous based solely on visual appearance of their emission colours, was checked using a CITL COS 8200 optical spectrometer. In our samples, calcite and dolomite were emitting at ca. 600 (yellow) and 645 nm (red), respectively, which is consistent with the published Mn2+-activated CL emission for these carbonate minerals (e.g. Marshall, 1988).

2.2.2.4.b.2 Petrography

Field observations permitted to discriminate three main rock textures implied in the "dolostone cavity type". Figure 19 shows core samples representing these three textures: i) porous, grey dolomite, ii) coarse calcite, which can take the form of cleaved rhombohedra, iii) reddish, microcrystalline calcite. The three macroscopic textures were studied under conventional microscopy and cathodoluminescence. The latter permitted to precise that the reddish microcrystalline calcite is most probably dedolomite.

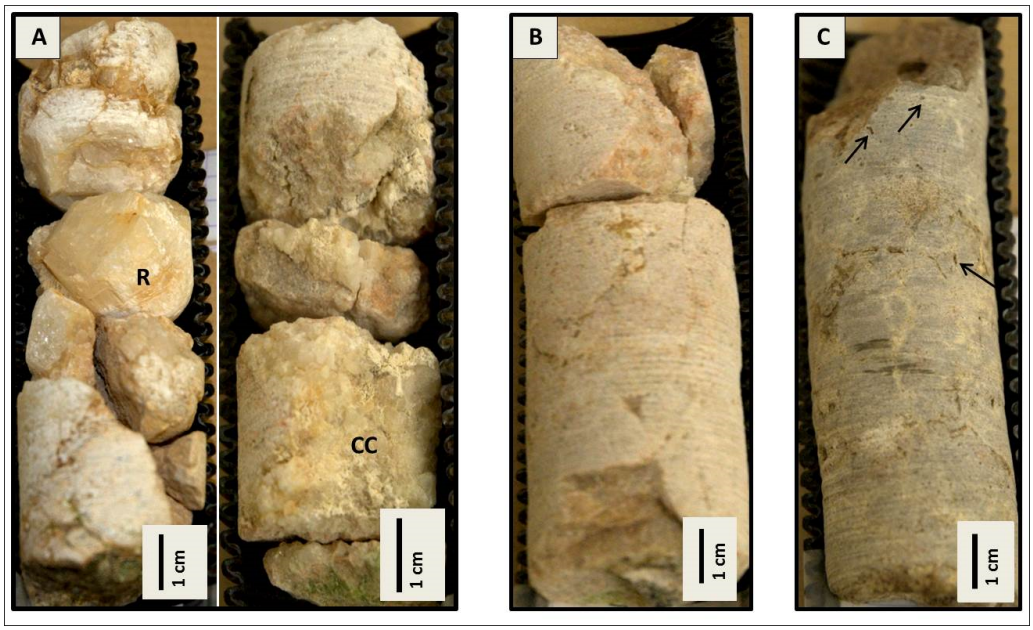

Figure 19. Main macroscopic aspect of the samples. (A) Rhombohedra [R] and coarse crystalline calcite [cc]; (B) reddish, fine crystalline to microcrystalline calcite; (C) grey dolomite, arrows point to porosity.

a. Dolomite (Figure 20 A)

The porous grey dolostone appears as a massive dolostone showing a dolospar fabric which consists of planar and non-planar dolomite. The planar crystals have a subhedral to euhedral morphology and a size between 50 and 250 µm. They commonly possess a more or less cloudy center. Anhedral, non-planar dolomite crystals are somewhat larger (150 to 350 µm) but their boundaries are not well-defined. The texture is thus close to the "planar-s hypidiotopic mosaic" described by Sibley & Gregg, 1987. This dolostone relates to a secondary

dolomitization of the Waulsortian mud-mounds obliterating the original limestone texture. Initial porosity of the dolostone is rather high (visual estimation at ~ 5%).

b. Calcite in cavities (Figure 20 B, C)

The calcite mentioned here is the one that fills cavities corresponding to enlarged fractures and not to an inter-granular porosity. The cavities are micrometer to centimeter large at the thin-section scale. Calcite crystals filling them up are subhedral to euhedral and their size is variable but they can reach a few centimeters. Under CL, a succession of three calcite phases can be observed from the wall to the center of the cavities: 1) dull yellow brown-luminescing calcite with patches of non-luminescing calcite ("patchy" or "P calcite"), 2) non-luminescing ("NL calcite") and 3) zoned calcite ("Z calcite"), in which luminescing and non-luminescing fringes are alternating. This third phase is not always present in the succession but may dominate in some of the largest cavities.

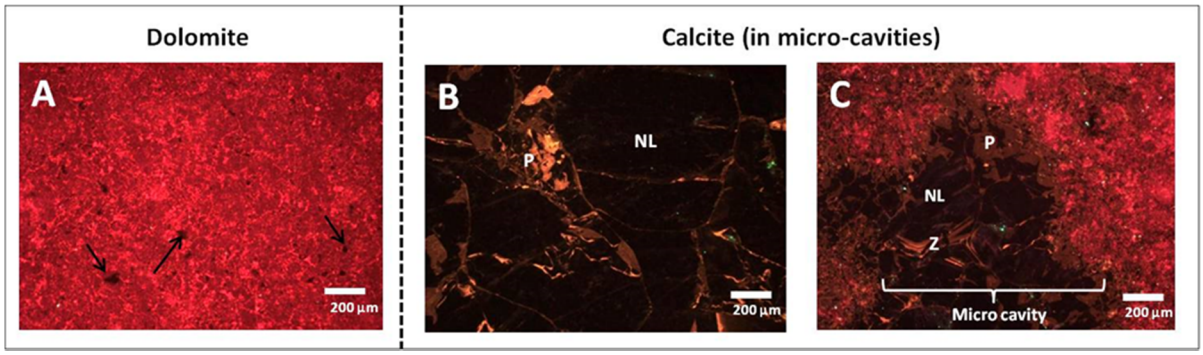

Figure 20. A) Dolomite fabric and calcite-filled micro-cavities under cathodoluminescence. Dolomite exhibits bright red luminescence. Porosity appears as dark spots (arrows). B) and C) Calcite filling micro-cavities. The calcite succession (patchy [P], non-luminescing [NL] and zoned [Z]) is well represented in (C) whereas in B the Z phase is not observed.

c. Dedolomite (Figure 21)

The third texture observed consists of a complex dedolomite fabric. Actually two fabrics can be distinguish. A first dedolomite -DD I- appears, under CL, as a mixture of calcite and corroded dolomite crystals (Figure 21A). Petrographic evidences for dedolomitization include: 1) corroded dolomite rhombs edges, 2) partial dolomite rhombs floating in a calcite matrix and 3) calcite patches within the core of dolomite rhombs (Budai et al. , 1984). The fabric shown in Figure 21A and A' reflects these three features. It can clearly be defined as dedolomite given that dolomite crystals exhibit both peripheral and internal corrosion. The calcite intergrown with corroded dolomite is interpreted as replacement calcite. This replacement calcite is mainly patchy-blotchy "P" calcite under CL (Figure 21A'). Another dedolomite fabric (DD II) can be differentiated and develop as coarser, euhedral calcite crystals with sharp boundaries and enclosing dolomite inclusions in their centre (Figure 21B'). In this dedolomite fabric, P calcite can still be present and in this case is intergrown with the dolomite relics in the center of the crystal. However, the major phases in terms of volume are the NL and Z

calcite that seem to have overgrown euhedral dedolomite crystals as if they cemented inter- and intra- granular voids.

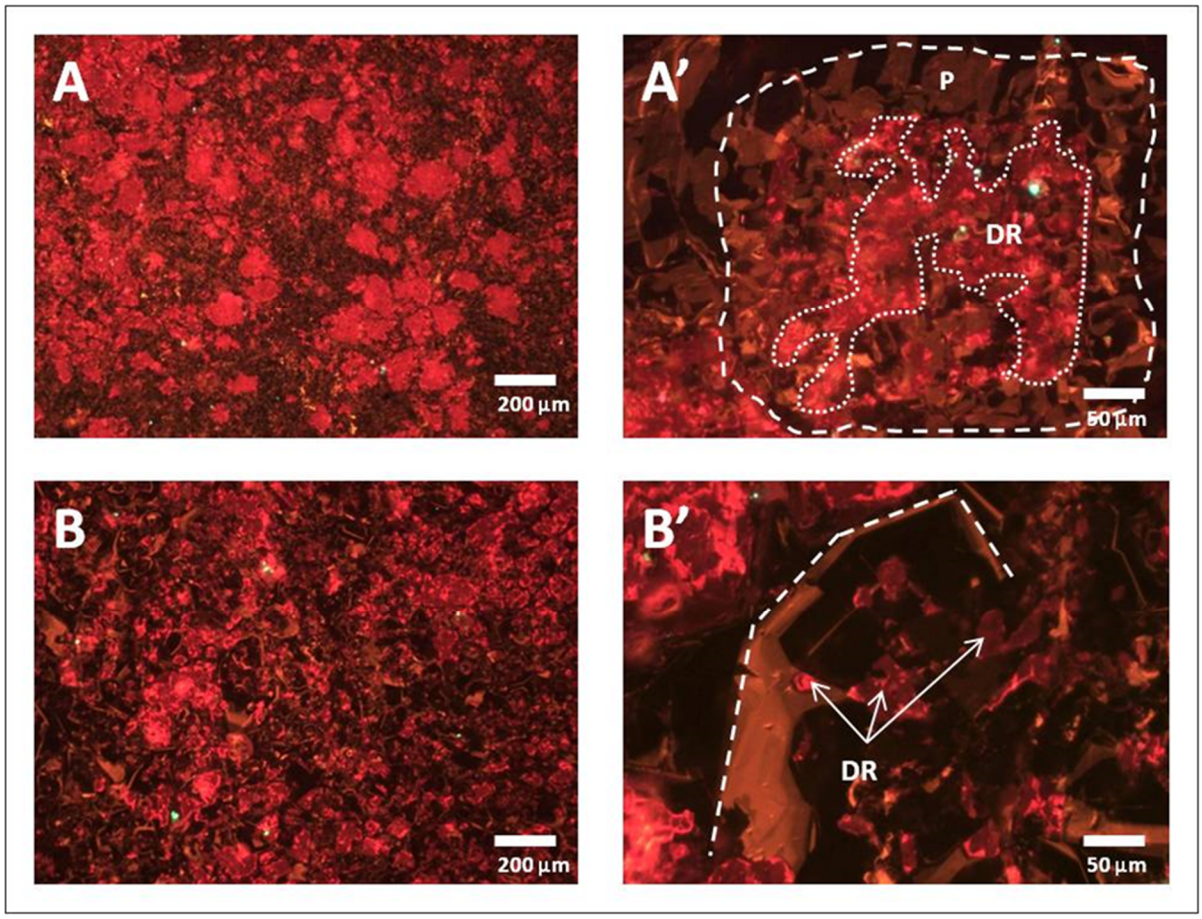

Figure 21. Dedolomite fabrics under cathodoluminescence. Dolomite exhibits bright red luminescence, calcite is yellow to brown or non-luminescing. (A) DD I fabric: Relic rhombs are floating in an intergrown patchy calcite matrix. Patchy calcite has partially replaced the corroded rhombs. (A') Detail of a dedolomite crystal with patchy calcite [P] replacing the corroded dolomite rhomb [DR]. (B) DD II fabric: euhedral dedolomite crystal. (B') Detail of euhedral dedolomite with sharp crystal boundaries (represented by the dashed line). Dolomite relics [DR] are visible in the center of the crystals.

d. Relationships between the fabrics and interpretation

The distribution of the three fabrics along a sequence 1) dolomite, 2) dedolomite and 3) calcite, reveals the existence of a petrographic gradient developing along the cavities network. The photomicrograph sequence presented in Figure 22 shows clearly the three fabrics and their organized relationship.

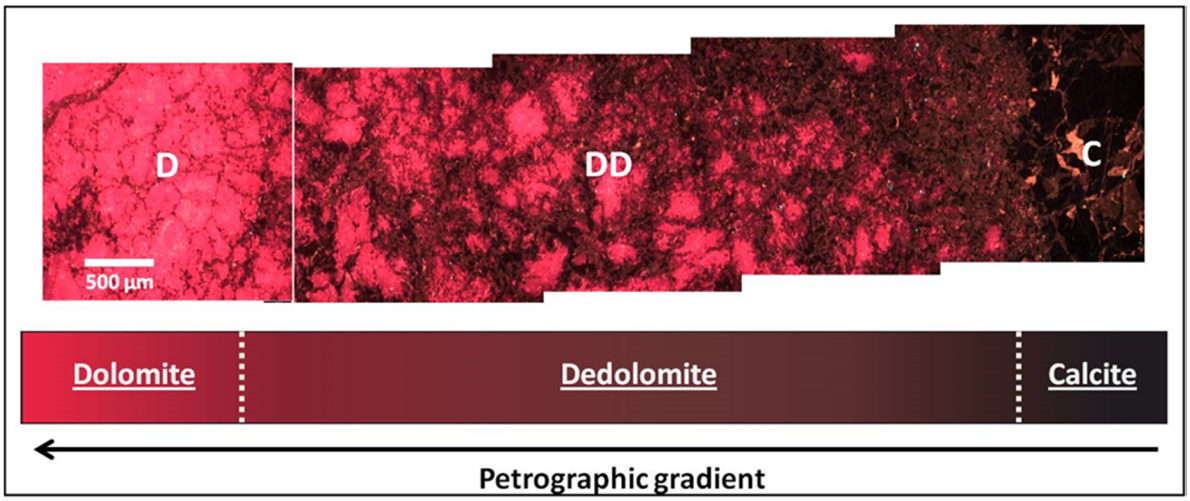

Figure 22. Sequence of cathodoluminescence photomicrographs showing a petrographic gradient from calcite to dolomite. [D] dolomite, [DD] dedolomite, [C] calcite-filled cavity.

Figure 23 sketches the various steps leading to the observed fabric distribution. The process presented here is clearly established from a cavity system being developed along a fracture network. The starting point is dissolution acting from permeable pathways (fractures) through the host rock. Dissolution enlarged the existing fractures creating cavities where dolomite dissolution was total and left a porous material made of corroded dolomite in the vicinity of the former fracture. Benefiting of the porosity created by dissolution, fluids flew through the rock operating a replacement of the already corroded dolomite by the patchy calcite (dedolomitization sensu stricto). Finally non-luminescing and zoned calcite cemented voids including intra- and inter granular porosity and larger cavities (cementation). The host dolostone replacement and cementation level follows a gradient which is decreasing as the distance from the cavity increases.

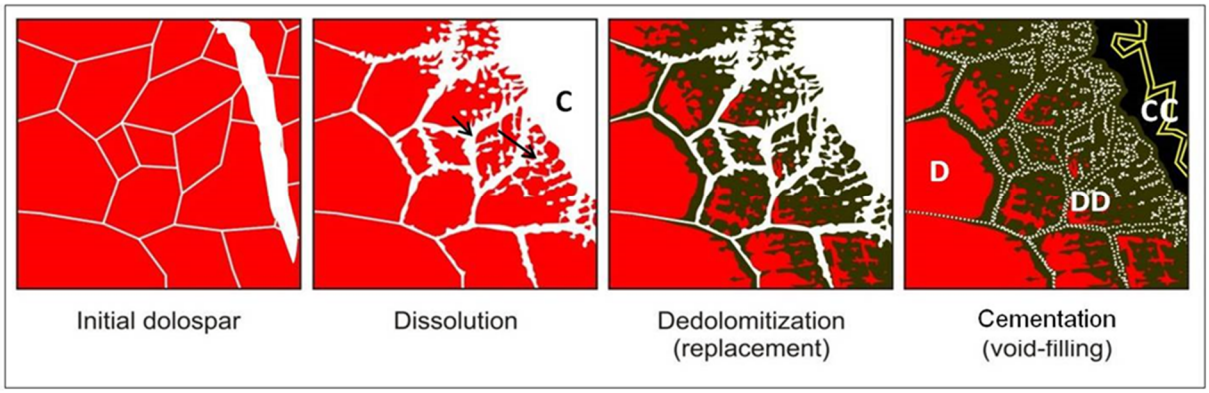

Figure 23. Sketch of the process leading to the observed fabrics and their distribution at thin-section scale. Dissolution occurs from a fracture affecting the initial dolospar. Dissolution creates a cavity [C]by enlargement of the initial fracture and inter- and intra-granular porosity (pointed by arrows) that decreases away from the initial fracture. The corroded dolomite crystals are then entirely or partly dedolomitized through replacement (DD I). The last step consists of calcite cementation (void-filling) in inter- and intra-granular porosity and in the cavity. The petrographic gradient is the end result with [CC] calcite in cavities, [DD] dedolomite texture, [D] dolomite. The replacement step is probably inexistent in DD II (euhedral dedolomite), the latter is then a dedolomite s.l. resulting from two processes not linked in time: first dolomite dissolution, second calcite cementation in the inter- and intra-granular porosity.

In the literature, dedolomitization process is described as a conversion from dolomite to calcite. This conversion is either described as a one-step replacement process, where dissolution of dolomite and calcite replacement occur almost synchronously within a thin, moving reaction front, or as a two-step process where calcite simply cemented the voids created by dissolution (Ayora, Taberner, Saaltink, & Carrera, 1998; Back et al., 1983; Budai et al., 1984; Evamy, 1967; Jones, Pleydell, Ng, & Longstaffe, 1989). Our observations suggest that both processes have occurred either separately or in combination. Indeed dissolution of dolomite followed by precipitation of calcite in the resulting voids is a two-step process which could correspond to the euhedral dedolomite fabric (DD II) and is consistent with other studies (James, Bone, & Kyser, 1993; Jones et al., 1989; Nader, Swennen, & Keppens, 2008; Nader, Swennen, & Ottenburgs, 2003; Qing, 1999; Ronchi, Jadoul, & Savino, 2004). DD II is then the result of cementation in the inter- and intra-granular voids of the corroded dolomite and could therefore be called dedolomite sensu lato. On the other hand, the fine-grained, patchy-luminescing calcite intergrown with dolomite (DD I) is interpreted here as replacive dedolomitization (dedolomitization s.s.). However, patchy-luminescing calcite is often reported as a first stage calcite cementation. It is thus possible that this calcite is at least partly void-filling and not strictly replacive.

2.2.2.4.c Discussion and perspectives

A preliminary karst genetic model based on morphological, petrographic and geochemical data can be proposed (Figure 24). This model reflects the processes presented in Figure 23 but at macroscopic scale. At first, dissolution of the initial dolostone took place along the discontinuities represented by the fracture network. Fluids penetrated the rock causing pervasive dissolution that progressed from the fractures into the rock. A heterogeneous highly porous material was created and open cavities developed locally. This porous material can be compared to the “Ghost Rock” (Quinif, 1999, 2010), whose formation is a general process of in situ dissolution of rocks (here dolomite) that can further evolve to more classical forms of karst. Subsequently, dedolomitization occurred by direct replacement of dolomite (dedolomitization s.s.). This replacement step is followed by cementation that came probably much later. On the one hand calcite cementation produced fabric DD II when occuring in the inter- and intra-granular voids of the altered dolomite, and on the other hand cement fluids precipitated coarse calcite in cavities, i.e. rhombohedra in the largest one. One must be aware that cementation is not necessarily linked to the timing of the karstification/dissolution. However as cementation profited of the voids created by dissolution and as the calcite cement is a major petrographic feature of the “dolostone cavity type”, the cementation is presented as a step of the karst genetic model in order to explain what is observed today in the field.

The environmental, dynamic and hydrological conditions in which this model could be contextualized have yet to be investigated. Indeed, it is generally accepted that limestone has a higher dissolution rate than dolostone, i.e. 3 to 60 times higher depending on the conditions (Liu, Yuan, & Dreybrodt, 2005). Dissolution is controlled by physico-chemical factors such as pCO2 and temperature but also by other agents such as the hydrodynamic conditions or the CO2 conversion rate in H+ and HCO3- (Liu and Dreybrodt, 1997; Liu *et al.*, 2005; Pokrovsky *et*

al., 2009). Specific conditions, such as a low Mg/Ca or the presence of dissolved sulphate, must then have prevailed to explain that at some stage dolomite was relatively more soluble than calcite.

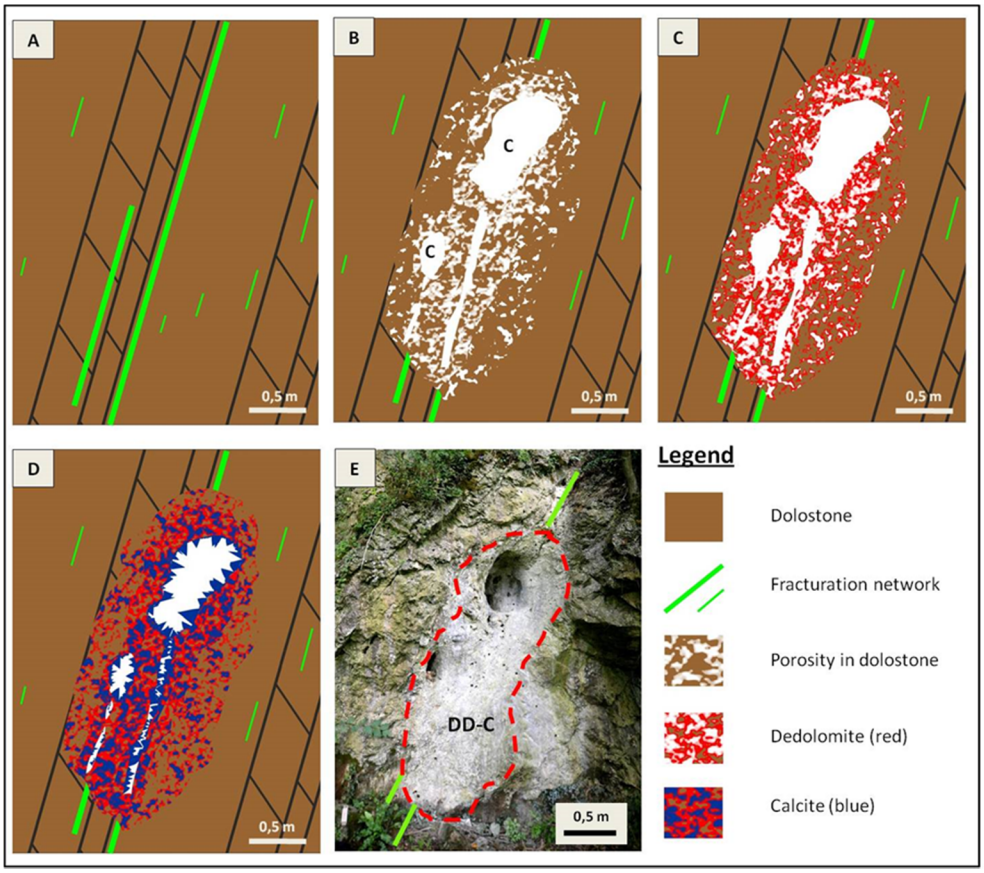

Figure 24. Proposed genetic model for the development of "dolostone cavity type" karst in Waulsortian mud-mounds. (A) Initial dolostone. Here presented with a crude subvertical stratification and a fracture network developed parallel to the stratification. (B) Creation of porosity and cavities [C] by heterogeneous dissolution of the dolostone. Porosity is preferentially developed along fractures. (C) Replacive dedolomitization of the altered dolostone occurs from the porosity development. Creation of the DD I. (D) Final step with cementation fluids precipitating calcite in the residual porosity. Creation of the sensu lato dedolomite and of calcite cement in the cavities. Cement grew as calcite rhombohedra in the largest voids (cavities) but the latter were not completely filled so that residual karstic cavities are observable today. (E) Comparison with field observation (the dedolomite/calcite zone [DD-C] is outlined).

Dedolomitization is commonly reported as related to subaerial exposure of dolostone (Canaveras, Sanchez-Moral, Calvo, Hoyos, & Ordonez, 1996; Friedman, 1994; Nader et al., 2008, 2003). Beside, other studies have suggested that the process also take place in deep environment, i.e. through burial diagenetic process (Budai et al., 1984; Land & Prezbindowski, 1981; Woronick & Land, 1985). As an important driving mechanism of dolomite dissolution, the presence of dissolved sulphate is often invoked: calcium sulfate-rich fluids deriving from the dissolution of evaporites (mainly gypsum) provide calcium and catalyze dedolomitization reactions (Arenas, Alonso-Zarza, & Pardo, 1998; Bischoff, Julia, Shanks, & Rosenbauer, 1994; Raines & Dewers, 1997). Evaporitic conditions are known in the Visean geological history in Belgium. Evaporite dissolution and subsequent circulation of sulfate enriched solutions have

been reported, essentially in the Dinant Sedimentation Area (Boulvain & Pingot, 2012). However evaporite dissolution is not systematically associated with dedolomitization and another source of calcium needs to be found, as pointed out by other studies (Frank, 1981; Theriault and Hutcheon, 1987; Deike, 1990; Khalaf and Abdal, 1993; Ronchi *et al.*, 2004). In the Waulsortian buildups, the origin of calcium ions responsible for dolomite replacement and for calcite cementation could be explained by the heterogeneity of the initial dolomitization and the resulting coexistence of limestone and dolostone. In addition, rocks are dominated by limestones in the study area. Therefore it is likely that fluids flowing through the mud-mounds were initially close to equilibrium with limestone, i.e. saturated with respect to calcite and undersaturated with respect to dolomite. These Ca-rich and Mg-depleted fluids were thus potentially reactive against Waulsortian dolostone and this resulted in dolomite dissolution and calcite precipitation. Changes in fluid chemistry and/or in flow regime must however have existed to explain the prevalence of either dolomite dissolution, dolomite replacement by calcite or calcite cementation.

Finally, the fact that karst occurs preferentially in the dolomitized parts of the mud-mounds can be explained by the petrophysical properties of dolostone relative to typical limestones. First, dolostone has in this case higher porosity than limestone. Our petrographic observations have indeed shown that the Waulsortian dolostone has a rather high porosity. Second, dolostone and limestone have a different response to geomechanical stress. Brodkom (1994) inferred that Waulsortian dolostone bodies acted as massive brittle nuclei during the Variscan orogeny whereas limestone had a more ductile behavior. Dolostone bodies with their higher permeability relative to the surrounding limestone are thus capable of channelizing fluids, which explains their high concentration in alteration and karst features. Likely the connectivity of these bodies at regional scale is an additional important parameter, but the latter remains to be investigated.

Assessing the paleoconditions is a key point in understanding the development of the “dolostone cavity type” karst and it will require the use of advanced techniques, including trace-element and isotope geochemistry, dating and fluid inclusions studies. Future analysis should also include the investigation of other cavities in order to check the consistency of our results at a wider scale and test the genetic model developed so far. Finally, a more detailed structural study has to be carried out in order to link the history of mud-mounds fracturing with the development of dedolomitization and karstification processes.

2.2.2.4.d New data

The data presented in the previous sections (2.2.2.4.a to 2.2.2.4.c) have established a link between the macroscopic scale of the outcrop and the microscopic scale of the thin section. The discussion has addressed the difficulty to attribute a paleo-environment to the processes suggested by the cathodoluminescence observations. The reason is mainly the lack of geochemical tracers for the environment of dolomite dissolution, dolomite replacement and calcitization.

2.2.2.4.d.1 Isotopic and fluid inclusions data

The data presented hereafter were gathered by two students of the KULeuven (Katholieke Universiteit of Leuven) that studied the Furfooz case for their end of bachelor dissertation. The following section presents only the final results of their observation performed on various Furfooz samples. Details about the material and methods are presented in their work (De Ridder, 2014; Van Offenwert, 2014).

Stable C and O isotope analyses were performed on various samples of the Furfooz area. Dolomite, reddish dedolomite and white crystalline calcite were treated separately. The results are gathered in Figure 25. The three groups show a distinct isotopic signature. Dolomite is characterized by positive $\delta^{18}O$ values around +3, and negative $\delta^{13}C$ ranging from -10 to -14. Dedolomite, represented only by three samples, has negative $\delta^{18}O$ (-3 to -5) and negative $\delta^{13}C$ of about -10. Finally, the different calcite samples have a wide range of $\delta^{18}O$ (-1 to -9) but a narrow range of $\delta^{13}C$ around -12, except for one sample at -10. Those groups of values are plotted in the theoretical diagram of C and O isotopes distribution of different carbonate phases (Figure 26). The dolomite samples stand close to the range of deep marine limestones. The positive $\delta^{13}C$ data underline the absence of organic carbon that would have depleted the $\delta^{13}C$ values. The wide range of $\delta^{18}O$ reflects a probable complex history of multi-step recrystallization of the dolomite, possibly during burial of the initial dolomite. Calcite and dedolomite both plot within the area of near-surface processes. They display negative $\delta^{13}C$ inherited from organic carbon.

Fluid inclusions were investigated but could only be found in the white calcite. One fluid inclusion containing small gaz bubbles was interpreted as a primary inclusion. For this particular inclusion, homogenization temperature is 66.3 °C, melting temperature is estimated at -1.3 °C and salinity at 2.2 eq. Wt. % NaCl. Those values are a bit high to correspond to strictly near-surface fluids. However, they should be taken with caution as they concern only one fluid inclusion that may be not completely primary.

2.2.2.4.d.2 LIBS data

The LIBS (Laser Induced Breakdown Spectroscopy) technique can, among others, provide images that correspond to elemental intensity maps of selected chemical elements. For our study case, the LIBS offers the advantage to obtain in-situ geochemical information (including trace elements) at hand-sample scale. Indeed, the cathodoluminescence, presented before, allows observations at the micro-scale that give very detailed information. It was necessary to define geochemical variations at a more general scale and have a global view of the sample chemical evolution. The LIBS imaging presented hereafter was performed on the equipment designed by J.-M. Baele (University of Mons, Belgium).

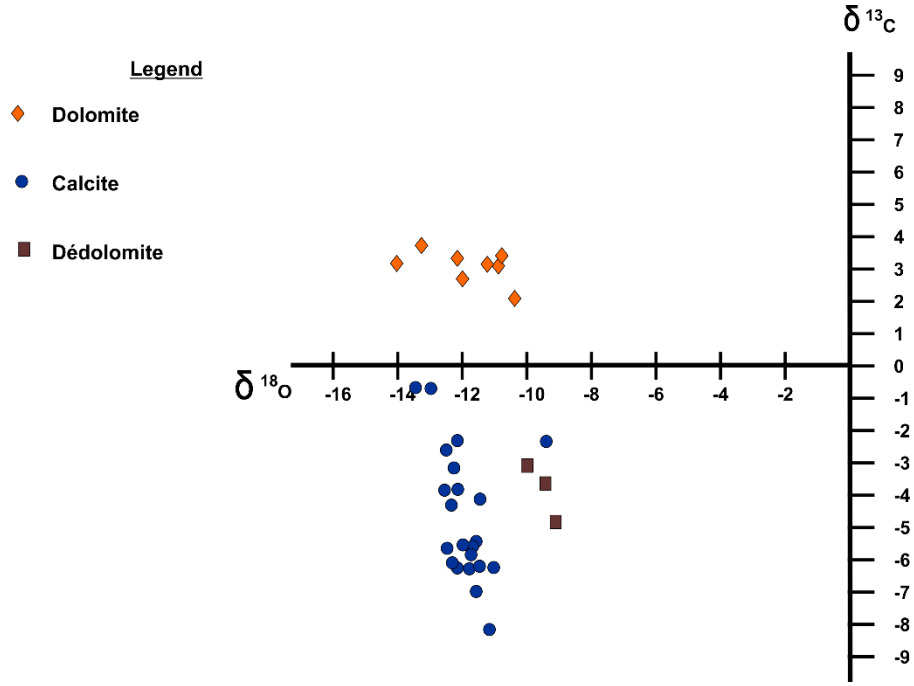

Figure 25. Cross plot of the stable isotope analysis: δ ^{18}O vs. δ ^{13}C scatter diagram. Dolomite, dedolomite and calcite are shown by different symbols.

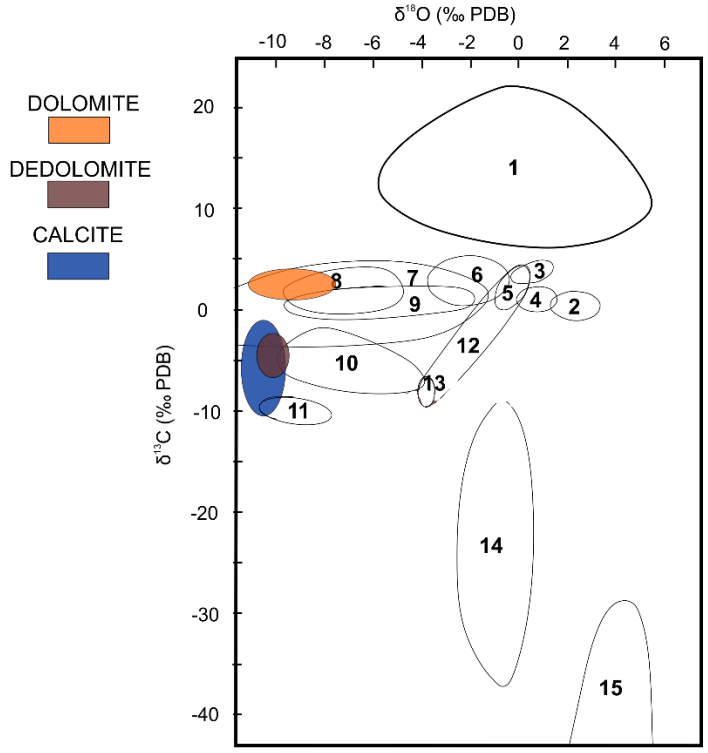

1. Heavy Carbon diagenetic cements
2. Deep limestones
3. Shallow cements
4. Oozone
5. Sediments
6. Chalks
7. Range common marine limestones
8. Late cements (Jurassic)
9. Average marine limestones
10. Freshwater limestones
11. Soil calcite, Europe
12. Pleistocene limestones, Bermuda
13. Secondary calcite, Bermuda
14. Early diagenetic concretions
15. Methane derived cements

Figure 26. Distribution of some important carbonate groups with regard to their stable C and O isotopic composition (modified from Hudson, 1977).

a. Material and method

LIBS measurements were performed on a fresh sample taken from the site shown in Figure 18. Two opposite sides of the core sample were ground with a diamond grindstone and a grit 600 SiC aqueous suspension to obtain a surface with good planarity and uniform roughness.

The LIBS technique is known since the 60's (Radziemski, Loree, & Cremers, 1983) but it emerged with a real interest in the last twenty years due to the increased availability of high-performance lasers and spectrometers (Cremers & Radziemski, 2006). The general principle of this technique is the generation of a micro-plasma by focusing a high-energy pulsed laser beam on the surface of a solid sample. A small amount of the sample is vaporized (ablated) and the atoms are ionized and excited. The resulting spectral emission, which is similar to atomic emission, is characteristic of the elemental composition of the sample hit by the laser and can be analyzed with an optical spectrometer (Cremers & Radziemski, 2006; Galbács, 2015; Harmon & Russo, 2013; Senesi, 2014). The major components of a LIBS system are (Figure 27): a short-pulsed laser that creates the hot plasma; an optical setup made of lenses for focusing the plasma on the target and for collection the emitted light to optical fibers; a spectrometer synchronized with the laser for recording the spectrum; and a computer for data processing and general control of the equipment. The sample is fixed on a motorized stage that can move in the X and Y directions, which enables scanning the surface to create compositional profiles or maps.

Figure 28 exposes the two analyzed faces of the sample. On both faces, the three textures described in section 2.2.2.4.b.2 can be identified distinctly: the grey dolomite, the reddish dedolomite and the white crystalline calcite. The LIBS imaging technique was applied on rectangular sections of about 9 x 1.3 cm. The stage carrying the sample moved first in the X direction, taking a line of measurements with a spacing of 0.5 mm. At the end of the line, the stage moved in the –Y direction with a single step of 0.5 mm and moved back to start a new line of measurements in the –X direction; and so on to obtain a raster scanning of the surface. The resulting images are not strictly quantitative. They give the relative spectral intensity of the analyzed element in each point of measure. Quantitative data could, theoretically, be obtained by calibration of the LIBS through calcite and dolomite rock standards. Those standards should however have the same structure as the sample, and be very homogeneous at a resolution of 0.5 mm (corresponding to the spacing between the measurements), which wuld be very difficult to obtain (Baele, personal comm.). References to this calibration technique are not really available, as it is still under development.

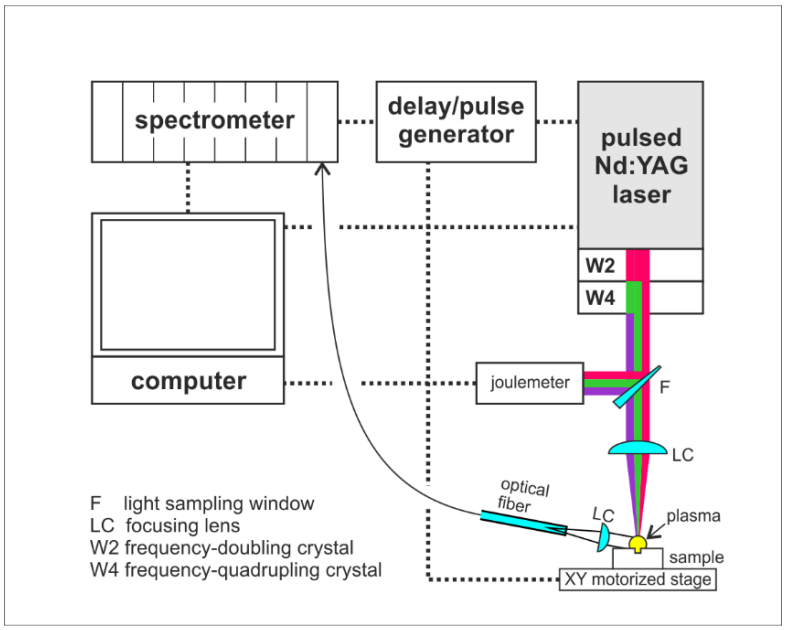

Figure 27. Simplified scheme of a LIBS composition (Baele, 2018 – personal comm.). The main components of a LIBS system are the pulsed laser, the focusing and light collecting lenses, the XY motorized stage carrying the sample, the optical fiber that transmits the emission spectrum to the spectrometer, and a computer.

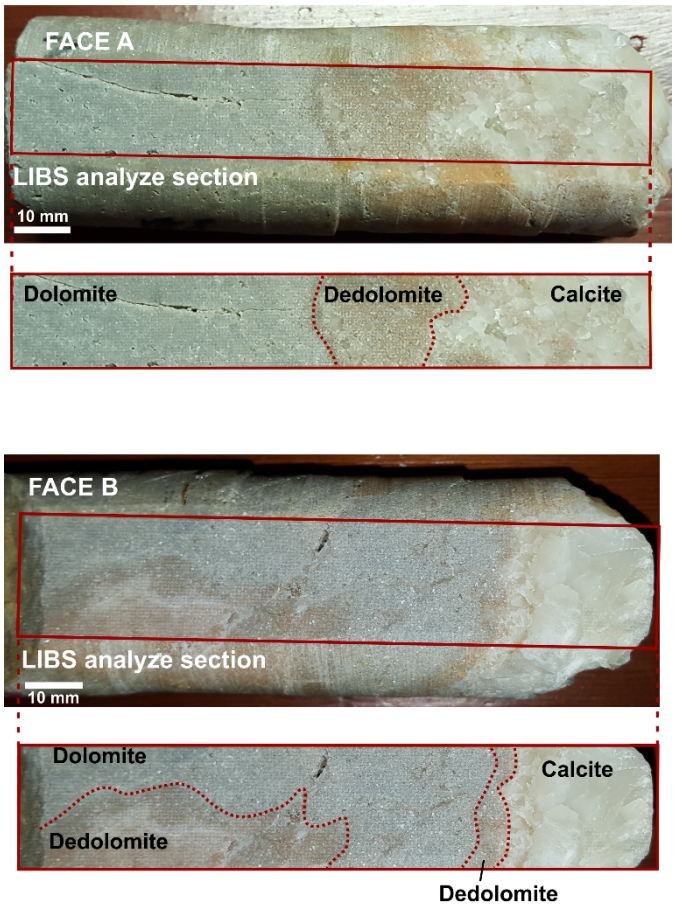

Figure 28. Sample on which the LIBS mapping was performed. The dolomite, dedolomite and calcite are clearly identified by their colour. The laser shots are visible as a regular grid of lighter spots.

b. Results

The LIBS elemental maps presented hereafter correspond to series of pixel of various intensity. The spectra acquired in each XY point on the surface (6000 in total) were treated by Spectragryph software (https://www.effemm2.de/spectragryph/) in order to automatically extract peak intensities for the selected elements. Raster (bitmap) images were then created using Fiji free software (Schindelin et al., 2012), each pixel in the image corresponding to the peak area measured in the spectra. The obtained images are not quantitative as no calibration was done, but the LIBS intensity for a given atomic emission line encoded in each pixel relates to the concentration of that particular atom.

Figure 29 shows the results of the LIBS imaging performed for the following elements: Mg, Ca, Sr, Mn and Fe. The small heterogeneities found on the sample (fractures, holes or patches of other textures) are delineated to avoid any false interpretation of the elemental maps. The analyzed elements do all show significant variations between the three petrographic zones (dolomite, dedolomite and calcite). As expected from the cathodoluminescence analysis, dedolomite is depleted in Mg compared to the dolomite and enriched in Ca. The highest Ca intensities are found in the white crystalline calcite. Variations can be found within the dolomite zone. A slight but noticeable decrease in Mg intensity is observed to the right in the dolomite zone, i.e. towards the dedolomite zone. A similar trend can be seen for Ca. In the calcite, the distribution of Sr looks like a crystal texture. It is probably related to differential incorporation of Sr as a substitutional impurity in the crystals due to the influence of the mineral surface structure (Baele, personal communication; Paquette and Reeder, 1995). An enrichment in iron is observed in the dedolomite, especially in the interface between dolomite and dedolomite. Finally, no conclusive trend is observed for Mn.

LIBS imaging performed on side B brought similar observations than on side A, although the presence of more heterogeneities makes the observations less clear (Figure 30). A complementary petrographic texture was identified: a finely crystalline reddish calcite (FC) is present between the dedolomite and the white calcite. This fine calcite should probably be interpreted as dedolomite as well, resulting from a total replacement of the initial dolomite.

A noticeable decrease in LIBS intensity of both Mg and Ca is observed within the dolomite zone while the Mg/Ca ratio is uniform (Figure 31). The decrease in intensity of the emission of these major elements towards the dedolomite could be explained by the influence of the structure of the rock, likely an increase in porosity. The depletion in Sr in dedolomite is clearly visible while the enrichment in Fe (and Mn) seems more irregular. The dedolomite zone to the left is enriched in Mn and Fe but this does not appear cleary in the narrow dedolomite fringe to the right.

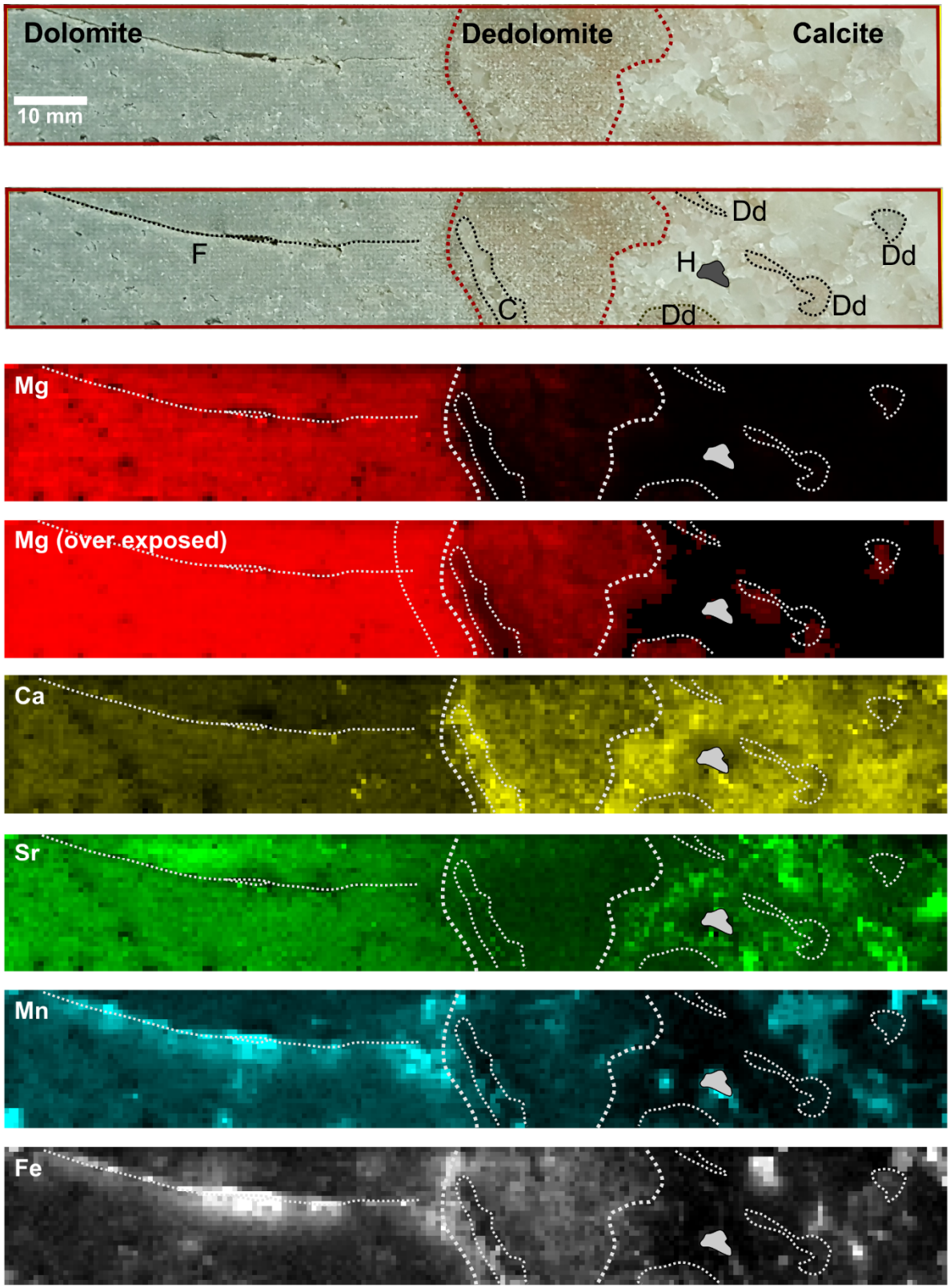

Figure 29. LIBS images on face A for Mg, Ca, Sr, Mn and Fe. Some heterogeneities in the different zones are highlighted. [F]: fracture, [C]: calcite, [Dd]: Dedolomite, [H]: hole.

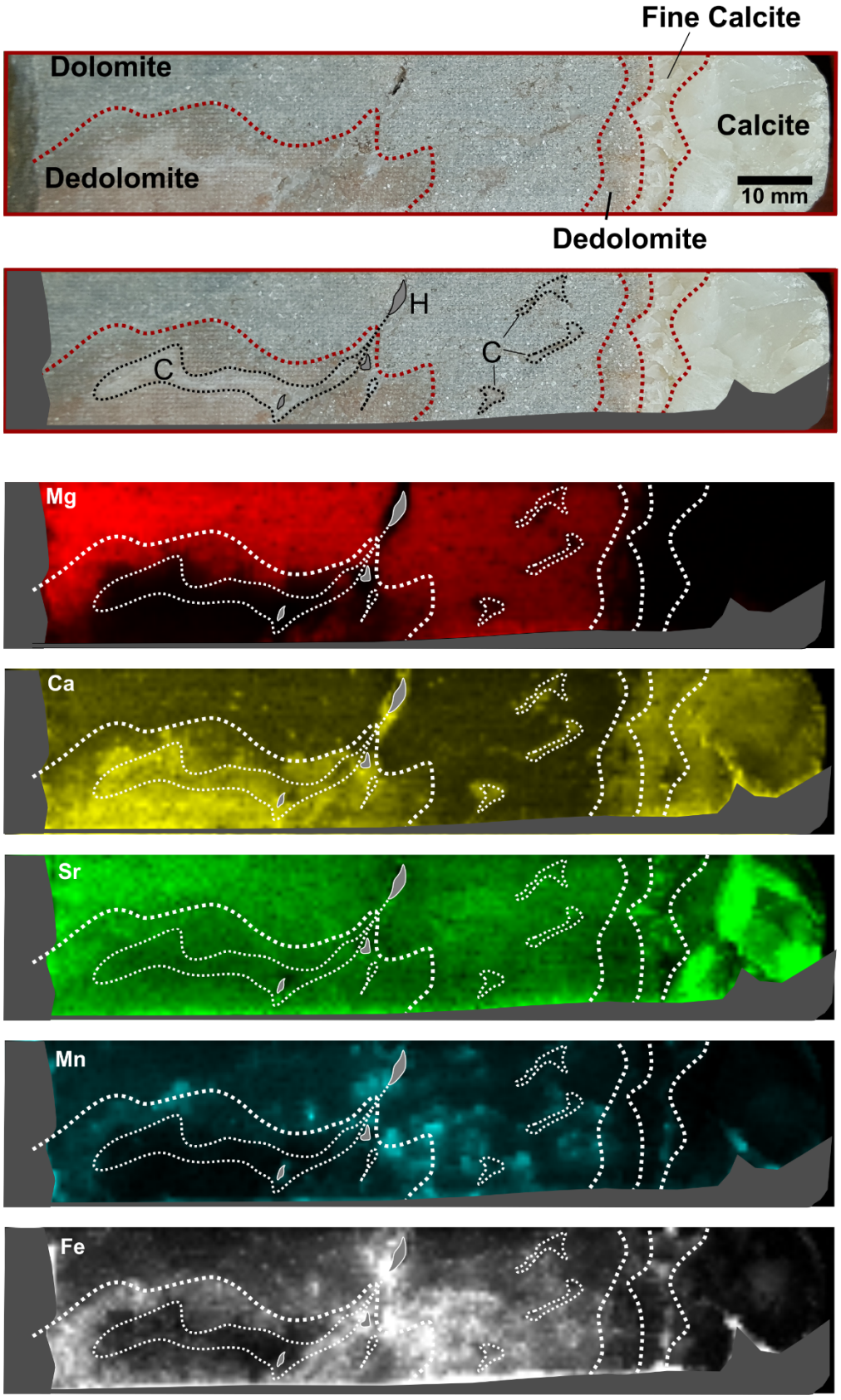

Figure 30. LIBS images on side B for Mg, Ca, Sr, Mn and Fe. Some heterogeneities in the different zones are highlighted. [C]: calcite, [H]: hole.

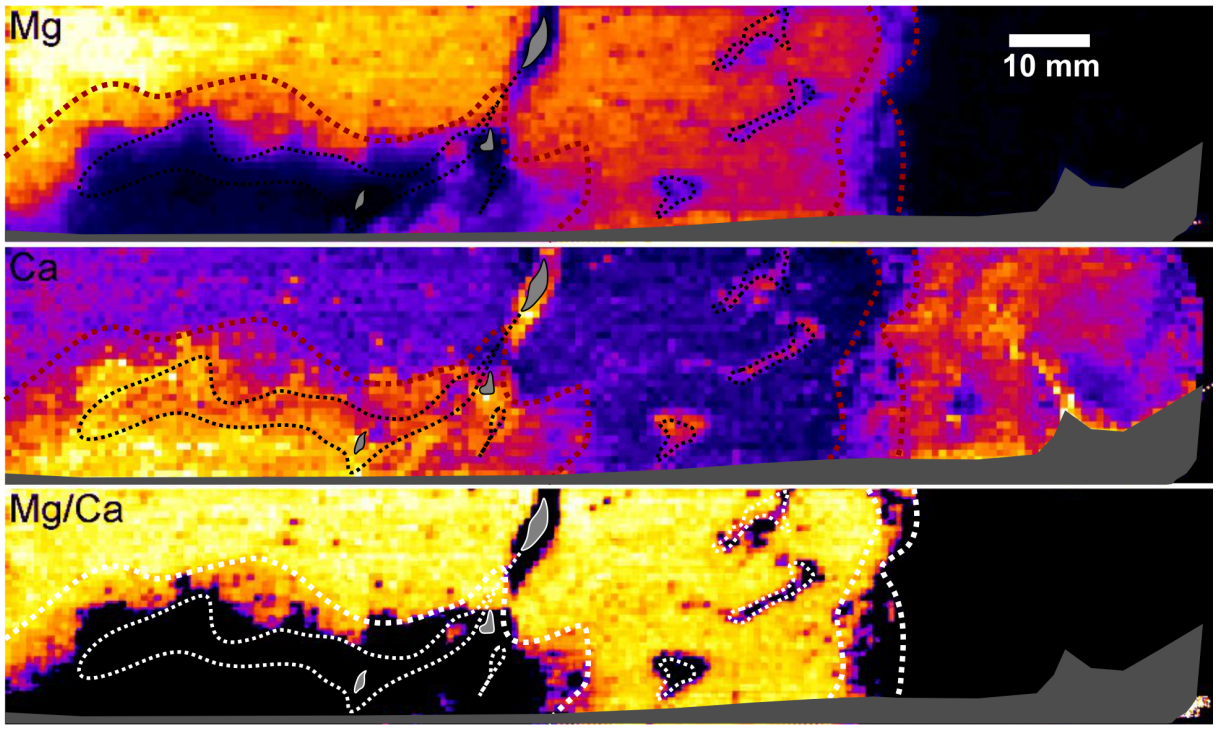

Figure 31. LIBS maps of Mg, Ca and Mg/Ca displayed with a "fire" lookup table (blue = low intensity, yellow = high intensity). The decreasing trend from left to right in Mg and Ca could reflect an increase of porosity in dolomite.

More elements were analyzed in a smaller zone of side B (Figure 32). Some interesting observations can be made. First, it appears that the FC zone still contains Mg. Al and Si are detected in dedolomite with the same intensity as in dolomite. The intensity of those elements drops sharply within the FC and the big white calcite zones. Li is slightly enriched in the dedolomite zone, but decreases in the FC zone and is no longer detected in the white calcite. The behavior of Fe and Mn in dedolomite is not clear on this section; but the FC and the white calcite zones are clearly depleted in those elements (in comparison to the dolomite), except at the boundary between the two zones. Cu drops in the white calcite zone only. K and Na act similarly: they increase steadily from the dolomite to the dedolomite and reach their maximum intensity in the FC zone. Then they drop in the white calcite zone. H yielded a noisy map but this element seems to behave similarily to K and Na, which could indicate the presence of fluid inclusions.

c. Discussion

LIBS imaging has brought to light significant geochemical variations in the "dolomite cavity type".

The elemental maps confirm a gradient of decreasing Mg from the dolomite to the dedolomite and then to the white calcite. Within the dolomite zone, the same decreasing Mg gradient is observed but it is accompanied by a decreasing gradient of Ca as well. This can seem surprising as dedolomite corresponds to Ca enrichment. However, it was shown that the Mg/Ca ratio

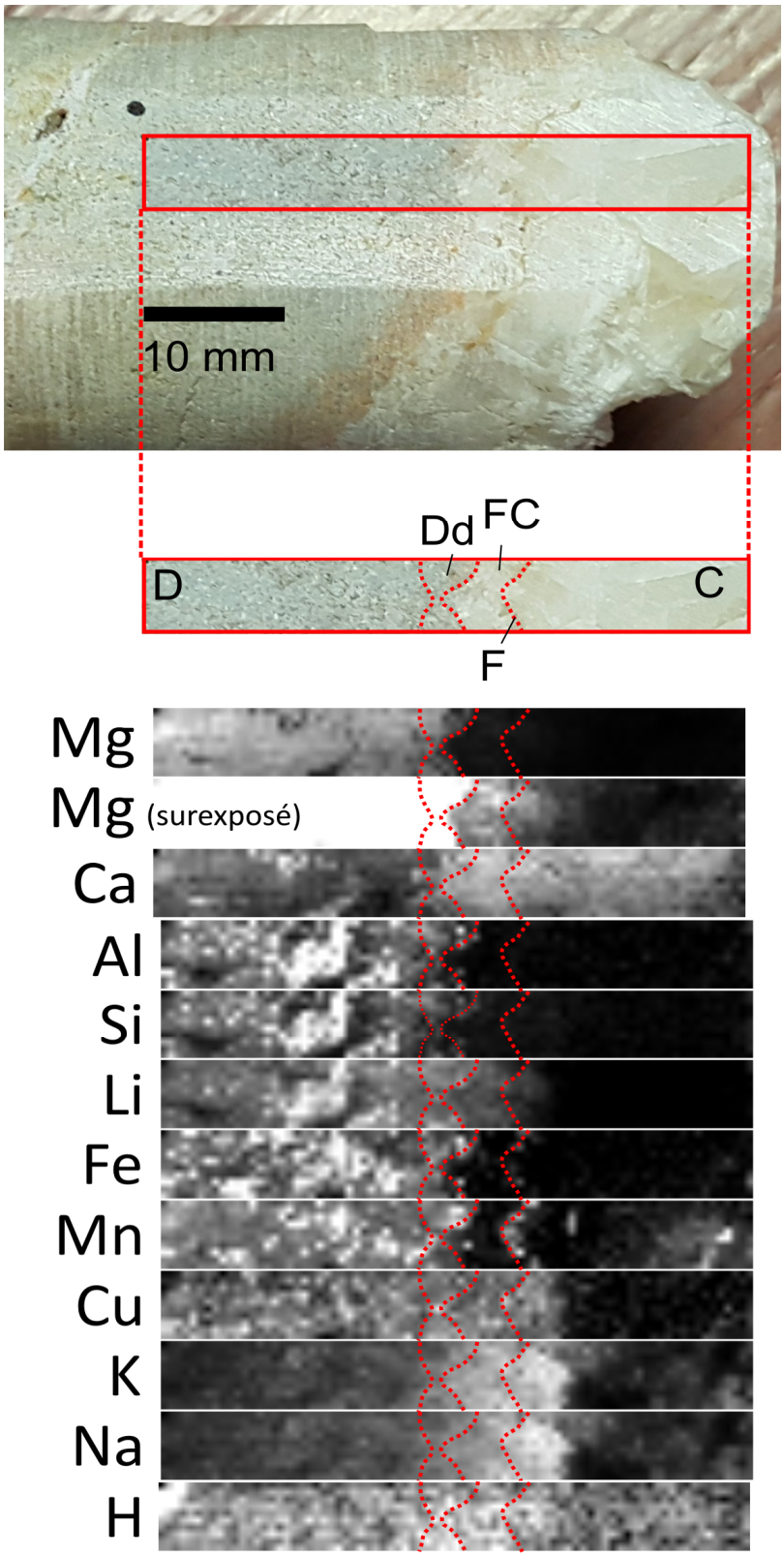

Figure 32. Complementary elemental maps from a smaller zone of side B. [D]: Dolomite, [Dd]: Dedolomite, [FC]: Finely crystalline calcite, [C]: Calcite. See text for details.

stays uniform along this gradient. An increase of porosity could explain the decreasing trend in major element intensity as it was observed in other LIBS analyses (Baele J.-M., pers. com.). This porosity increase is consistent with the model proposed in Figure 23, in which there is a first step of dolomite dissolution, previously or contemporaneously to the dedolomitization step. This increase in secondary porosity could be checked on thin sections, which may be stained to facilitate the observation and the quantification of the porosity. Excess calcium is needed for effective dedolomitization. One model often applied for dedolomitization is the reaction of dolomite with calcium sulfate (Frank, 1981; von Morlot, 1847). This reaction can happen under various conditions, from deep burial to shallow waters. Budai *et al.* (1984) highlighted Sr enrichment and Mn and Fe depletion in dedolomites. They related those data to the dissolution of evaporites in deep burial conditions and subsequent dedolomitization. The data presented above have shown a clear Sr depletion, while Fe and Mn tend rather to be enriched in the dedolomite. This would exclude the possibility that the Furfooz dedolomite was associated to evaporite dissolution under burial conditions. Mn and Fe enrichment, if confirmed, could be explained by the presence of iron and manganese oxydes derived from dolomite dissolution and deposited as inclusions in the dedolomite (Frank, 1981). That could therefore indicate oxidizing conditions for the formation environment of the Furfooz dedolomite, which is more consistent with near-surface processes (Evamy, 1967; Katz, 1968).

The increase of K, Na and H in the dedolomite and the fine calcite zones suggests the presence of fluid inclusions, which may be associated with rapid crystallization. The slight increase of Li could be related to its fixing on clays (Starkey, 1982), that would also be reflected by the presence of Si and Al in the dedolomite, but also by fluid inclusions.

Some elements (Si, Al, Li, Fe, Cu, K, Na, H) show a clear drop, or even disappearance in the white calcite zone. Using Al as a tracer for the clay minerals in the original dolomite, the absence of this element in the late stage white calcite would indicate that a void was created and then filled with new calcite. The fine calcite fringe that is observed on the face B of the sample show some similarities with the dedolomite elemental composition, or at least evolve in the same sense than the dedolomite. Then the reddish calcite is a completely dedolomitized zone where no dolomite remnants subsist but relict clay minerals.

2.2.2.4.d.3 Conclusion

The new data gathered through fluid inclusions, isotopes analysis and LIBS imaging have given new insights about the paleoconditions under which dedolomitization proceeded. Indeed, the results all point out to near-surface or meteoric environment. This is also consistent with the patchy distribution of the dedolomite around discontinuities and the association with karst development (Schoenherr et al., 2018). The clear Sr depletion observed in dedolomite indicates that the geo-hydro-chemical system hosting these processes is open (Canaveras et al., 1996), as it would be the case in a karst setting.

The results of these new investigations are, so far, consistent with the karstogenetic model proposed in Figure 24. Especially, the textural gradient (porosity development) that comes with the geochemical gradient is an essential finding that would confirm a first step of dolomite dissolution as a process creating permeability pathways in this karstic environment. However, a few detail questions still need to be adressed:

- the presence of Mn oxydes in dedolomite (that would be easily seen through a SEM) ;
- the confirmation of the increase in porosity in the dolomite adjacent to the dedolomite ;
- the concentration in fluid inclusions in dedolomite and early calcite.

The LIBS imaging was performed on only one sample; it would also be desirable to multiply LIBS measurements on other samples to confirm the observed trends.

Finally, some more fundamental questions are still on hold as the origin of the Ca excess that initiated dedolomitization, or the destination of the Mg leached from the dolomite during the initial dissolution phase. For the origin of the Ca excess, perhaps the input fluids experienced some enrichment in Ca through dissolution of calcite somewhere upstream, given the heterogeneous distribution of the dolomite patches in the Furfooz massif.

Chapter key points :

- The Furfooz Waulsortian massif constitutes a Natural Reserve located in Southern Belgium, along the Lesse River valley;
- The Waulsortian buildup of Furfooz, lenticular deposit of Tournaisian-Visean Ages, is a rigid structure that reacts with a competent behavior to tectonic constraints. Due to its heterogeneity, the Furfooz mud-mound experienced however different deformation types. Shear zones and diaclases are the main deformation objects of the mud-mound s.s.;
- Heterogeneous dolomitization, taking the form of dolomite patches, affects the Furfooz massif;
- Different types of karst are observed within the massif : a “classical” karst with galleries developed in the direction of discontinuities, and the “dolomite cavity type” developed in the dolomite patches and in close relation with the discontinuity network;
- Cathodoluminescence observations on the “dolomite cavity type” revealed a microscopic petrographic gradient (dolomite-dedolomite-calcite cement) developed from the porosity network;
- A karstogenesis model is proposed. The starting point is the dolomite dissolution;
- LIBS images established a geochemical gradient, accompanying the petrographic gradient, at the sample-scale. It highlighted also the existence of a textural gradient (porosity increase) within the dolomite zone;
- LIBS results, fluid inclusions and isotope analyses point out the possible meteoric conditions in which the geochemical changes could have taken place. This is coherent with a context of karstification in an open system.

2.3 References

Arenas, C., Alonso-Zarza, A. M., & Pardo, G. (1998). Dedolomitization and other early diagenetic processes in Miocene lacustrine deposits, Ebro basin (Spain). *Sedimentary Geology*, *125*, 23–45.

Averbuch, O., Lacquement, F., Mansy, J., Szaniawski, R., & Lewandowski, M. (2006). Déformations au front septentrional de la chaîne varisque: L'exemple des Ardennes franco-belges dans la région de Givet. *Géologie de La France*, (1–2), 85–90.

Ayora, C., Taberner, C., Saaltink, M. W., & Carrera, J. (1998). The genesis of dedolomites: A discusion based on reactive transport modeling. *Journal of Hydrology*, *209*(1–4), 346–365. https://doi.org/10.1016/S0022-1694(98)00095-X

Back, W., Hanshaw, B. B., Plummer, L. N., Rahn, P. H., Rightmire, C. T., & Rubin, M. (1983). Process and rate of dedolomitization : Mass transfer and 14C dating in a regional carbonate aquifer. *Geological Society of America Bulletin*, *94*(12), 1415–1429. https://doi.org/10.1130/0016-7606(1983)94<1415

Belanger, I., Delaby, S., Delcambre, B., Ghysel, P., Hennebert, M., Laloux, M., … Pingot, J. L. (2012). Redéfinition des unités structurales du front varisque utilisées dans le cadre de la nouvelle Carte géologique de Wallonie (Belgique). *Geologica Belgica*, *15*(3), 169–175.

Bischoff, J. L., Julia, R., Shanks, W. C., & Rosenbauer, R. J. (1994). Karstification without carbonic acid: bedrock dissolution by gypsum- driven dedolomitization. *Geology*, *22*(11), 995–998. https://doi.org/10.1130/0091-7613(1994)022<0995:KWCABD>2.3.CO;2

Boulvain, F., & Pingot, J. L. (2012). Genèse du sous-sol de la Wallonie. *Mémoire de La Classe Des Sciences*, *2082*, 190.

Brodkom, F. (1994). *Les roles et comportements tectoniques de mud-mounds waulsortiens au sein de séries calcaro-schisteuses dinantiennes lors des déformations varisques.* PhD thesis, Univeristé Catholique de Louvain.

Budai, J. M., Lohmann, K. C., & Owen, R. M. (1984). Burial dedolomite in the Mississippian Madison Limestone, Wyoming and Utah Thrust Belt. *Journal of Sedimentary Petrology*, *54*, 276–288.

Bultynck, P., & Dejonghe, L. (2001). Devonian lithostratigraphic units (Belgium). *Geologica Belgica*, *4, 1-2*, 39-68.

Canaveras, J. C., Sanchez-Moral, S., Calvo, J. P., Hoyos, M., & Ordonez, S. (1996). Dedolomites associated with karstification. An example of early dedolomitization in lacustrine sequences from the Tertiary Madrid Basin, Central Spain. *Carbonates and Evaporites*, *11*(1), 85–103.

Cremers, D. A., & Radziemski, L. J. (2006). *Handbook of Laser-induced Breakdown Spectroscopy*. John Wiley & Sons Ltd. https://doi.org/10.1002/0470093013

de Dorlodot, H. (1895). Le Calcaire Carbonifère de la Belgique et ses relations stratigraphiques avec celui du Hainaut français. *Bulletin de La Société Belge de Géologie*, *25*, 119–155.

De Ridder, G. J. (2014). *The origin and cementation process of calcite in the Waulsortian mud-mounds*. Bachelor thesis. Katholieke Universiteit of Leuven.

Deike, R. D. (1990). Dolomite dissolution rates and possible Holocene dedolomitization of water bearing units in the Edwards aquifer, south-central Texas. *Journal of Hydrology*, *112*, 335–373.

Delcambre, B., & Pingot, J. L. (1993). *Carte géologique Hastière-Dinant*. *Map and notice*. Service Public de Wallonie, DGO 3.

Dewaide, L., Baele, J.-M., Collon-Drouaillet, P., Quinif, Y., Rochez, G., Vandycke, S., & Hallet, V. (2014). Karstifcation in dolomitized Waulsortian mud-mounds (Belgium). *Geologica Belgica*, *17*(1).

Dupont, E. (1883). Sur les origines du Calcaire Carbonifère de Belgique. *Bulletin de l'Académie Royale Des Sciences de Belgique*, *3ème Série*(5), 211–229.

Evamy, B. D. (1967). Dedolomitization and the development of rhombohedral pores in limestones (Upper Cambrian), Southeast Missouri. *Journal of Sedimentary Petrology*, *5*, 7–17.

Ford, D., & Williams, P. (2007). *Speleogenesis: The development of cave systems*. *Karst Hydrogeology and Geomorphology*. John Wiley & Sons Ltd. https://doi.org/10.1002/9781118684986

Frank, J. R. (1981). Dedolomitization in the Taum Sauk Limestone (Upper Cambrian), Southeast Missouri, *51*(1), 7–17.

Friedman, G. M. (1994). Upper Cambrian-Lower Ordovician (Sauk) platform carbonates of the Northern Appalachian (Gondwana) passive margin. *Carbonates and Evaporites*, *9*, 143–150.

Galbács, G. (2015). A critical review of recent progress in analytical laser-induced breakdown spectroscopy. *Analytical and Bioanalytical Chemistry*, *407*(25). https://doi.org/10.1007/s00216-015-8855-3

Hance, L., Poty, E., & Devuyst, F.-X. (2001). Stratigraphie séquentielle du Dinantien type (Belgique) et corrélation avec le Nord de la France (Boulonnais, Avesnois). *Bulletin de La Société Géologique de France*, *172*(4), 411–426.

Harmon, R. S., & Russo, R. E. (2013). Laser-Induced Breakdown Spectroscopy. *Treatise on Geochemistry: Second Edition*, *15*(October), 245–272. https://doi.org/10.1016/B978-0-08-095975-7.01417-0

Hudson, J.D. (1977). Stable Isotopes and limestone lithification. *Journal of the Geological*

Society, 133 (6), 637-660.

James, N. P., Bone, Y., & Kyser, T. K. (1993). Shallow Burial Dolomitization and Dedolomitization of Mid-Cenozoic, Cool-Water, Calcitic, Deep-Self Limestones, Southern Australia. *Journal of Sedimentary Petrology*, *63*(3), 528–538.

Jones, B., Pleydell, S. M., Ng, K. C., & Longstaffe, F. J. (1989). Formation of poikilotopic calcite-dolomite fabric in the Oligocene-Miocene Bluff Formation of the Ground Cayman British West Indies. *Bulletin of Canadian Petroleum Geology*, *3*, 255–265.

Katz, A. (1968). Calcian dolomites and dedolomitization. *Nature*, *217*, 439–440.
Khalaf, F. I., & Abdal, M. S. (1993). Dedolomitization of dolocrete deposits in Kuwait, Arabian Gulf. *Geologische Rundschau*, *82*, 741–749.

Lacquement, F., Averbuch, O., Mansy, J. L., Szaniawski, R., & Lewandowski, M. (2005). Transpressional deformations at lateral boundaries of propagating thrust-sheets: The example of the Meuse Valley Recess within the Ardennes Variscan fold-and-thrust belt (N France-S Belgium). *Journal of Structural Geology*, *27*(10), 1788–1802.
https://doi.org/10.1016/j.jsg.2005.05.017

Land, L. S., & Prezbindowski, D. R. (1981). The origin and evolution of saline formation waters, lower Cretaceous carbonates, south-central Texas, U.S.A. *Journal of Hydrology*, *54*, 51–74.

Lees, A. (1961). The Waulsortian “reefs” of Eire: a carbonate mudbank complex of Lower Carboniferous age. *Journal of Geology*, *69*, 101–109.

Lees, A. (1982). The paleoenvironmental setting and distribution of the Waulsortian facies of Belgium and southern Britain. In K. Bolton, H. R. Lane, & D. V. LeMone (Eds.), *Symposium on the Environmental Setting and Distribution of the Waulsortian Facies* (pp. 1–16). El Paso Geological Society and University of Texas at El Paso.

Lees, A., Hallet, V., & Hibo, D. (1985). Facies variation in Waulsortian buildups. Part 1. A model from Belgium. *Geological Journal*, *20*, 133–158.

Lees, A., & Hennebert, M. (1982). Carbonate rocks of the Knap Farm Borehole at Canningnton Park, Somerset. *Report, Institute of Geological Science*, *82*(5), 18–36.

Lees, A., & Miller, J. (1995). Waulsortian Banks. *Carbonate Mud-Mounds: Their Origin and Evolution, International Association of Sedimentologists Special Publication*, *23*, 191–271. https://doi.org/10.1002/9781444304114.ch7

Liu, Z., & Dreybrodt, W. (1997). Dissolution kinetics of calcium carbonate minerals in H2O-CO2 solutions in turbulent flow: the role of the diffusion boundary layer and the slow reaction H2O+CO2↔H+ + HCO3-. *Geochemica and Cosmochemica Acta*, *61*, 2879–2889.

Liu, Z., Yuan, D., & Dreybrodt, W. (2005). Comparative study of dissolution rate-determining mechanisms of limestone and dolomite. *Environmental Geology*, *49*, 274–279.

Marshall, D. J. (1988). *Cathodoluminescence of Geological Materials*. Boston: Unwin Hyman.

Nader, F. H., Swennen, R., & Keppens, E. (2008). Calcitization/dedolomitization of Jurassic dolostones (Lebanon): results from petrographic and sequential geochemical analyses. *Sedimentology*, *55*, 1467–1485.

Nader, F. H., Swennen, R., & Ottenburgs, R. (2003). Karst-meteoric dedolomitization in Jurassic carbonates, Lebanon. *Geologica Belgica*, *6*, 3–23.

Paquette, J., & Reeder, R. J. (1995). *Relationship between surface structure, growth mechanism, and trace element incorporation in calcite*. *Geochimica et Cosmochimica Acta* (Vol. 59), 4, 735-749.

Pokrovsky, O. S., Golubev, S. V, Schott, J., & Castillo, A. (2009). Calcite , dolomite and magnesite dissolution kinetics in aqueous solutions at acid to circumneutral pH , 25 to 150 ° C and 1 to 55 atm p CO 2 : New constraints on CO 2 sequestration in sedimentary basins. *Chemical Geology*, *265*(1–2), 20–32. https://doi.org/10.1016/j.chemgeo.2009.01.013

Poty, E; Hance, L; Lees, A; Hennebert, M. (2001). Dinantian lithostratigraphic units (Belgium). *Geologica Belgica*, *4*(1–2), 69–94.

Qing, Z. (1999). *Carbonate diagenesis and porosity evolution in the Guelph Formation, Southwestern Ontario*. PhD thesis, University of Waterloo, Ontario, Canada.

Quinif, Y. (1999). Fantômisation, cryptoaltération et altération sur roche nue. Le tryptique de la karstification. In *Actes du colloque Europée Karst-99* (pp. 159–164).

Quinif, Y. (2010). Fantôme de roche et Fantômisation. Essais sur un nouveau paradigme en karstogenèse. *Karstologia - Mémoires*, *18*, 196.

Radziemski, L. J., Loree, T. R., & Cremers, D. A. (1983). Laser-Induced Breakdown Spectroscopy (LIBS): A New Spectrochemical Technique (pp. 303–307). Springer, Berlin, Heidelberg. https://doi.org/10.1007/978-3-540-39552-2_39

Raines, M. A., & Dewers, T. A. (1997). Dedolomitization as a driving mechanism for karst generation in Permian Blaine Formation, Southwestern Oklahoma, USA. *Carbonates and Evaporites*, *12*(1), 24–31.

Ronchi, P., Jadoul, F., & Savino, R. (2004). Quaternary dedolomitization along fracture systems in a late Triassic dolomitized platform (western southern Alps, Italy). *Carbonates and Evaporites*, *19*(1), 51–66.

Schindelin, J., Arganda-Carreras, I., Frise, E., Kaynig, V., Longair, M., Pietzsch, T., … Cardona, A. (2012). Fiji: an open-source platform for biological-image analysis. *Nature Methods*, *9*(7), 676–682. https://doi.org/10.1038/nmeth.2019

Schoenherr, J., Reuning, L., Hallenberger, M., Lüders, V., Lemmens, L., Biehl, B. C., … Strohmenger, C. J. (2018). Dedolomitization: review and case study of uncommon mesogenetic formation conditions. *Earth-Science Reviews*, *185*(July), 780–805. https://doi.org/10.1016/j.earscirev.2018.07.005

Senesi, G. S. (2014). Laser-Induced Breakdown Spectroscopy (LIBS) applied to terrestrial and extraterrestrial analogue geomaterials with emphasis to minerals and rocks. *Earth-Science Reviews*, *139*(December), 231–267. https://doi.org/10.1016/j.earscirev.2014.09.008

Sibley, D. F., & Gregg, J. M. (1987). Classification of dolomite rock structure. *Journal of Sedimentary Research*, *57*(6), 967–975.

Starkey, H. C. (1982). The Role of Clays in Fixing Lithium. *Geological Survey Bulletin*, *1278*(F).

Theriault, F., & Hutcheon, I. (1987). Dolomitization and calcitization of Devonian Grosmont Formation, Northern Alberta. *Journal of Sedimentary Petrology*, *57*(6), 955–966.

Thys, G., & Michel, G. (2014). Atlas du karst wallon : Bassin de La Basse Lesse. Commission Wallonne d'Etudes et de Protection des Sites Souterrains (CWEPSS), SPW Editions, 400p.

Van Offenwert, S. (2014). *Sediment petrological study of dolomite occurences in Waulsortian mud-mounds*. Bachelor thesis, Katholieke Universiteit of Leuven.

von Morlot, A. (1847). Ueber Dolomit und seine kuenstliche Darstellung aus Kalkstein: Haidinger Naturwiss. *Abhanlinger*, *1*, 305–315.

Woronick, R. E., & Land, L. S. (1985). Late burial diagenesis, Lower Cretaceous Pearsall and Lower Glen Rose formations, South Texas. In N. Schneidermann & P. M. Harris (Eds.), *Carbonates cements* (Special Pu, pp. 265–275). Tulsa.

Chapter 3

Hydrogeological Setting

Chapitre 3 Hydrogeological setting

In brief, in this chapter:

- Regional and local hydrogeological settings of the Furfooz area are described;
- Focus is given to the Furfooz karst system description;
- Strategies and methods for the karst system monitoring are defined;
- Analyses of the long-term monitoring and conclusions about the system functioning are presented.

3.1 Regional setting

The Condroz groundwater is a major water resource in south of Belgium as 25% of the annual extracted water in Wallonia are pumped in this water table (Service Public de Wallonie, 2010). The regional flow scheme is constrained by the geological structure, i.e. the typical alternation of sandstone anticlines and limestone synclines, and the strong contrast in the encountered lithologies. The Furfooz karst lies in a syncline that corresponds mainly to a large Carboniferous aquifer crossed from SE to NW by the river Lesse. The southern and northern edges of this aquifer are limited by the aquifer of the Famennian sandstones. In between, a few other hydrogeological units are to be considered.

3.1.1 Hydrogeological units

This section describes the hydrogeological units encountered on the hydrogeological map of the Furfooz area (Figure 1). These unit descriptions and definitions are based on the official hydrogeological map of the area and its explicatory note (Nogarède et al., 2003). The hydrogeological map is based on the geological map: the hydrogeological units re-group, indeed, together the geological formations according to the similarity of their hydrodynamic features. This re-grouping is summarized in Table 1.

The three types of encountered hydrogeological units are defined as:

- Aquifer: pervious formation containing water in exploitable quantities.
- Aquitard: geologic formation, rather impervious and semi-confined. The flow speed is much slower than in an aquifer.
- Aquiclude: water saturated formation with very poor permeability. Water cannot be extracted in profitable quantities.

Geological formation	Hydrogeological units
Alluvial deposits recents / ancients	Alluvium Aquifer / Terraces Aquifer
Lives Formation	Carboniferous Aquifer
Neffe Formation	
Molignée Formation	
Leffe Formation	
Bayard Formation	
Maurenne Formation	Carboniferous Aquitard
Landelies Formation	Carboniferous Aquifer
Pont d'Arcole Formation	Carboniferous Aquiclude
Hastière Formation	Hastière Aquifer
Ciney Formation	Famennian Sandstones Aquifer

Table 1. Comparison between the geological formations and the corresponding hydrogeological units. The colors correspond to the chosen coloring of the hydrogeological map.

Famennian Sandstones Aquifer (AF_FAM_SANDSTONE)

This aquifer corresponds to the Ciney sandstones. Given to the geological context, these sandstones are mainly found on topographic hills, which make them prone to long-term weathering into sand. Porosity and permeability are mainly due to the combined effect of weathering and the deep fracturation of sandstones. Furthermore the weathering sands have a filtering capacity that offers good quality infiltration waters. The water table of this aquifer is unconfined.

Hastière Aquifer (AF_HASTIERE)

As the name suggests, the Hastière Formation constitutes this aquifer. This crinoidal limestone has a high permeability and is limited on its top by an aquiclude. The water table of this aquifer can be unconfined or artesian when below the aquiclude. However, due to the beds verticality (dips close to 90°), this situation doesn't occur at the Furfooz site.

Carboniferous Aquiclude (AC_CARBO)

It corresponds to the shales of the Pont d'Arcole Formation. This impervious formation has a very important role on the regional hydrogeology as it separates the Hastière Formation and the Upper Carboniferous aquifer. Due to the vertical bedding, this formation can play the role of hydrogeological threshold when it crosses the valleys.

Carboniferous Aquifer and Aquitard (AF_CARBO and AT_CARBO)

The Carboniferous Aquifer starts with the Landelies Formation up to the Lives Formation. It constitutes a large unconfined water table that is widely exploited. The base of the aquifer is however interrupted by the Maurenne Formation. The shaly limestones of this formation are not impervious but they can locally decrease the permeability and therefore constrain the flows. The Maurenne Formation is, for this reason, defined as “aquitard”.

Alluvium and terraces Aquifer (AF_ALLUVIUM and AF_TERRACES)

They correspond to local aquifers existing in alluvial or ancient alluvial deposits. They can bear a valuable amount of water.

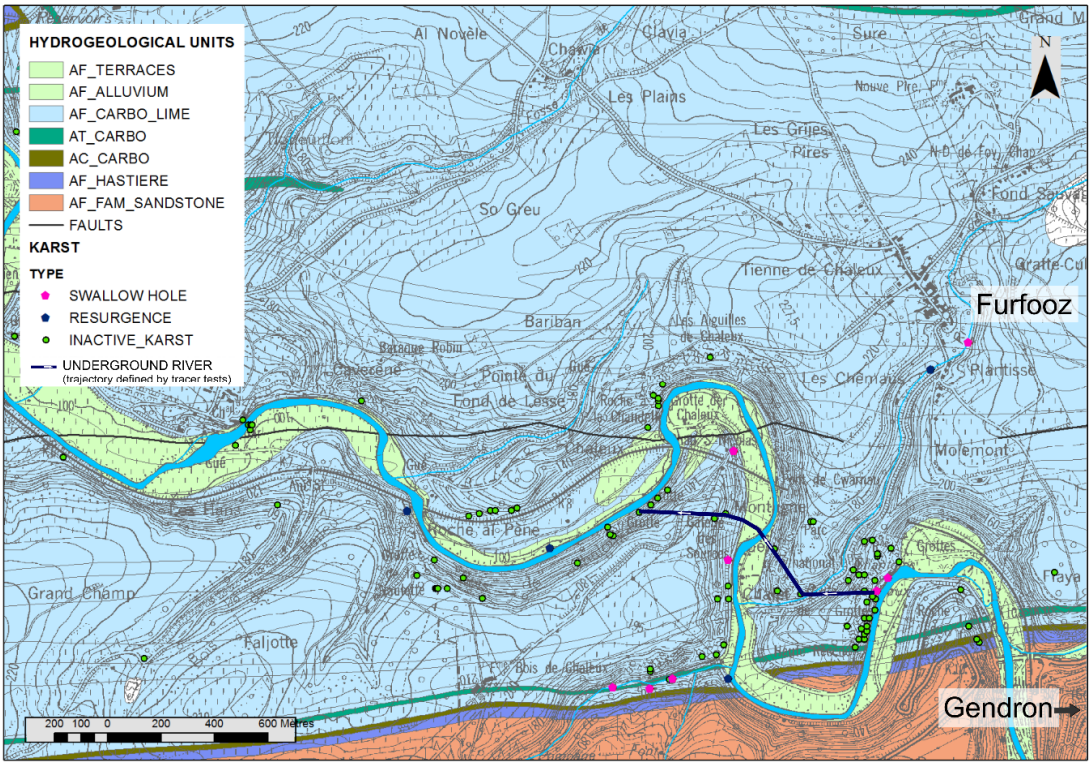

Figure 1. Hydrogeological map of the Furfooz area (modified from Nogarède et al., 2003).

3.1.2 The flow scheme at a mid- to local-scale

The regional alternation of the Devonian anticlines and Carboniferous synclines imposes the regional flow scheme. The Carboniferous aquifer has a very high permeability and the flows are influenced by geological structures. Indeed, the water table flows preferentially in the trend of the bedding towards the base level (the draining rivers). In the Famennian aquifer the flow scheme is different. The permeability being lower, the piezometric level is closer to the surface and the hydraulic gradient is higher. The topography has therefore a strong influence

on the flows. In the sandstone anticlines, the water table flows perpendicularly to the fold axis, following the hill slope. Then, given the geological structure, the Famennian water table supplies the Carboniferous aquifer in a diffuse way.

In the studied area, the Carboniferous aquifer water supply is also ensured by the runoff, the efficient precipitations, and of course by the karst infiltrations. There is numerous karst occurrences described in the studied zone; the active swallow holes or resurgences being limited to the valley floors (Figure 1). The Sebia and The Ri des Vesses are both infiltrating rivers as reflected in the numerous swallow holes described in those - often dry - valleys. The drainage of the aquifer can only be ensured by the river Lesse when it is not infiltrative. In the Furfooz Natural Reserve, the Lesse is infiltrative and characterized by the development of an important conduit system that crosses two of its aerial meanders. The general trajectory of this karst system (E-W), defined by tracer tests, is displayed on Figure 1.

3.2 The Furfooz karst system

From a hydrogeological point of view, a karst aquifer is classically structured and defined by two major domains: the unsaturated and the saturated zones (Stevanovic, 2015). The unsaturated – or vadose – zone can be divided in two parts, i.e. the epikarst that constitutes a discontinuous and temporary water storage, and the infiltration zone where water flows vertically through preferential fissured paths (Mangin, 1975; Dörfliger, 2010). The saturated – or phreatic – zone is constantly saturated with water. It is drained mainly by karst conduits that interact with the fissured host rock, and in which the water flows quickly to one or several discharge areas. The term of “karst system” was introduced by Mangin (1974) who defines it, sensu stricto, as an entity in which the drainage is ensured by organized and interconnected drains. These drains interact with capacitive – or storage – zones that do not participate to the drainage. A karst system, under this definition, corresponds therefore to the entire hydrogeological basin (saturated and unsaturated) upstream the discharge area, and which is characterized by strong contrasts of hydraulic conductivity.

In this study however, the Furfooz karst system refers mainly to the fast drainage system represented by the karst conduits in which flows the underground river. The entire recharge area is not specifically taken into account, nor is the issue of the aquifer water budget. Indeed, as it will be explained hereafter, the discharge of the all system cannot be measured precisely. The issues tackled in this research are mainly linked to the hydrodynamics of the underground river that flows in the karst conduit system.

As exposed in chapter 2, the massif of Furfooz hosts numerous karst occurences that have different scale of development. In the saturated zone of the aquifer, several major cave networks are known and they host groundwater flows. As it will be demonstrated in chapter 4 by dye tracing, these different cave networks are actually on the path of the same underground river (Figure 2): when the surface Lesse River, flowing from north-east, arrives on the Waulsort Formation, it sinks partially from its right bank into a swallow hole (“Chantoir

des Nutons" - CN) and flows underground on about 1.2 km before the resurgence ("Trou de la Loutre" - TDL). On its path, the underground river crosses two lakes: the "Trou Qui Fume" (TQF) lake and the "Puits des Vaux" (PDV) lake. Two other karst networks guarantee the access to the underground Lesse: the "Sepulture" (SEP) and the "Galerie des Sources" (GDS). In these cave networks, the underground river can be followed with more or less continuity. Between the caves, the trajectory of the river can only be guessed, and the distances are estimated on basis of drawn lines on the map. They constitute therefore minimum distances. The underground river main trajectory (from the swallow hole to the resurgence) is guessed by linking the different sites where the river is observed. It appears that the river flows in two main direction: E-W and SSE-NNW. These directions correspond actually to, respectively, the bedding direction and the direction of the main diaclase family (chapter 2, Figure 17, p. 27). In doing so, the underground river cuts two meanders of the surface Lesse River (Figure 2). The description that has just been made of the Furfooz underground river constitutes what is called hereafter "the Furfooz karst system". A 3D conception of this system (Poulain, 2013) is given in Figure 2. The study of this system is limited to what can be observed through the different known cave networks. These are described in details in chapter 3.2.1.

3.2.1 Description

3.2.1.1 The Chantoir des Nutons swallow hole (CN) and the Trou Qui Fume cave (TQF)

Photos illustrating this part of the system are shown in Figure 3. The CN is a small hole on the right bank of The Lesse. The chantoir can be easily seen in moderate to low flow conditions. From there the underground river follows an unknown path on about 70 m before to emerge in the lower gallery of the TQF cave. The river follows then a very confined and very muddy conduit on about 140 m before to arrive into a lake. This lake was explored by diving by Michel Pauwels who described a narrow lake of about 30 m long and a maximum of 10 m in large (in surface). The lake is becomes narrower in depth. The reached depth is 27 m but the diver found there an accumulation of rock boulders that stopped his progression further on. He could evaluate that the bottom should be around -31 m. The lake has, more or less, the shape of an inverted cone (Figure 4). The volume of the lake could be estimated, on basis of a cone volume calculation, at about 7000 m^3. The diver mentioned also the instability of the rock boulders throughout the lake, and the clouding of the lake by suspended matter. When one progress to the lake, turbidity due to the suspending of sedimented matter (organic and inorganic) can be observed into the lake. As illustrated on Figure 3, the turbidity cloud doesn't disperse throughout the lake but stays very concentrated and tends to sink rapidly to the depth of the lake.

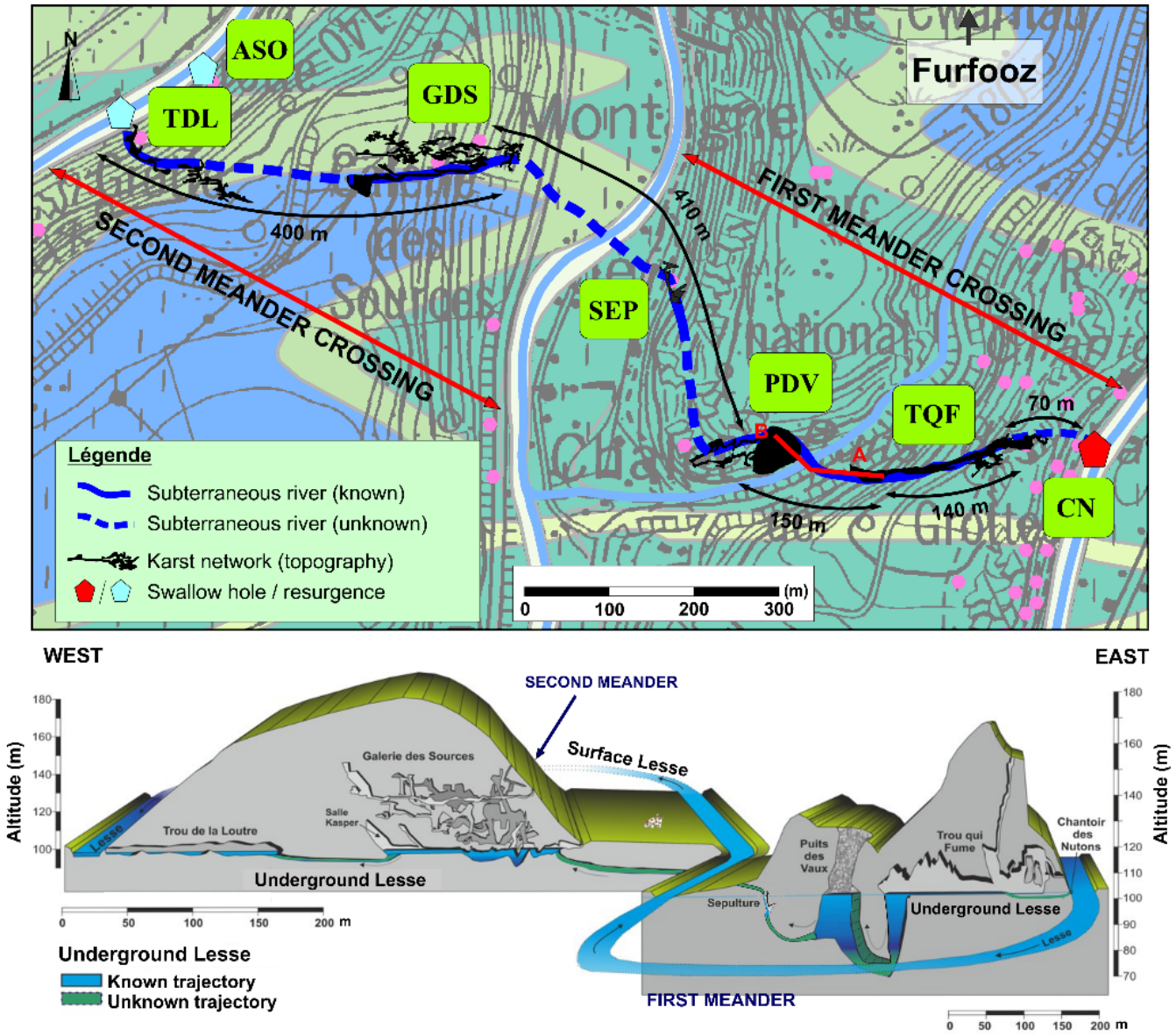

Figure 2. General view of the Furfooz karstic system and the caves that give access to the underground river. Above : Plan view on the geological map; Below : section view of the system in a block diagram (modified from Poulain, 2013).

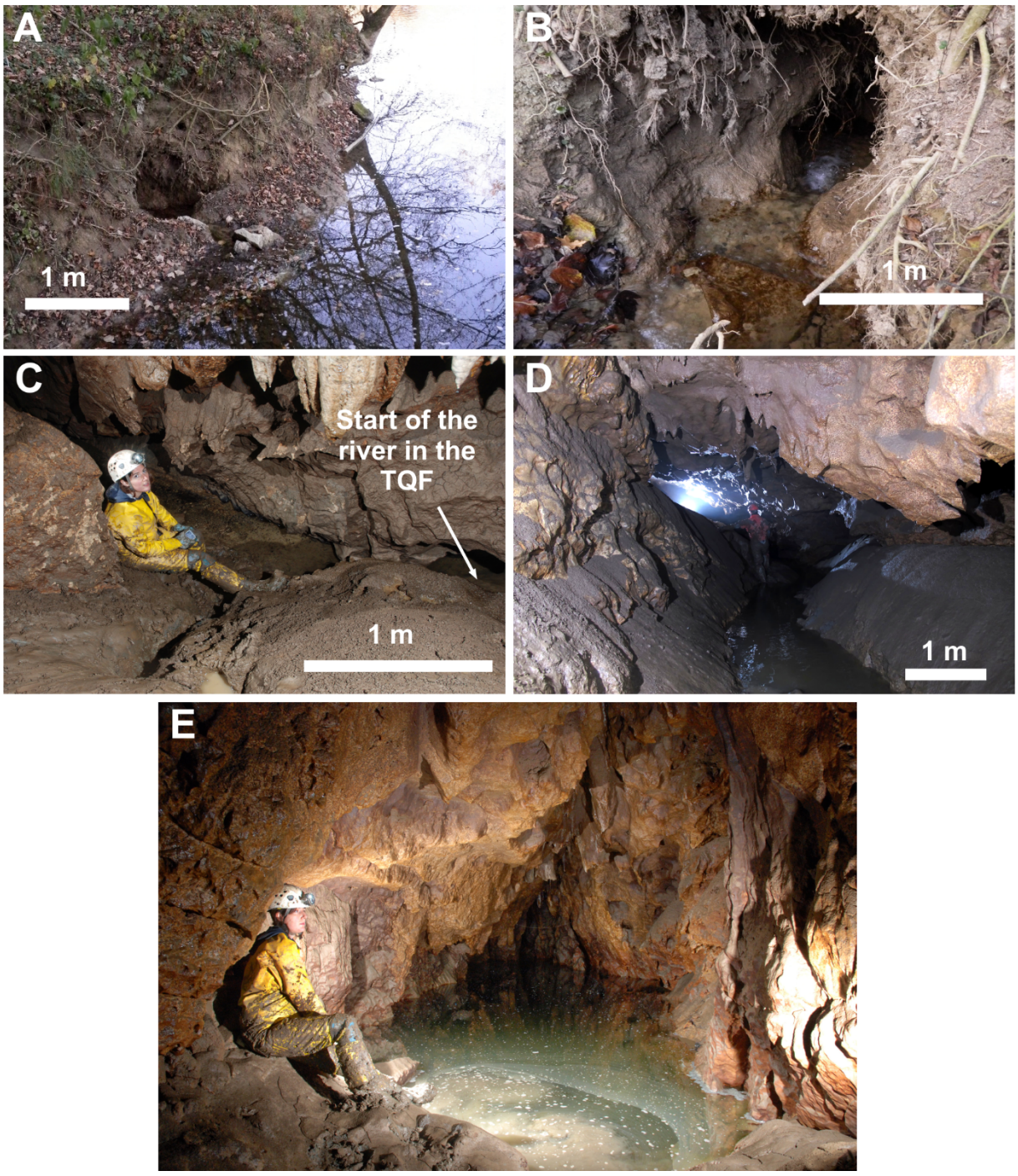

Figure 3. Photos of the CN swallow hole and the TQF underground river and lake. [A] and [B] illustrate the CN swallow hole; [C] shows the arrival of the river at the TQF; after 70 m of unknown progression; [D] illustrates the muddy and secluded section of the TQF river; [E] pictures the TQF narrow lake, an important turbidity is remarkable on the foreground. This cloud of turbidity doesn't disperse throughout the all lake but sinks rapidly to the bottom. Photos: G. Rochez.

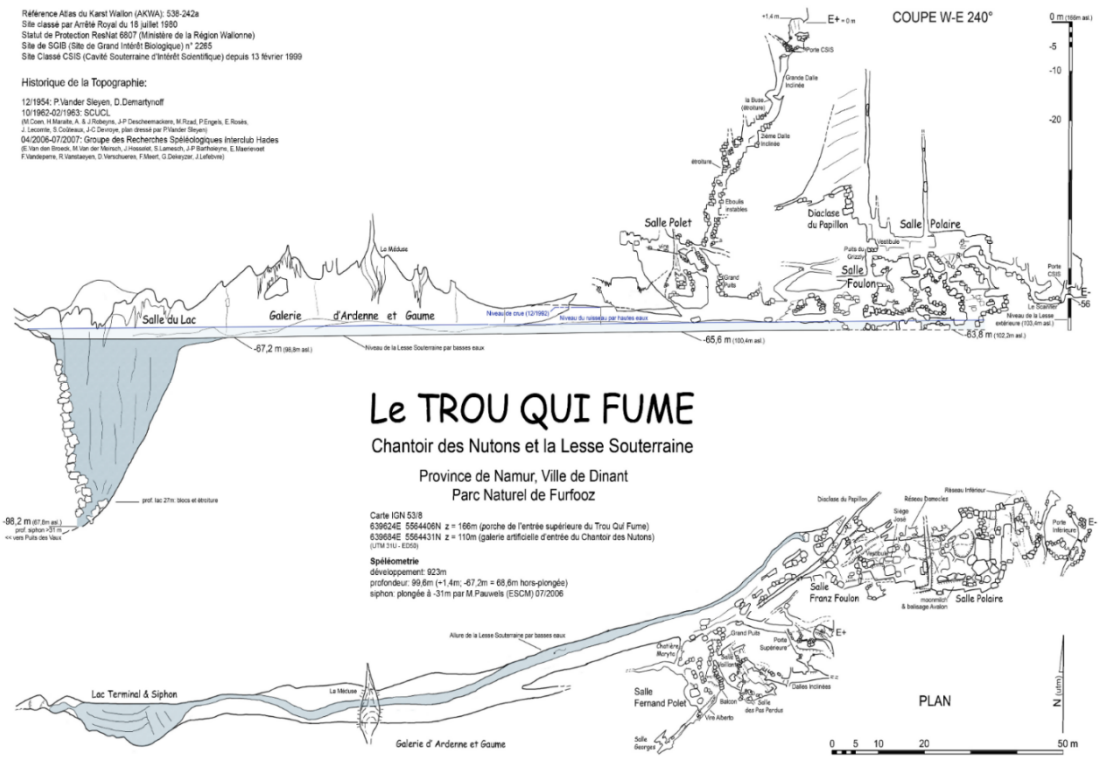

Figure 4. Topographical map of the TQF cave drawn by the speleoclub Hades in 2007. The river can be followed in the lower gallery on about 140 m before to reach the TQF lake.

3.2.1.2 The Puits des Vaux cave and lake (PDV)

The PDV lake is located about 60 m downstream the TQF. The surface of this lake appears at the bottom of a pit and can therefore be reached from the outside, without speleological progression needed (Figure 5). The lake has also been dived several times by Michel Pauwels who mentioned the feeling of a very big volume of water in which big rock boulders are scattered. The water is rather still and cloudy (whatever the flow conditions) and the diver progression is stopped at about – 25 m where a narrow passage leads into a small room closed by rock boulders. The diver could not identify a real upstream and downstream flow into the lake but he mentioned a small gallery at about -15 m on the western side of the lake. This conduit contains a rather clean water suggesting some flow in it and the conduit show a strong positive slope that leads rapidly to – 9m and ends onto rock boulders. The volume of the PDV lake is very difficult to estimate as the limits of the lake are not really known. Based on estimated dimensions of 25 m (depth) on 50 m (length) and on 20 m (width), and considering a cone-shape, the volume of the PDV lake approximates 16000 m^3. Based on the dive reports, a conceptual scheme of the two lakes can be drawn (Figure 6).

Two small inactive galleries exist on the western side of the PDV pit. Their development is limited and one of those galleries (the lower one) can contain some water. It seems to be some confined water that appears only in high flow conditions. A topography of these galleries has been made in 1961 (Figure 7). It supposes the passage of the underground Lesse both in

the lake and in the lower gallery but the recent observations made on the field suggest that the water present in this gallery is only stagnant water in equilibrium with the lake level.

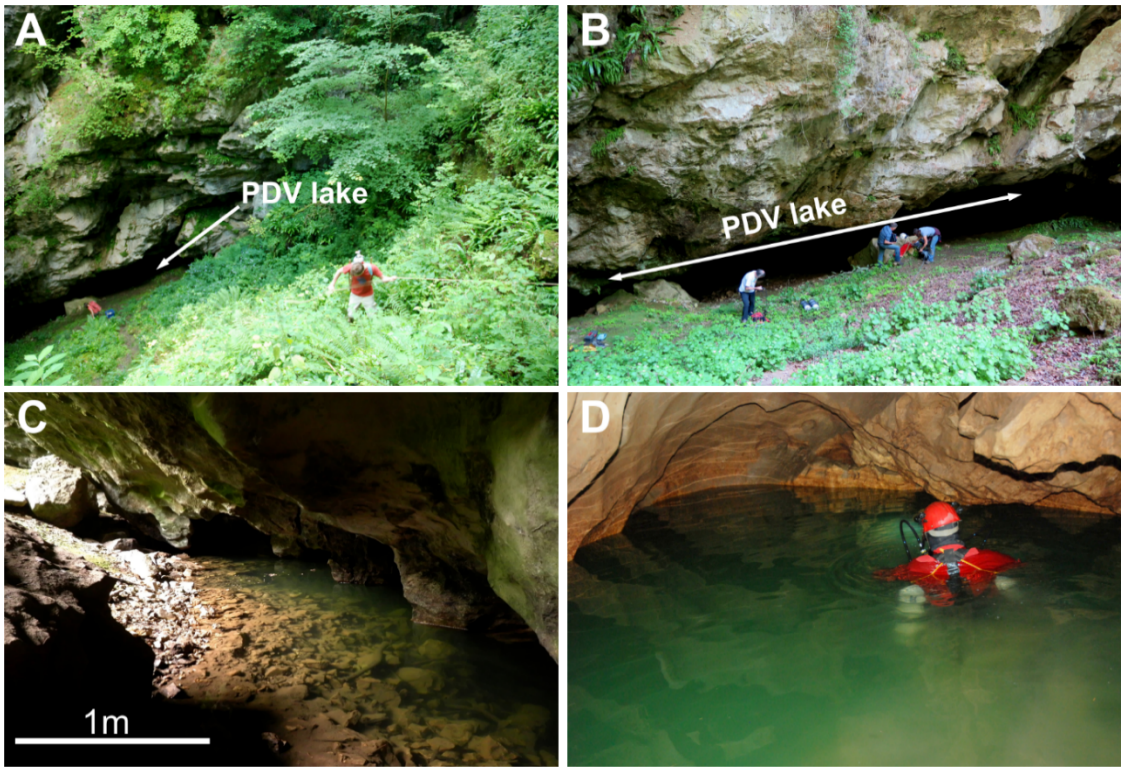

Figure 5. Pictures of the PDV lake. [A]: progression to the bottom of the PDV pit; [B]: preparation of a dive; [C]: bank of the lake from which the progression further on can only be made by diving; [D]: Michel Pauwels starting a dive. Photos: G. Rochez.

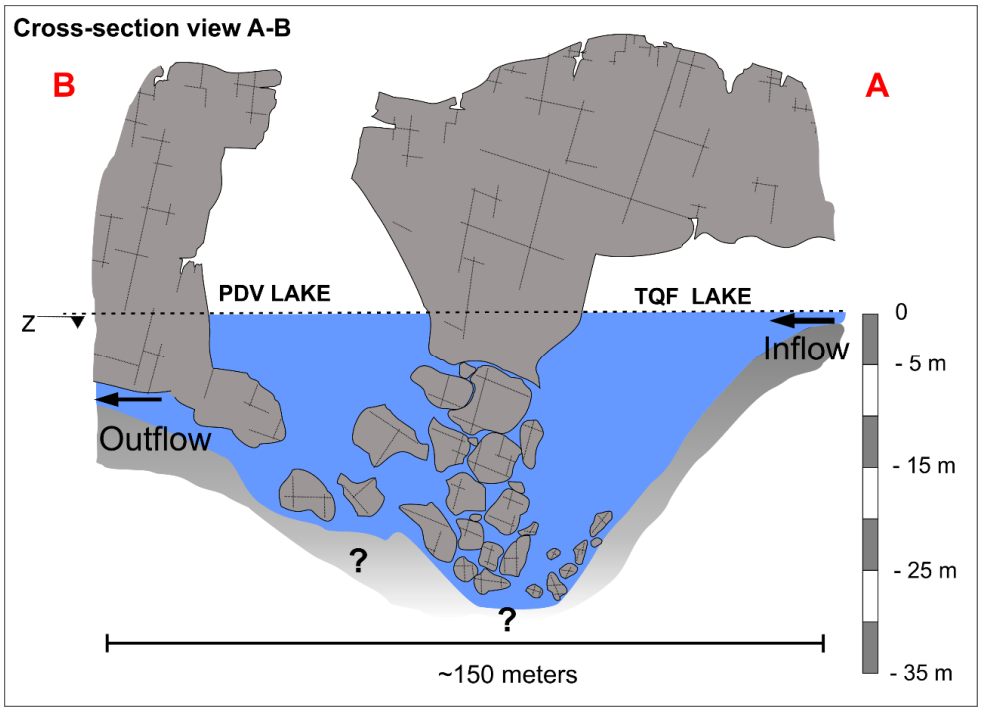

Figure 6. Conceptual idea of the two lakes and their connection. The section A-B is positioned on Figure 2.

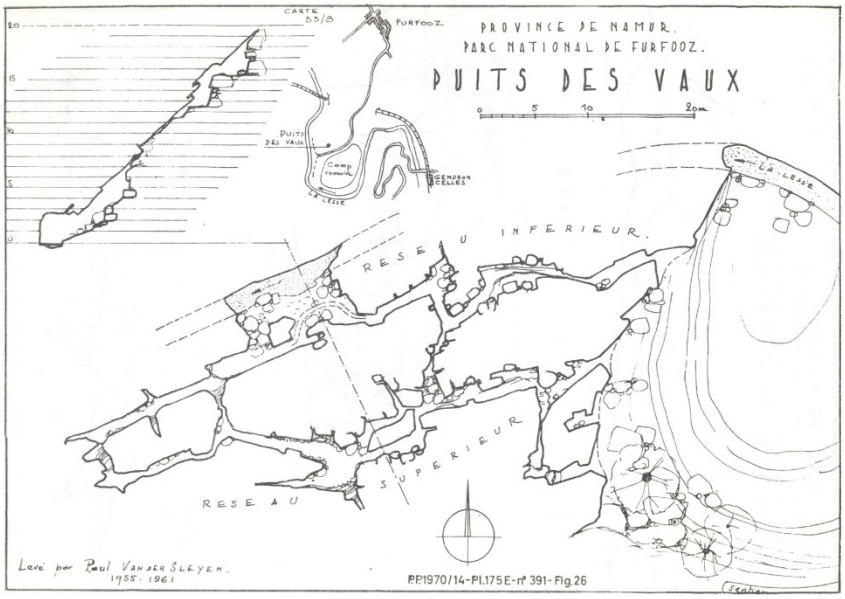

Figure 7. Topographical map of the PDV lake and inactive galleries, drawn in 1961 by Paul Van der Sleyen. The map supposes the passage of the underground Lesse in the lower gallery. However, present field observations don't validate this information.

3.2.1.3 The Sepulture cave (SEP)

This cave has been discovered only recently by local speleologists (in 2017). It is, however, a major discovery as this cave is located just upstream the crossing of the surface Lesse by the underground river. The entrance of this cave leads onto the downstream end of a gallery where flows an underground river, coming from about 20 meters upstream. The river has a rather large and deep flow section (1 to 1.5 m^2). The upstream end of this cave is a small lake explored by a diver (Michel Pauwels) who was stopped at – 5 m because of a too narrow passage filled with mud (Figure 8).

3.2.1.4 The Galerie des Sources cave (GDS)

The GDS is a large mazy network with 2300 m of galleries organized in several levels (Figure 9). The lower level is partly flooded. Several permanent and temporary "sources" appear in this gallery but the river is fed by two major resurgences that are permanently active that will be called herafter "GDSa" and "GDSb" (Figure 10). On about 70 m, the river follows a conduit that is interrupted by several small pools and disappear into a final siphon downstream.

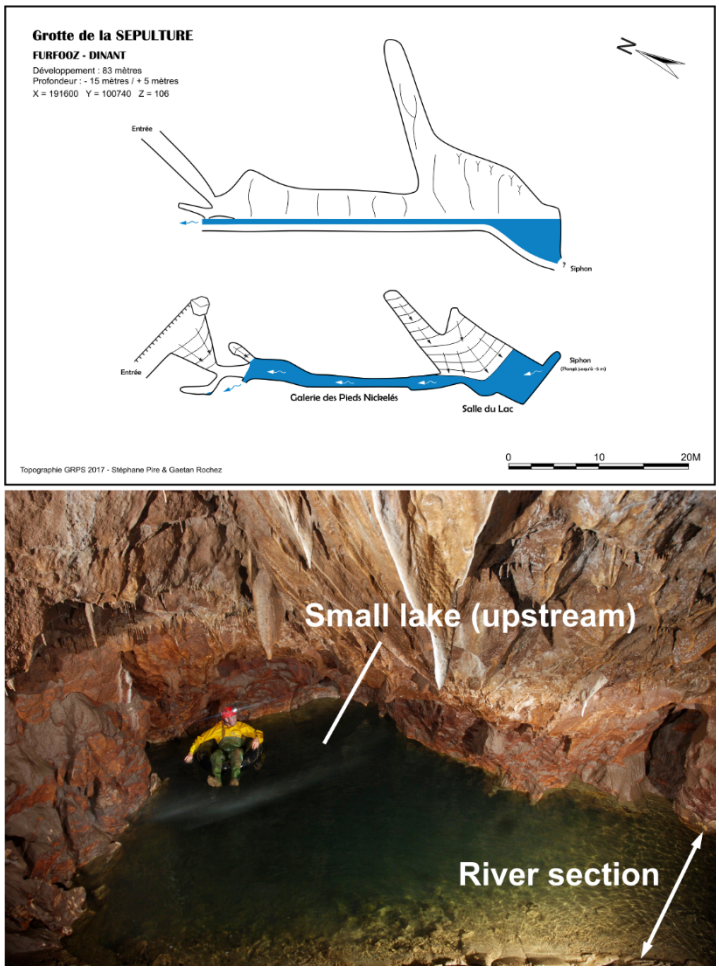

Figure 8. Above: topographical map of the Sepulture cave (by G. Rochez and S. Pire from the Speleoclub GRPS). Below: Photo of the small pool located at the upstream end of the Sepulture cave and illustration of the large river section. Photo: G. Rochez.

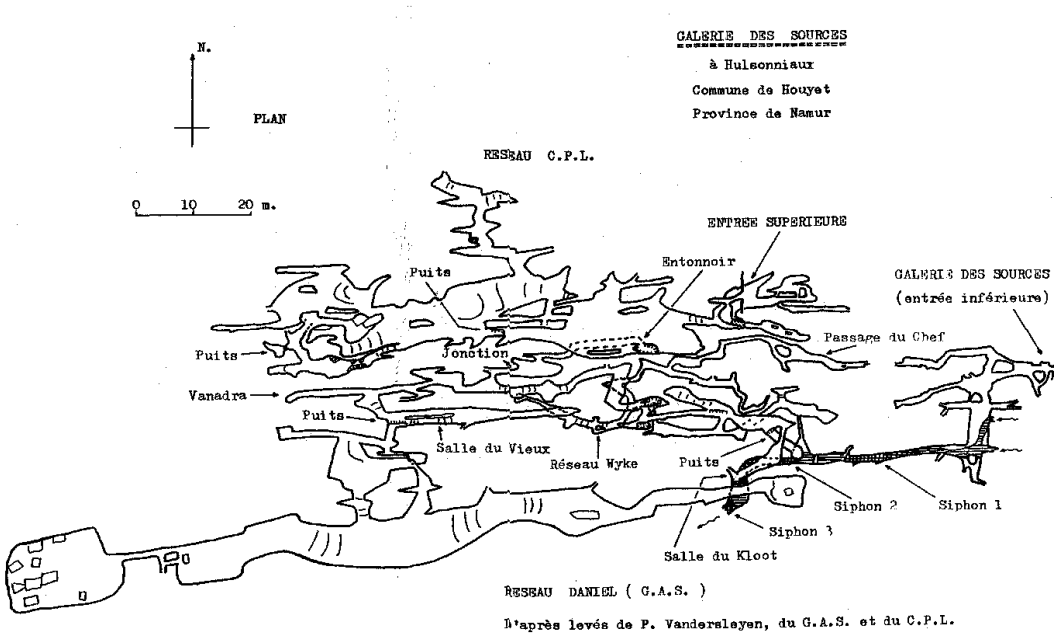

Figure 9. Partial topography of the mazy network of the GDS cave. The river, fed by two major "sources", flows into the lower gallery and disappear into a final siphon (Siphon 3 on the topography).

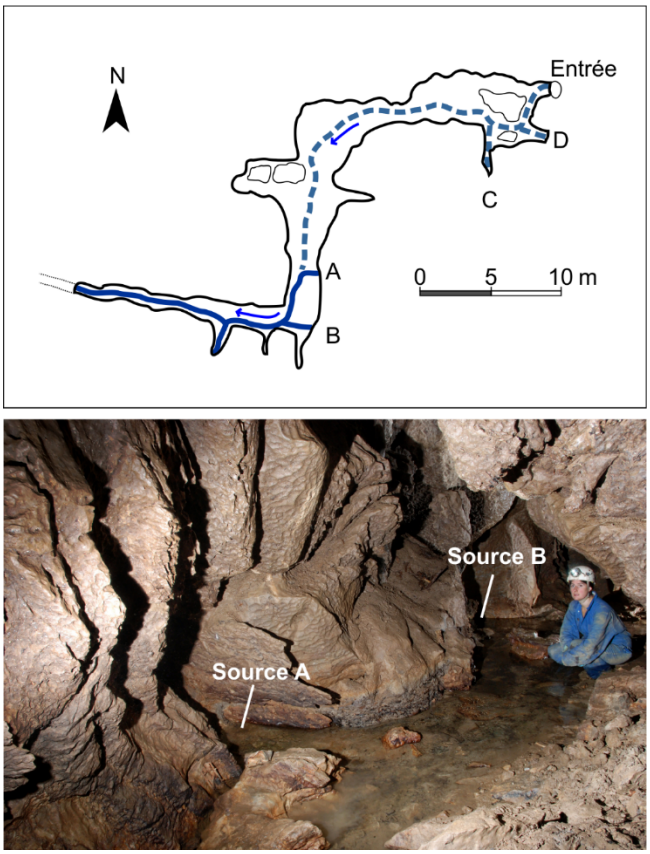

Figure 10. Above: Lower entrance of the GDS cave. The underground river comes out from two permanent sources (A and B). Three non-permanent emergences (Entrée, C and D) are active only in high flow conditions (modified from Van den Broeck and Rahir, 1903). Below, picture of the underground river at the GDS with localization of the two sources (GDSa and GDSb) separated by a few meters only. Photo: G. Rochez.

3.2.1.5 The Trou de la Loutre cave (TDL) and the Abri de la Source (ASO)

About 150 m west of the GDS final siphon, starts the TDL cave. The river crosses there a sequence of conduits obstructed by boulders and small pools before the final resurgence onto the left bank of the aerial Lesse (Figure 11). The resurgence is very diffuse and flows through ensembles of blocks, so that the discharge cannot be measured (Figure 12). The TDL cave can be accessed only by its downstream end; the progression into the cave is difficult and can be made by swimming only. The ASO is a small resurgence located 70 m upstream along the Lesse, but it is only active in high flow conditions and acts probably to evacuate the overflow of the TDL.

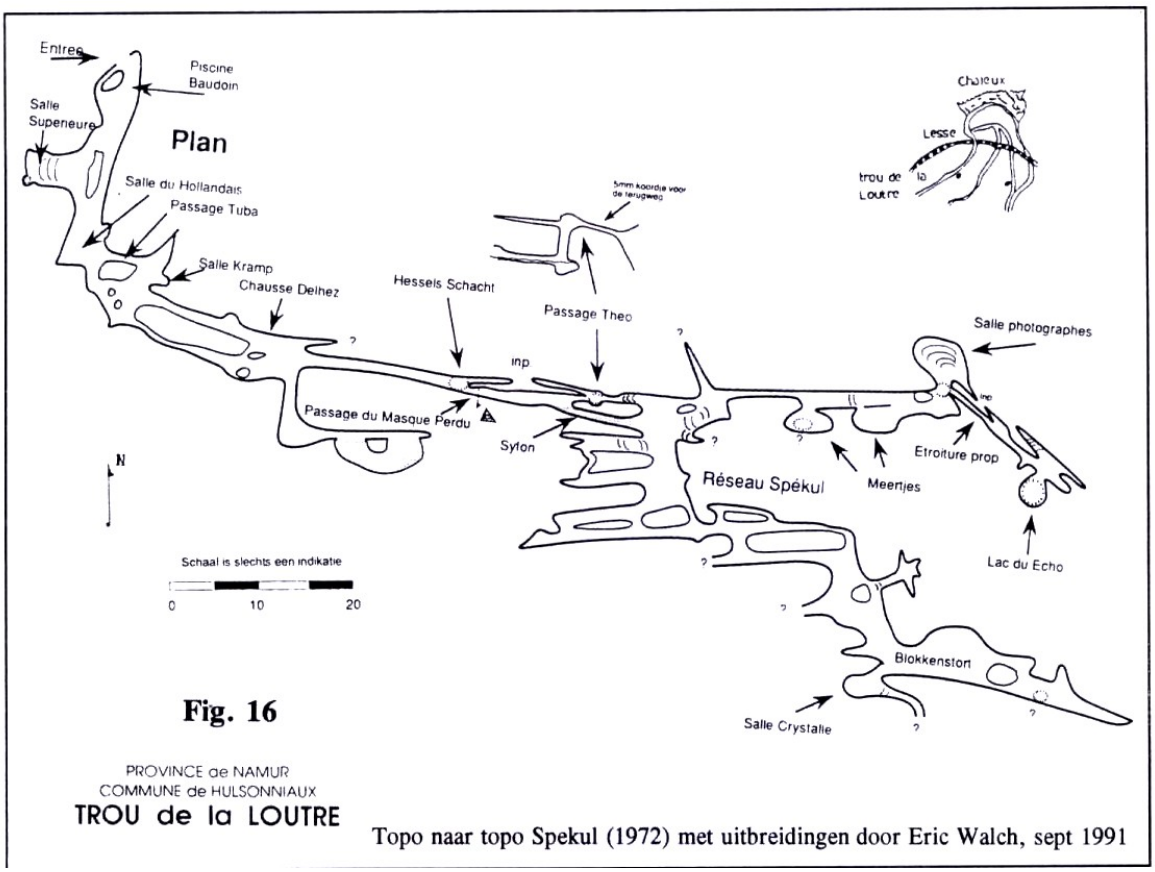

Figure 11. Topographical map of the TDV cave. The cave can be accessed from its downstream end, and on the few first meters only. To progress downstream, it is necessary to swim onto several pools and under low level passages.

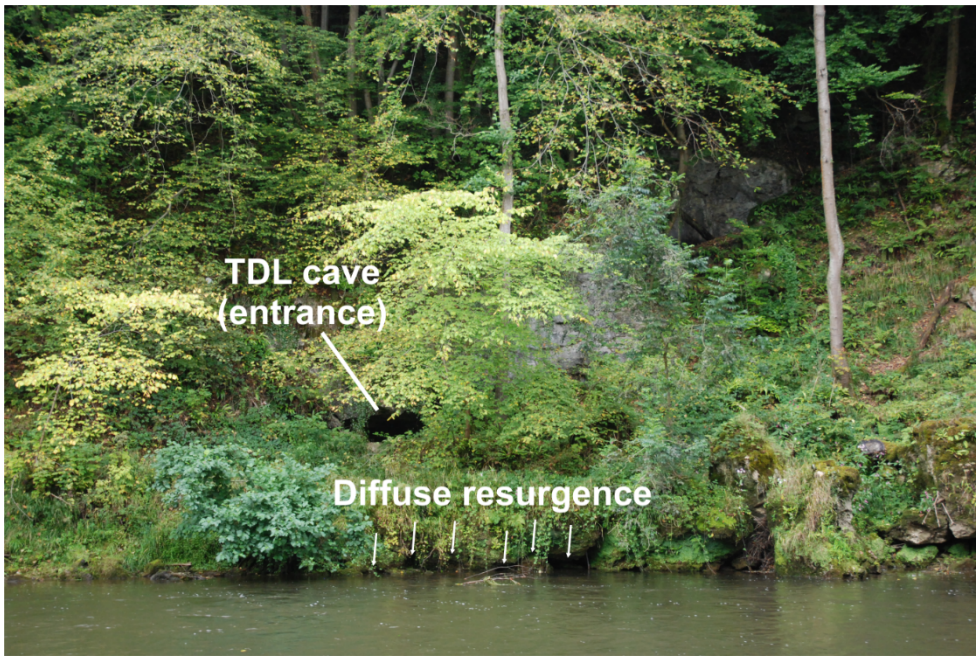

Figure 12. Resurgence of the Furfooz karst system at the TDL cave. The resurgence is scattered through blocks, so that discharges cannot be measured at this site. Photo: G. Rochez.

3.2.2 Characterization of the system hydrodynamic

Different types of measurements were performed in the various sites of the studied system. They aimed at:

- characterizing the underground Lesse;
- understanding the evolution of the river along its subterraneous path;
- evaluating how the system reacts to changes in flow conditions.

3.2.2.1 Methodology

The physico-chemical variability of the system in space and time has been monitored from 2012 to 2018, thanks to continuous measures of water temperature and electrical conductivity in several locations. The water pressure has also been registered during the same period. Once compensated with the atmospheric pressure, it provides a continuous record of the water level. Differential GPS was used to determine the exact altitude of the measurement stations, allowing us to transform the water level data into water level altitudes. Two kinds of probes were used for the data record: the CTD – divers (Eijkelkamp) for temperature, water pressure and electric conductivity, and the mini-divers (Eijkelkamp) for temperature and water pressure. A baro-diver (Eijkelkamp) was also placed in the Furfooz site for the atmospheric pressure monitoring. All the probes recorded data with a 15 minutes time-step.

Regular measures of the discharge (flow-rate gauging) were also performed in the site to build a rating curve relating the water level data to discharge data. Thanks to this rating curve, a hydrograph of the underground river could be constructed. However, this hydrograph could not be built at the CN location because the discharge can only be measured there in low flow conditions; nor at the final resurgence (TDL) because the flow out there is too diffuse to measure a correct discharge. The GDS is the only location of the system where the discharge can be measured easily and in a large range of flow conditions. The rating curve and hydrograph were then built for this site only. Occasional discharge measurements were made in the CN sinkhole and in the TQF river when the flow conditions were low.

Continuous discharge data are also available for the surface Lesse River. These data were recorded by a governmental gauging station located in Gendron (Figure 1), about 600 m upstream the CN swallow hole.

Finally, water chemical analyses were also performed to characterize the hydrochemistry of each measurement site of the system. One sampling survey was conducted in summer time (September 2013). Water samples were taken at different locations of the main system and also on the Sebia and the Ri des Vesses rivers.

Figure 13 summarizes the different kind of measurements made on each site.

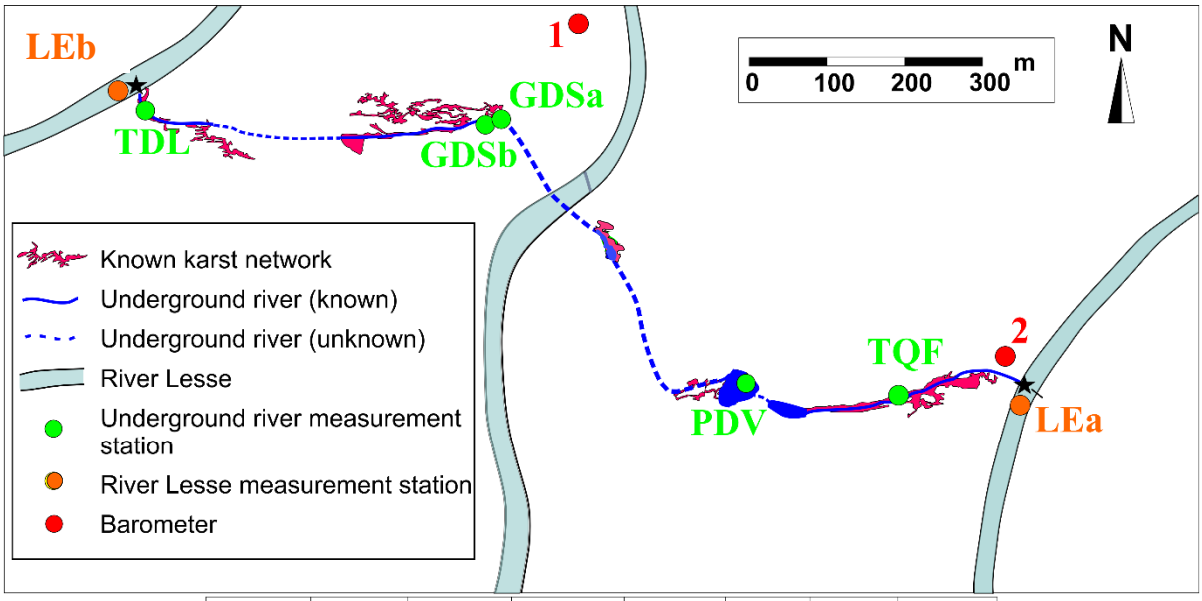

	TQF	PDV	GDSa*	GDSb*	TDL	LEa	LEb
CTD/Mini-Diver	CTD Avr-12	CTD Avr-12	CTD Avr-12	CTD Avr-14	CTD Avr-12	CTD Avr-12	Mini Avr-12
Discharge	OCC		REG	OCC		OCC	
Chemical analysis	sept-13	sept-13	sept-13	sept-13	sept-13	sept-13	

GDSa corresponds to the upstream permanent source of the GDS, while GDSb is the downstream permanent source of the GDS

Figure 13. Monitoring strategy of the Furfooz karst system. The dates mentioned in the first line corresponds to the date of the first placement of the corresponding probe on the site. [OCC]: occasional measures, [REG]: regular measures.

3.2.2.2 Monitoring results

The following chapter presents and analyses the combined information given by the probes recording, the discharge measurements and the chemical analysis. The probes data are provided in various graphics. Some gaps appear in the data monitoring: they are due to various technical problems encountered when performing the measures (probe dysfunction, loss of the probe,…).

3.2.2.2.a Hydrometry

3.2.2.2.a.1 Hydrological context

To understand the behavior of the underground river, it should first be mentioned what are the general hydrological conditions that prevail in the study area. The closest weather station (PAMESEB asbl station) from where data could be gathered is located near Rochefort, located about 20 km south-east of Furfooz in the River Lhomme Basin, a major tributary of the River

Lesse. Therefore, these data cannot be used to be directly compared to the hydrometric data recorded in Furfooz but they are used to define a general context of the aquifer recharge.

Daily rainfall (R) and potential evapotranspiration (ETP) data from 2011 to 2018 were considered. The ETP is calculated via the Penman – Monteith equation (Allen et al., 1998). R and ETP mean values were extracted for each month over these 7 years. From these mean values, monthly available water (AW) was calculated via the Thornthwaite method (Thornthwaite & Mather, 1955), along with effective rainfall (ER), real evapotranspiration (ETR) and soil water reserve (SWR). The results are presented in Figure 14. The graph shows that the recharge of the aquifer must be considered from November to March. From April to August, the evapotranspiration is higher than the rainfall, and so there is almost no water available for run-off or infiltration (on a monthly basis). The soil water reserve decreases over these months. In September and October, effective rainfall is available but it is used in priority to recharge the soil water reserve.

At a local scale, the hydrological conditions can be partly assessed from the discharge data available for the Gendron gauging station (Figure 15). On this hydrograph, higher discharge conditions are observed each year in winter time, during a period that would correspond to the recharge period for the aquifer. The lowest discharges (1.5 m^3/s) are observed in summer time during low flow period when there is no useful water to sustain the river discharge.

3.2.2.2.a.2 Water- level data

The water level data that are presented here in altitude thanks to the Z topography made by a DGPS. Figure 16 A presents the data recorded during about 6 years. A comparison is made here between the river Lesse that represent the surface runoff (LEa upstream and LEb downstream) and the underground sites that are probably in equilibrium with the water-table piezometry (PDV, GDS and TDL). The surface Lesse shows water-level variations. As said before, no precipitation data are available for this specific basin, though, it can be guessed that these water-level sudden changes are linked to precipitation events. The underground system reacts accordingly to the observed water-level changes of the surface Lesse River. It should be noted that the probe at the PDV has encountered technical problem during the last year of recording and displays abnormally high levels.

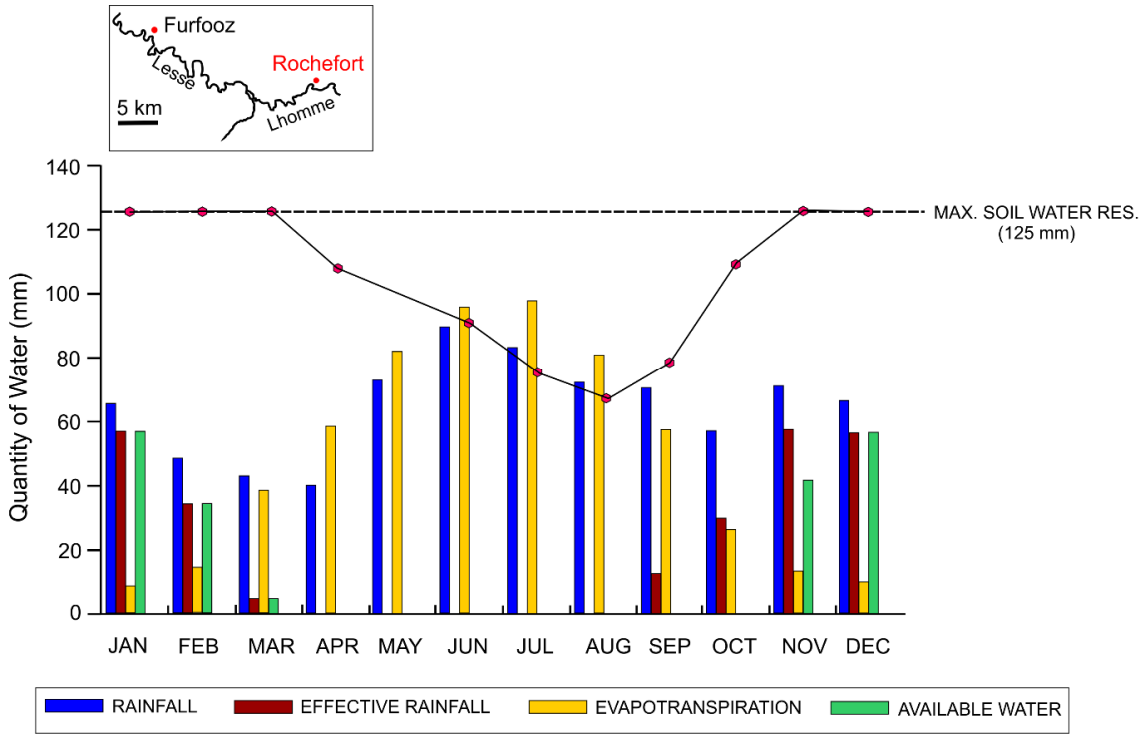

Figure 14. Calculation of the monthly useful water over a year, using mean values from seven years of data (2011-2018). The aquifer recharge is effective from November to March.

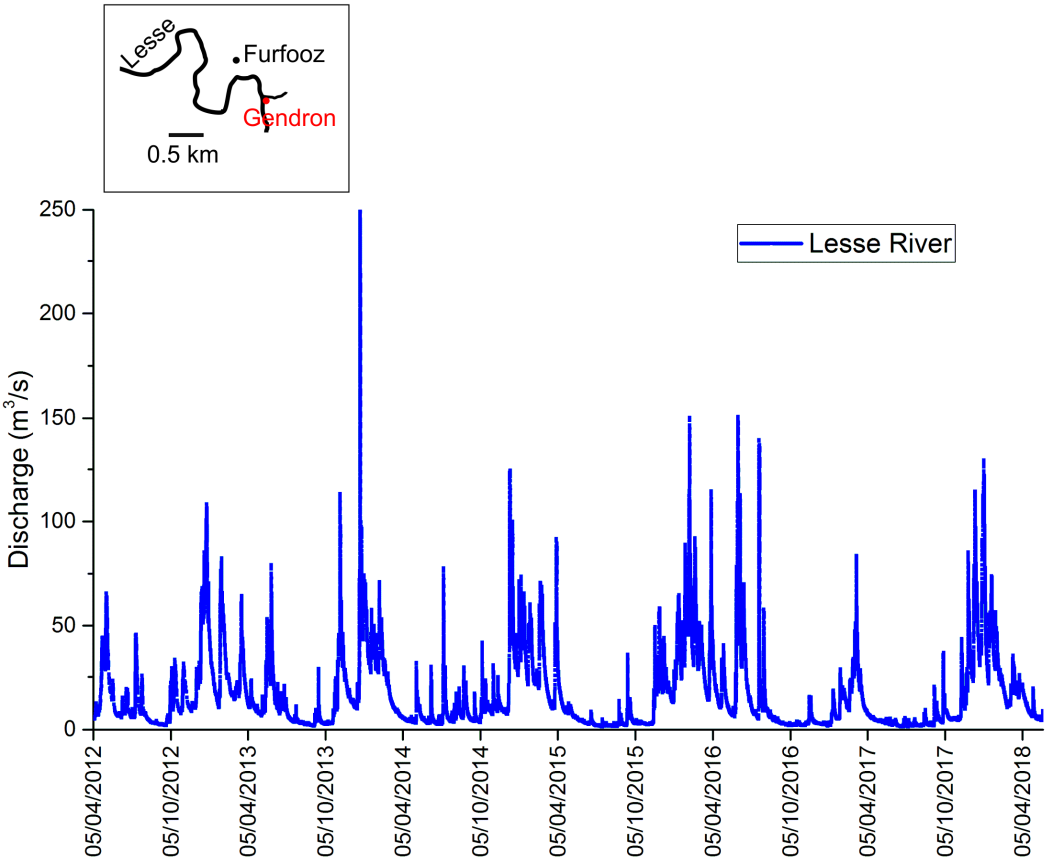

Figure 15. Discharge variations in the surface Lesse River, recorded at the Gendron governmental gauging station.

The maximum altitude recorded in the surface river is 105 m and the minimum 101.55 m. The CN swallow hole is clearly perched above the underground system. Indeed, the altitude difference between the CN swallow hole and the PDV station is about 3 m. When the water-level is low, the PDV stands about 0.3 m above the GDS low-water level, and the latter stands about 0.2 m above the TDL . Considering 410 m between the PDV station and the GDS station, and 400 m between the GDS and the TDL, the piezometric gradient would be of 0.073 % between the PDV and the GDS, 0.062 % between the GDS and the TDL. During floods, the water-level difference between the stations tends to decrease, and so does the gradient. The water-level at the GDS and the TDL tends even to be higher that the level recorded at the PDV, during a short moment at the peak of the flood (Figure 16 B and C). It is also interesting to see, from the zoomed figures (Figure 16 B, C, D), that the floods reach the PDV with some delay (5 to 7 h later). The water-level decrease, after the peak of the flood, is also more buffered at the PDV. These observations are probably due to the fact that the GDS (and the TDL) are in direct equilibrium with the water-table, as they are very close – in distance - to the surface river bed; while the PDV is a bit higher than the water-table and reacts, therefore, a bit later to the water-table rise. It should also be said that the TDL, that is separated from only a few meters of the surface Lesse River (LEb) is very much influenced by any slight increase of the water-level of the surface river that infiltrates directly the TDL. This would explain why the TDL water-level is sometimes higher than the one recorded at the GDS. The GDS site can also be infiltrated directly by the surface Lesse River that overflows its banks, but only in the case of very big flood events.

Finally, an important comment to be considered regards the extent of the knowledge of the system. Indeed, our data interpretation is limited to what we know of the underground river. The functioning of this river is probably more complex than what has been underlined, due to its interaction with the aquifer in its whole. The possibility of inflows or outflows cannot be excluded, nor are the potential geometrical changes that affect the system through time and space.

Box charts presented in Figure 17 were calculated for these most representative sites, on the periods where data loss is not too important. This graph presents the mean water-level value for each site, with no distinction of the hydrological conditions. Different percentiles, and minimum and maximum values are also considered. The range of values (between percentile 25 and percentile 75) is higher for the surface river than what is recorded in the underground system. The mean elevation of the surface river is about 3 m higher than the mean water-level at the PDV. The water-level mean value decreases slightly from the PDV to the TDL. The GDSa and the TDL mean water-level are nearly in equilibrium. However, the range of value for the TDL is higher probably due to the infiltration of the surface river directly into the TDL during floods.

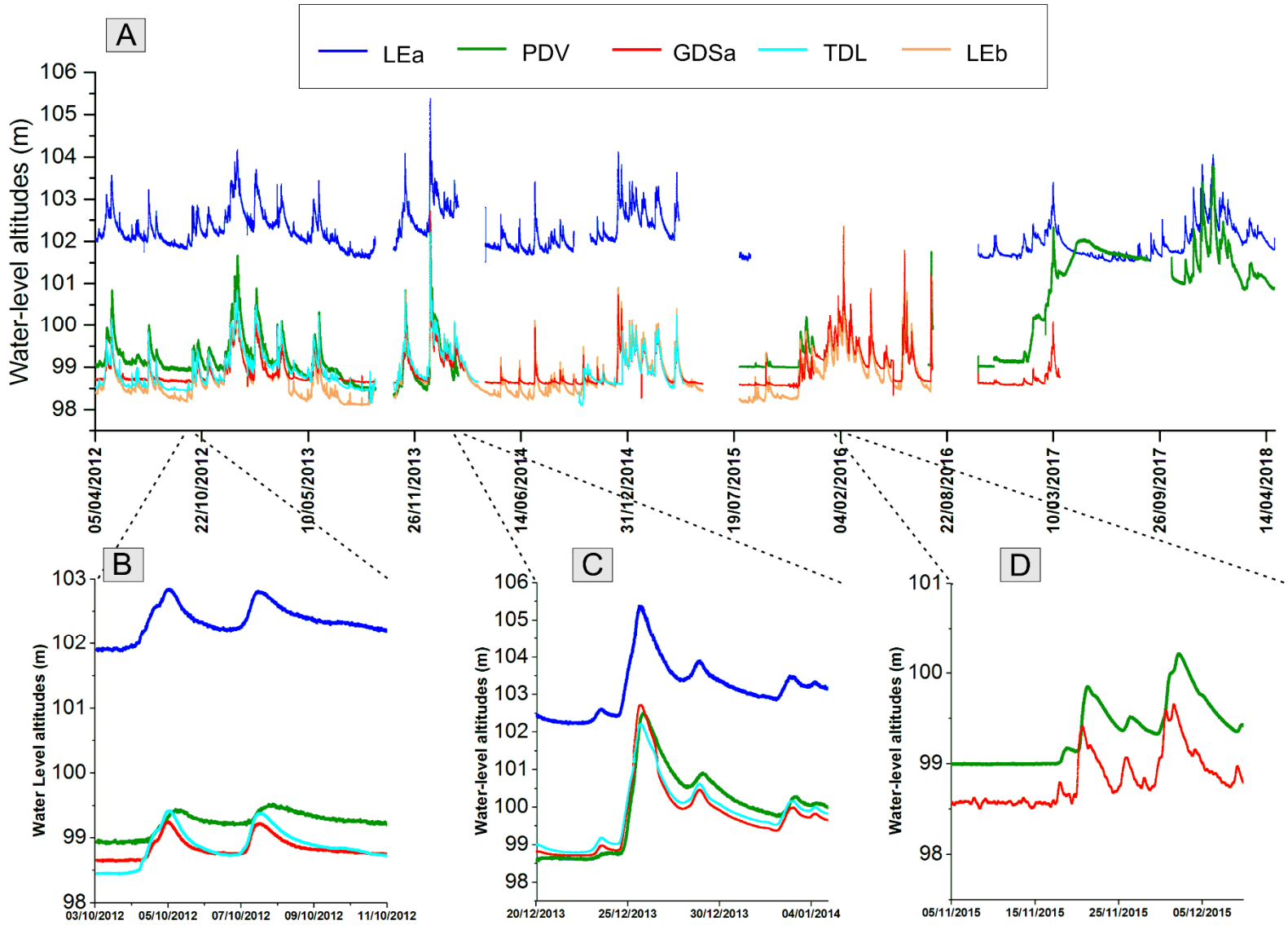

Figure 16. Water-level altitudes monitoring. Graph A exposes the data recorded from April 2012 to April 2018. The inset graphs B, C, D detail some short periods where more precise observations can be made.

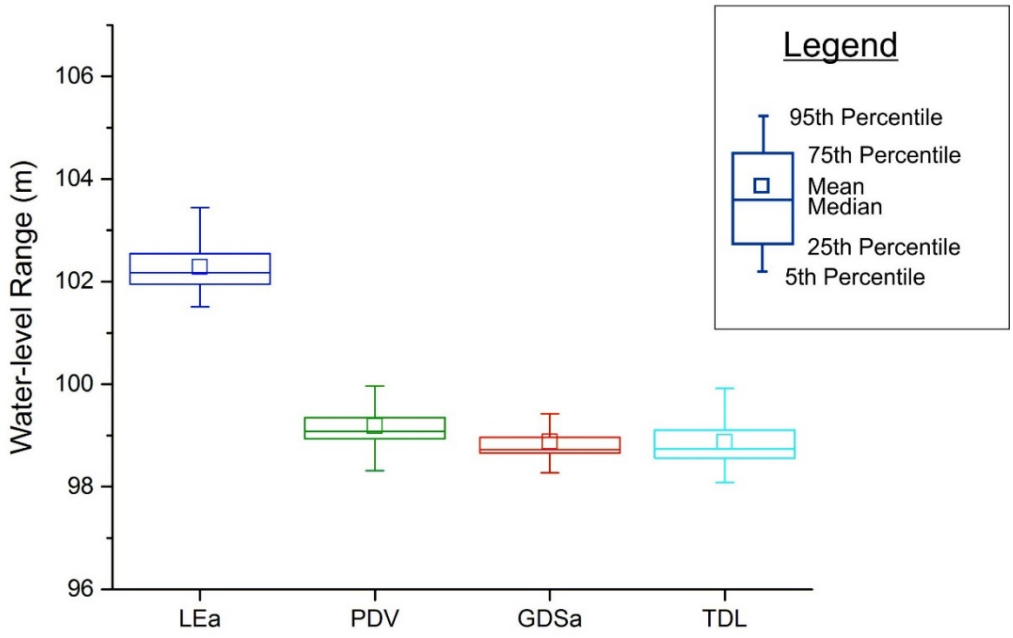

Figure 17. Box charts calculated in two different flow regime. Only the measurements sites that are the most representative for the system dynamic were selected.

3.2.2.2.a.3 Flow-rate data

Flow-rate measurements have been made at different sites of the system, in various flow conditions. The sites where accurate discharge measurements can be done are:

- The CN swallow hole: due to its accessibility, gauging of the flow entering the CN swallow hole is possible in low flow conditions only;
- The TQF river: gauging is possible in low to moderate flow conditions. However, due to te long speleological progression that is needed to reach out this part of the underground river, regular measurement were not done at this site;
- The GDS cave: gauging of the underground river is easily done at this site in a large range of flow conditions (from very low flow to a maximum of about 35 l/s because the cave cannot be accessed over these flow-rates). The measurements can be done at two places of the cave; i.e. upstream and downstream the GDSb source. Most of the gauging where made upstream GDSb in order to construct a rating curve.

Table 2 exposes the measurements made at the different sites. From these data, several observations should be mentioned. First, there is more water flowing through the TQF river than entering the CN swallow hole. An addition of 2l/s (in low flow conditions at least) is to be considered between those two gauging points. As there is an estimated unknown zone of 70 m between these two points, it is impossible to say if the supplement of water is added at once by a complementary sinkhole or if it is added in a diffuse way. In September 2016 a little net was settled around the swallow hole. Indeed, mud and trees were often obstructing the

CN influencing the flow entering the underground system (Figure 18). A second important finding is the similarity of the measures at the TQF river and at the GDS (upstream GDSb). The gauging measurements made within the same day at the TQF and the GDS show nearly identical discharges in both sites. This shows that the discharge is in equilibrium in the two sites, in the range of the performed measures at least. Finally, a last observation concerns the measures made downstream GDSb. They show that the GDSb source brings an additional but limited amount of water to the system (0.6 to 1 l/s in the tested flow conditions).

These findings are important because they define the flow evolution in the system. It appears that, despite the lakes presence and the crossing of the surface river meanders, the underground river flows with a rather steady discharge along the system.

	CN swallow hole (l/s)	TQF (l/s)	GDS (upstream GDSb) (l/s)	GDS (downstream GDSb) (l/s)
23/08/12			4.7	
26/03/13			24.1	
29/03/13			21.0	
04/04/13			15.8	
25/04/13			8.1	8.7
02/09/13	3.5	5.5	6.0	
08/04/14			6.2	7.1
07/07/15			2.9	3.9
18/05/16			8.8	
05/09/16	/ 2.9	*1: 3.0 *2: 5.6	/ 5.9	
02/11/16	2			
23/02/17			10	
16/11/17			13	
29/03/18		9.3	8.7	
30/05/18			10.3	

Table 2. Comparison of discharge data measured at the CN, the TQF and the GDS. *1: measure before the CN disobliteration; *2: measure after the CN disobliteration.

Figure 18. Photos of the obstructed swallow hole (on the left) and after disobliteration and installation of the net (on the right). Photos: G. Rochez.

Thanks to the regular gauging performed at the GDS, upstream GDSb, a rating curve could be built. This curve expresses a mathematical relationship between the measured discharge and water-level (Figure 19). It was chosen to establish the rating curve upstream GDSb because, as it will be demonstrated later, this downstream source is not related to the underground Lesse upstream. Fourteen gauging points were used. Two relationships are proposed depending of the discharge conditions, the rising of the water-level being steeper for the low discharges (under 15 l/s).

The rating curve should however be taken with caution, at least for the higher discharge part. Indeed, three points don't fit the built rating curve. The discharge value measured for these three points have lower value than what is expected by the rating curve. That significates that, considering a constant section, the velocities implied in the flow are slower for these three points. It appears, furthermore, that these three gaugings were made in high water-level periods (in February 2017, November 2017 and March 2018). It could therefore be proposed that, in high flow conditions, the water-table would rise and increase the general water level with a limited impact on the velocities. As for the three points (in orange) on the rating curve, they would correspond to a rise of water-level that is rather linked to flood run-offs in lower flow conditions, implying higher velocities.

The equations of the rating curve were transposed to the probe data. An hydrograph could then be constructed for the GDS and compared to the surface river Lesse hydrograph (Figure 20). Given what has just been said, this hydrograph is probably rather accurate for low to moderate discharge conditions, but must be taken with caution regarding the high flow water periods. Therefore, the interpretation that can be made of this hydrograph is kept limited. The general behavior of the GDS hydrograph can be compared with the discharge data recorded for the surface River Lesse. The comparison of the discharge evolution between the underground and the surface rivers shows a tight link.

3.2.2.2.b Physico-chemical variability

3.2.2.2.b.1 Probes data

Temperature and electrical conductivity were also recorded, as presented in Figure 21. The water-level altitudes are also indicated on this figure to show the influence of the flow on the physico-chemical parameters. Along with these graphics, box charts graphs have been constructed for the relevant sites (Figure 22).

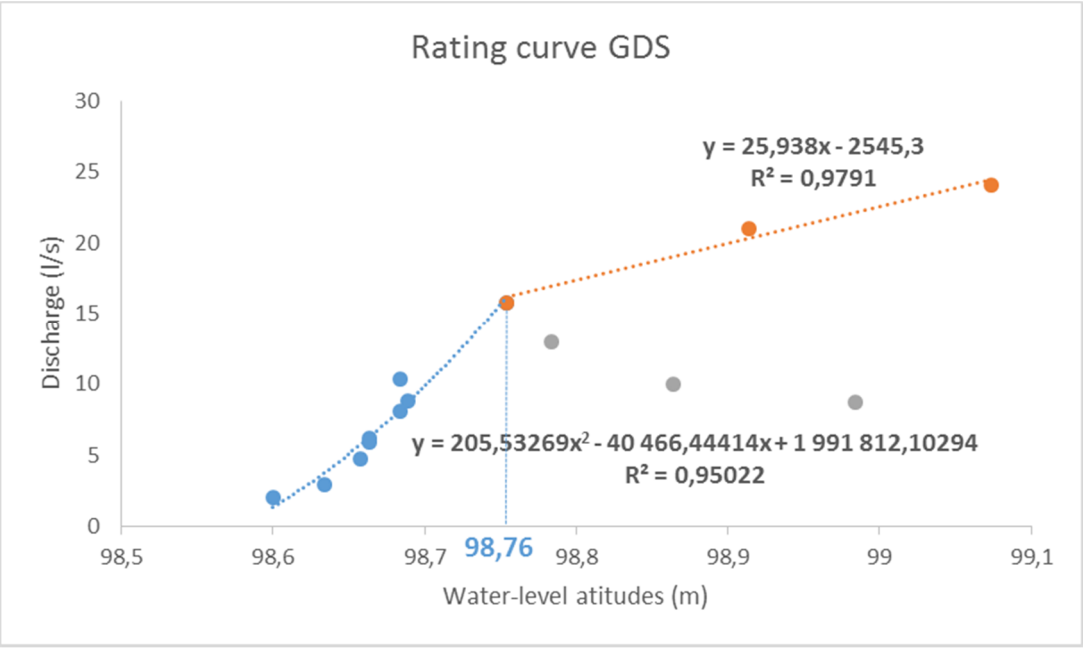

Figure 19. Rating curve built at the GDS (upstream GDSb). The evolution of the discharge related to the water-level is different in low and high flow conditions.

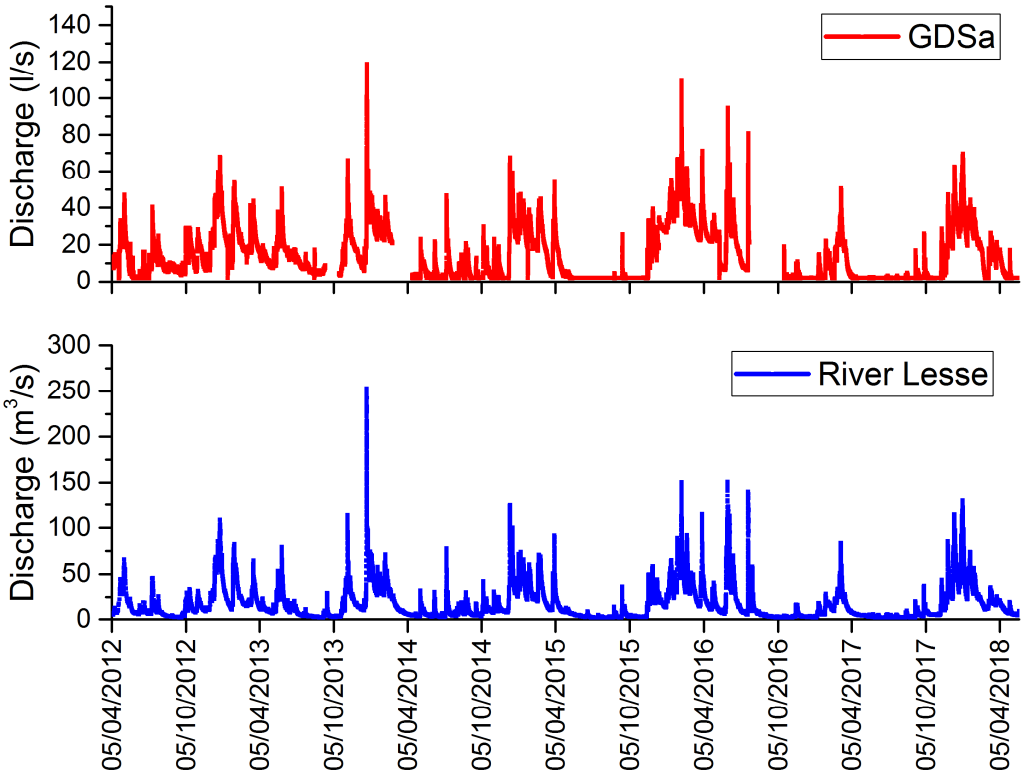

Figure 20. Discharge data at the GDSa station (l/s) and at the Gendron station (m^3/s) along the surface River Lesse. The surface river data were recorded by a permanent limnimetric station of the Wallonia Public Service (SPW – Direction Générale des Voies Hydrauliques) located in Gendron, just downstream the confluence with the River Saint-Hadelin.

The conductivity values of the TQF station were deliberately put aside. Indeed, they show very high values (Figure 21) but this is clearly due to mud accumulation in the probe vicinity. The electrical conductivity of the surface river has a mean value of 0.130 mS/cm. The range of values of the surface water is wide as it shows minimum values around 0.030 mS/cm and maximum of 0.350 mS/cm. Those changes are linked to external events in surface waters upstream the studied system, and are not necessarily linked to runoff, i.e. there is no clear link with the water level changes. The low conductivity tendency of the surface river is to oppose to the conductivity signal of the underground system where the values are more stable and fluctuate around 0.400 mS/cm. Given this difference, the wide variations observed in surface waters have a small impact on the underground system. This is probably because the groundwater of the karstic system is in equilibrium with the aquifer groundwater. Minor fluctuations in those curves are to be attributed to flood events where massive importation of low conductivity waters from the surface leads to sudden drop of the underground water conductivity as shown on Figure 21. The TDL site records conductivity drops of variable importance during most of the floods. Indeed, the level of the water at the TDL is very close to the one recorded in the Lesse (LEb). A small rise of the surface water-level has for consequence a direct infiltration of the surface water into the underground system of the TDL cave. The river at the GDS system is also impacted by surface water infiltration, in case of major floods only. Now, if one compares the data between the underground sites (Figure 22), it appears that the PDV lake as a higher conductivity (mean value of 0.422 mS/cm) than the more downstream sites GDSa (mean value of 0.407 mS/cm) and TDL (mean value of 0.389 mS/cm). This fact would show that waters have a longer transit time into the lake and are less renewed than in the other sites. Regarding the weaker mean value of the TDL that is the most downstream point on the underground path of the river, this has to be explained by frequent infiltration of the surface Lesse into the TDL, the probe being located very close to the level of the surface river. Finally, it should be noticed that the conductivity of the GDS b is much lower than in the other site. This is the sign that this source could be unrelated with the actual underground Lesse system upstream the GDS.

The water temperature evolution follows a classical scheme. A clear cyclic summer-winter behavior is observed in both the surface river and the karst system. The mean temperature and the median are very close for each site (about 10 °C). The values range however is much wider in the surface river than underground. Temperatures are more and more buffered downstream-ward. It is interesting to notice that the temperatures recorded at the TQF monitoring point (located only 120 m downstream the swallow hole) are already nearly in equilibrium with the temperature of the underground river observed more downstream. It must be mentioned furthermore that the PDV probe is only 1 m deep into the lake which is in direct contact with the outside atmosphere. Therefore, the water temperature there is obviously influenced by the outside air temperature fluctuations.

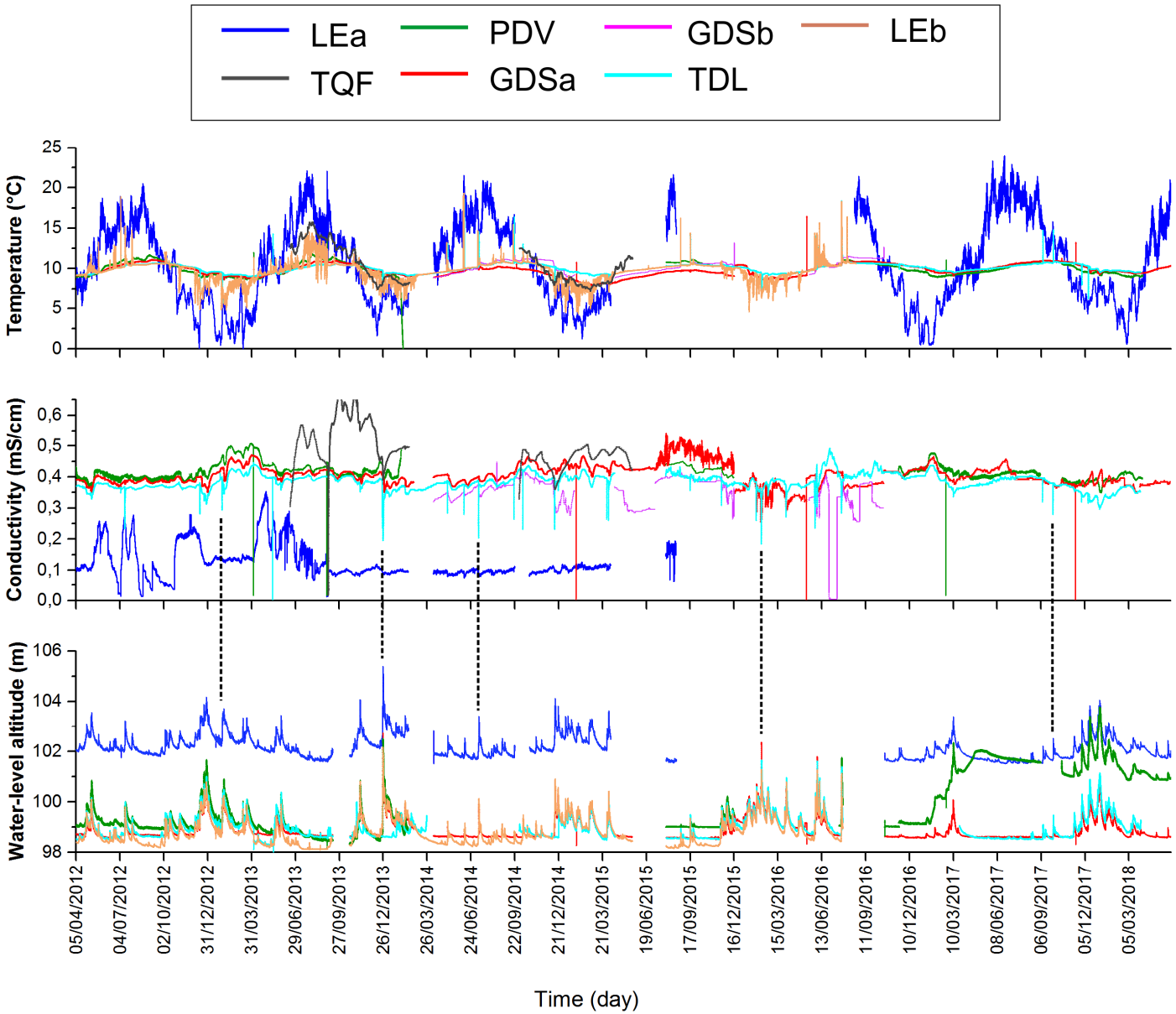

Figure 21. Comparison of the electrical conductivity and the temperature evolution in each site, in regard with the water-level changes. The vertical dashed lines indicates some examples of coincidence between conductivity drops in the underground system and flood events.

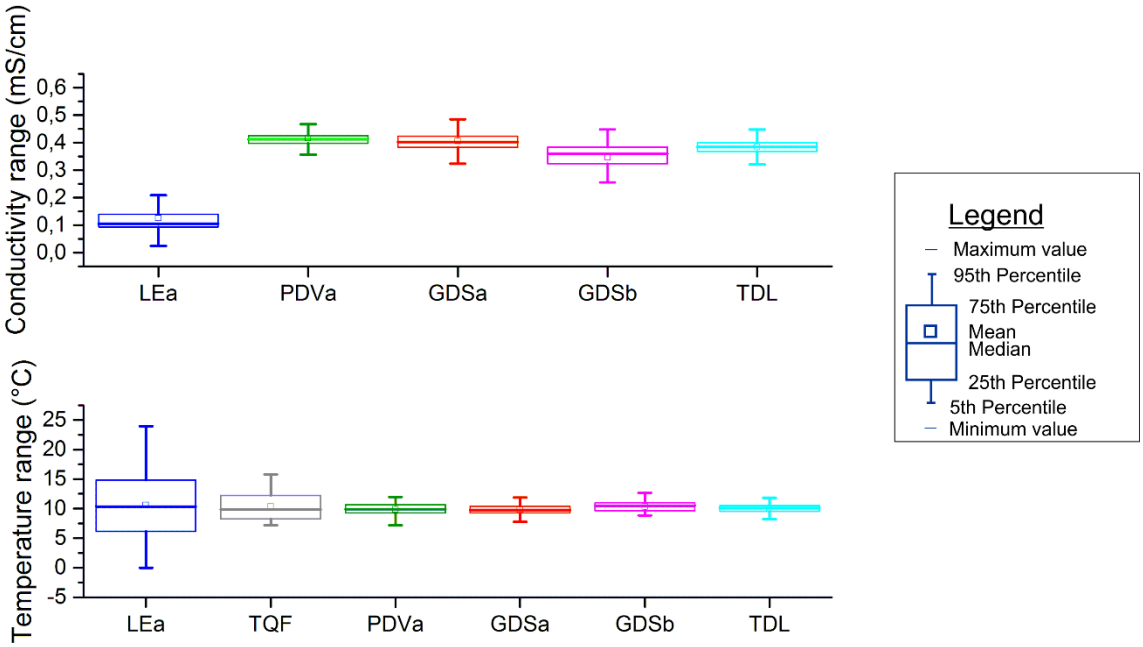

Figure 22. Box charts for temperature and electrical conductivity data.

3.2.2.2.b.2 Chemical analyses

One sampling survey was conducted in 2013 on different sites of the study area. This sampling was done to have a general idea of the study site hydrochemistry and provide information for a general data bank of the belgian aquifers hydrochemistry. No systematic samplings were done, and so the conclusions that can be brought to light from this first set of analyses a rather limited. The complete analysis results are presented in Appendix 1. The analyses were performed by the laboratory of the "Hydrogéologie et Géologie de l'Environnement" Unit of the University of Liège (Ulg). In this appendix, the results are exposed in the form of two different graphics: the Piper and the Schoeller diagrams.

The data reveals differences in the chemical signatures of the Ri des Vesses and Sebia waters compared to the waters of the Furfooz underground river. The samples from the Furfooz system show a very similar anions and cations content, although a slight enrichment in Ca^{2+} downward the system (from the CN to the TDL) can be highlighted. GDSa and GDSb show some differences in their content despite their very close location indicating some possible difference in their origin or path upstream their sampling point.

Key points of this chapter:

- The Furfooz karst system is established on the south edge of a regional carbonate aquifer that is a major source of groundwater in Belgium;
- It consists in a swallow hole – resurgence system developed in conduits. It presents the particularity of crossing two meanders of the surface river. On its path, the underground river flows into two successive underground voluminous lakes (of several thousands of cubic meters) ;
- Several cave networks give the opportunity to follow and monitor the underground river;
- Discharge cannot be measured at the resurgence of the system but gauging of flow-rates at other points of the system show that the discharge seems to stay steady along the system;
- Water-level data of the underground system react accordingly to the changes observed in the surface river. The PDV lake reacts with delay to the floods compared to the GDS;
- Physico-chemical monitoring illustrates a classical behavior of the river and indicates infiltration of the surface river during flood events at the GDS and the TDL. The PDV lake has a slightly higher electrical conductivity than all the other sites.

3.3 References

Allen, R.G., Pereira, L.S., Reas, D., & Smith, M. (1998). Crop Evapotranspiration – Guidelines for computing crop water requirements. FAO, Rome, Italy, FAO Irrigation and Drainage paper, 56.

Dörfliger, N. (2010). *Guide méthodologique : Les outils de l'hydrogéologie karstique pour la caractérisation de la structure et du fonctionnement des systèmes karstiques et l'évaluation de leur ressource*. Avec la collaboration de Ph. Crochet, R. Guerin, N. Jozja, B. Marsaud, P-H. Mondain, Ph. Muet, V. Plagnes ; BRGM RP- 58237-FR, 246 pp., 82 ill., 5 ann.

Mangin A. (1974). *Contribution a l'etude hydrodynamique des aquiferes karstiques. Lere partie. Generalites sur le karst et les lois d'ecoulement utilisees*. Annales de Speleologie, v. 29, n. 3, p. 283-332 ; v. 29, n. 4, 495-601.

Mangin, A. (1975) *Contribution à l'étude hydrodynamique des aquifères karstiques.* Doctorat ès Sciences naturelles, Université de Dijon. In : Ann. Spéléol 29 (3):283-332; (4):795-601; 30 (1):21-124.

Nogarède, P., Vanbrabant, Y., Rekk, S., & Hallet, V. (2003). *Notice explicative de la carte hydrogéologique Hastière-Dinant (53/7-8)*.Service Publique de Wallonnie, DGO 3.

Piper, A. M. (1944). *A graphic procedure in the geochemical interpretation of water analyses*. American Geophysical Union Transactions, *25*, 914–923.

Poulain, A. (2013). Etude hydrogéologique et dimensionnement par modélisation des essais de traçage de La Lesse souterraine de Furfooz (Dinant, Belgique). Master thesis, ULB, 106 p.

Service Public de Wallonie. (2010). *Etat des lieux de la masse d'eau souterraine RWM021 "Calcaires et Grès du Condroz."*

Stevanovic, Z. (2015). Karst aquifers – Characterization and Engineering. Professional Practices in Earth Sciences. doi : 10.1007/978-3-319-12850-4_3

Thornthwaite, C.W., & Mather, J.R. (1955). *The Water Balance*. Publication 8, 1- 86, Centeron N.J., Laboratory of Climatology.

Van den Broeck, E., & Rahir, E. (1903). *La Lesse souterraine et la traversée des deux boucles de la rivière à Furfooz démontrée au moyen de la fluorescéine* (Hayez-im). Bruxelles.

Chapter 4

The dye-tracing system of Furfooz

Chapitre 4 The dye-tracing system of Furfooz

In brief, in this chapter:

- The methodology and strategy of tracer testing in the Furfooz system are defined;
- Fifteen tracer tests are individually described and analyzed in details;
- A synthesis of the different behavior highlighted by the tracer-tests is proposed;
- The chapter ends with a discussion and the elaboration of a conceptual model.

The following chapter focuses on the study of the hydrodynamic prevailing in the Furfooz underground river system, which was deduced from many dye-tracer tests.

4.1 Introduction

The underground river of Furfooz is characterized by a heterogeneous development. The TQF and the PDV lakes are big volumes of water (estimated volume of 7000 m^3 for the TQF lake and 16000 m^3 for the PDV lake) that contrast with the secluded underground river upstream (flow section of about 0.05 m^2) and downstream (flow section of about 0.5 m^2 to 1 m^2). On the solute transport point of view, it has been shown by several studies (Hauns, Jeannin, & Hermann, 1998; Massei et al., 2006; Morales, Uriarte, Olazar, Antigüedad, & Angulo, 2010) that the geometry of a karst system has a major influence on the parameters that control the transport of a solute. In order to characterize this influence, hydrogeologists resort usually to dye tracing. A tracer test consists in the injection of an artificial tracer in a system at a defined spot and time. Other places of the system are monitored to detect the tracer. This detection can be qualitative (presence or not) or quantitative if a breakthrough curve (BTC) can be constructed. A BTC is a graphical representation of the tracer concentrations plotted versus time. It can be obtained by two methods: a discrete sampling with an automatic sampler or a continuous monitoring thanks to fluorimeters (Goldscheider, 2015).

In karst conduits, a solute is transported by advection and dispersion that are dominant in the longitudinal direction. Solute transport can be mathematically defined by the one-dimensional advection-dispersion equation (Bear, 1979; Kreft & Zuber, 1978):

$$R_f \frac{\partial C}{\partial t} = D_L \frac{\partial^2 C}{\partial x^2} - v_L \frac{\partial C}{\partial x} - \mu C \quad (1)$$

Where C is the solute concentration [L^3/T], t is the time [T], x the distance [L], D_L the longitudinal dispersion [L^2/T], v_L the longitudinal (effective) velocity [L/T], R_f a retardation factor linked to sorption on particles, and μ a decay coefficient [T^{-1}]. The advection represents the actual transport of the tracer due to the movement or velocity of water. The dispersion

(i.e. the hydrodynamic dispersion) is the combined effect of the mechanical dispersion and the molecular diffusion (Schudel et al., 2003). Mechanical dispersion results from particle velocity variations and is a much more dominant process than the diffusion (Zheng & Wang, 1999). The hydrodynamic dispersion is responsible for the widening of the BTC due to dilution and the spreading out of the tracer cloud. The effect of longitudinal (and transverse) dispersion is shown by Figure 1.

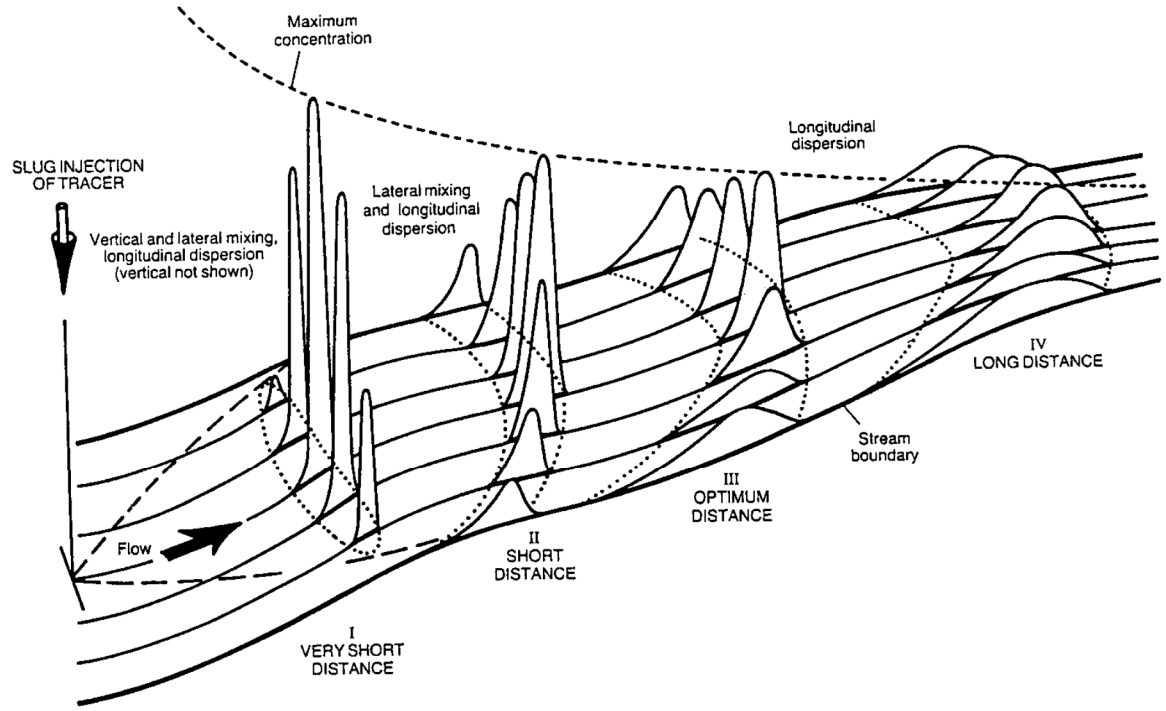

Figure 1. Evolution of the tracer cloud along flow, from an initial slug injection. The graph shows the effect of lateral mixing and longitudinal dispersion on solute concentration downstream (from Hubbard *et al.*, 1982).

The present chapter proposes a first step of characterization of the karst system thanks to multi-sampling point tracer tests. Indeed, the geometrical heterogeneity of the studied karst system must be taken into account to analyze solute transport in the Furfooz system. To this purpose, the tracing strategy consists in establishing a sampling site upstream and downstream each major heterogeneity in the system (when possible of course).

A first campaign of tracer tests was led in 2013 on the Furfooz site (hereafter tracer tests 1, 2, 3, and 10 to 13), to characterize the solute transport in each portion of the system. Field results and a first qualitative interpretation were published as a report paper in *Hydrogeology Journal* (Dewaide, Collon, Poulain, Rochez, & Hallet, 2017), available in Appendix 2. The paper focuses on the observation of double-peaked breakthrough curves (BTCs) on the site and proposes a conceptual model in which this dual recovery is the consequence of the tracer flowing through the underground lakes of the TQF and PDV. Since this 2013 campaign, new results have been gathered on the site. Some additional computations have also shown us that some shortcuts in the data interpretation were made in the paper: they are here rectified. The new results recently obtained on the field, led us to think over the proposed conceptual model that ought to be improved. The present chapter aims to present all the tracer tests

performed on the Furfooz site and their results. A global interpretation and the proposition of conceptual models conclude this chapter.

4.2 Tracer tests in the karst conduit system of Furfooz

4.2.1 Methodology

Tracer tests were conducted with fluorescent dyes, given their low cost and the availability of evolved detection devices (fluorimeters). Two kinds of fluorimeters were used in this study: the GGUN-FL 30 (Schnegg & Dörfliger, 1997) and the Fluo-G (Poulain et al., 2017). These devices have a detection resolution of 0.02 ppb for the GGUN and 0.06 ppb for the Fluo-G, and a saturation threshold of, respectively, 2500 mV (about 3000 ppb, depending on the calibration) and 3000 ppb. The tests were performed with different artificial fluorescent dyes: fluorescein and sulforhodamine B. Both chosen dyes are known for their low genotoxicity and ecotoxicity, though sulforhodamine B has been pointed out for its toxicity to algae at concentration exceeding 16 mg/l during 48h (Behrens et al., 2001). Fluorescein and sulforhodamine B have different properties that can affect their recovery. Fluorescein has a very low sorption tendency but is highly photo-sensisitive. Sulforhodamine B do not experience significate decay under sunlight but has a moderate sorption tendency (Field, 2002; Smart & Laidlaw, 1977). The injections of the dye were performed either in swallow hole (CN swallow hole) or in underground rivers (TQF river and GDS). The tracer powder is mixed to water in a big bucket just before its injection, which is kept as instantaneous as possible (dirac type). The mixture is then chased by some buckets of water (for the sinkhole injection mainly) to help it to move along and avoid its trapping into stagnant water. Injections of the tracer at the swallow hole in moderate to high flow conditions were not possible with a bucket due to a too high water-level. Therefore, they were realized with a pipe directed in the swallow hole (Figure 2). The choice of the injected mass of tracer is detailed in the tracer tests description. For calibration, blank water samples were taken in each site, before injection (one sample per site), in order to remove the background concentration that would influence the resulting BTC. The overall background noise is, however, rather low in this system (under 0.5 ppb for fluorescein, under 0.2 ppb for sulforhodamine B).

The resulting BTCs are analyzed to characterize solute transport in karst conduits, as usually done in karst hydrogeology (Dewaide, Bonniver, Rochez, & Hallet, 2016; Käss, 1998; Schudel et al., 2003). Direct interpretation of the BTC allow the determination of the main transport parameters (Figure 3): first arrival ($1^{st}A.$), mean travel time (T_{mean}), maximum velocity (V_{max}), mean velocity (V_{mean}), maximum peak concentration (C_{peak}), time to the maximum peak concentration (T_{peak}), recovery rate ($R.R.$). On Figure 3, the BTC is clearly asymmetric because the recession branch of the curve displays an important “tail” shape. This tailing is known to be a retardation effect that can be due to several hydro-physical processes whose most dominant are the exchange with less mobile (immobile) zones, effect of transverse dispersion, or sorption-desorption on sediments (Bencala & Walters, 1983; Field & Pinsky, 2000).

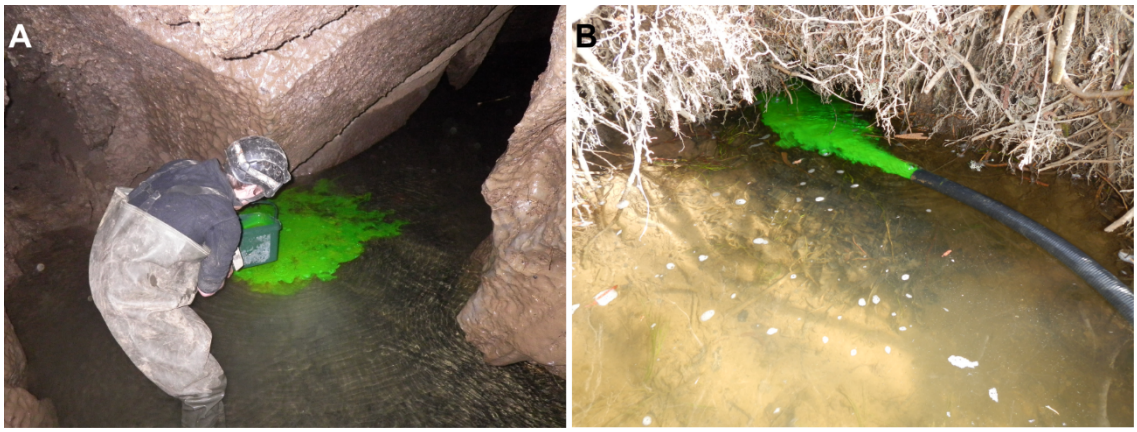

Figure 2. Instantaneous injection of a tracer mixture into the underground river, with a bucket (here at the GDS cave) and with a pipe directly into the swallow hole.

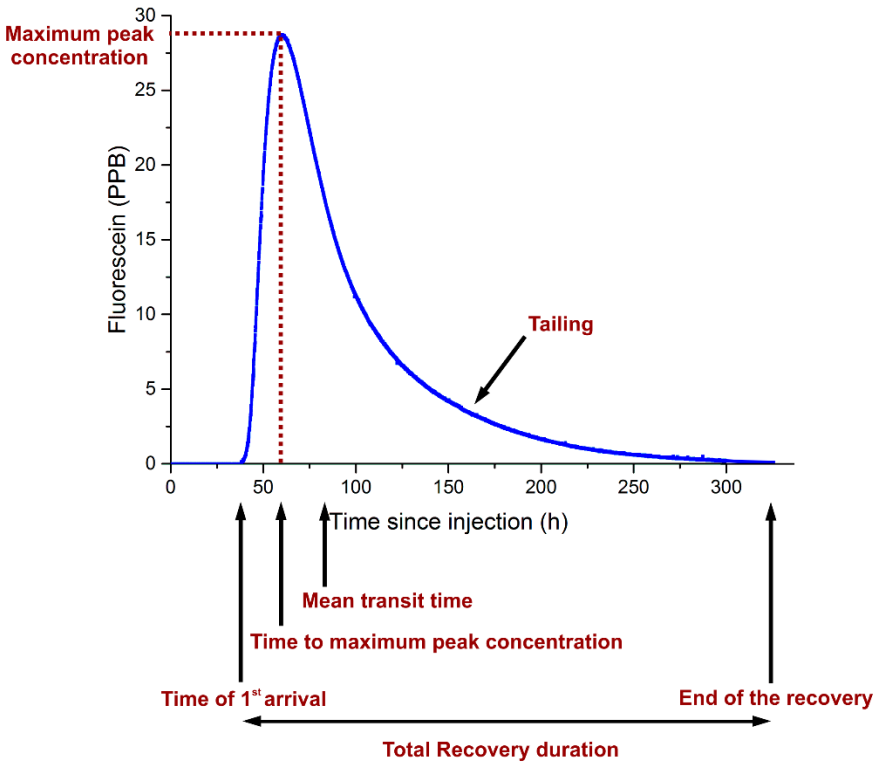

Figure 3. Illustration of the transport parameters that can be deduced from a BTC analysis. The example BTC was sampled in the Furfooz system.

The calculation of a recovery rate at one sampling station supposes the measure of the discharge during the recovery, according to the following equation (Benischke, Goldscheider, & Smart, 2007; Gaspar, 1987):

$$M_R = \int_{t=0}^{t=t_{tr}} C(t)\, Q(t)\, dt \quad (2)$$

Where M_R is the mass of tracer recovered [M] and t_{tr} is the time of the total recovery.

In the Furfooz system, to calculate the recovery rates, it was chosen to approximate the discharge in each site to the discharge measured at the GDS during the recovery (as there is a constant monitoring at this site). Indeed, in chapter 3, it has been shown that the discharge seems to stay steady along the Furfooz system in the underground river sections. The TQF lake and the PDV lake correspond to big volumes of water where no discharge can be estimated. Furthermore, evaluate a recovery on the basis of the BTC observed at the surface of the lakes supposes that the tracer distribution is homogeneous within the lakes, which is clearly not the case as it will be shown in section 4.2.3.4.b. It is therefore chosen not to give any recovery rate for the curves sampled at the PDV.

Some hydrodynamic parameters needs to be estimated by numerical analysis. The QTracer2 program (Field, 2002) is used, when possible, to estimate some global hydrodynamic parameters. QTRACER2 is a software developed to facilitate BTC analysis for tracer tests performed in different media (surface streams, granular aquifer, fractured-rock aquifer, sub-surface channels). It is designed to be run in the inverse mode: it solves the necessary equations from user-generated data to propose parameters optimization. QTRACER2 was used here to define the following parameters: the longitudinal dispersion coefficient (D_L), the longitudinal dispersivity (a_L), the conduit cross-sectional area (Cs), and the Peclet (Pe) and Reynolds (Re) numbers. The methods and equations used for the estimation of these parameters are widely explained in (Field, 2002). Pe gives an idea about the relative contribution of dispersion to transport, while Re represents the resistance to flow. Pe and Re are defined as (Grey & Pinder, 1976):

$$Pe = \frac{v\, l}{D_L} \quad (3)$$

$$Re = \frac{\rho\, v\, d}{\mu} \quad (4)$$

Where v is the solute mean velocity (m/s), l is the distance of transport (m), D_L the longitudinal dispersion (m^2/s), ρ the density of the fluid (g/m^3), d the conduit diameter (m) and μ the fluid viscosity (g/m.s). It is usually admitted that karst transport in conduits should be characterized by a Pe value that exceeds several times the value of 6 and by a Re value far greater than 2000, which reveals a turbulent flow (Landau & Lifshitz, 1987). The analysis of the curves and their transport parameters allow us to characterize the transport in Furfooz and to make comparisons to estimate the influence of the contrasted geometries in the system, the influence of the discharge, or again the impact of the location of the injection point.

Several tracer tests are presented hereafter. They were performed through several years in different hydrological conditions. Different points of injection are tested and various sampling

sites are used to characterize the solute transport via BTCs. The map of Figure 4 summarizes the different locations of the injection and sampling sites used for the tracer tests. At the TQF, the fluorimeter was placed in the underground river upstream the lake, at various distance from the swallow hole. At the PDV, the fluorimeter was placed on the eastern side of the lake, in surface. At the GDS, the fluorimeter was placed in the upstream resurgence (GDSa) of the cave and, for one of the test, in the downstream resurgence (GDSb). Finally, at the TDL, the fluorimeter was placed in the river, inside the cave, a few meters upstream the final resurgence (where, as a reminder, the flow out is dispersed through blocks and fluorimeter cannot be sited). The estimated distance between the injection point and the sampling sites are indicative and based on straight lines drawn on a map; so they underestimate probably the real distances.

The flow conditions, different for each test, are detailed in the introduction of each concerned test. As stated in chapter 3, there is only two sites where the discharge can be measured in a large range of discharge conditions: the TQF river and the GDS. However, given the difficult access to the TQF river, regular measurements could only be performed at the GDS in order to build a hydrograph (chapter 3, Figure 17, p. 73). For each test, a mean discharge was computed for the duration of the test on basis of this hydrograph. For most of the tests, the discharge was also measured the day of the injection at the GDS, and, when possible, at the TQF and/or at the swallow hole.

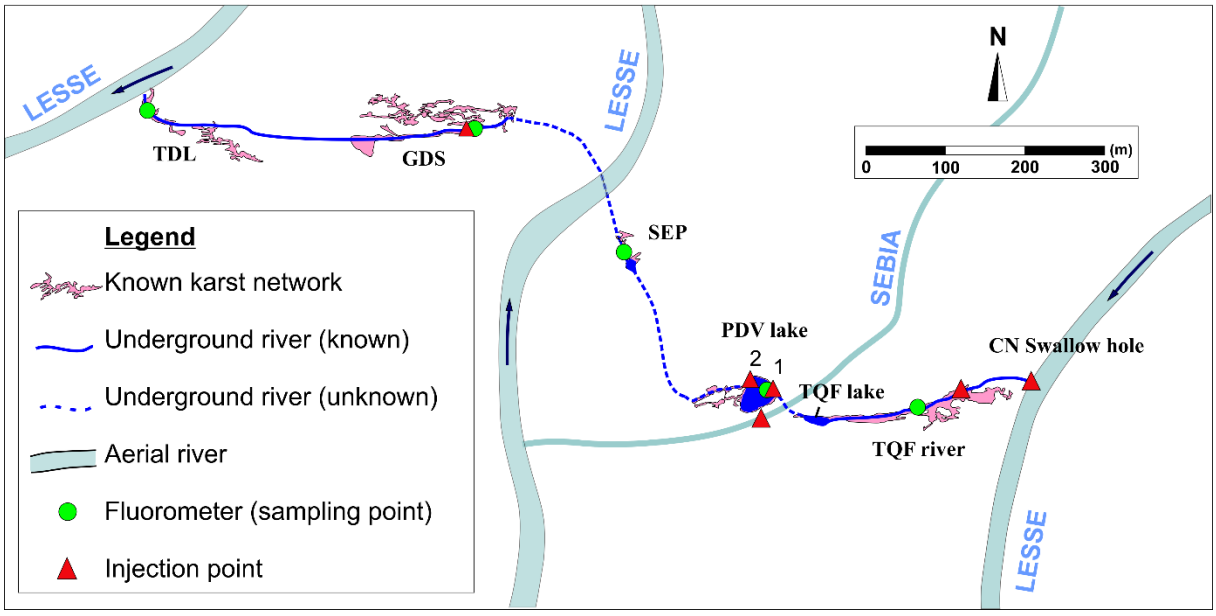

Figure 4. Map of the different injection and sampling points in the Furfooz karst system.

After a brief presentation of the available historical data regarding solute transport studies on the Furfooz system, the tracer tests realized in the context of this thesis will be described and their results analyzed in details. The tests have been gathered in regard with the injection point, starting from the most upstream to the most downstream.

4.2.2 Historical data

The first ones who highlighted the double meanders crossing of the Furfooz system are Van den Broeck and Rahir at the beginning of the 20th century (Van den Broeck & Rahir, 1903). Their tests were purely qualitative and rely on eye detection. They injected 500 g of Fluorescein at the CN swallow hole and could detect the dye at the PDV (17 h after injection), the GDS (63 h after injection) and the TDL (72 h after injection) caves. This test was conducted in high discharge conditions (not quantified). They elaborated a first functioning scheme of the Furfooz system, highlighting the double meander crossing (Figure 5). Much later, in the 90's, those hydraulic connections were confirmed by active-coal tests led by speleological groups (Werkgroup Fysische Speleologie and Speleoclub Hades).

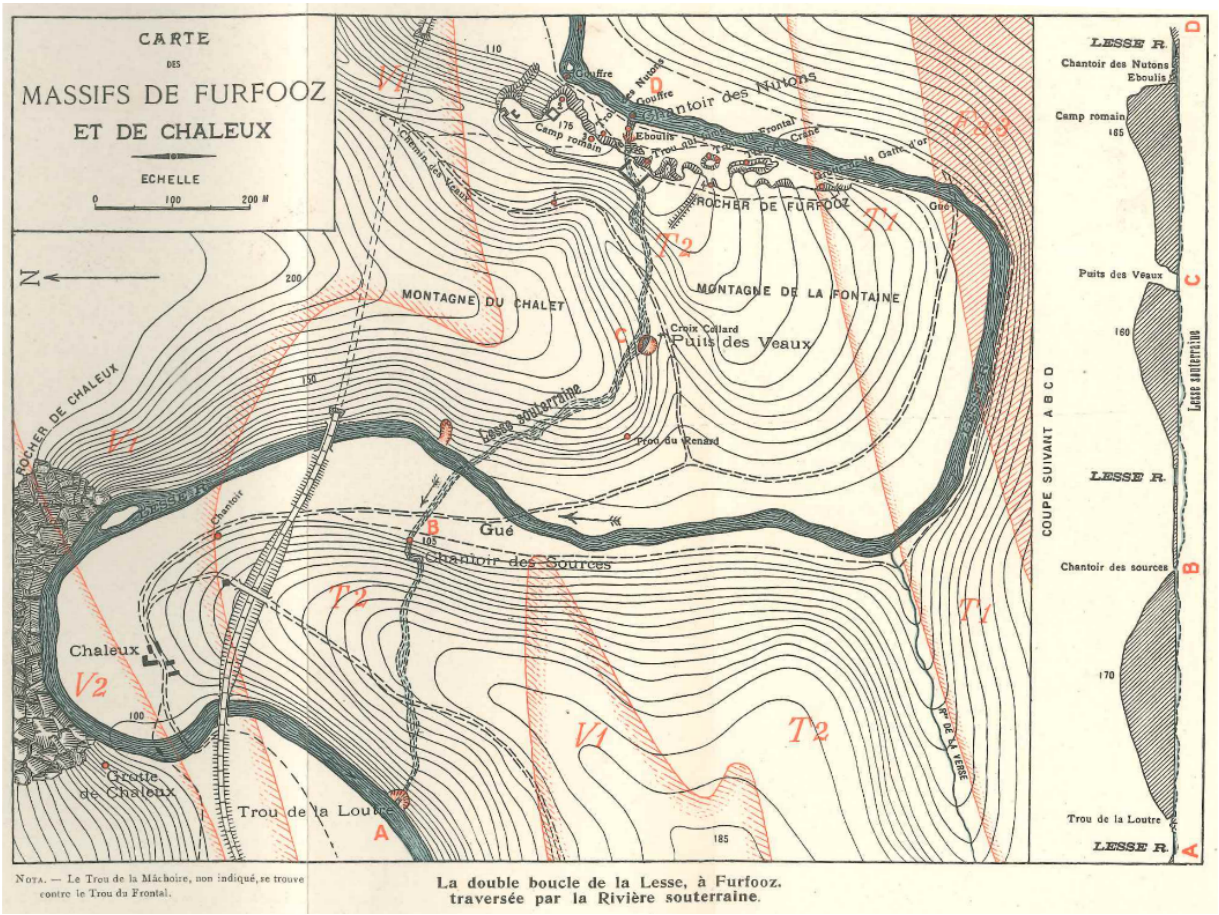

Figure 5. Scheme and cross-section of the Furfooz system, established by Van den Broek and Rahir (Van den Broeck & Rahir, 1903).

The first quantitative tracer tests were performed in 2008 in the context of the "synclin'Eau" project (Brouyère et al., 2009). They performed four injections in the summer time, at different points of the system (Table 1). Figure 6 details the location of the two injection points at the PDV lake. The BTCs obtained from these injections are presented in (Figure 7) and (Figure 8).

		Sampling sites				
DATE	INJECTION	PDV	GDS	TDL	Q_{TQF} (l/s)	Q_{GDS} (l/s)
JUNE 2008	TQF (100 g FL)	v	v	v	4.8	13.2
JUNE 2008	GDS (25 g SR)			v		
AUGUST 2008	PDV1 (200 g FL)		v	v	x	7.2
AUGUST 2008	PDV2 (200 g SR)		v	v		

Table 1. Summary of the tracer tests performed in the "Synclin'Eau" project. [SR]: Sulfo-Rhodamine B; [FL] : Fluorescein; [PDV1] and [PDV2] are two different points of injection within the PDV lake.

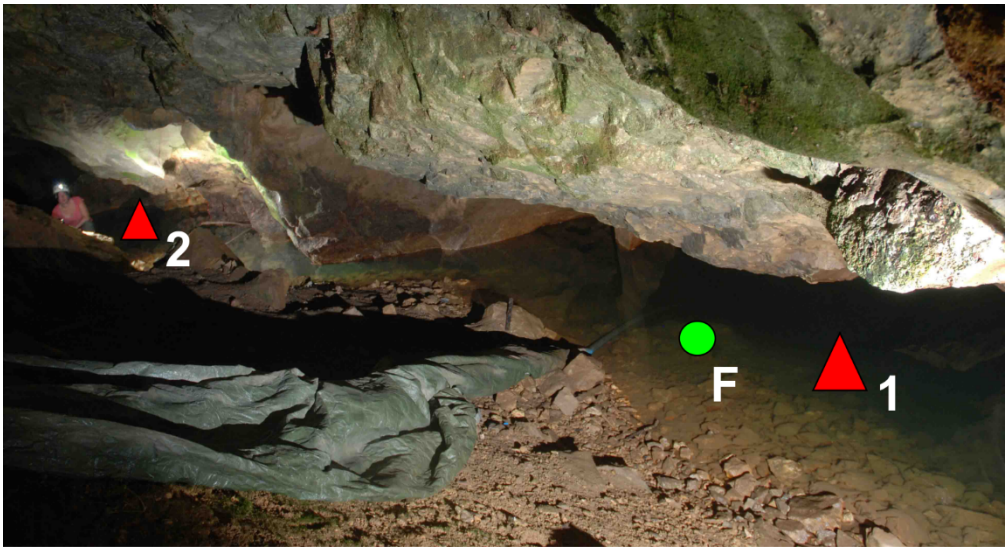

Figure 6. Picture of the PDV lake with the position of the two injection points. The red triangles [1] and [2] are injection point 1 and 2 on Figure 4, [F] locates the fluorimeter.

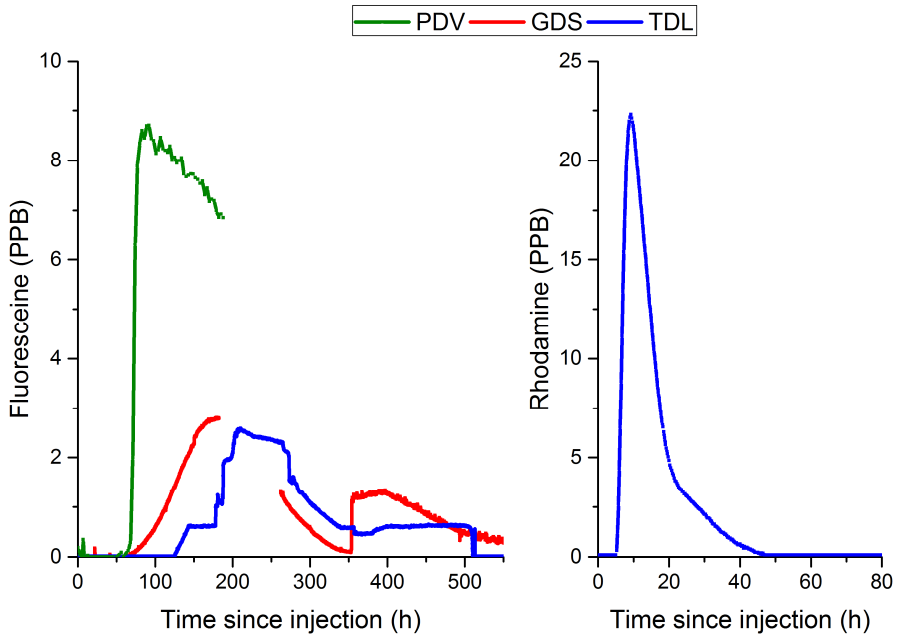

Figure 7. BTCs resulting from the injections made in June 2008. The left graph shows the results of the injection of Fluorescein made at the TQF; while the right graph shows the BTC resulting from the injection of sulforhodamine at the GDS

Regarding the tracer tests made in june 2008 (Figure 7), the resulting BTCs show important data gaps due to technical problems that make the interpretation difficult. The tests confirm the hydrogeological connection between the different sites. They also show a strong influence of the lake on the tracer behavior. Indeed, the GDS and TDL BTCs sampled after the crossing of the lake by the tracer (left graph) show a dispersive behavior with a tracer cloud dispersed on more than 300 h. This behavior is to oppose with the BTC shown on the right graphic that demonstrates a very narrow curve resulting from a transport dominated by strong advection.

At the PDV, two injection points were defined (injection points 1 and 2 in Figure 4). The two points of injection are separated by 10 meters only as shown in the picture of Figure 6. Figure 8 presents the BTCs resulting from injections within the PDV lake. They show rather contrasted results depending on where the injection is made in the lake. The fluorescein (injected at point 1) arrives 7 hours before the sulforhodamine B at the GDS and there is a difference of almost 30 h between the peaks of the two curves. This difference show that the location of the injection point within the lake has a strong influence on the resulting BTC. The BTC that is delayed may result from an injection in a less mobile zone of the lake, which supposes a spatial heterogeneity of the flow distribution within the lake. All the BTCs show an important skewness that underlines retardation effect. This important retardation is most probably the result of interaction with immobile water that should represent an important volume of the PDV lake. It should also be underlined that the injected dyes are different (fluorescein vs. sulforhodamine B); this could have a small influence on the shape of the BTCs and more specifically on the tailing effect that could be due, in part, to sorption-desorption process that could affect differently the different dyes.

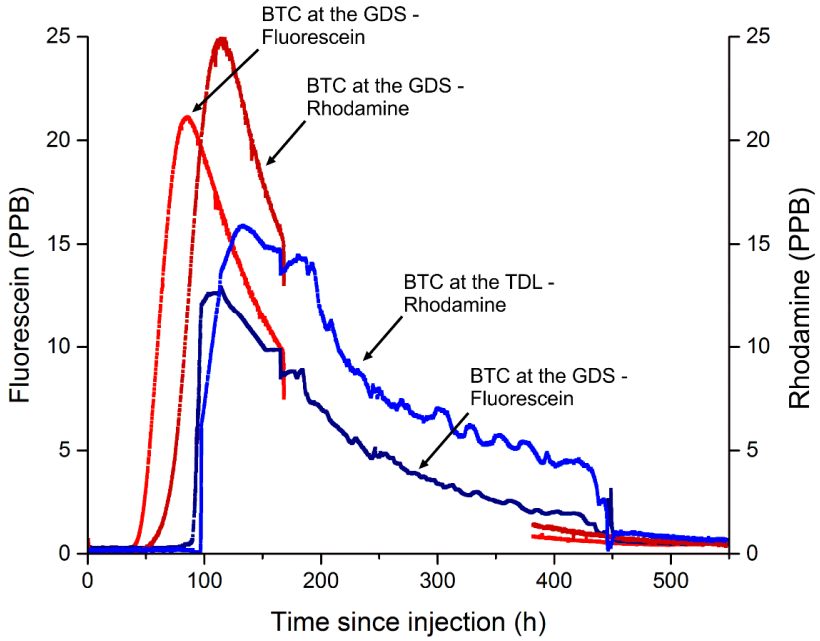

Figure 8. Results of the injections made at the same time (august 2008) but at different locations in the PDV lake. GDS-FL and TDL-FL result from the Fluorescein injection made at the injection point 1; while GDS-SR and TDL-SR result from the injection of sulforhodamine B at injection point 2. Technical problems are responsible for the gap in the GDS data.

4.2.3 Injections at the CN swallow hole

The characteristics of each injection and the sampling strategy are summarized in Table 2. Regarding the injected mass of tracer, it was decided to inject always the same quantity whatever the flow conditions and whatever the chosen dye (fluorescein or sulforhodamine B). This was decided in order to compare properly the different tests and to, possibly, characterize the influence of the discharge on the tracer recovery, or the influence of some decay processes due to the choice of tracer. All the tracer tests were conducted in low to moderate flow conditions. The chosen injected mass is 200 g. Indeed, in the *Synclin'Eau* project (chapitre 4.2.2), the injected mass was 100 g of fluorescein. The maximum concentration observed at the TDL cave was 2.8 ppb. It was then decided to double the injected mass, to ensure a significant signal in higher flow conditions. We could also have based the calculation of the injected mass on the following equations (Dörfliger, 2010):

$$M_r = (T * Q * C_s)/2 \,,$$
$$M_i = M_r * C_c$$

Where M_r is the mass recovered (g), T is the total time of the recovery (h), Q is the discharge (l/h), C_s is the wanted maximum concentration (g/l), M_i is the injected mass (g), C_c is the correction coefficient. This correction coefficient is usually considered between 1 and 4, and depends on the possible decay of the tracer.

In the Furfooz case, we could consider a total transit time of about 300 h at the GDS cave, a discharge of about 20 l/s (about the maximum discharge in which the tracer were conducted), and a wanted concentration at the GDS of 10 ppb. The calculated M_r would then be 108 g. Applying a C_c of 2 (considering possible decay, especially into the lakes), the calculated M_i is 216 g, which is quite consistent with our experimentation.

4.2.3.1 Tracer test 1

The test was performed between the 26th of March 2013 and the 15th of April 2013. The fluorimeters used for this test is the GGUN-FL30. The results of this injection at the CN swallow hole (200 g sulforhodamine B) are shown in Figure 9. It exposes the BTCs sampled at different sites of the Furfooz underground system, as well as the discharge evolution monitored at the GDS during the test. A discharge of 24 l/s was measured on the day of the injection at the GDS cave. The discharge, that can be followed on the first 300 h after the injection (probe dysfunction after 300 h), decreased steadily during the test. The mean discharge, computed on these 300 h, is 20 l/s. Given the variation of the discharge during the test, the recovery rates are calculated on basis of the variable discharges measured at the GDS.

Table 3 gathers the main transport parameters directly deduced from the BTCs. The observations at the TQF show a rather rapid arrival of the first particles of tracer (1.5 h) and a

T_{peak} of 2.3 h implying a V_{peak} of 65 m/h. The concentration reaches 2100 ppb. The curve shows very little dispersion and a few skewness on the descending branch. The entire mass of injected tracer flows through this point. The calculated recovery is actually of 130 % during this test. This excess of tracer comes probably from an over-estimation of the discharge at the TQF – based here on the variable discharges observed at the GDS – at the time of the recovery. At the PDV lake, a wide curve appears. It is affected by a strong tailing that expresses retardation in the tracer transport. Surprising results are observed at the GDS and the TDL. Even if an important data loss (due to the fluorimeter dysfunction) is observed in the GDS curve between 72 h and 219 h, it can easily be imagined that a second peak should appear in this time gap as it is observed at the TDL. Two distinct peaks are indeed observed and they present contrasted T_{peak} (41 h vs 125 h) and C_{peak} (3 ppb vs 6.8 ppb). On a qualitative point of view, it seems that the first peak is narrower than the second one, suggesting less dispersion. It cannot be said if the first peak presents some tailing because the descending branch of this first peak is hidden in the second one. The latter shows an important skewness. Note that the recovery calculated at the TDL (36.5 %) is rather low. This low recovery supposes loss of tracer that could be linked to different processes as adsorption of the dye on suspended matter (Talbot & Henry, 1968) or trapping and extreme dilution (under the detection limit of the fluorimeter) of the solute in some less mobile zones. In Furfooz, the TQF and the PDV lakes represents big volumes of water (respectively 7000 and 16000 m^3 of estimated volume) where non- or less mobile zones are likely. Finely, it is important to notice that the first arrival at the GDS is nearly the same than the first arrival at the surface of the PDV lake. The T_{peak} of the first peak at the GDS (and at the TDL) is even shorter that the T_{peak} at the PDV. Given the location of the fluorimeter at the PDV, it could be proposed that the BTC observed at that point is “off-path” of the main tracer cloud and reflects a dispersion effect through the lake; which corresponds to its wider shape.

		Sampling sites Distance from the injection point									Discharge measurements			Q_{Mean} GDS
Date of injection in the CN swallow hole	Quantity and dye	TQF 70 m	TQF 150 m	TQF Lake*	PDV surf 300 m	PDV in depth*	SEP 550m	GDSa 760 m	GDSb 767 m	TDL 1170 m	CN	TQF	GDS	
26 March 2013 Tracer test 1	200 g SR		Y		Y			Y		Y	-	-	24 l/s	20 l/s
19 April 2013 Tracer test 2	200 g FL				Y			Y		Y	-	-	14 l/s	11 l/s
2 September 2013 Tracer test 3	200 g SR		Y		Y			Y	Y	Y	3.5 l/s	5.5 l/s	6 l/s	6 l/s
13 May 2016 Tracer test 4	200 g FL			Y	Y	Y		Y			-	-	-	8.5 l/s
23 September 2016 Tracer test 5	200 g FL							Y			-	-	-	-
2 November 2016 Tracer test 6	200 g FL							Y			0.2 l/s	-	-	2.1 l/s
23 February 2017 Tracer test 7	200 g FL						Y	Y			-	-	14 l/s	19.6 l/s
30 April 2018 Tracer test 8	200 g FL	Y			Y		Y	Y		Y	-	9 l/s	8.7 l/s	16 l/s

Table 2. Overview of the tracer tests performed in 2013. [Y] indicates that a fluorimeter was present at the given site. Q_{Mean}GDS is the mean discharge calculated via the GDS hydrograph during the time of the test. *The exact location of the sampling sites in the lakes are detailed in the test description

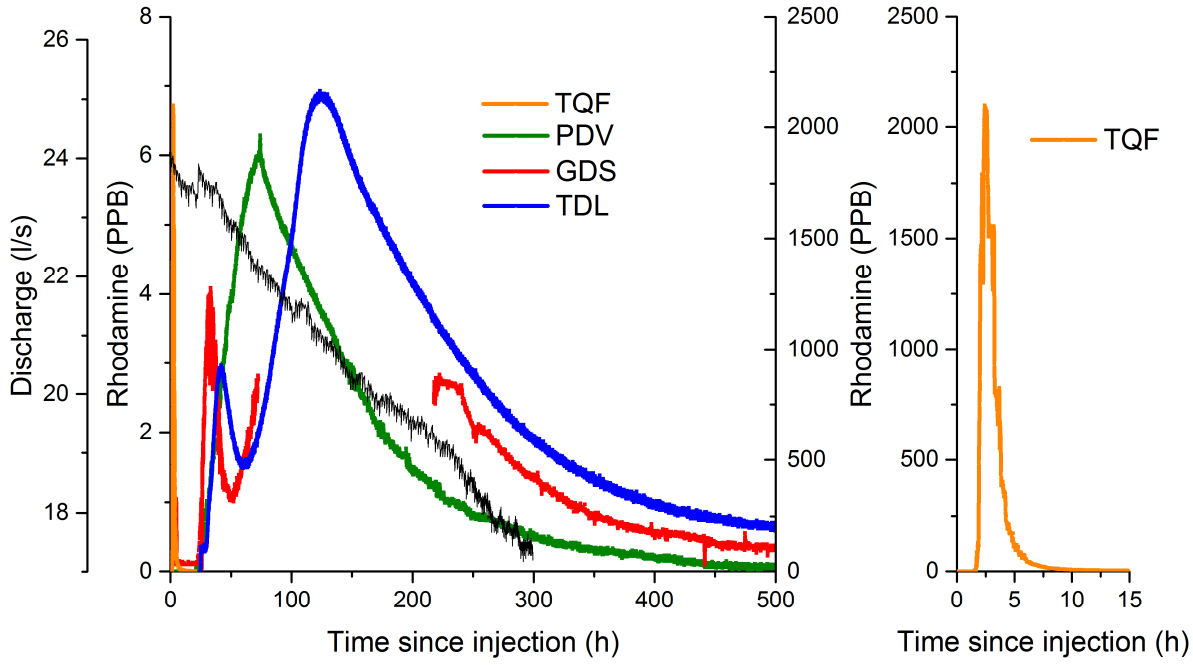

Figure 9. BTCs observed at different sampling points in tracer test 1 (March 2013). Discharge is the black decreasing curve. On the left graph, the right Y axis stands for the concentration at the TQF. The gap on the GDS curve is due to a dysfunction of the fluorimeter. The insight graph on the right presents the BTC at the TQF, given the scale difference in time and concentration with regard to the other curves.

Tracer test 1 **26 March 2013**		**1st A.** **(h)**	**V_{max}** **(m/h)**	**T_{peak}** **(h)**		**V_{peak} (m/h)**		**T_{mean}** **(h)**	**V_{mean}** **(m/h)**	**C_{peak}** **(ppb)**		**R.R.** **(%)**
	TQF	1.5	100	2.3		65.2		3.1	48.4	2100		130*
	PDV	19.7	15.2	74.1		4.0		143.6	2.1	6.4		-
	GDSa	22	35	1st	2nd	1st	2nd	-	-	1st	2nd	-
				33	-	23.3	-			4.1	-	
	TDL	29.5	39.7	1st	2nd	1st	2nd	198.3	5.9	1st	2nd	36.5
				41	125.1	28.5	9.3			3	6.8	

Table 3. Main transport parameters deduced from the observed BTCs. (*): this excess of tracer comes probably from an over-estimation of the discharge in the TQF – based here on the Q_{mean} GDS – at the time of the recovery.

Regarding the use of the QTRACER2 program, it was decided to restrict it to the single-peaked BTCs. Indeed, if it was to be used on the dual-peaked BTCs, a decomposing should be performed to separate the two peaks. However, this decomposing would be hazardous as, so far, there is no way to tell how would evolve the descending branch of the first peak and when would start the ascending branch of the second peak. The two peaks could furthermore have a strong influence on the shape of each other. Even if QTRACER2 could have given a global estimation of the transport parameters, the absence of an accurate method to separate the peaks led us to not apply QTRACER2 on the double-peaked BTCs. Therefore, in the case of tracer test 1, QTRACER2 is used on the BTC observed at the TQF and the PDV only (Table 4).

For the BTC observed at the TQF, QTRACER2 was run with a constant discharge, assimilated to the Q_{Mean} GDS computed on the first 10 h after the injection (24 l/s). The results characterize an advective transport with a very short dispersivity (2.22 m) and high values of Pe (67.5) and Re (17718). The cross-section estimated by QTRACER2 (1.79 m^2) seems rather big in comparison to what can be observed at the TQF river (about 0.5 m^2 in these flow conditions). However, the underground river can be observed in the TQF cave, only at an estimated distance of 70 m downstream the injection point. What kind of section is crossed by the tracer upstream this point is not known and could be much bigger than the river observed at the TQF cave. Furthermore, the distance between the CN swallow hole and the start of the river at the TQF cave is estimated on basis of a straight line on a map. This distance of 70 m could be underestimated, and that could imply an overestimation of the cross section.

Regarding the use of QTRACER2 on the PDV curve, defining a discharge through the lake is not possible. The parameters are calculated here on the basis of a mean discharge computed at the GDS (20 l/s). Therefore, the values presented in Table 4 have to be taken with caution and kept in proportion. The BTC observed at the PDV is clearly dominated by dispersion in a big volume of water (Cs of 34.4 m^2). Pe (4.71) and Re (3372) are very low in comparison to more classic values observed in the karst conduit of the TQF river.

Tracer test 1	D_L (m^2/s)	a_L (m)	Cs (m^2)	Pe	Re
TQF	0.029	2.22	1.79	67.5	17718
PDV	0.037	63.8	34.4	4.71	3372

Table 4. Parameters computed by QTRACER2 for the TQF and the PDV BTCs.

4.2.3.2 Tracer-test 2

The test, performed between the 19th of April 2013 and the 10th of May 2013, consisted in an injection of 200 g of fluorescein at the CN swallow hole. The BTCs were sampled in different

sites by the GGUN-FL30 fluorimeters (Figure 10). The main transport parameters are displayed in Table 5. The discharge conditions are not strictly stable during the test, as shown by the discharge evolution curve on Figure 10. A mean discharge of 11 l/s is calculated on the duration of the test. Variable discharge is used for the calculation of the recovery rates.

The BTC observed at the surface of the PDV lake shows a slow transport of the tracer (V_{mean} of 2 m/h). Its wide shape supposes some dispersion. The curve is asymmetric due to an important tailing affecting the descending branch. The spooky behavior of the curve should probably be explained by some turbidity effects. However, due to a dysfunction of the turbidity probe, no turbidity data was recorded. At the GDS and the TDL, double-peaked BTCs are observed. Again, the two peaks are very well distinguished by their contrasted T_{peak} (61 vs 153.7 at the GDS, 72.9 vs 190.9 at the TDL). They reach similar C_{peak} (4.4 ppb vs 4.2 ppb at the GDS). Furthermore, the flared summit of the second peak suggests a greater dispersion. This second curve shows also a long and strong tailing, that does seem more important than in the descending branch of the first peak even if it is not complete. It is reasonable to propose that the second peak results from a slower or longer transport through a possible bigger section with slow zones along the path. Finally, the recoveries are rather low (15.1 at the GDS, and 11.9 at the TDL).

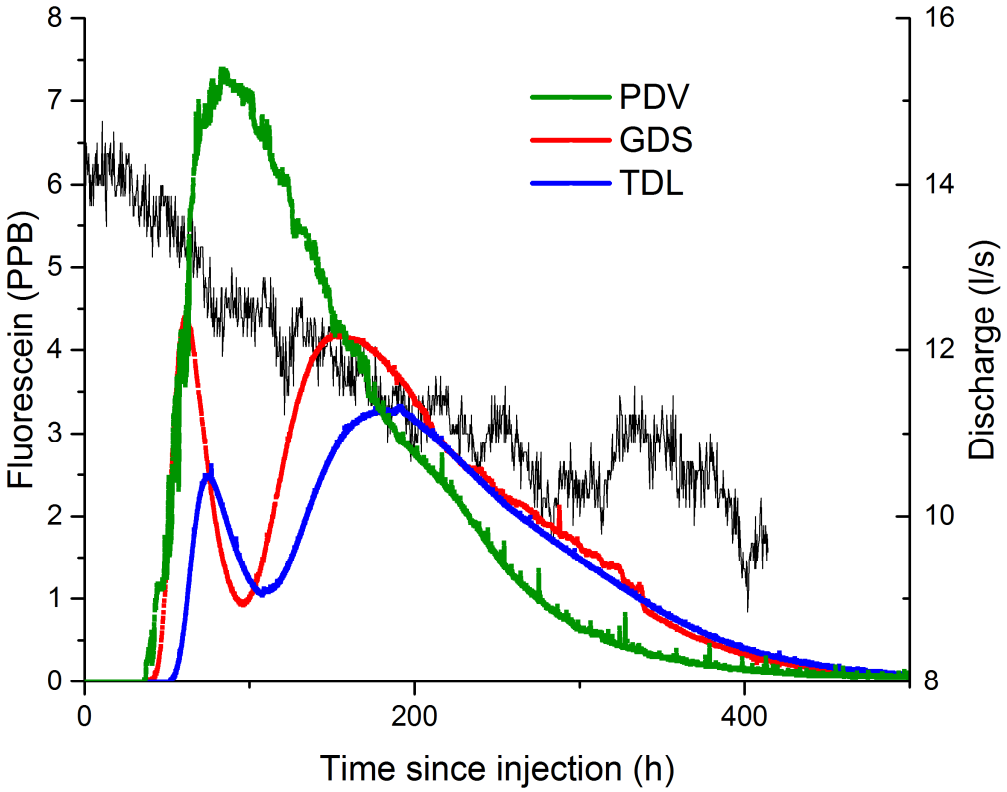

Figure 10. BTCs observed at different sampling points (injection at the CN swallow hole, April 2013). Discharge is given by the black curve.

		1st A. (h)	V_{max} (m/h)	T_{peak} (h)		V_{peak} (m/h)		T_{mean} (h)	V_{mean} (m/h)	C_{peak} (ppb)		R.R. (%)
Tracer test 2 April 2013	PDV	36.4	8.2	82.9		3.6		148.3	2.0	7.37		-
	GDSa	38.7	19.6	**1st**	**2nd**	**1st**	**2nd**	195.7	3.8	**1st**	**2nd**	15.1
				61	153.7	12.4	4.9			4.4	4.2	
	TDL	52.0	14.6	**1st**	**2nd**	**1st**	**2nd**	215	5.4	**1st**	**2nd**	11.9
				72.9	190.9	10.4	3.9			2.5	3.3	

Table 5. Transport parameters deduced from the observed BTCs.

QTRACER2 can be applied here to the PDV curve that is single-peaked (Table 6). The parameters are calculated here on the basis of a mean discharge computed at the GDS (11 l/s). The longitudinal dispersion coefficient is estimated to 0.023 m^2/s. Given the slow velocities encountered at the PDV, the dispersivity is estimated to 41.4 m and the cross-section to 19.6 m^2. Pe (7.2) and Re (2461) are low. They contrast with the values encountered in usual karst conduits (like for example in the TQF river in tracer test 1 with Pe and Re of 67.5 and 17718 respectively) and suggest a transport dominated by dispersion. Those values, with all the caution that should be taken regarding the rightness in their estimation, match with the qualitative analysis that can be made on basis of the shape of the PDV curve.

Tracer test 2 – April 2013	D_L (m^2/s)	a_L (m)	Cs (m^2)	Pe	Re
PDV	0.023	41.4	19.6	7.2	2461

Table 6. Hydrodynamic parameters calculated by QTRACER2 for the PDV curve.

4.2.3.3 Tracer test 3

The test, performed between the 2nd and the 27th of September 2013, consisted in an injection of 200 g of sulforhodamine at the CN swallow hole. The sampling was performed with the GGUN-FL 30 fluorimeters. The results of this test are exposed in Figure 11 (BTCs) and Table 7 (transport parameters). The discharge conditions are not strictly stable during the test, as shown by the discharge evolution curve on Figure 11. A mean discharge of 6 l/s is calculated on the duration of the test (discharge data stops 271 h after the injection due to probe dysfunction). Variable discharge is used for the calculation of the recovery rates, except at the

TQF where a gauging was performed at the injection. This value (5.5 l/s) was used for the estimation of the recovery rate and the use of QTRACER2 for the TQF curve.

At the TQF, the tracer arrives nearly 2 hours after the injection and the maximum concentration is reached after 2.4 h. The curve is very narrow and supposes a very low dispersion of the tracer cloud. C_{peak} is 3368 ppb. However, this value exceeding the saturation level of the fluorimeter (3000 ppb), it is indicative. The recovery rate is estimated at 33.8 %. An important loss of tracer is therefore to be considered on these first 150 m. A wide single-peaked BTC is observed at the surface of the PDV lake. The concentration reaches 12.7 ppb. Retardation affects the descending branch. Again, double-peaked BTCs are observed downstream the PDV lake. Their T_{peak} are contrasted (78.2 vs 214.9 at the GDSa, 100.9 vs 239.2 at the TDL), and they have different C_{peak} (9.5 vs 8.5 at the GDSa). Tracer recoveries are low: only 33.8 % at the TQF and 21.4 % at the GDS. This could be linked to the low flow conditions (see the discussion in section 4.3). Finally, the fluorimeter that was placed in GDSb (downstream spring of the GDS) did not show any recovery of the fluorescein. That confirms, as it was said in chapter 3, that this resurgence of water is not linked with the upstream part of the Furfooz system.

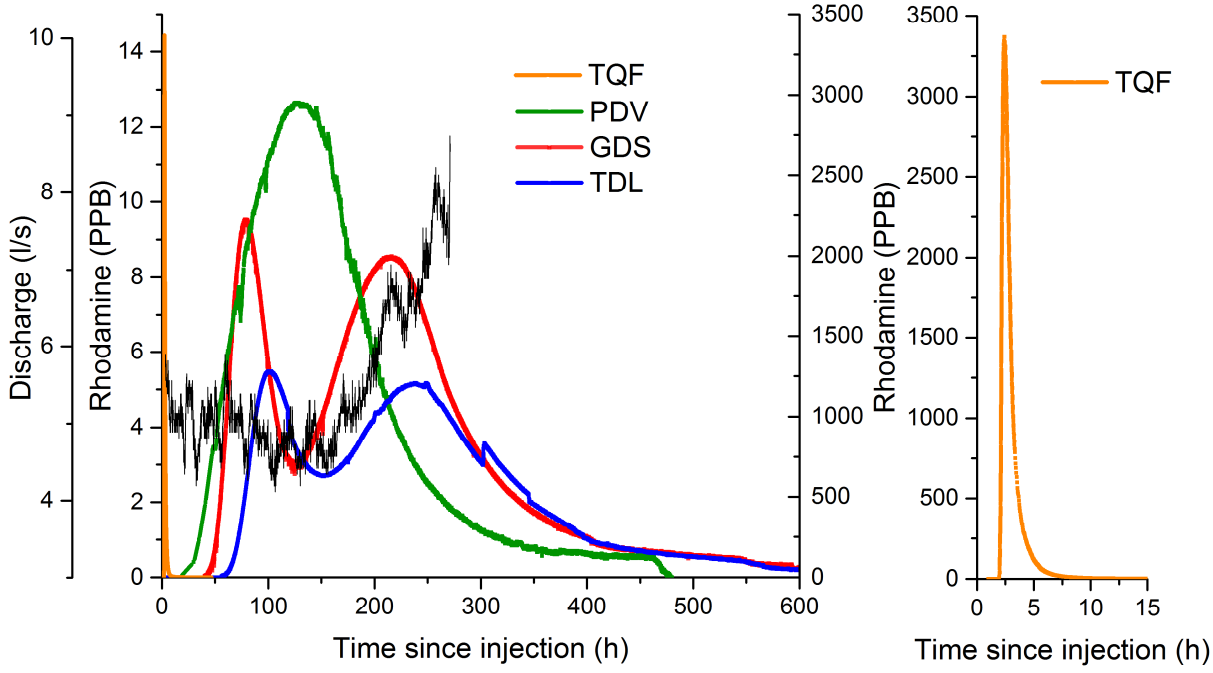

Figure 11. BTCs observed at different sampling points (injection at the CN swallow hole, September 2013). Discharge is given by the black curve.

The QTRACER2 analysis on the TQF and the PDV curves is shown in Table 8. Contrasted behavior are observed at this two sites. The TQF curve illustrates a very advective behavior with high Pe (121.9) and Re (8299). The cross-section estimation of 0.43 m2 is about ten times bigger than the section measured on the field (0.05 m^2 in these flow conditions). This supposes

that the unknown part between the CN swallow hole and the TQF river has a much bigger section or is under-estimated in length. The BTC observed at the PDV is the result of a dispersive transport (dispersivity of 37.9 m) through volumes of big mean cross-section (11.4 m^2). Pe (7.92) and Re (1761) are very low.

		1st A. (h)	**V_{max} (m/h)**	**T_{peak} (h)**		**V_{peak} (m/h)**		**T_{mean} (h)**	**V_{mean} (m/h)**	**C_{peak} (ppb)**		**R.R. (%)**
Tracer test 3 - September 2013	TQF	1.9	78.9	2.4		62.5		3.8	38.6	3368		33.8
	PDV	30.0	10.0	125.8		2.4		157.8	1.9	12.7		-
	GDSa	40.3	18.9	**1st**	**2nd**	**1st**	**2nd**	230.4	3.3	**1st**	**2nd**	21.4
				78.2	214.9	9.7	3.5			9.5	8.5	
	TDL	56.1	20.9	**1st**	**2nd**	**1st**	**2nd**	250.9	4.7	**1st**	**2nd**	15.3
				100.7	239.2	11.6	4.9			5.5	5.1	

Table 7. Transport parameters deduced from the observed BTCs.

Tracer test 3	**D_L (m^2/s)**	**a_L (m)**	**Cs (m^2)**	**Pe**	**Re**
TQF	0.016	1.23	0.43	121.9	8299
PDV	0.020	37.9	11.4	7.92	1761

Table 8. Parameters computed by QTRACER2 for the TQF and the PDV BTCs.

4.2.3.4 Tracer test 4

This test was realized to characterize the tracer behavior throughout the PDV and the TQF lakes that represent big volumes of water. In this purpose, a dye injection (200g of fluorescein) was realized at the CN swallow hole on the 13th of May 2016. Three sites were equipped with fluorimeters: the TQF lake (GGUN-FL30), the PDV lake (Fluo-G and GGUN-FL24) and the GDS (Fluo-G). To focus on the tracer behavior within the lake, special equipment were set into both the TQF and the PDV lakes. These are described in the following paragraphs.

The access to the TQF lake is difficult: long progression into a speleological cave with narrow passages and muddy galleries. Therefore, the supply of equipment to the lake is limited. The lake was explored once by diving; however, given the dangerousness of this dive, the diver

was not asked to intervene further regarding the equipment. A boat was used to navigate through the lake and place the fluorimeters. The lake was equipped with three fluorimeters (Figure 12): one at the lake entrance (point A) and two in the center, about 30 m from the shore. One of those two devices was placed 1 m below the water surface (point B) and the second 20 m deep (point C). Electrical conductivity and temperature profiles were also performed from the boat, which consisted of taking measurements every meter on a vertical profile from the surface to the bottom of the lake.

At the PDV, it was decided to equip the lake with a screened casing from the surface to the bottom (about 25 m deep), which was possible thanks to the help of a diver (Figure 13). The casing was chosen large enough so that a piezometric fluorimeter (GGUN – FL24) could be inserted in it. The experiment consisted of making a concentration profile through the depth of the lake following the injection made at the CN swallow hole. A sounding of the lake with the fluorimeter through the casing was realized 60 h after the injection. Two concentration profiles were realized: one in ascending the fluorimeter from the base of the casing to the top, and the other in descending the device.

Finally, a fluorimeter was placed at the GDSa, to confirm the results of the previous tracer tests.

4.2.3.4.a Observations at the TQF lake

The conductivity and temperature profiles, made in the springtime, showed very homogeneous results with no clear changes in temperature or conductivity with the depth. A small variation of less than 1°C was observed between the surface (12.1 °C) and the bottom at 21 m (11.3 °C). A conductivity value of 330 µS/m was constant along the profile except at the bottom where it reached 360 µS/m, but this is probably due to sediment accumulation.

Regarding the tracer test, results of this test show a clear difference in the tracer behavior between the surface and the bottom of the lake (Figure 14 and Figure 15). Indeed, the two fluorimeters at the surface (points A and B) show a rapid arrival of highly concentrated tracer: the signal at point A shows a first arrival 1 h after the injection and the concentration increases in a few minutes up to 600 ppb. At point B the tracer arrives 1.8 h after injection and reaches a concentration of 450 ppb; for those two BTCs, the concentration drops rapidly (within three hours) below 50 ppb and both show a little retardation in the recovery. After 6 h, the concentration at point A is about 5 ppb while 20 ppb are recorded at point B. From there the concentration at both points rises again to reach 36 ppb in point A and 56 ppb in point B after 15 h. Then the concentration drops suddenly at the two locations and there is a complete disappearance of the tracer after 20 h. This second rising of the concentration is difficult to interpret. A turbidity effect, given the very muddy conditions of the TQF, could explain an artificial rise of the water fluorescence. However, there isn't any flood at that time to justify the sudden turbidity. Therefore, this second recovery is probably linked to the trapping of the tracer in annexed zones of transport like eddies or turbulent zones that release the tracer with retardation.

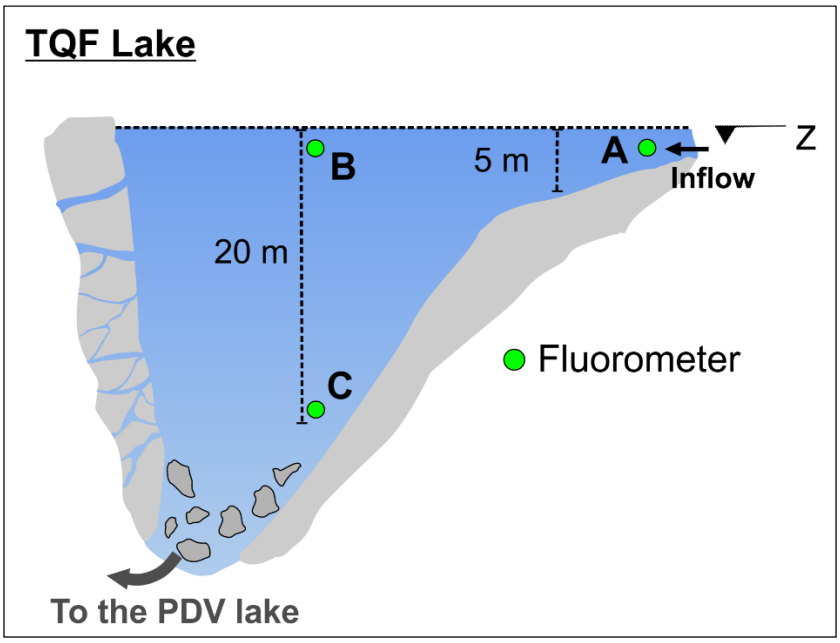

Figure 12. Equipment of the TQF lake. Three fluorimeters (A, B, C) are placed at different positions and different depths during tracer test 4.

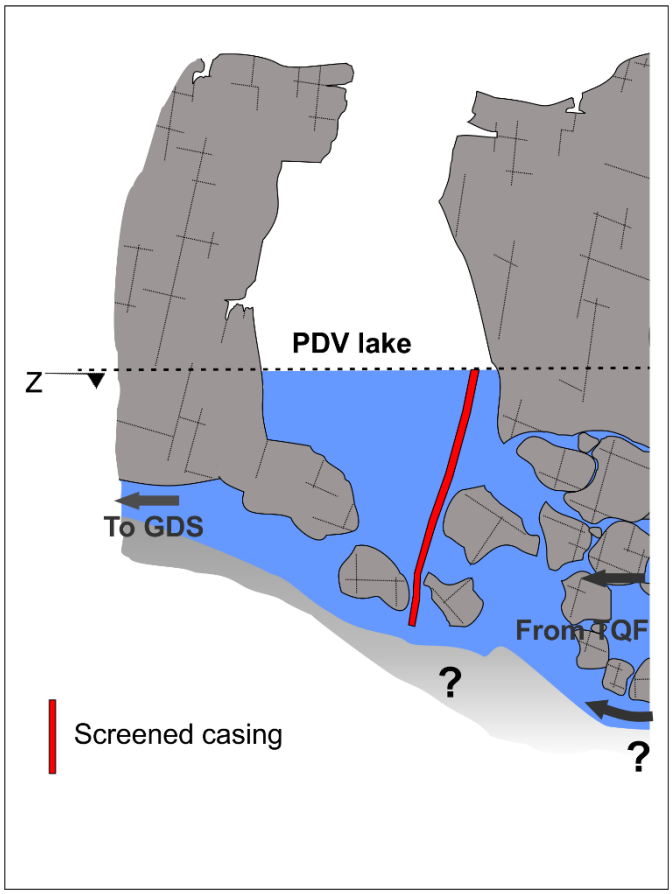

Figure 13. Equipment set at the PDV lake during tracer test 4. A screened casing through which a fluorimeter is inserted crosses the lake from its surface to the supposed bottom.

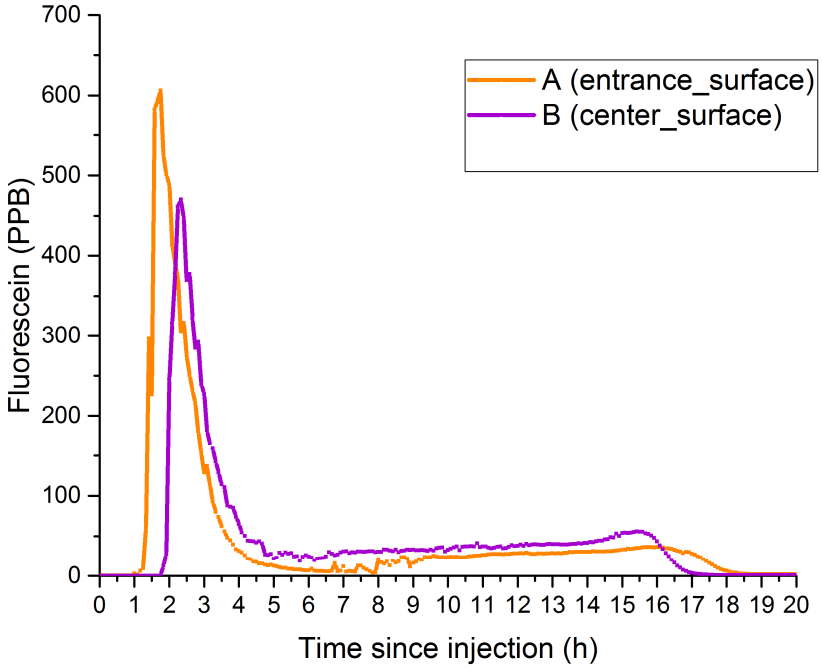

Figure 14. BTCs recorded by the two fluorimeters located at the surface of the TQF lake

At point C (Figure 15), the situation is very different. The tracer first reaches the fluorimeter at the bottom of the lake after nearly 5 h and the peak concentration there does not exceed 50 ppb. The BTC shows a rather wide and skewed shape indicating some dispersion compared to what happens at the surface. The peak time is about 20 h but the total transit time is very long: the concentration stops to drop after about 250 h where the concentration stays around 2.5 ppb that should be a background concentration. This long transit time is due to a long queue of recovery corresponding to retardation. This retardation could possibly originate from an effect of the dye exchange with immobile water zones within the lake and/or a sorption-desorption effect of the fluorescein on the important quantity of sediments present in the water and on the bottom of the lake.

4.2.3.4.b Observations at the PDV lake

An electrical conductivity profile was performed; this parameter stayed stable along the profile during the test (0.437 mS/cm). Regarding the concentration profiles (Figure 16), fluorescein is observed from the surface of the lake to the bottom, but a higher concentration zone is highlighted at a depth between 15 and 22 m (Figure 16). The maximum difference of concentration is observed between the bottom of the lake, where the recorded concentration is 1.5 ppb, and 16 m of depth where the concentration reached 3.5 ppb.

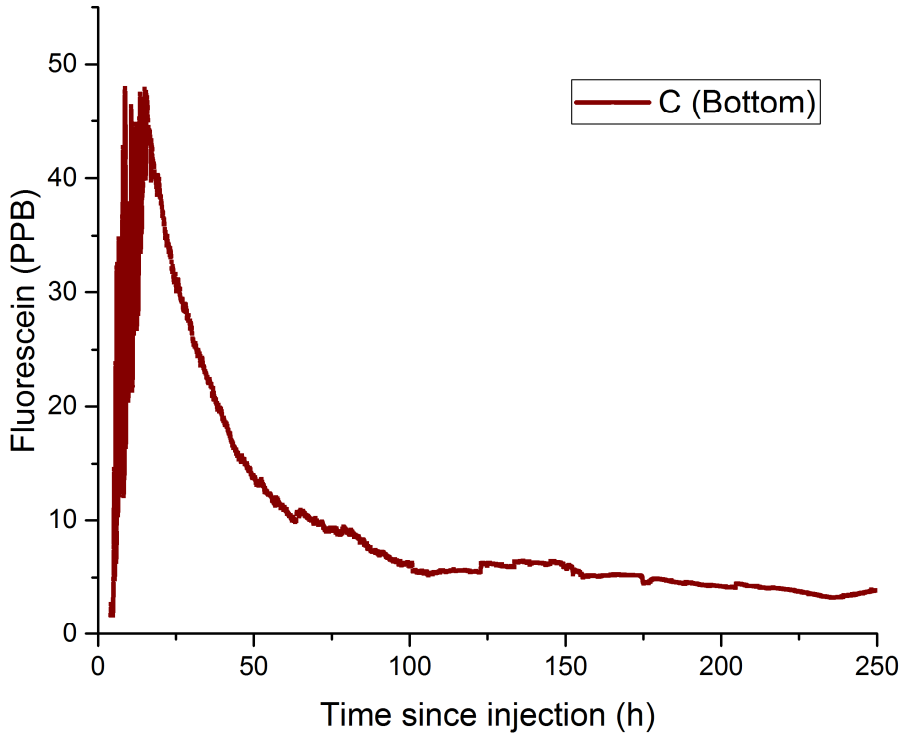

Figure 15. BTC observed at the bottom of the TQF lake (fluorimeter C)

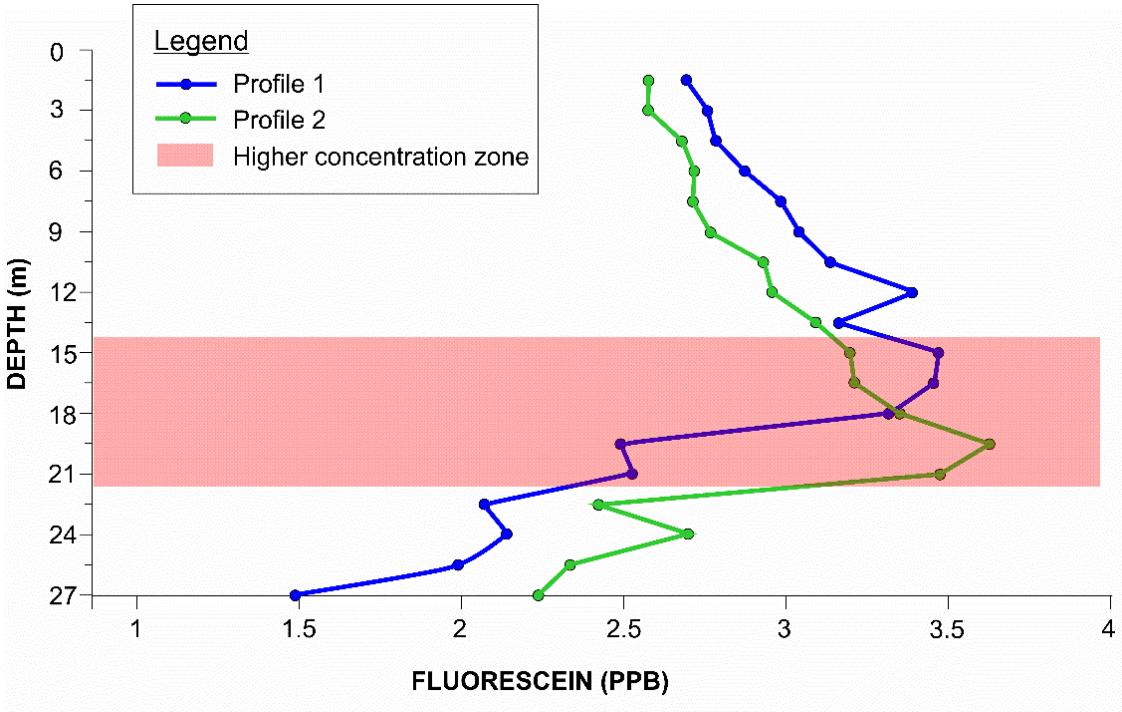

Figure 16. Concentration profile performed into the PDV lake during a tracer test

4.2.3.4.c Observations at the GDS

The discharge stayed steady during the test (Q_{Mean} of 8.5 l/s) except at the very end of the test (378 h after the injection) where a flood event occurs. Variable discharge is used for the recovery rate calculation.

A double-peaked BTC was recorded (Figure 17). Transport parameters are summarized in Table 9. The difference in the two peaks behavior is very well marked. The first peak reaches its maximum concentration (3.5 ppb) 71.1 h after the injection; it exhibits a narrow shape and seems affected by a limited dispersivity. The second peak, on the contrary, shows a very wide and flared shape with an important tailing. The C_{peak} (1.8 ppb) is reached only 231.7 h after the injection. The recovery rate is of 7.9 % only.

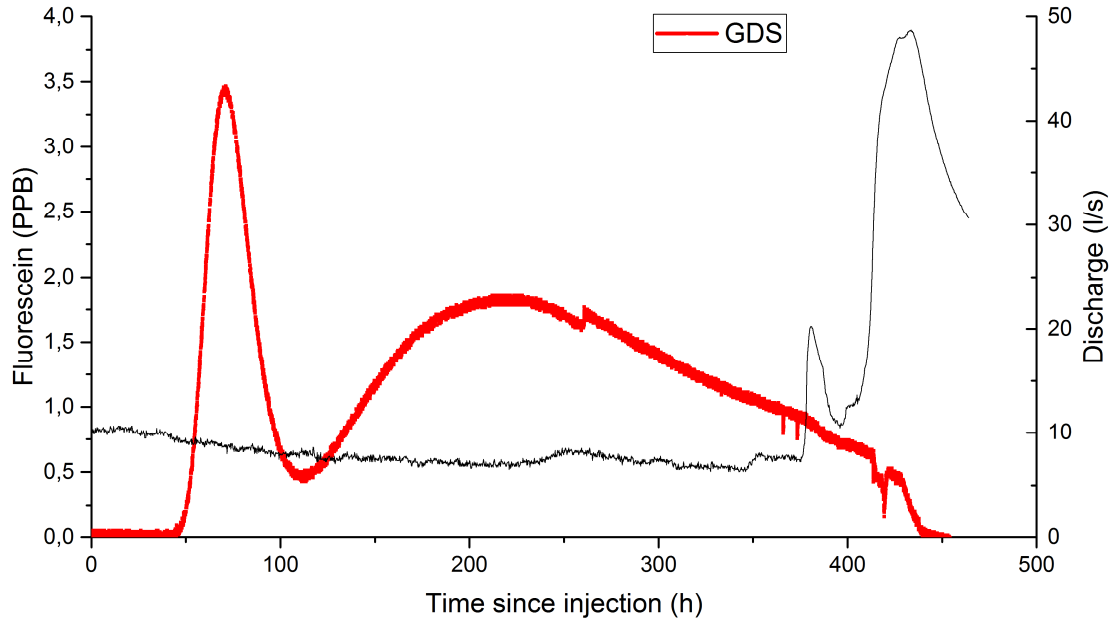

Figure 17. BTC observed at the GDSa, resulting from an injection at the CN swallow hole in May 2016 (Tracer test 4). The black line is the discharge evolution measured at the GDS.

Tracer test 4 May 2016	**1st A. (h)**	***V*max (m/h)**	***T*peak (h)**		***V*peak (m/h)**		***T*mean (h)**	***V*mean (m/h)**	***C*peak (ppb)**		**R.R. (%)**
			1st	**2nd**	**1st**	**2nd**			**1st**	**2nd**	
GDSa	47.9	15.9	71.1	231.7	10.7	3.3	221.6	3.4	3.5	1.8	7.9

Table 9. Main transport parameters, deduced from the BTC exposed in Figure 17.

4.2.3.5 Tracer test 5

The test, perfomed between the 23rd of September and the 18th of October 2016, consisted in an injection of 200 g of fluorescein at the CN swallow hole. A sampling device (Fluo-G) was placed at the GDS cave only. The flow conditions for this tracer test are not well defined. Indeed, no gauging was performed on the day of the injection and unfortunately, due to probe dysfunction, the discharge data at the GDS are not available for this period. However, one can estimate the flow conditions stability by looking at the discharge data of the surface River Lesse for that period (Figure 18). The mean discharge in the River Lesse, calculated on the duration of the tracer test, was 2.4 m^3/s. By comparing other data with similar discharge in the surface river, the mean discharge value at the GDS could be estimated around 3 l/s for this tracer test.

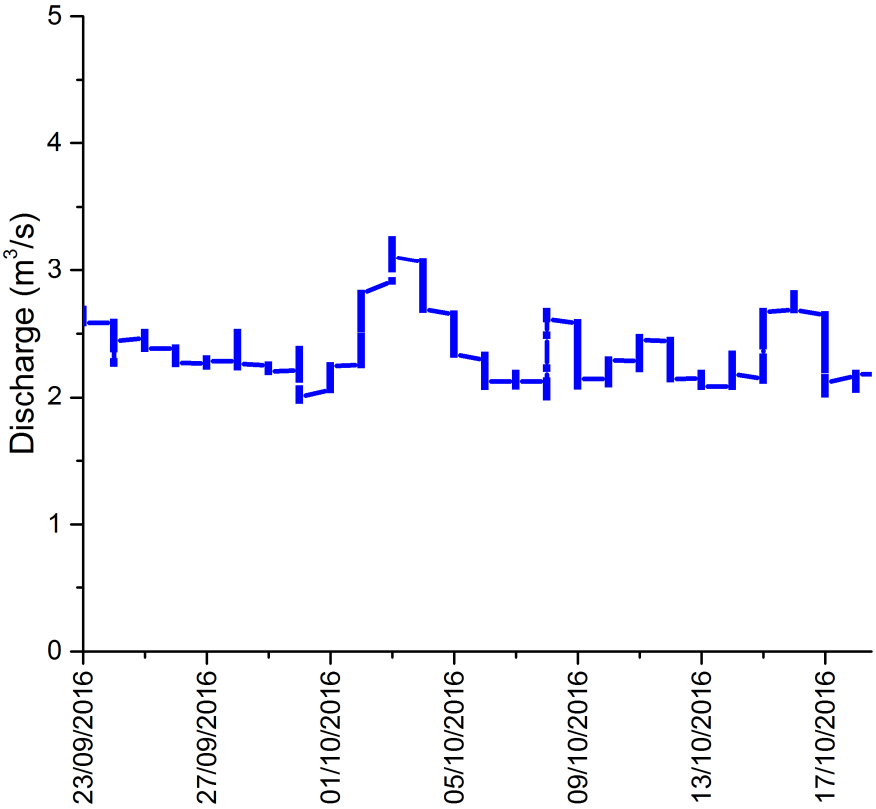

Figure 18. Discharge data recorded at the Gendron station in the surface River Lesse. The conditions are stable for that period corresponding to the duration of tracer test 5. A small flood is recorded around the 2nd of October.

Figure 19 shows a curve that seems single-peaked but with a very strong and long tailing effect. The transport generating the peak is however rather quick: 1st A. is 50.7 h and T_{peak} is 90h (Table 10). When considering an estimated mean discharge of 3 l/s, the recovery rate reaches 7.5 %. However, the recovery being not completed after 600 h (1.3 PPB remaining when the fluorimeter was taken off), this recovery rate is a minimum value. As for the

QTRACER2 parameters, they are presented in Table 11. Due to the very long tail observed in the curve, the dispersivity calculation is very high (150 m) and Pe (5.05) and Re (1578) are very low. Nevertheless, the transport of the main tracer cloud is rather quick (V_{max}: 15 m/h and V_{mod}: 8.2 m/h).

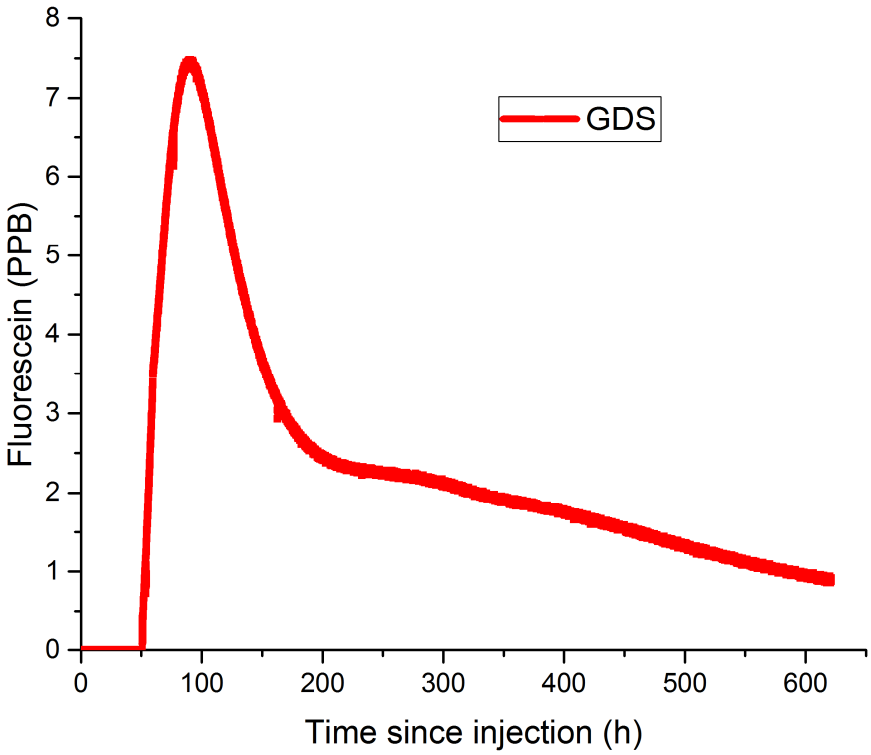

Figure 19. BTCs observed at the GDS resulting from the injection made in September 2016 at the CN swallow hole

Tracer test 5	1st A. (h)	T_{peak} (h)	T_{mean} (h)	V_{max} (m/h)	V_{mean} (m/h)	C_{peak} (ppb)	R.R. (%)
GDS	50.7	89.9	249.0	15.0	3.0	7.47	7.5

Table 10. Main transport parameters deduced from the BCT observed at the GDS

Tracer test 5	D_L (m^2/s)	α_L (m)	Cs (m^2)	Pe	Re
GDS	0.12	150	3.5	5.05	1578

Table 11. Parameters calculated with the QTRACER2 program

4.2.3.6 Tracer test 6

A new injection was performed at the CN swallow hole (200 g of fluorescein) in November 2016 in very low flow conditions. The mean discharge at the GDS is estimated at 2.1 l/s. Due to a dysfunction of the fluorimeter (Fluo-G), the first 50h of the test are missing (Figure 20). The first arrival (Table 12) can however be supposed around 48 h after the injection, and so the maximum velocity at 15.8 m/h. The T_{peak} is 81 h for a C_{peak} at 6.3 ppb. The concentration of tracer was still 1.3 ppb when the fluorimeter was taken off (550 h after the injection). The calculated recovery rate (4.8 %) is then a minimum value. As observed for tracer test 5, the tailing effect is very important. In consequence the dispersivity calculated by QTRACER2 (Table 13) is high: 157 m, and Re (1201) and Pe (4.8) show domination of the dispersion. The important oscillations observed in the tailing are due to the change of position of the fluorimeter Fluo-G (Poulain A., personal communication).

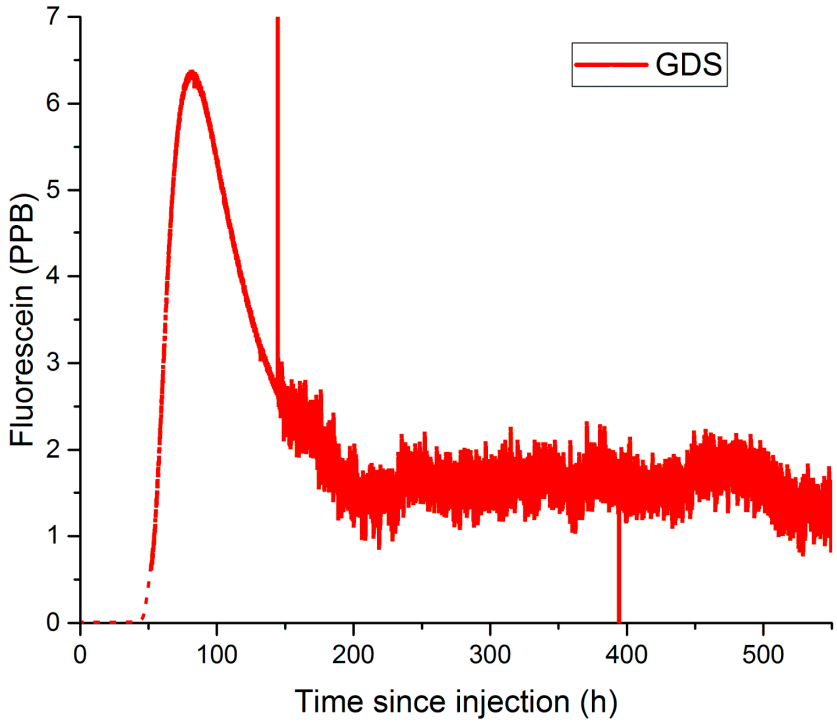

Figure 20. BTC observed at the GDS resulting from an injection made in November 2016 at the CN swallow hole. The data are missing in the beginning of the test (dashed line).

Tracer test 6	1st A. (h)	V_{max} (m/h)	T_{peak} (h)	V_{peak} (m/h)	T_{mean} (h)	V_{mean} (m/h)	C_{peak} (ppb)	R.R. (%)
GDS	~48	~15.8	81.0	9.4	300.1	2.5	6.3	4.8

Table 12. Main transport parameters for tracer test 6. First arrival was not recorded but is supposed around 48 h.

Tracer test 6	D_L (m^2/s)	a_L (m)	Cs (m^2)	Pe	Re
GDS	0.11	157	2.9	4.8	1201

Table 13. Parameters calculated with the QTRACER2 program.

4.2.3.7 Tracer test 7

This test consisted in an injection of 200 g of Fluorescein at the CN swallow hole on the 23rd of February, 2017. Fluorimeters (Fluo-G) were placed at the SEP cave (in the river section) and at the GDS cave. The discharge, measured at the GDS was 14 l/s on the day of injection. The mean discharge at the GDS for the test duration is 19.5 l/s indicating unsteady conditions during the test. Due to the fluorimeter dysfunction, no data could be recorded at the GDS cave. Figure 21 exposes the BTC recorded at the Sepulture cave, where the fluorimeter is located 550 m downstream the injection point.

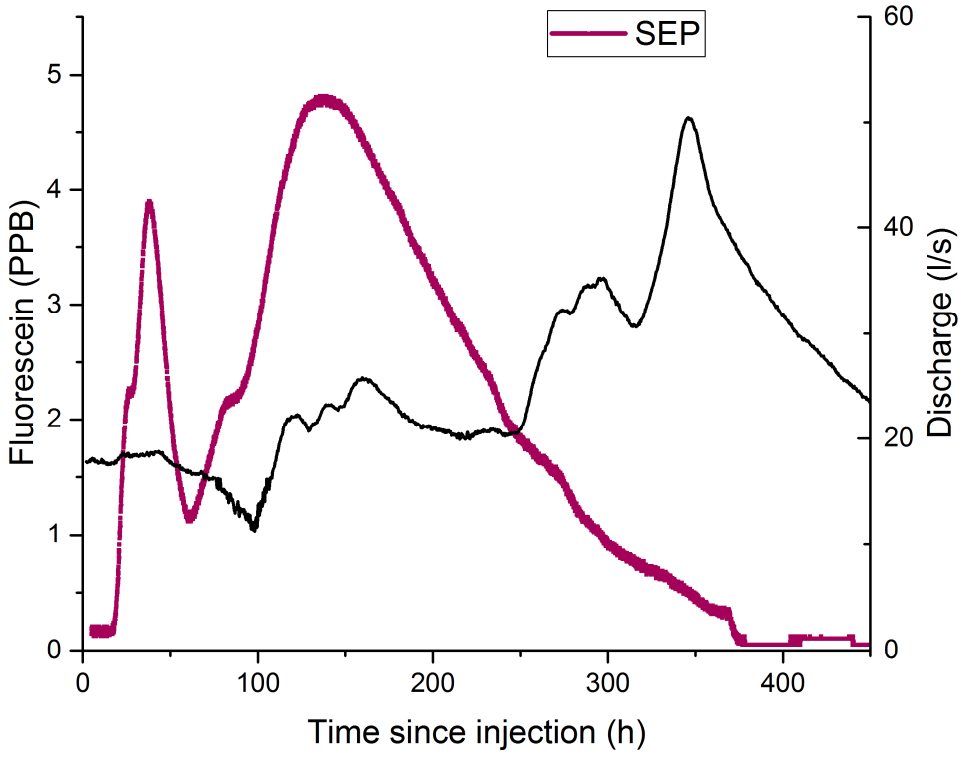

Figure 21. BTC observed at the Sepulture cave in March 2017, resulting from an injection at the CN swallow hole in February 2017. The black curve is the discharge evolution during the test.

The BTC observed at the SEP cave is a double-peaked BTC. Again, different behavior are illustrated in the two peaks: a first quick and narrow peak and a second slower and wider peak. The small steps that can be observed in the curves have probably to be imputed to the

unsteady flow conditions. Table 14 gathers the main transport parameters for this curve. The calculations confirm a very quick velocity of the first peak (first arrival after only 16.5 h and T_{peak} of 38.2 h), and the much slower behavior of the second peak (T_{peak} of 138.1 h). The recovery is low (29.4 %), indicating, once more, a loss of tracer upstream.

Tracer test 7 February 2017	**1st A. (h)**	***V*max (m/h)**	***T*peak (h)**		***V*peak (m/h)**		***T*mean (h)**	***V*mean (m/h)**	***C*peak (ppb)**		**R.R. (%)**
			1st	**2nd**	**1st**	**2nd**			**1st**	**2nd**	
SEP	16.5	33.3	38.2	138.1	14.4	4.0	301	2.5	3.9	4.8	29.4

Table 14. Transport parameters for the BTC observed at the Sepulture cave in March 2017.

4.2.3.8 Tracer test 8

A very last injection (200 g Fluorescein) at the CN swallow hole was performed in April 2018. Each site was equipped with a fluorimeter (Fluo-G), including the Sepulture cave. The discharge could be measured at the TQF river, and at the GDS the day of the injection. The discharge is similar at the TQF and the GDS (9 l/s and 8.7 l/s respectively). However, the mean discharge calculated on the duration of the test at the GDS is 14.7 l/s. Indeed, the test has been made during a flood event that has risen the discharge for several weeks. Given that the tracer transits within 4 h after the injection at the TQF, the discharge considered for the TQF is 9 l/s, as it was measured just before the injection. The recovery rates in the other sites are calculated on basis of the variable discharges measured at the GDS. It has to be noticed that the sampling station of the TQF was located more upstream than in the previous tests; i.e. at 70 m downstream the swallow hole instead of 150 m.

Figure 22 presents the BTCs observed at different sites. Transport parameters of these curves are shown in Table 15. The dye at the TQF arrives very quickly (0.4 h) and the sampled BTC is very narrow with almost no retardation. The recovery rate is 19.5 % only. Downstream, the BTC sampled at the surface of the PDV lake shows a rather steep rising branch but a slower decrease that shows an important tailing effect. The curve observed at the Sepulture, that is only 240 m downstream the PDV lake, is double-peaked. The first arrival at the Sepulture (18.9 h) is nearly concomitant with the first arrival at the surface of the PDV (18.2 h). The first peak has a lower C_{peak} (3.1 ppb) than the second one (5.0 ppb). Its shape is narrower than the second peak whose submit is wide. The first peak tends to attenuate downstream-ward, so that it is completely merged with the second peak at the TDL (where the small step observed in the rising limb is probably a reminiscence of the first peak). The recovery at the SEP is 17.4 %, 19.6 % at the GDS and 24.8 % at the TDL. There is no reason for having a higher recovery at the TDL. This probably due to a wrong estimation of the discharge at the TDL (based here on the GDS discharge).

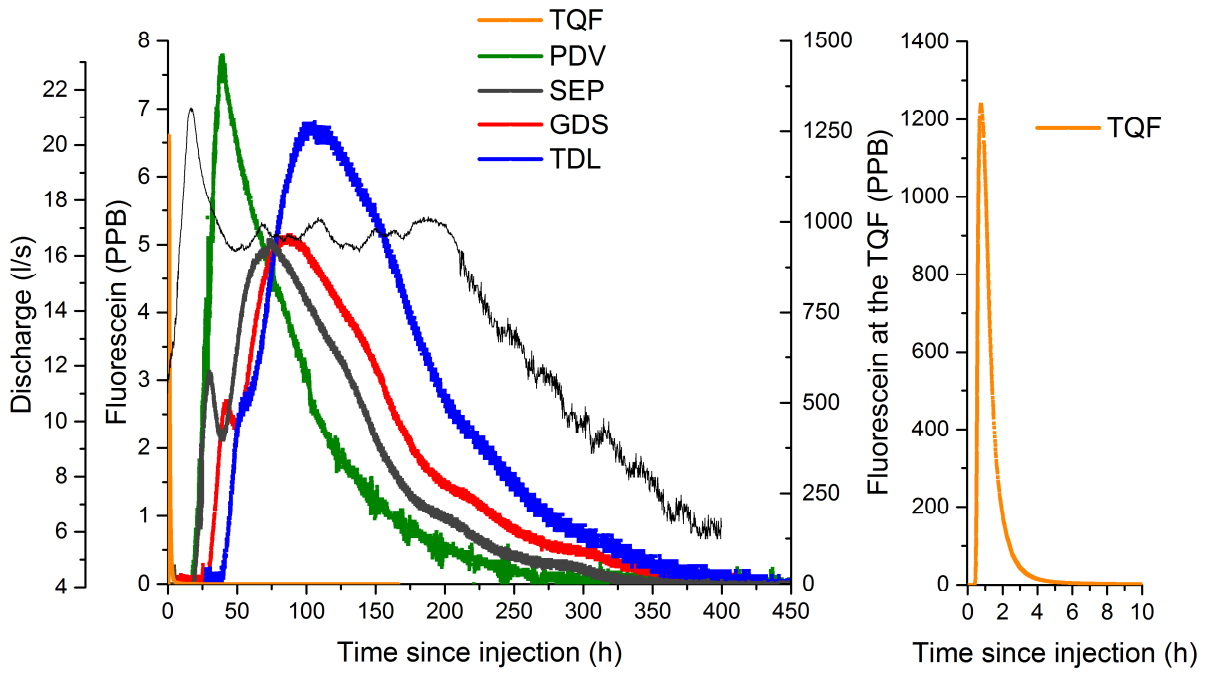

Figure 22. BTCs observed in different sites and resulting from an injection (200 g Fluorescein) at the swallow hole in April 2018.

Tracer test 8 **April 2018**	**1st A.** **(h)**	**V_{max}** **(m/h)**	**T_{peak}** **(h)**		**V_{peak} (m/h)**		**T_{mean}** **(h)**	**V_{mean}** **(m/h)**	**C_{peak}** **(ppb)**		**R.R.** **(%)**
TQF	0.4	175	0.8		87.5		1.8	39.6	1220		19.5
PDV	18.2	16.5	38.9		7.7		122.9	2.4	7.8		-
SEP	18.9	28.6	**1st**	**2nd**	**1st**	**2nd**	110.7	4.9	**1st**	**2nd**	17.4
			29.4	74.1	18.4	7.3			3.1	5.0	
GDSa	27.8	27.3	**1st**	**2nd**	**1st**	**2nd**	230.4	3.3	**1st**	**2nd**	19.6
			40.7	86.3	18.7	8.8			2.7	5.1	
TDL	40.6	28.8	102.0		11.5		149.6	7.8	6.7		24.8

Table 15. Main transport parameters for tracer test 8

QTRACER2 (Table 16) was run on the TQF BTC (Q: 9l/s) and on the PDV and TDL curves (Q: 14.7 l/s). The TQF curve shows here a greater dispersion than previously, and, in consequence, a low Pe (8.37). Re is high (9842) confirming a turbulent transport. The parameters calculated for the PDV confirm a dispersive behavior (low Pe and Re) and a very wide cross-section (21.7 m^2). Finely, at the TDL, the curve is very wide due to the merging of the first and the second peak. In consequence the dispersion is high (0.26 m^2/s) and Pe is low (9.64). QTRACER2 estimates a cross-section of 6.7 m^2, which actually represents a mean section for all the conduits between the CN swallow hole and the TDL resurgence.

Tracer test 8 **April 2018**		D_L **(m^2/s)**	a_L **(m)**	**Cs** **(m^2)**	**Pe**	**Re**
TQF Q = 9 l/s		0.092	8.37	0.82	8.37	9842
Q_{Mean}= 14.7 l/s	PDV	0.087	129.4	21.7	2.32	3125
	TDL	0.26	121.2	6.7	9.64	5593

Table 16. Parameters calculated with the QTRACER2 program

4.2.3.9 Brief summary

The seven tests conducted in the Furfooz karst system by dye injection at the CN swallow hole have shown contrasted results. Tests 1, 2, 3 and 4, made in mean discharge conditions of respectively 20, 11, 6 and 8 l/s resulted in the detection of a double-peaked BTC at the GDS sampling site (and at the TDL). In these tests, the two peaks are well distinct and display different shape. The first peak results from a rather quick transport and exhibits a narrow shape, in comparison to the wider shape of the second peak that is transported through a much slower flow. Tracer test 7 shows that this double-peaked recovery existsalready at the Sepulture cave, that is located only 240 m downstream the visible part of the PDV lake. Tests 5 and 6, performed at very low discharge (3 and 2.1 l/s respectively) result in a single-peaked BTC that shows a very strong tailing. The single peak of these BTCs has a rather quick T_{peak} and exhibits a narrow shape – apart from the long tailing. Finally, tracer test 8 (mean discharge of 9 l/s) produces a double-peaked BTC but with a first peak that is nearly merged with the second one.

Figure 23 gives an overview of the hydrological conditions in which each tracer test was performed, in comparison with the discharge evolution in the underground river (GDS). Tracer tests 5 and 6 are the only ones that were performed in very low flow period of the Lesse River, along with very low discharges in the underground river.

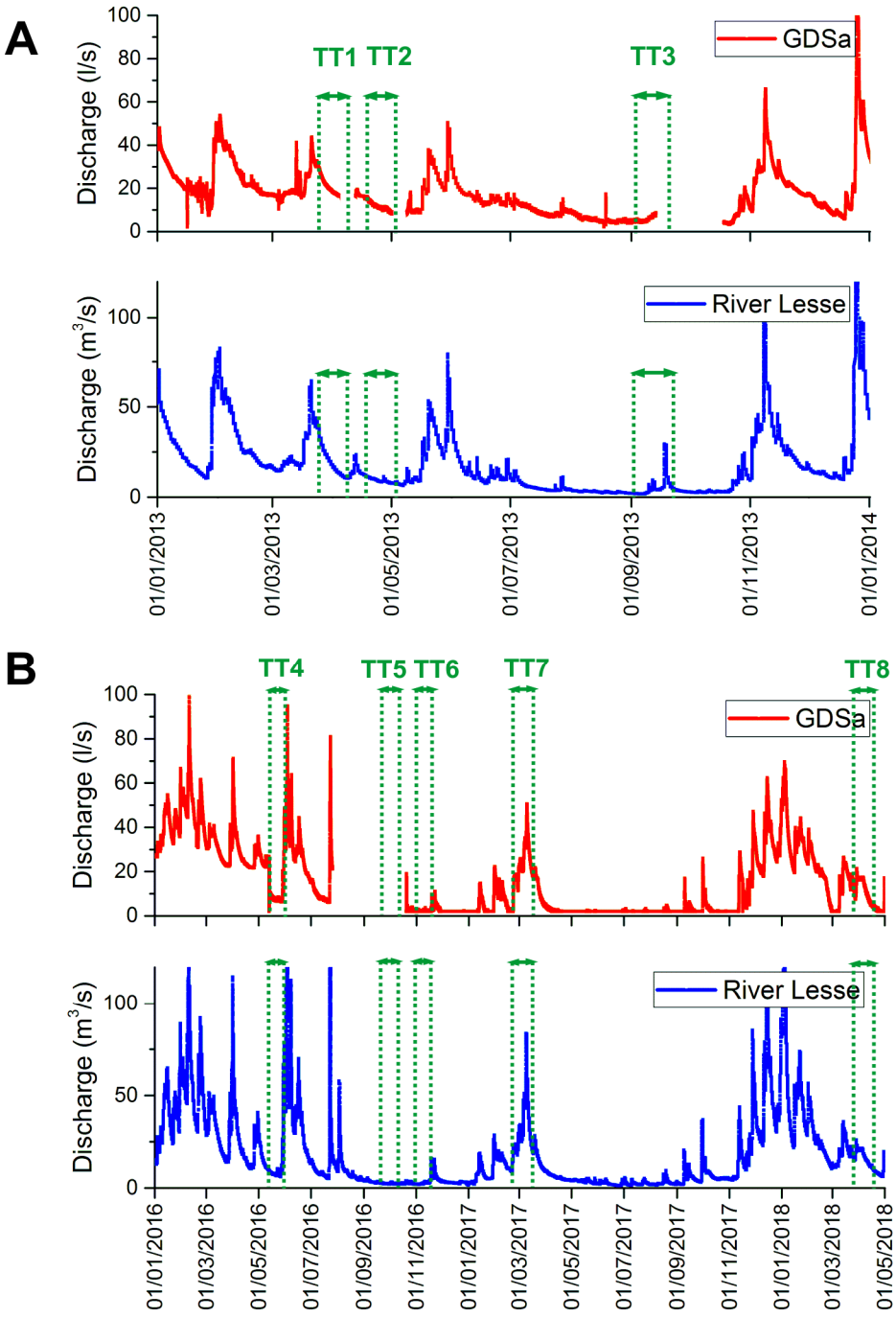

Figure 23. Tracer tests 1 to 8 related to the discharge conditions of the Lesse River and of the underground river at the GDS cave. [A] exposes the discharge evolution in 2013 (tracer tests 1, 2 and 3); [B] presents the discharge data from 2016 to 2018 (tracer tests 4 to 8).

4.2.4 Injections at the TQF river

Two injections of 200 g of fluorescein, made at different times, were performed at the TQF river. More precisely, these instantaneous injections were made at the start of the underground river in the TQF cave, so about 70 m downstream the CN swallow hole.

4.2.4.1 Tracer test 9

The test was performed in July 2016. A fluorimeter (Fluo-G) was placed at the GDSa only. No gauging was performed, so the discharge conditions are evaluated on the discharges measured through the hydrograph at the GDS. The discharge is steady around 7 l/s during the first 200 h of the test and then it raises suddenly to 80 l/s due to a flood. On Figure 24, that presents the BTC at the GDS, it can be seen that this sudden flood affects greatly the recording of the recovery. The first arrival of the tracer is detected about 70 h after the injection and the maximum concentration is reached out 176 h after the injection. The flood starts just after the C_{peak} and, from there, no good interpretation of the BTC can be made. Indeed, from the start of the flood, the fluorimeter encountered a technical problem in the data recording due probably to extreme dilution of the tracer and turbidity of the water. When the discharge decreases under 25 l/s after the flood peak, the concentration data could have been recorded properly but the link with the BTC before the flood cannot be extrapolated.

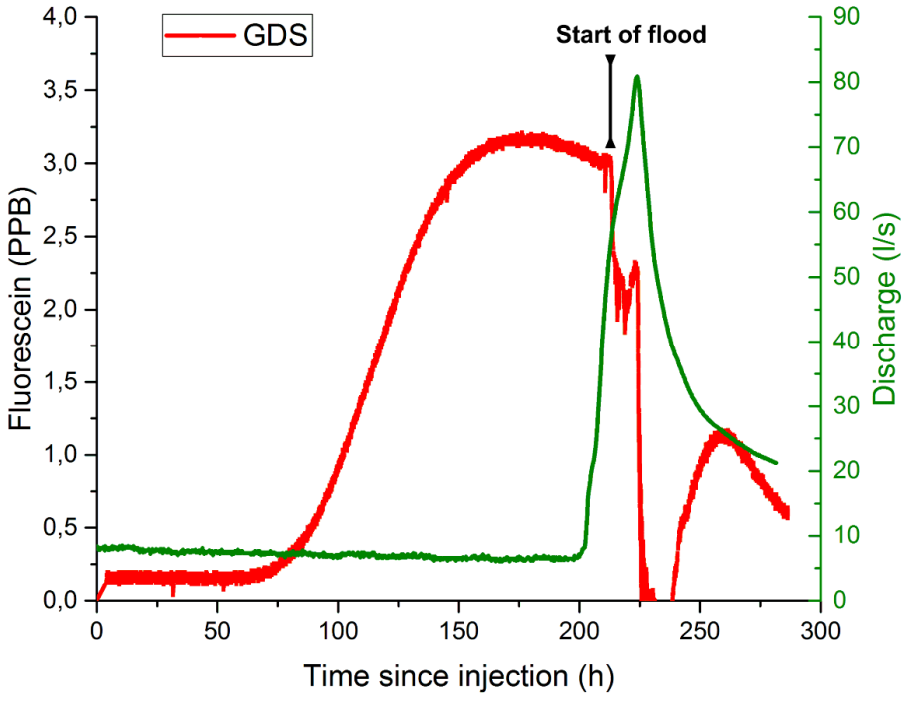

Figure 24. Single peaked BTC observed at the GDS, from an injection made at the TQF river (July 2016). A flood event occurs 200 h after the injection making the interpretation of this test uncertain.

4.2.4.2 Tracer test 10

The injection was performed on the 6th of September 2016. Gauging measurements were performed on the same day at the CN swallow hole (2.9 l/s), at the TQF (5.6 l/s) and at the GDSa (6.5 l/s). Due to a probe dysfunction during this period, the information of the variability of the discharge is not available. However, the surface river conditions indicate a regular decrease of the discharge for this period. In comparing other data with similar discharge in the surface river, the mean discharge value at the GDS could be estimated around 3 l/s for this test.

The obtained BTC (Fluo-G) is shown in Figure 25. The observed curve is inherited from a very slow transport. Indeed, the first arrival is at 171.8 h and the T_{peak} is 373.5 h. The recovery was not completed when the fluorimeter was taken off after 400 h, so that the descending limb of the BTC was not sampled. The interpretation of this curve is therefore very limited.

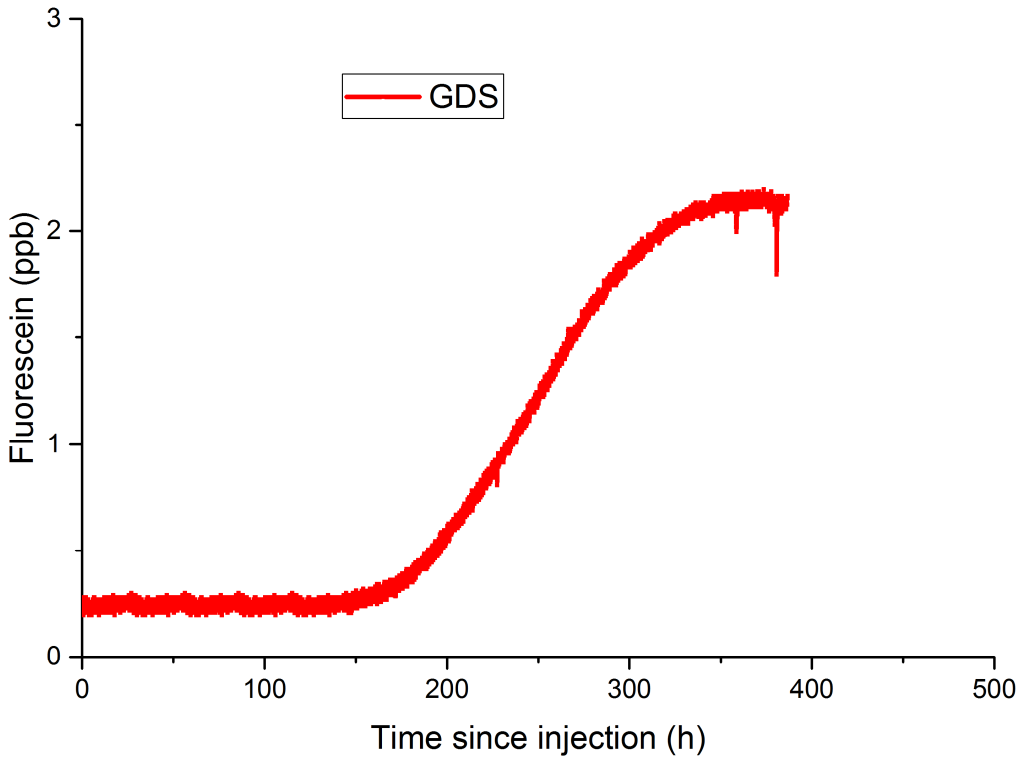

Figure 25. BTCs observed at the GDS resulting from two injections made in September 2016: one at the swallow hole and one at the TQF river

4.2.5 Injections at the PDV lake

Two Injections were performed at the surface of the PDV lake (injection point PDV1 in Figure 4), that is close to the bank of the lake. Fluorimeters (GGUN-FL 30) were set at the GDS and the TDL sites.

4.2.5.1 Tracer tests 11 and 12

The two tests were realized in different flow conditions. Tracer test 11 was realized in March 2013 under flow conditions characterized by a mean discharge of 19 l/s. The test 12 was performed in September 2013 in lower flow conditions as the mean discharge is estimated at 6 l/s. Figure 26 shows the BTCs obtained from these injections. No data were obtained at the GDS in March 2013 due to a dysfunction of the fluorimeter; so the only BTC obtained for this injection is at the TDL site. The BTCs are single-peaked and show some skewness due to retardation effect. The shapes of the BTC are contrasted in regard with the discharge conditions, as are the transport parameters (Table 17 and Table 18). The transport velocities are of course much slower for tracer test 12 due to the lower discharge. The recovery rates are also very different: 57.5 % at the TDL in tracer test 11 and only 3.5 % in test 12. It seems so that the flow conditions influence the recovery and so the loss of tracer. This important loss of tracer could be linked to the passage of the tracer through the lake and its dead zones. This trapping of the dye into dead zones could be more important in low flow due to the lack of advection of the flow transporting the tracer. This low advection is indeed reflected in the low Re calculated for tracer test 12. Pe is rather low in both tests; this due to the high dispersion calculated, even in test 11. The high dispersivity that characterizes the tracer cloud in both tests is probably brought by the crossing of the PDV lake.

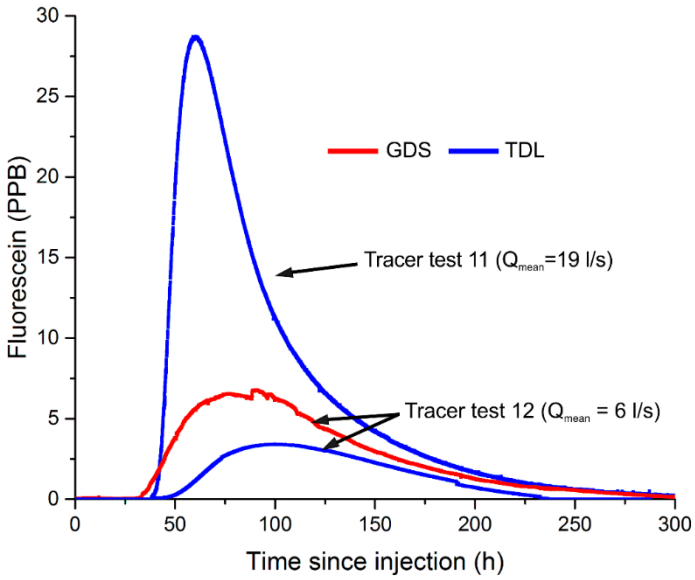

Figure 26. BTCs observed at the GDS and TDL sampling sites, resulting from injections at the PDV in March (test 11) and September (test 12) 2013. Note that there is no BTC at the GDS for tracer test 10 due to a dysfunction of the fluorimeter.

Tracer tests 11 & 12		1st A. (h)	V_{max} (m/h)	T_{peak} (h)	V_{peak} (m/h)	T_{mean} (h)	V_{mean} (m/h)	C_{peak} (ppb)	R.R. (%)
Tracer test 11	TDL	27.6	31.6	49.2	23.8	85.1	10.2	28.6	57.5
Tracer test 12	GDSa	33.0	14.2	76.2	6.2	104.0	4.4	6.5	6.3
	TDL	39.7	21.9	99.9	8.7	122.8	7.1	3.4	3.5

Table 17. Main transport parameters of the BTCs resulting from an injection at the PDV site.

Tracer tests 11 & 12		D_L (m^2/s)	a_L (m)	Cs (m^2)	Pe	Re
Tracer test 11	TDL	0.18	64.2	6.8	13.5	7306
Tracer test 12	GDSa	0.045	36.6	4.9	12.5	2682
	TDL	0.088	44.9	3.0	19.4	3400

Table 18. Estimation of some hydrodynamic parameters calculated by QTRACER2

4.2.6 Injections at the GDS site

4.2.6.1 Tracer tests 13 and 14

Two injections were performed (in March and September 2013) at the GDS cave (20 g of Fluorescein), downstream the two resurgences (GDSa and GDSb). The fluorimeter (GGUN-FL 30) was placed at the TDL site, located 410 m downstream the GDS. Tracer test 13 was realized in high flow conditions (Q_{Mean} 21.7 l/s); tracer test 14 in low flow (Q_{Mean} 6l/s).

The obtained BTCs (Figure 27) are both single-peaked but show different shapes, indicating a strong influence of the discharge. Some retardation is observed through the long tailing of both curves. In Table 19 and Table 20, it appears that the transport is rather fast (V_{max} of 98.4 and 44.3 m/h, depending on the discharge) in conduits sizing a few square meters. This Cs estimation (3.1 and 1.6 m^2) seems rather big regarding the flow sections that are observed on the field (about 0.8 m^2 to 0.2 m^2). This could be linked to the presence of some pools between the GDS and the TDL that could slow down the transport and increase the mean cross section estimation. These siphons could also explain the important dispersivity (95.9 and 36.7 m) estimated with QTRACER2, as well as the long tailing (retardation caused by immobile water

zones in the siphons). A high dispersion combined with a short length of transport (410 m), explains the very low value computed for Pe (4.3 and 10.4). The recovery rate is very low for tracer test 14 (15.9 %) when the discharge was very low. This could be linked to a wrong estimation of the discharge (discharge at the TDL assimilated to the discharge at the GDS) and probably to adsorption or trapping of the dye (into the siphons for example, or any anfractuosity or pool) that would finally be so diluted that it would not be detected by the fluorimeter.

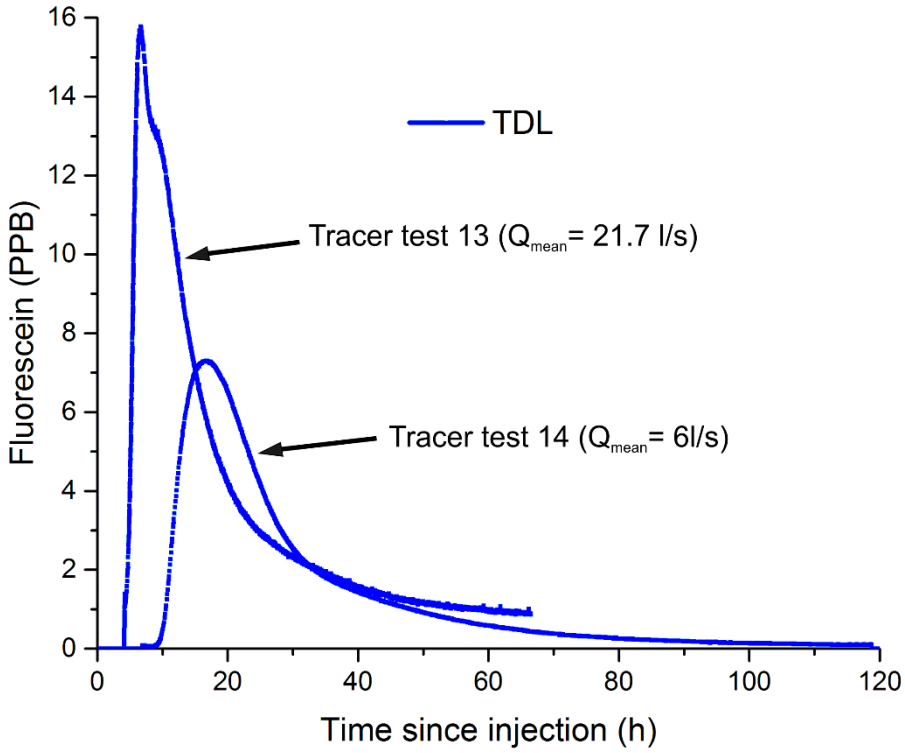

Figure 27. BTCs obtained at the TDL sampling site resulting from an injection at the GDS site.

Tracer tests		1st A. (h)	V_{max} (m/h)	T_{peak} (h)	V_{peak} (m/h)	T_{mean} (h)	V_{mean} (m/h)	C_{peak} (ppb)	R.R. (%)
Tracer test 13	TDL	98.4	4.2	6.7	61.2	16.1	25.4	14.9	66.8
Tracer test 14	TDL	44.3	9.25	16.7	24.5	30.5	13.4	7.3	15.9

Table 19. Main transport parameters of the BTCs resulting from injections at the GDS site

Tracer tests		D_L (m^2/s)	a_L (m)	Cs (m^2)	Pe	Re
Tracer test 13	TDL	0.68	95.9	3.1	4.3	12253
Tracer test 14	TDL	0.15	36.7	1.6	10.4	4683

Table 20. Estimation of some hydrodynamic parameters calculated by QTRACER2

4.2.7 Injection at the Sebia (tracer test 15)

In November 2013, an injection was performed in the Sebia (tracer test 15) that is a small stream starting in the village of Furfooz and flowing SW to join the Lesse. On its path, the Sebia runs along the PDV site. The sharp valley in which this valley flows is often dry on its downstream course. A series of sinkhole are easily observed on the bed of the Sebia, most of them being located just east of the PDV. The injection of 100 g of sulforhodamine B was performed in the sinkhole that was located the most downstream (Figure 4), at about 480 m of the GDS cave. The mean discharge computed at the GDS for the duration of the test is 18.8 l/s.

Fluorimeters (GGUN-FL 30) were placed at the PDV and at the GDSa and the GDSb. Results are presented in Figure 28, Table 21 and Table 22. Due to a fluorimeter breakdown, no data could be gathered at the PDV. No fluorescent signal was detected by the fluorimeter placed at GDSb. At GDSa a single-peaked curve was sampled. It shows a rather dispersive behavior with a skewed shape. The velocities are rather low (V_{mean} 5.2 m/h). The C_{peak} (1.5 ppb) and the recovery (7.8 %) are very low. QTRACER2 estimates an important cross section (12.6 m^2), a low Pe (12.9) and medium Re (5149) indicating a dispersive but rather turbulent transport. From these parameters and given the location of the injection point, it can be supposed that the BTC observed at the GDS has crossed the PDV lake upstream. The very low recovery are probably due to the loss of tracer into the lake. Some of it could also be diverted to another route that could start between the Sebia and the PDV but, so far, there is no information about it.

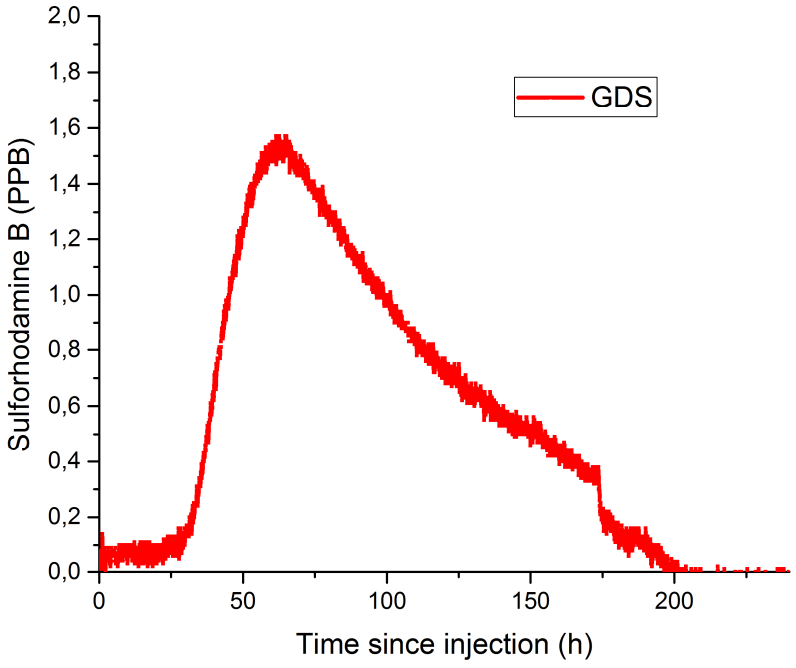

Figure 28. BTC observed at the GDSa sampling site, resulting from an injection at the Sebia site.

Tracer test 15	1st A. (h)	V_{max} (m/h)	T_{peak} (h)	V_{peak} (m/h)	T_{mean} (h)	V_{mean} (m/h)	C_{peak} (ppb)	R.R. (%)
GDS	28.4	16.9	61.5	7.8	91.1	5.2	1.5	7.8

Table 21. Main transport parameters for the BTC resulting from an injection at the Sebia in November 2013.

Tracer test 15	D_L (m^2/s)	a_L (m)	Cs (m^2)	Pe	Re
GDS	0.05	36.9	12.6	12.9	5149

Table 22. QTRACER parameters for the BTC in Figure 28.

4.3 Discussion

The tracer tests presented in the previous sections have highlighted a complex functioning of the Furfooz karst system. Several injections, at different points and in different flow and piezometric conditions were performed and some contrasted results were obtained. The different tests allow to characterize the different segments of the heterogeneous system of Furfooz. Figure 29 summarizes every injection points and each type of BTC recorded from different tracer tests.

The BTCs sampled in the TQF river show an advective behavior with limited dispersivity. The calculated velocities, however, imply cross sections much bigger than what is observed on the field in the TQF cave. As discussed before, this should probably originates from the unknown zone just downstream the CN swallow hole. It could indicate that the length of this first segment (70 m if a straight line is supposed) is under-estimated or that the transport is slowed down by the presence of low transmissivity zones. The recovery rates of the different BTCs sampled at the TQF river are very contrasted. Tracer test 1, done in high discharge conditions, brings out 100 % of the tracer through this point. In tracer tests 3 (sulforhodamine B) and 8 (fluorescein), done in mean discharge conditions of, respectively 6 l/s and 9 l/s, the recoveries are much lower (33.8 % and 21.4 %). These low recoveries at only 150 m of the injection point are surprising. The possibility of a bifurcated path that could be taken by the tracer upstream this point is unlikely. Indeed, the occasional gaugings (chapter 3, p. 72) have shown that there is no loss of water between the swallow hole and the underground river; on the contrary, there is more water in the underground river than what enters the swallow hole. A possible explanation of the low recovery is a strong adsorption of the tracer on suspended matters or the mud covering the conduits. The TQF is indeed a very muddy network. The tracer could indeed be more sensitive to sorption at low flow conditions (Perrin & Luetscher, 2008; Talbot & Henry, 1968), though this is mainly true for the sulforhodamine B, fluorescein being known as a more conservative tracer (Geyer et al., 2007). The low recovery rates could also be linked to the nature of the segment upstream the TQF river. Low transmissivity zones were evoked to explain the large cross-section estimation; this could also explain the trapping and loss of tracer in dead zones.

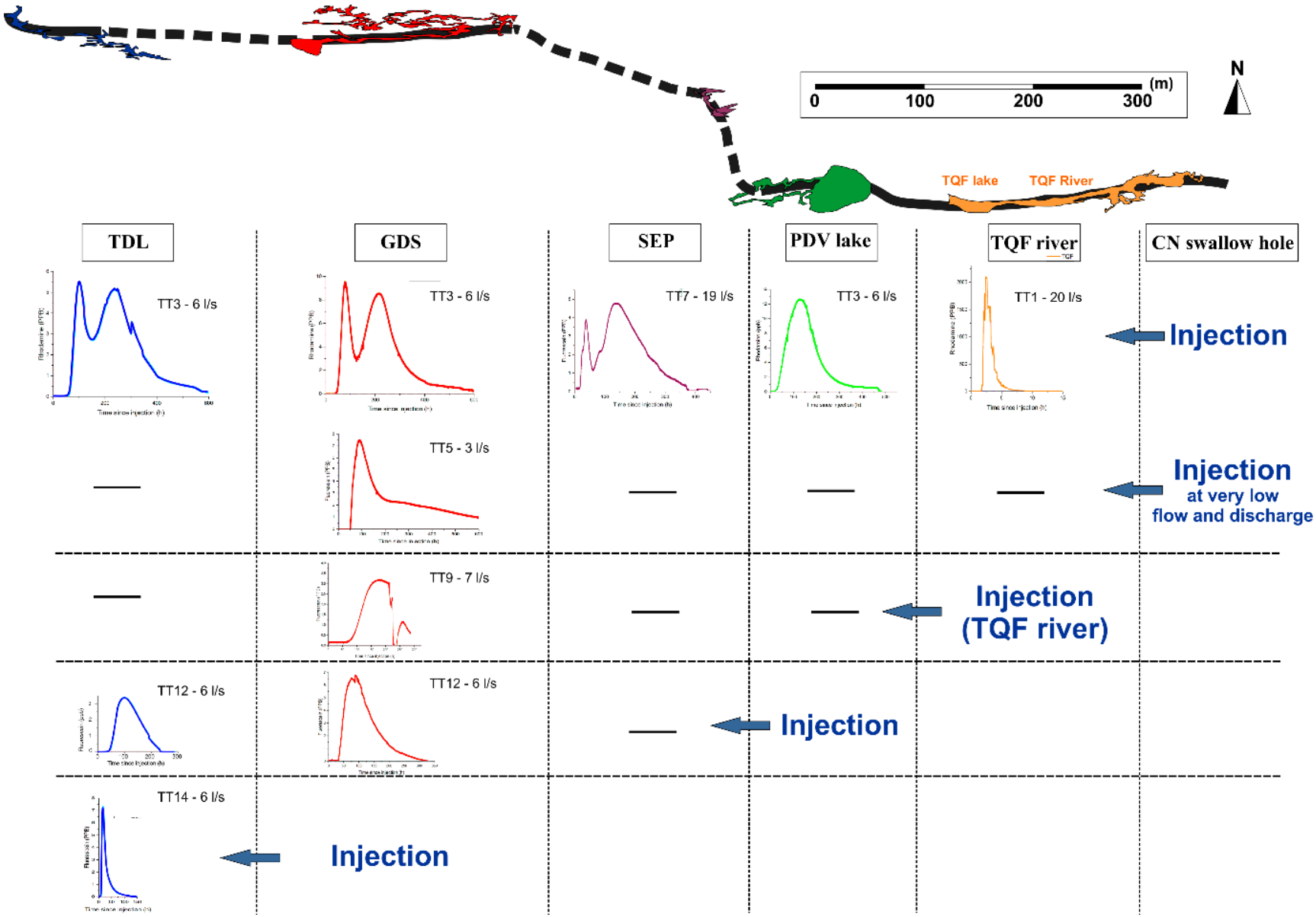

Figure 29. Summary of the different injections and different types of BTC observed along the tracing system. [TT] : tracer tes

Downstream the TQF river, starts the lakes zone. The physical characterization of this zone is difficult as the lakes were only explored through dives made in difficult conditions. The investigations led within the lakes during tracer test 4 have, however, underlined the influence of the lakes on the tracer transport. It has been shown that the tracer distribution is not homogeneous into these big volumes of water. In the TQF lake, quick and narrow BTCs are sampled at the surface, probably under the influence of the advective influx coming from the TQF river; while important dispersion affects the tracer at the bottom. The PDV lake shows also contrasted behavior of the tracer. Higher concentration zone was highlighted in depth (probably at the depth where comes the flow from the TQF), while the BTCs sampled at the surface (tracer test 1, 2 and 3) are dominated by a slow and dispersive transport of the tracer. Retardation in the form of strong tailing characterizes also these curves. It was also shown that the surface of the PDV is probably located out of the main path and reflects the dispersion effect through the lake. The injections performed directly into the PDV lake or at the Sebia, show also the important dispersion and retardation brought by the crossing of the lake.

The segment between the GDS and the TDL resurgence characterized by tracer tests 12 and 13 shows a rather quick transport through narrow curves that are, however, affected by strong tailings. Solute transport through this segment could be affected by the presence of some siphons that tend to slow down the tracer cloud, or to bring some dispersion and retardation. Losses of the tracer can be observed in those part of the underground river (especially in low flow conditions) indicating possible adsorption of the dye on suspended matter and trapping of the solute in dead zones where it would dilute.

Finally, the most surprising results of these tests, the double-peaked BTCs, needs an important discussion. The injections at the CN swallow hole have given different results. Double-peaked BTCs appear downstream the PDV lake, i.e. at the Sepulture cave and at the GDS cave, in some conditions (tracer tests 1, 2, 3, 4, 7 and 8). The two peaks are very well distinguished on the BTCs as reflected by their T_{peak} that are separated by several tens of hours. The first peak points out a quicker and rather advective transport. Less dispersion seems to affect this peak in comparison to the second one that shows a much wider shape. The descending branch of the first peak cannot really be characterized as it is somehow merged with the second peak; so, at this point, the retardation that could affect the first peak cannot be characterized. The second peak does show some tailing due to retardation but part of it could be imputed to the first one. The contrasted features of these two peaks – characterized in the previous sub-chapters – imply that they are the results of different path, and so of different modes of transport. The shape of the double-peaked BTCs seems very sensitive to the discharge conditions. Figure 30 plots the T_{peak} of the double-peaked BTCs observed at the GDS, in regard with the discharge conditions (here assimilated to the mean discharge computed during the test). This figure shows that the time to peak decreases with increasing flowrate, except for the second peak of the test conducted under 6l/s. The range of T_{peak} is wider for the second peak (86 to 231 h) than for the first one (40 to 78 h) that seems less sensitive to the flow conditions, in terms of velocity at least. In consequence, the time difference between the two peaks in each test increases for decreasing discharge (except for tracer test 3 at 6l/s). The distribution of the tracer between the two peaks is, however, more difficult to characterize. The relative C_{peak} of each peak changes constantly (for the same injected mass of tracer) and

no clear link can be established with the discharge conditions (Figure 31). One possibility to explain these unpredictable distributions of the tracer in each zone of transport would be the effect of geometrical and physical changes in the system, and more specifically into the lakes. It can easily be imagined that the path followed by the tracer within the big volume of the lakes would vary with the discharge. Rock boulder collapses could also be responsible for physical changes within the lakes.

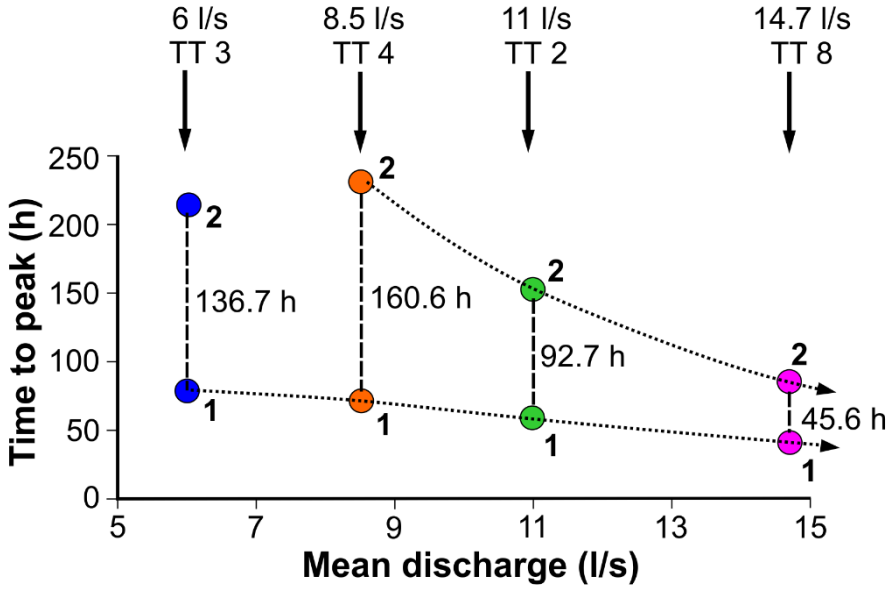

Figure 30. Peak concentration plotted against the time to peak. The numbers 1 and 2 refer to the first and second peak respectively. The different colors represent different tests. Tracer test 1 (20 l/s) is not plotted on the graph as the second peak is missing.

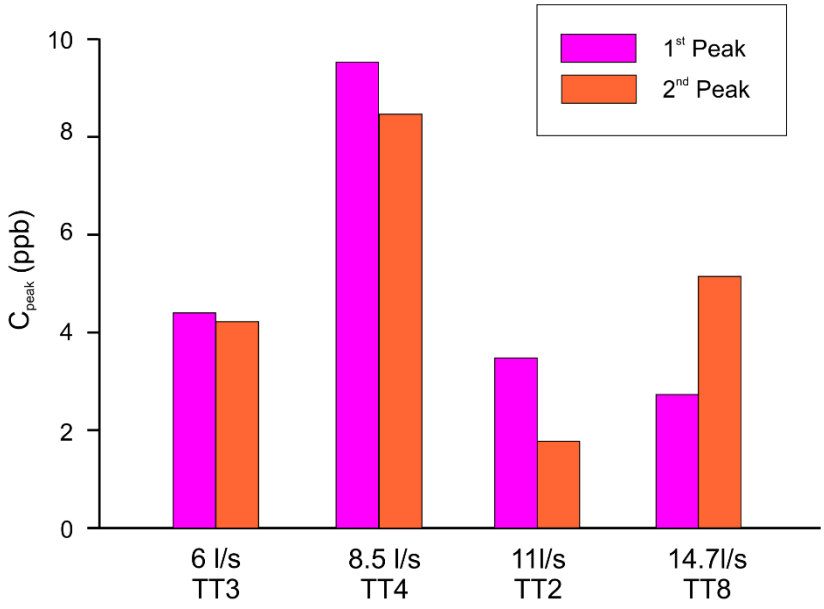

Figure 31. Histogram of the C_{peak} for each peak observed at the GDS for different tracer tests, in different discharge conditions but with the same mass of injected tracer. [TT]: tracer test.

However, these BTCs characterized by two well separated peaks do not appear systematically. Tracer tests 5 and 6 result in a single-peaked BTC with a very strong and long tailing. The mode of injection was the same than for the tests 1, 2, 3, 4, 7 and 8 but they were, however, performed in very low flow conditions (Q_{Mean} of 3 l/s and 2.1 l/s respectively). Figure 32 plots the T_{peak} (recorded at the GDS) of all the tracer tests performed by injection at the CN, against the estimated mean discharge. This graph shows clearly the dependency of the dual recovery appearance to the discharge conditions. It seems that the discharge must be above 5 l/s for the double peak to appear. This figure shows also that, given the low discharge, the T_{peak} of tests 5 and 6 are way too early to correspond to the second peak but could correspond to the first peak. Finally, through Figure 32, a comment can be made about the tracer test 8 that shows a singular behavior of the two peaks (a very small first peak nearly merged with the second one). Looking at the T_{peak} and comparing it with the other dual recovery BTCs, it appears that the two peaks are closer in time than in all the other tests. This could be linked to the flood that occurs during the test, and that could have flushed away the tracer and accelerated the flow implied in the second peak.

The origin of the double-peaked BTCs in the Furfooz system is hard to define given that some zones of the system are unknown. The existence of double-peaked breakthrough curves (BTCs) in karst systems is well documented but often poorly understood. Few studies have considered the physical origin of those double curves. Goldscheider (Goldscheider, Meiman, Pronk, & Smart, 2008) recorded double peaks in a tracer test at Mammoth Cave, USA, for which they explained the double-peaked curves by the possible presence of an unknown bifurcated flow path. Several sampling sites were settled for the Mammoth Cave system, from the injection point to the main resurgence, so that the researchers could identify the likely location at which subsurface flow conditions resulted in double-peaked recovery curves.

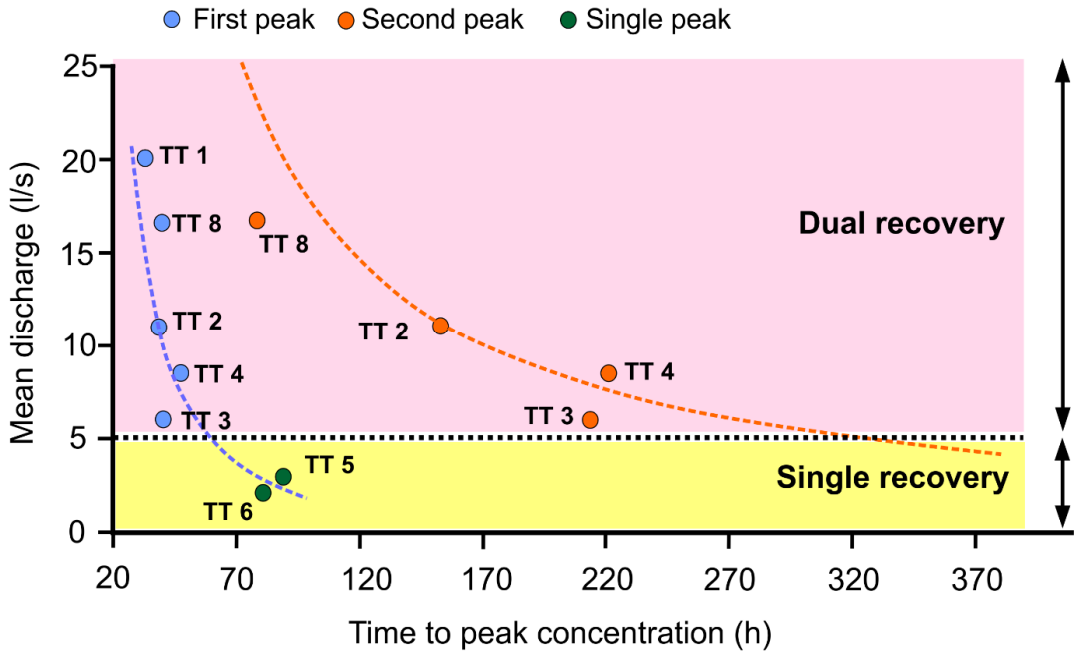

Figure 32. Time to peak plotted against the mean discharge. [TT]: Tracer Test.

Two studies have established a link between those double peaks and the existence of a lake or a pool on the tracer path. Hauns (Hauns et al., 1998) showed that a secondary peak can appear when important changes in a section of the conduit system are observed, which could potentially be linked to the presence of a pool in the flow path. The authors attribute secondary peaks to the trapping of the tracer in eddies. They produced double-peaked BTCs through physical and numerical modelling. Field and Leij (Field & Leij, 2012) realized laboratory analogs to produce experimental double-peaked BTCs. One of those analogs simulated a pool where water flows in and out via small pipes simulating solitary conduits. In both cited studies, the authors have highlighted the strong control of conduit geometries on the resulting BTCs, as also shown in other studies (Hauns, Jeannin, & Atteia, 2001; Massei et al., 2006; Morales et al., 2010).

Following what has just been said, the double-peaked BTCs in Furfooz could be due to either: the existence of an unknown bifurcated flow path, and/or the effect of an important change of section along the path.

To evaluate these possibilities, some field facts must be taken into account. The most upstream point where double-peaked BTC have been observed is the Sepulture cave. The division of the tracer cloud should then be located upstream this point, in the unknown parts of the system. Those can be limited to the first 70 m downstream the CN swallow hole, and to the lakes area. What happens through the first 70 m is not known but it has already been said that it is unlikely that a bifurcation starts there. Therefore, the most probable location of the double peak origin seems constrained to the zone of the lakes. The investigations performed through the lakes showed that the behavior of the tracer is not homogeneous and that it seemed to be conveyed by some preferential flow paths. These observations support the idea that an important change of section – i.e. the small section of the TQF river vs. the big section of the lakes – can imply some dual behavior of the solute. At the TQF lake, a quicker and more advective transport is observed at the surface of the lake in comparison to the bottom where the dye undergoes dispersion and is delayed. At the PDV lake, the tracer that reaches the surface is dispersed and the observed concentrations are weaker than around 20 m of depth where the tracer is probably quicker. This dual behavior is reflected in the two peaks observed downstream. It is reasonable to propose that the first peak is the result of an advective flow that crosses the two lakes and that represents the shortest and most direct pathway to the sites downstream. The advective flow is the first transport zone in the conceptual model. Figure 33A illustrates the conceptual idea of this advective flow path through the lakes. In this illustration the location of the advective path is located around 15 to 20 m of depth because of the investigations leaded into the lake in May 2016, but there are chances that the form and the location of this path changes in regard to the flow conditions or to geometrical change into the lakes (rock collapses or so), as it was proposed earlier.

Regarding the second peak, we suppose a second transport zone within the lakes that interacts with the first one (the advective flow). The wide shape of the second peak is therefore linked to the important and slow dispersion that takes place through the big volumes of the lakes. Two hypotheses can be proposed about the exit of the tracer from this second flow zone (Figure 33B). The first explanation is that the dispersed tracer flows out of the lake via a bifurcated conduit located somewhere at its surface. The tracer would then be

diverted back to the main conduit before the Sepulture cave. The second hypothesis supposes an exit of the dispersed cloud of tracer by the same path than the quick and advective flow.

The conceptual model of the solute transport through the lakes support thus the idea that two transport paths co-exist within the lakes. They have a different control on the tracer transport, probably due mainly to their different geometries, but must probably have a strong interaction to exchange solute. The exit of the second, slower, transport zone could be located at the surface of the PDV lake, or, in depth, at the same location than the exit of the first transport zone. There is no relevant field evidences to choose between these two possibilities.

Finally, regarding the single-peaked curves observed at very low discharge conditions, the conceptual model needs some adaptations. From these tests (tracer tests 5 and 6), it appears that the second peak is not visible on the BTC observed at the GDS. No data was recorded at the Sepulture. Regarding the conceptual model of Figure 33, the absence of the second peak could be explained in two different ways:

- The second peak is absent because, due to the very low flow conditions, the second transport zone is deactivated. This could be explained by the fact that the velocities are so slow in the second flow zone that the latter is not effective as transport zone. It could also be proposed that the absence of a second flow zone is due to the inactivation of the hypothetic exit at the surface of the lake. If an exit, at the surface of the PDV lake, was deactivated, it should be possible to establish a link between the single-peaked BTC events and the water-level recorded at the PDV lake. Unfortunately, due to important data gaps (probe dysfunction), no conclusion can be driven regarding the possible link between the PDV lake level and the activation or inactivation of a possible bifurcated conduit. The question still remains.

- The second peak is present in the “single-peaked” BTC, but is hidden in the strong tailing observed on the BTCs. Therefore, the second flow zone is still effective, but the very slow transport would produce a second peak with a very wide and flared shape as illustrated in Figure 34.

All the hypotheses supposed by the conceptual model of Furfooz, either at low to moderate, or at very low discharges, need to be confronted. The hydrodynamic process and the physical explanation of the conceptual model is not evident and should be tested. For this reason, a physical model was built to imitate the karst conduit system and confront the possibility of the conceptual model. This laboratory analog is the object of chapter 5. Once this physical testing is made, the next and last chapter 6 will examine the conceptual system of Furfooz through the numerical approach. The numerical method will also give a more precise dimensioning to the system that has been made mainly through a qualitative analysis in the present chapter.

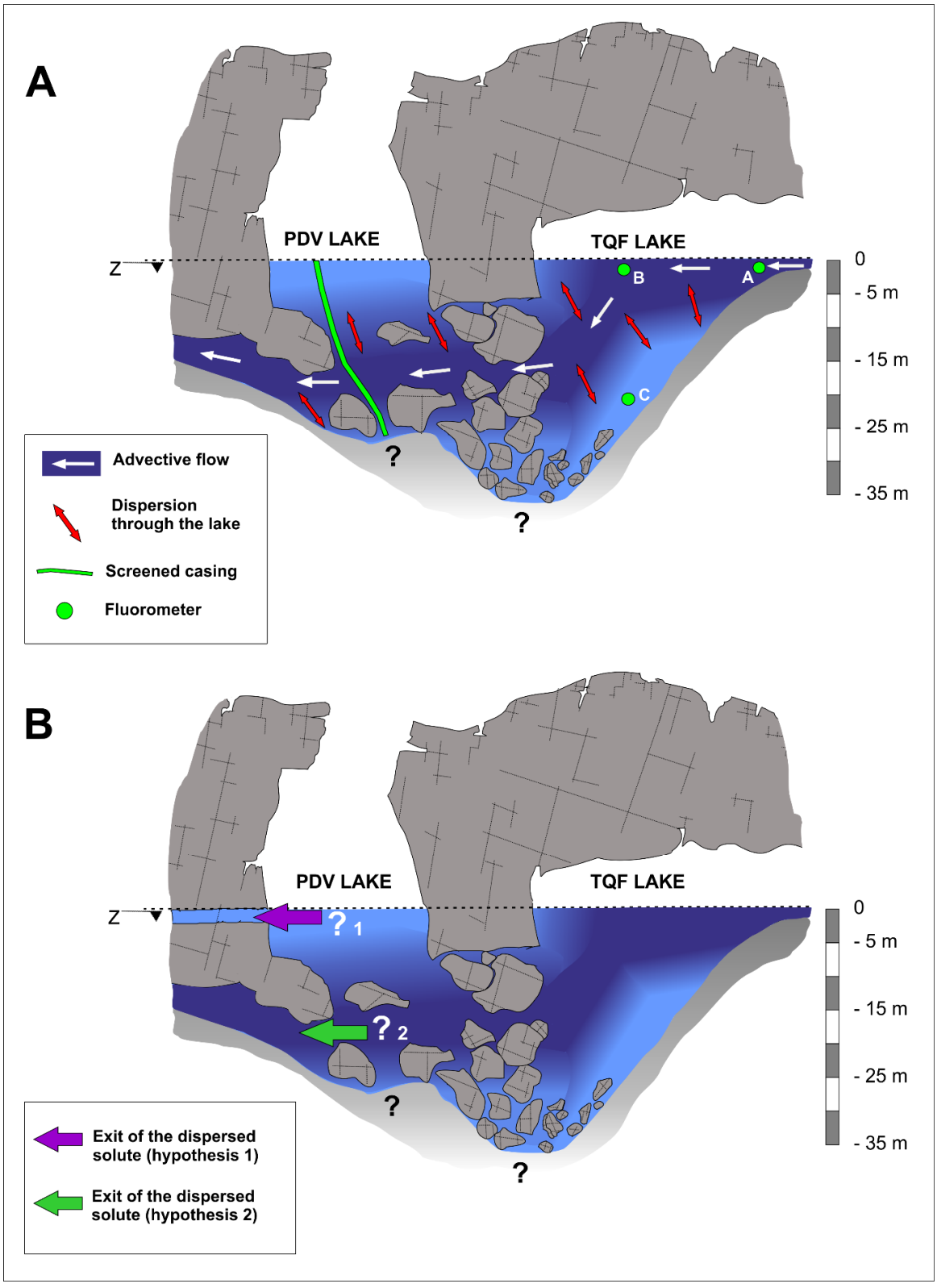

Figure 33. Conceptual model proposed to explain the dual recovery observed downstream the PDV lake. The advective flow coming from the TQF river crosses the lakes through preferential pathways that constitute a first transport zone. This first cloud of tracer exits the PDV lake towards the SEP and the GDS caves. On its path, this quicker flow exchange solute with the surrounding big volumes of the lake where the solute is dispersed slowly (second transport zone). The evacuation of this second, dispersed cloud of tracer could either be done by the same exit than the advective flow or by an unknown bifurcated flow path.

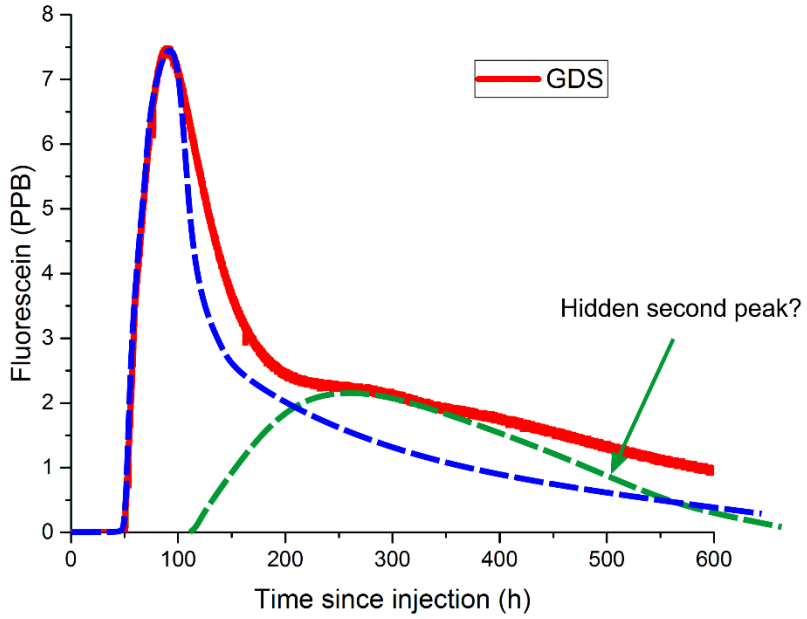

Figure 34. The strong tailing observed in the single-peaked curve at low discharge could be due to the second peak that is hidden in the tail.

Chapter key points:

- Fifteen tracer tests are described. They were realized in various flow conditions and from different injection points;
- Interpretations of the BTCs were done in considering that the discharge of the whole system can be assimilated to the discharge measured at the GDS;
- Low recoveries are recorded at various points of the system. This is interpreted as, both, a loss of the tracer within the lakes (in immobile zones), and as the effect of a strong adsorption on sediments;
- Discharge conditions have a strong influence on the results;
- Double-peaked BTCs are observed downstream the lakes, i.e. at the Sepulture cave, the GDS and the TDL. A separation of the tracer cloud is needed to create these double-peaked BTCs, and the origin of this separation is located in the area of the lakes;
- A conceptual model is proposed. It links the double recovery phenomena to the existence of a double transport hydrodynamic within the lakes. This has been highlighted notably by the strong heterogeneities that affect the tracer distribution within the large volume of the lakes;
- This conceptual model should be nuanced at very low discharge conditions.

4.4 References

Bear, J. (1979). *Hydraulics of Groundwater*. New-York: McGraw-Hill.

Behrens, H., Reims, U., Dieter, H., Dietze, G., Eikmann, T., Grummt, T., … Tilkes, F. (2001). Toxicological and ecotoxicological assessment of water tracers. *Hydrogeology Journal*, *9*(3), 321–325. https://doi.org/10.1007/s100400100126

Bencala, K. E., & Walters, R. A. (1983). Simulation of solute transport in a mountain pool-and-riffle stream: a transient storage model. *Water Resources Research*, *19*(3), 718–724.

Benischke, R., Goldscheider, N., & Smart, C. (2007). Tracer techniques. In N. Goldscheider & D. Drew (Eds.), *Methods in Karst Hydrogeology. International Contributions to Hydrogeology* (pp. 147–170). London, UK: Taylor and Francis.

Brouyère, S., Gesels, J., Jamin, P., Robert, T., Thomas, L., Dassargues, A., … Hallet, V. (2009). *Caractérisation hydraulique des aquifères et estimation des ressources en eaux souterraines, délivrable D.3.12 – partie RWM021. onvention RW et SPGE-Aquapole : Caractérisation hydrogéologique et support à la mise en œuvre de la Directive Européenne 2000/6*.

Dewaide, L., Bonniver, I., Rochez, G., & Hallet, V. (2016). Solute transport in heterogeneous karst systems: Dimensioning and estimation of the transport parameters via multi-sampling tracer-tests modelling using the OTIS (One-dimensional Transport with Inflow and Storage) program. *Journal of Hydrology*, *534*. https://doi.org/10.1016/j.jhydrol.2016.01.049

Dewaide, L., Collon, P., Poulain, A., Rochez, G., & Hallet, V. (2017). Double-peaked breakthrough curves as a consequence of solute transport through underground lakes: a case study of the Furfooz karst system, Belgium. *Hydrogeology Journal*. https://doi.org/10.1007/s10040-017-1671-4

Dörfliger, N. (2010). Guide méthodologique : Les outils de l'hydrogéologie karstique pour la caractérisation de la structure et du fonctionnement des systèmes karstiques et l'évaluation de leur ressource. Avec la collaboration de Ph. Crochet, R. Guerin, N. Jozja, B. Marsaud, P-H. Mondain, Ph. Muet, V. Plagnes ; *BRGM RP- 58237-FR*, 246 pp., 82 ill., 5 ann.

Field, M. (2002). The QTRACER2 Program for Tracer-Breakthrough Curve Analysis for Tracer Tests in Karstic Aquifers and Other Hydrologic Systems. *U.S. Environmental Protection Agency*, 1–179.

Field, M. S., & Leij, F. J. (2012). Solute transport in solution conduits exhibiting multi-peaked breakthrough curves. *Journal of Hydrology*, *440–441*, 26–35. https://doi.org/10.1016/j.jhydrol.2012.03.018

Field, M. S., & Pinsky, P. F. (2000). A two-region nonequilibrium model for solute transport in solution conduits in karstic aquifers. *Journal of Contaminant Hydrology*, *44*(3–4), 329–351. https://doi.org/10.1016/S0169-7722(00)00099-1

Gaspar, E. (1987). *Modern Trends in Tracer Hydrology. Volume I.* CRC Press.

Geyer, T., Birk, S., Licha, T., Liedl, R., & Sauter, M. (2007). Multitracer test approach to characterize reactive transport in karst aquifers. *Ground Water*, *45*(1), 36–45. https://doi.org/10.1111/j.1745-6584.2006.00261.x

Goldscheider, N. (2015). Overview of methods applied in karst hydrogeology. In Z. Stevanovic (Ed.), *Karst Aquifers - characterization and engineering*, pp. 127–145.

Goldscheider, N., Meiman, J., Pronk, M., & Smart, C. (2008). Tracer tests in karst hydrogeology and speleology. *International Journal of Speleology*, *37*(1), 27–40. https://doi.org/10.5038/1827-806X.37.1.3

Grey, W., & Pinder, G. (1976). An analysis of the numerical solution of the transport equation. *Water Resources Research*, *12*(3), 547–555.

Hauns, M., Jeannin, P.-Y., & Atteia, O. (2001). Dispersion, retardation and scale effect in tracer breakthrough curves in karst conduits. *Journal of Hydrology*, *241*(3–4), 177–193.

Hauns, M., Jeannin, P.-Y., & Hermann, F. (1998). Tracer transport in karst underground rivers: tailing effect from channel geometry. *Bulletin d'Hydrogéologie*, *16*(16), 123\,--\,142.

Hubbard, E. F., Kilpatrick, F. A., Martens, L. A., & Wilson, J. F. (1982). Measurements of time of travel and dispersion in streams by dye tracing. In *Techniques of Water Resources Management - Book 3*. Washington, DC.: US Geological Survey.

Käss, W. (1998). *Tracing technique in Geohydrology*. Rotterdam: Balkema.

Kreft, A., & Zuber, A. (1978). On the physical meaning of the dispersion equation and its solutions for different initial and boundary conditions. *Chemical Engineering Science*, *33*(11), 1471–1480. https://doi.org/10.1016/0009-2509(78)85196-3

Landau, L. D., & Lifshitz, E. M. (1987). *Fluid mechanics* (Pergamon P). London: Reading, Mass.: Addison-Weslay.

Massei, N., Wang, H. Q., Field, M. S., Dupont, J. P., Bakalowicz, M., & Rodet, J. (2006). Interpretixng tracer breakthrough tailing in a conduit-dominated karstic aquifer. *Hydrogeology Journal*, *14*(6), 849–858. https://doi.org/10.1007/s10040-005-0010-3

Morales, T., Uriarte, J. A., Olazar, M., Antigüedad, I., & Angulo, B. (2010). Solute transport modelling in karst conduits with slow zones during different hydrologic conditions. *Journal of Hydrology*, *390*(3–4), 182–189. https://doi.org/10.1016/j.jhydrol.2010.06.041

Perrin, J., & Luetscher, M. (2008). Inference of the structure of karst conduits using quantitative tracer tests and geological information: Example of the Swiss Jura. *Hydrogeology Journal*, *16*(5), 951–967. https://doi.org/10.1007/s10040-008-0281-6

Poulain, A., Rochez, G., Van Roy, J.-P., Dewaide, L., Hallet, V., & De Sadelaer, G. (2017). A compact field fluorometer and its application to dye tracing in karst environments. *Hydrogeology Journal*, *25*(5). https://doi.org/10.1007/s10040-017-1577-1

Schnegg, P. A., & Dörfliger, N. (1997). An inexpensive flow-through field fluorimeter. In U. of N. Centre of Hydrogeology (Ed.), *6th Conference on Limestone Hydrology and Fissured Media - Proceedings* (pp. 47–50). La-Chaux-de-Fonds.

Schudel, B., Biaggi, D., Dervey, T., Kozel, R., Müller, I., Ross, J. H., & Schindler, U. (2003). Application of artificial tracers in hydrogeology - Guideline. *Bulletin d'Hydrogéologie, University of Neuchatel*, *20*(Special Issue), 91.

Smart, P. L., & Laidlaw, I. M. S. (1977). An evaluation of some fluorescent dyes for water tracing. *Water Resources Research*, *13*(1), 15–33. https://doi.org/10.1029/WR013i001p00015

Talbot, J. W., & Henry, J. L. (1968). The adsorption of rhodamine-b on to materials carried in suspension by inshore waters. *ICES Journal of Marine Science*, *32*(1), 7–15. https://doi.org/10.1093/icesjms/32.1.7

Van den Broeck, E., & Rahir, E. (1903). *La Lesse souterraine et la traversée des deux boucles de la rivière à Furfooz démontrée au moyen de la fluorescéine* (Hayez-im). Bruxelles.

Zheng, C., & Wang, P. (1999). *MT3DMS: A Modular Three-Dimensional Multispecies Transport Model for Simulation of Advection, Dispersion, and Chemical Reactions of Contaminants in Groundwater Systems; Documentation and User's Guide. Final Report*. US Army Engineer Research and Development Center, 239 p.

Chapter 5

Physical modelling

Chapter 5 Physical modelling

In brief, in this chapter:

- The conceptual model of Furfooz, exposed in chapter 4, is tested through a scale model;
- The scaling method is described;
- Results of the tracer tests performed on the physical model are presented;
- Influence of the discharge is evaluated.

5.1 Introduction

The field experiments exposed in chapter 4 have brought to light the possibility of a dual behavior of the tracer transport within the TQF and the PDV lakes. A link was made between this duality and the double-peaked BTCs observed downstream the PDV lake. More precisely, a conceptual model exposed in chapter 4 proposes the existence of an advective flow coming from the TQF river that crosses the two lakes and exits the PDV lake at some depth to generate the first quick and more advective peak of the dual-peaked BTCs downstream. Along its path through the lakes, a part of the tracer is exchanged with the surrounding volume of water that constitutes the lakes. In this part of the lake, advection exists but the transport is dominated by dispersion and retardation, and is responsible for the second peak occurrence downstream the lakes. As debated in chapter 4, the exit of this slow and dispersed tracer out of the lake could either be done by a bifurcated conduit located at the surface of the PDV lake or by the same exit than the one followed by the advective flow.

The idea of a local auxiliary conduit that diverts the solute that has dispersed slowly to the surface of the lake and then transports it back to the main conduit is rather easy to conceive. The second hypothesis though, would suppose hydrodynamic processes that are not so evident to imagine. Therefore, to test this hypothesis and to understand how, physically, it could be possible, a scale model of the Furfooz system was built.

Although the purpose of the scale model is not to reproduce the exact replica of the field BTCs, it was nevertheless important to apply an adequate scaling to propose some analogies with the reality. Scale modelling aiming to replicate the flow in a karst system is a very complex matter. First of all, it should be kept in mind that a replica of a karst system is above all a replica of a conceptual model and not of the reality, because most of the time in a karst study the exact geometry of the entire system is not known. Furthermore, to be perfectly realistic, a scaled physical model should replicate all the physical processes implied in the flow. So, in addition to a simple geometric scaling, a scaled analog should also consider physical parameters that influence the hydrodynamic such as viscosity, wall roughness, sinuosity, among other. It is clear, therefore, that a perfect replica of the reality cannot be built.

However, the dimensional analysis theory (Bridgman, 1922; Sonin, 2001) can help to ensure of a reliable similarity between the reality and the scale model regarding the hydrodynamic processes. According to this theory, both the geometric and dynamic similarities should be achieved. The geometric similarity will be ensured if the same scale ratio is applied on the characteristic dimensions of the system (lengths, conduit diameter or depth mainly). Regarding the dynamic similarity in a free flow issue, two dimensionless numbers are potentially implied: Reynolds (Re – eq. (1)) and Froude numbers (Fr – eq. (2))

$$Re = \frac{\rho\, v\, l}{\mu} \tag{1}$$

$$F_r = \frac{v}{\sqrt{g\, l}} \tag{2}$$

Where ρ is the fluid density [M/L^3]; v is the effective velocity [L/T], *l* the characteristic length [L], μ the fluid viscosity [M/L.T], g the gravity [L^2/T].

However, in practice and because the fluid in the reality and in the model is the same (water), it is nearly impossible to conserve both Reynolds and Froude numbers. It is generally accepted that, in a free flow case in turbulent regime, the Froude number should be preferentially respected. This implies that the viscosity effect on the flow is neglected but the scale model must be in the same flow regime than the real system (Fay, 1994; Ginocchio & Viollet, 2012; Hauns, Jeannin, & Hermann, 1998).

5.2 Scaling operation

The discretized system on which the physical model has been based is simplified with regard to the field knowledge. The segment GDS-TDL is not considered here, so the scaled system ends at the GDS. The simplified reality supposes three segments from the swallow hole to the GDS, with a total length of 760 m:

- The first segment corresponds to the 210 m that separates the CN swallow hole from the TQF lake. So, in these 210 m are considered : the first unknown 70 m of the system downstream the swallow hole, and the straight conduit of the TQF river. It will be considered that the entire 210 m has the same feature than the very small section observed at the TQF river;
- The lakes segment that is constrained to the observed lake area and should approximate 150 m;
- The last segment that starts from the exit of the PDV to the GDS and extends on about 410 m. The Sépulture cave is not considered in the scale model. Indeed, it had not been discovered yet when the model was built.

To operate the scaling, it is first needed to define the characteristic dimensions that will be submitted to the scaling process to ensure of the geometric similarity. Regarding the issue of solute transport in a karstic system, the lengths are surely the characteristic dimensions to consider in priority given the control of the longitudinal dimension on the transport. It was chosen to apply a scaling factor of 1:100 to build the scale model. Therefore, the entire set up

is about 7.6 meters long (Figure 1). A deviation regarding the three segments defined above had to be applied. Indeed, due to the equipment available to build the scale model, the lake segment had to be restrained to 1.2 m, and not 1.5 m as expected. In consequence, 0.3 m were added to the last segment.

Regarding the flooded sections implied in the physical model, equipment limitations have somehow imposed the material used for the realization of the conduits in the analog. The conceptual idea is to reproduce the strong contrasts observed in the real system regarding the flow section: a very small section at the TQF river, a very big section and volume for the lakes, and, for the unknown segment PDV-GDS, a section that corresponds to a river but probably bigger than the TQF river section. The first segment (the TQF river) is represented by a pipe of 3 cm in diameter. The inflow is imposed by a tap connected to a pressiometric valve and a flow-meter. This first pipe enters then the lake segment. The field information is so poor about the lake dimension that an accurate scaling is not possible. It was chosen to conceive the lake as a big tank (1 m^3) that would contrast with the flow section of the entrance conduit. This tank is divided in two by a watertight compartment that is open at mid-height, in order to represent the connection between the TQF and the PDV lakes. The last segment exits the tank at mid-height in a pipe of 8.5 cm of diameter. The water is under pressure in this exit pipe until the pipe is elevated at the same level than the surface of the water in the tank. Then, the last bit of the pipe is turned down to allow the water to flow out of the system. The discharge can be measured manually at this point. With this system, the exit discharge (at the GDS) should be similar to the entrance discharge at the TQF. Figure 1 and Figure 2 illustrate the scale model.

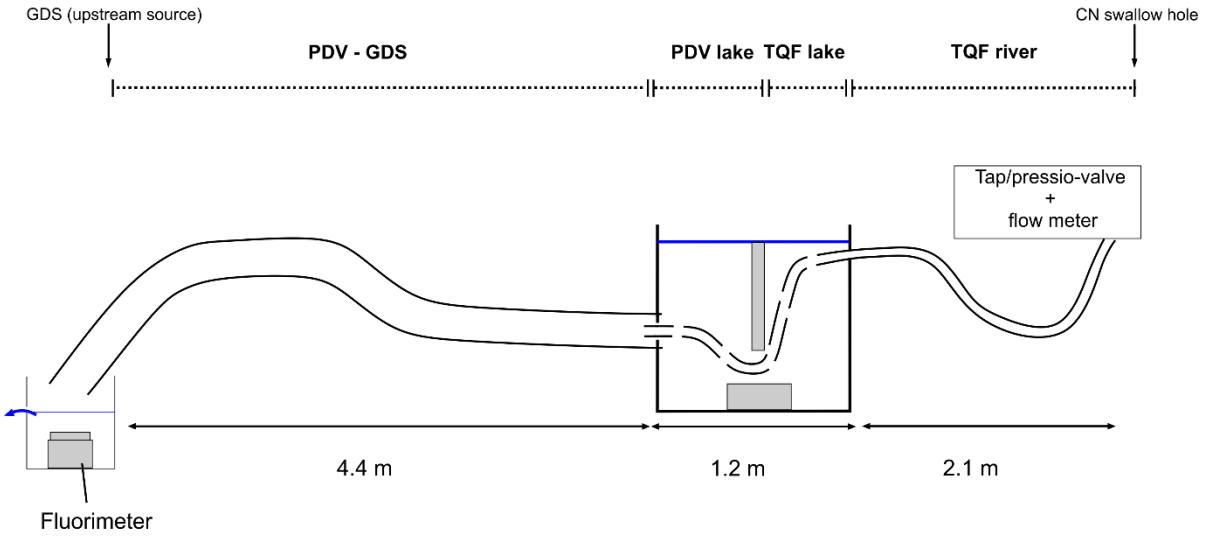

Figure 1. Representation of the scale model of the Furfooz system. The flow in is ensured by a tap controlled by a pressio-valve and a flow-meter. The tracer mixtureis injected through a syringe in a pipe of 2.1 m that corresponds to the simplified segment of the TQF river. It arrives then in a perforated pipe that crosses a big water tank. The tracer can be exchanged between the holey pipe and the water within the tank. The water exits then the second segment through an 8.5 cm pipe.

Concerning the flow similarity issue, the characteristic velocities that flows into the pipes imposes the Froude number. In the scale model, a steady discharge of 2l/min was imposed at

the entrance of the system. The effective velocity in the entrance pipe is then $4.7*10^{-2}$ m/s. Given equation (2), to keep a Fr in the scale model equivalent to the Fr on the field, the characteristic velocity must be scaled by the square root of the scale ratio that is applied in the model. Therefore, the velocity in the entrance pipe corresponds to:

$$4.7 \times 10^{-2} \times \sqrt{100} = 4.7 \times 10^{-1} \text{ m/s (theorical corresponding velocity on the field)}$$

In the field, considering a flow section of about 0.05 m^2 for the TQF river, those velocities would be reached with a discharge of 0.0235 m^3/s. This is a realistic discharge in the Furfooz system. The tracer test 1 was performed in this scale of discharge conditions (Q_{Mean} of 0.020 m^3/s). It can therefore be said that the Froude number in the scale model respects the hydrodynamic of the real system as initial boundary conditions.

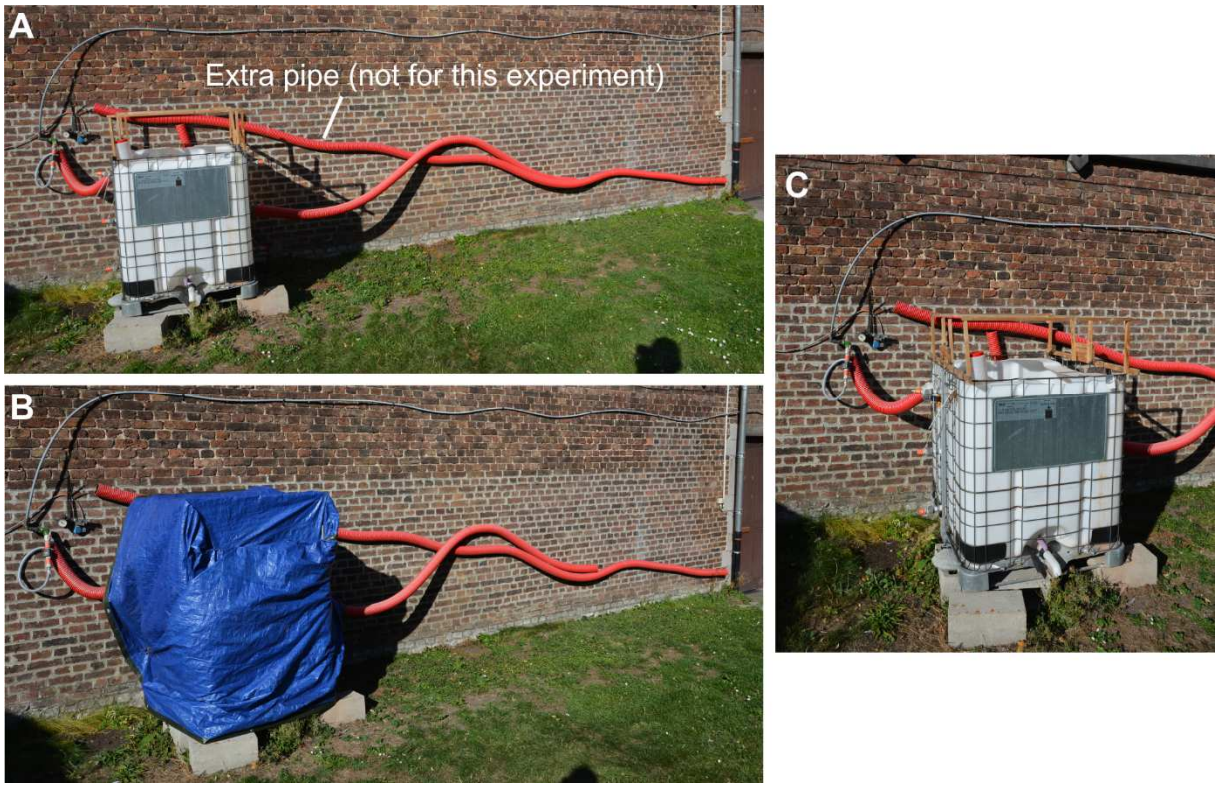

Figure 2. Photos of the scale model. A: entire setup without the cloth covering the tank, B: entire setupe with the cloth protecting the tracer in the tank from sunlight decay, C: details of the flow control system at the entrance of the model.

5.3 Tracer tests

5.3.1 Testing of the conceptual model

Tracer tests were performed in the scale model in order to test the conceptual model exposed in chapter 4 (Figure 33, p 129). In this conceptual hypothesis, a double advection-dispersion transport occurs within the lakes. To simulate the more advective flow that is supposed to be responsible for the first peak of the double-peaked BTC, a pipe of 3 cm in diameter was

connected to the pipe entering the tank and to the one exiting the tank (Figure 1). Small round holes (diameter of 0.004 m) were made in this pipe so the tracer could be partly transferred to the water in the tank. The cumulated area of all the holes represent about 5% of this pipe total area. A fluorimeter (FL-30 GGUN) was connected at the exit of the model. The tracer injected in the model was a fluorescent tracer (fluorescein) and it was injected instantaneously through a syringe. The same mass of tracer diluted in the same volume of water was injected for each test. As the model was built outside, it was entirely covered to limit the decay of the fluorescein caused by sunlight. The initial discharge imposed by the tap is 2 l/min. The discharge at the exit was controlled several times during the test. It fluctuates between 1.7 and 2.4 l/min, depending of the small level fluctuations into the tank. The tracer experiment was performed three times to ensure the reliability and accuracy of the resulting BTCs.

The results of the three tracer tests performed in the same conditions are shown in Figure 3. The three BTCs are very similar. The differences that can be pointed out between the three tests concern mainly the C_{peak}. These differences demonstrate that some unknown factors influence the tracer concentration and that this factor are not controlled in the experiment. Strong similarities should be underlined and that resides mainly in the presence of two peaks in each curve. Table 1 presents the transport parameters calculated on the BTC named “scale A-3”. The first one is very quick (T_{peak}: 5.5 min) and has a high peak concentration (33.9 ppb) compared to the second one (T_{peak} : 47 min, C_{peak}: 8.9 ppb). The latter has a shape that is atypical and does not reveal transport dominated by advection. It is obvious that the first peak corresponds to the direct flow of the tracer through the pipes of the scale model while the second recovery results from the transfer of the tracer from the internal pipe to the water of the tank. The second recovery results from a slow and dispersive transport into the tank, plus a very strong tailing effect. A surprising data is the very low recovery rates. That should mean that the majority of the tracer is transferred to the water of the tank without exiting it in measurable concentration. The tracer stays probably long enough into the tank to be extremely diluted and, possibly, affected by decay due to sunlight, the cloth covering the scale model being not 100 % sun-proofed. Furthermore, it should not be forgotten that at the time of the fluorimeter removal, the recovery was not complete (final sampling at 2.3 ppb). A substantial amount of tracer could have been recovered in addition if the fluorimeter had been left until the concentration falls to nil.

5.3.2 Discharge influence

A few additional tests were performed in order to define if the discharge is restrictive for the double peak appearance. The influence of the discharge was tested by performing tracer tests at low and high discharge.

Three different flow rates were imposed at the system entrance: 4.7 l/min, 2.0 l/min and 0.7 l/min. At high discharge of 4.7 l/min, the obtain BTCs (Figure 4) show that the dual recovery does still appear. In comparison with the tests performed with a discharge of 2l/min (scale-A3), the second peak arrives more quickly (C_{peak} reached in about 25 minutes). At low discharge (1.4 l/min), a double peak is also produced but with the C_{peak} of the second peak that is reach after 72 min only (Figure 4). Finally, a very low discharge of 0.7 l/min was applied. In these conditions, the dual recovery doesn’t appear. On the curve shown in Figure 4, the

tracer arrives only after 50 minutes and reach a maximum concentration of 12.8 ppb after 2.3 h. After 300 min, 2 ppb of tracer were still detected. Not much interpretation can be made regarding the variation of the concentration between each test because, as it was underlined in section 5.3.1, some uncontrolled factors influence the distribution of the tracer.

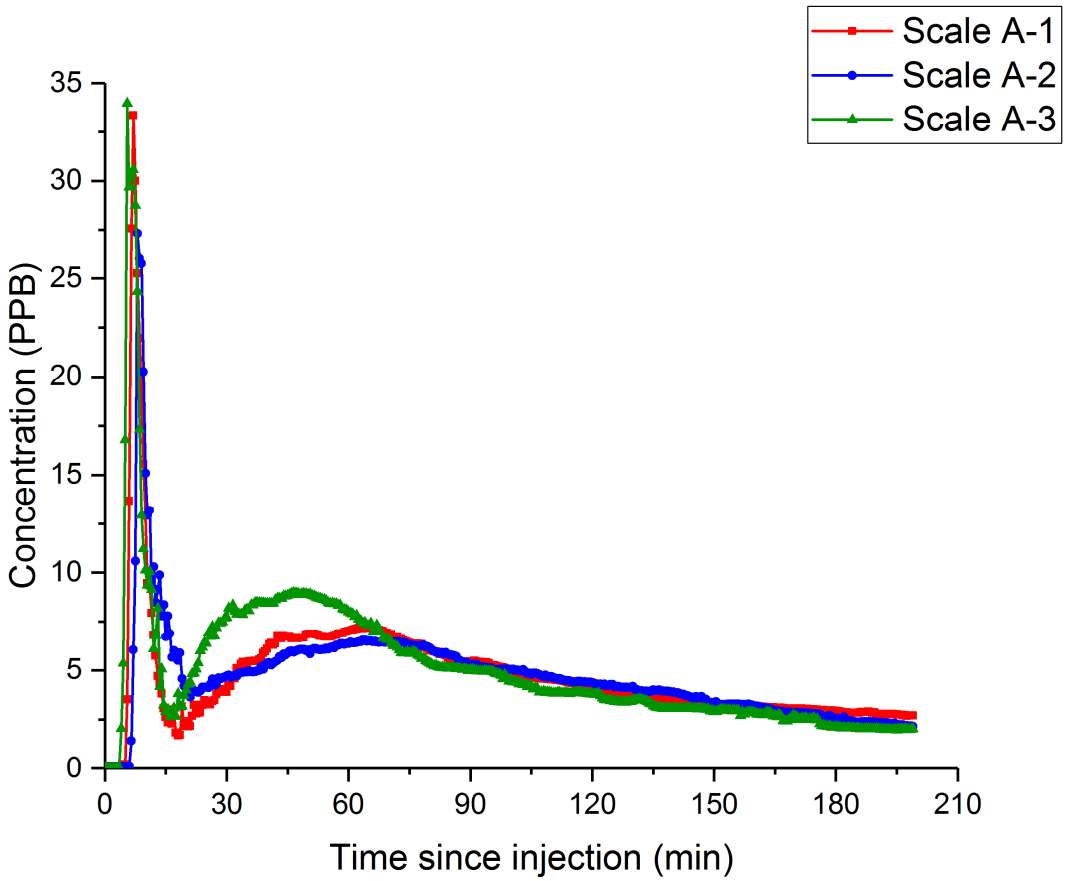

Figure 3. BTCs observed at the exit of the scale model resulting from fluorescein injection at 2 l/min.

Tracer test	1st A. (min)	V_{max} (m/min)	T_{peak} (min)		V_{peak} (m/min)		T_{mean} (min)	V_{mean} (m/min)	C_{peak} (ppb)		R.R. (%)
Scale A-3	4.0	1.9	1st	2nd	1st	2nd	73.3	0.10	1st	2nd	3.3
			5.5	47.0	1.4	0.17			33.9	8.9	

Table 1. Main transport parameters calculated from the BTC "scale A-3".

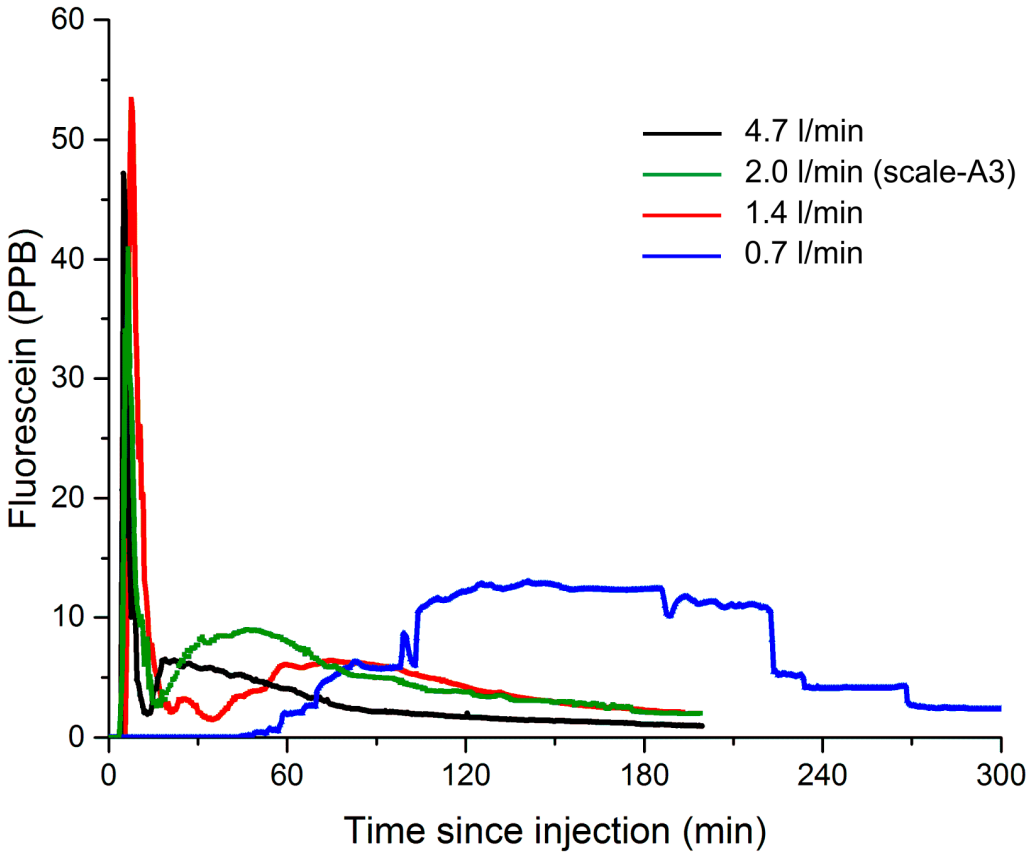

Figure 4. BTCs resulting from tracer-tests performed in different discharge conditions.

5.4 Discussion

The physical model of the Furfooz system is a very simplified vision of a supposed reality. The building of this model relies on some conceptual postulates that are already a simplification or extrapolation of a – sometimes unknown – reality. The parameters that were considered for the scaling of the system are those that are measurable and that define mainly the advective transport in karst conduits: the velocities and the length of the system. The dispersive aspect of the transport into the conduits is not really taken into account in the scaling because it is inherent to the environment and difficult to reproduce or to imitate. The first aim of the scale model is to address this question: is it possible to create a double-peaked BTC with the tested configuration?

The answer is yes. Double-peaked BTCs exposing similarities with the one observed on the field have been produce. The shape of the double-peaked BTCs produced by the scale model have however noticeable differences from those observed on the field. The first peak is too narrow compared to the field one, while the second peak is dominated by very important retardation that produces a very slow decrease of the concentrations. These difference are mainly due to similarity issues. The dispersion is here too small in the first peak to widen its shape. In the real system, the first peak is the result of an advective transport but some dispersion is brought by the fact that the conduits have inconstant diameter and are

interrupted by obstacles. An important difference regarding conduit transport in the scale model and in the reality should also be pointed out: in the reality, the water flows in free flow conditions while in the model, the flow is under pressure in closed pipe. Even if the Froude number condition is respected, it cannot be exclude that “enclosing” the flow in a pipe has no influence on the tracer transport. As for the second peak, inherited from the tracer transport into the tank, the very long tail is due to a too important effect of immobile water into the tank. Indeed, the second peak is due here to the return of the tracer to the holey pipe that crosses the tank. There is probably not enough advection into the tank to allow a real transport to take place and what is observed here is mainly a storage zone effect.

Regarding the influence of the discharge, it has been shown that the shape of the BTC is greatly influenced by the discharge conditions. A test done at very low discharge results in a single peak showing a very wide shape and that arrives rather late. What happens is actually that, due to too low advection, all the tracer that arrives in the internal pipe exits this pipe to disperse in the tank. In consequence, the first peak does not exist and the final BTC corresponds only to the dispersive transport of the tracer through the tank. In the field, single-peaked BTCs are also observed at very low discharge but the shape is not similar to the scale model one. The process on the field is probably not exactly the same of what happens on the scale model but it could be an intermediate state between two well distinctive peaks and one flared, wide and slow BTC.

All in all, even if this scale model could be improved, it clearly shows that the hypothesis proposed by the conceptual model, exposed in chapter 4, in which two transport zones coexists within the lake, can actually produce a dual recovery.

Chapter key points:

- A scale model of the Furfooz system is used to test the conceptual model of Furfooz;
- Geometric and dynamic similarities between the field and the model are respected;
- The scale model supposes that the exit of the lakes is common to the two flow zones;
- Reliable double-peaked BTCs could be produced out of the scale model. While some discrepancies can be pointed out, evident similarities exist between the field BTCs and the scale-model ones;
- Discharge influence greatly the results. At very low discharge, the double-peaked feature disappears.

5.5 References

Bridgman, P. W. (1922). *Dimensional analysis*. New Haven: Yale University Press. 140 p.

Fay, J. A. (1994). *Introduction to fluid mechanics*. Cambridge, MA, MIT Press. 444 p.

Ginocchio, R., & Viollet, P. L. (2012). *L'énergie hydraulique*. Collection EDF R&D, Éd. Lavoisier Tec & doc. 637 p.

Hauns, M., Jeannin, P.-Y., & Hermann, F. (1998). Tracer transport in karst underground rivers: tailing effect from channel geometry. *Bulletin d'Hydrogéologie*, *16*(16), 123-142.

Sonin, A. A. (2001). *The Physical Basis of dimensional analysis*. Cambridge, MA, MIT Press. 57 p.

Chapter 6

Numerical modelling

Chapter 6 Numerical modelling

In brief, in this chapter:

- Theoretical considerations for solute transport modelling in karst conduits is exposed;
- A new numerical tool is briefly described;
- This tool is applied on the conceptual model of the Furfooz system;
- The aim of this application is to test the conceptual model of Furfooz from a numerical point of view. Some critics of the resulting dimensioning of the system are proposed.

6.1 Introduction

In this work, we consider the numerical models that aim to describe mathematically solute transport processes and estimate average values for different parameters. In karst conduits, the flow is turbulent due to the encountered high velocities. Darcy's Law, which prevails in matrix flow, is invalid in the turbulent flow conditions that exist in conduit flow. The mathematical expression used to describe solute transport in karstic conduits is the Advection-Dispersion Equation (ADE) (Kreft and Zuber, 1978). The ADE (Equation (1)) expresses that, in equilibrium models, evolution of the solute concentration (C) with time (t) is only dependent on the longitudinal flow velocity (v_L) and their longitudinal dispersion (D_L). It is indeed usually admitted that the longitudinal component of the transport is way dominant over the other directions. Equation (1) also integrate a decay coefficient (μ) that can affect the recovery rate and a retardation factor (R_f) that is here only linked to solute sorption on solid particles:

$$R_f \frac{\partial C}{\partial t} = D_L \frac{\partial^2 C}{\partial x^2} - v_L \frac{\partial C}{\partial x} - \mu C \quad (1)$$

However, the asymmetry generally observed in field BTCs is not explain by this formulation. This persistent skewness and tailing has been widely discussed and considered as the results of complementary processes as adsorption-diffusion, molecular diffusion, dilution effects, multiple conduits effects, but the main process responsible for BTCs skewness is the interaction with immobile water (Hubbard et al., 1982; De Marsily, 1986; Maloszewski and Zuber, 1989; Rossier and Kiraly, 1992; Maloszewski, Harum, and Benischke, 1992; Werner, Höltz, and Maloszewski, 1997). Transient storage exists in regular or irregular conduits due to the velocity gradient between the main flow zone and the conduits walls that causes turbulent flow (Martin and McCutcheon, 1998; Hauns, Jeannin, and Atteia, 2001). Field and Pinsky (Field and Pinsky, 2000) proposed a "two-region non-equilibrium model" that supposes the existence of immobile water zones along the solute transport path. An exchange exists

between mobile and immobile zones but transport is only effective in the mobile, dynamic zone. A term implying a mass transfer coefficient (α) between the mobile and immobile regions should therefore be added to Equation (1).

Modelling programs offer the possibility to estimate the hydrodynamical and geometrical parameters that control solute transport and constrain the resulting BTC. In chapter 4, the complexity of the Furfooz system has been shown through multi sampling sites tracer tests. The results were partly analyzed thanks to the QTRACER2 program, that proposes some hydrodynamical and geometrical parameter assessment, but these are average values estimated for a virtual conduit between the point of injection and the sampling point. The field observations and investigations have, however, show that the underground river in the Furfooz system flows into variated and contrasted flow section. The tracer tests lead to the conclusion that the presence of these contrasted sections are determinant over the tracer transport. More specifically, the presence of the lakes on the tracer path, has been pointed out for being responsible of the possible existence of dual hydrodynamic within the lakes. A conceptual model, exposed in chapter 4, proposes that this dual hydrodynamic is responsible for the double-peaked BTCs observed downstream the lake. The aim of the present chapter is to evaluate, through numerical modelling, if, for a given conceptual model, the double-peaked BTC can be reproduce downstream the lakes. To do so, and because it was demonstrated in chapter 4 that the dual hydrodynamic exists only in the lakes area, the conceptual system of Furfooz needs to be discretized from the point of injection and to the end of the system. This discretization is made accordingly to the observations made on the field (observed change of section, recorded BTCs). In theory (Figure 1), the system should be divided in segments – or reaches - characterized by specific dimensions and transport parameters. Each reach should then be calibrated on basis of the intermediate sampling points; which means that each intermediate BTC is used as upstream boundary condition.

The present chapter first introduces the modelling tool chosen for the Furfooz system. Then, it describes the conceptual Furfooz system and its discretization in “reaches”. The modelling tool is then applied to the discretized conceptual Furfooz system. Validation of this global model is proposed through the use of sensitivity tests. Finally, the discrete numerical model will be used to evaluate the reaction of the system to low discharge, thanks to the calibration of the model on the single-peaked curves observed at very low discharge conditions (chapter 4, tracer tests 5 and 6, p. 108-111).

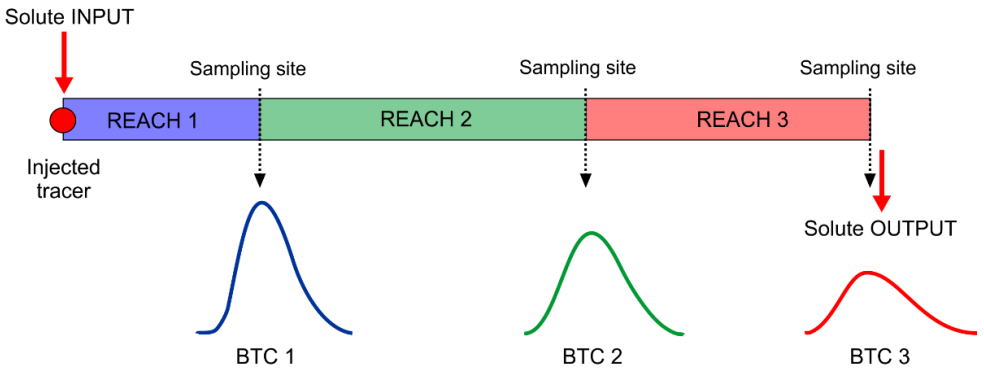

①

Calibration	USBC	DSBC
Reach 1	injected tracer	BTC 1
Reach 2	BTC 1	BTC 2
Reach 3	BTC 2	BTC 3

②

Discretization	USBC	DSBC
Whole system (reaches 1, 2,3)	Solute INPUT Injected tracer	Solute OUTPUT BTC3

Figure 1. The different steps of the modelling process of a heterogeneous karst system. USBC: Upstream Boundary Condition; DSBC: Downstream Boundary Condition (from Dewaide *et al.*, 2016).

6.2 The modelling tool

As said in introduction, the possibility to discretize the flow system offered by some programs is essential for the modelling of the Furfooz system. The OTIS program (Runkel, 1998) is one of the rare "open access" tool that offers this discretization possibility. In her PhD thesis, Bonniver (Bonniver, 2011) applied successfully the OTIS tool to the Belgian karst system of Han-sur-Lesse. The developed methodology and the efficiency of OTIS has been demonstrated in an article released in 2016: "Solute transport in heterogeneous karst systems: Dimensioning and estimation of the transport parameters via multi-sampling tracer-tests modelling using the OTIS (One-dimensional Transport with Inflow and Storage) program" (Dewaide et al., 2016). This paper is presented in Appendix 3. OTIS, developed by Runkel (Runkel, 1998), is a 1-D model considering only the longitudinal component of the dispersion and based on a two-region non equilibrium approach. OTIS was initially created to solve solute transport problematic in surface streams implying concentration variation in longitudinal direction only, and free elevation of the water level, features that are relevant for karst conduit flows. As shown in Figure 2, OTIS supposes a main dynamic flow in mobile zone, in which solute is transported by advection and affected by dispersion and, possibly, adsorption and decay. Next to the main channel, immobile zones, equally distributed along the main flow zone, exist. They act as transient storage zones for the solute that can be affected by chemical reactions, but where there is no transport by advection and dispersion. To permit storage in stagnant zones, an exchange between mobile and immobile water zones takes place. Finally, lateral flow can be added and/or retract from the main flow.

In accord with all these features, the OTIS program is guided by the following equations for conservative and non-conservative solutes (terms in square brackets):

$$\frac{\partial C}{\partial t} = -\frac{Q}{A}\frac{\partial C}{\partial x} + \frac{1}{A}\frac{\partial}{\partial x}\left(AD_L\frac{\partial C}{\partial x}\right) + \frac{qlin}{A}(C_{lin} - C) + \alpha(C_s - C) + [\rho\lambda'(C_{sed} - K_d C) - \lambda C] \quad (2)$$

and,

$$\frac{\partial C_s}{\partial t} = \alpha\frac{A}{A_s}(C - C_s) + [\lambda'_s(C'_s - C_s) - \lambda_s C_s] \quad (3)$$

where C, C_{lin} and C_s [M/L^3] are solute concentrations in, respectively, the main channel, the lateral inflow and the storage zone; A and A_s [L^2]the cross-sectional areas in the main channel and storage zone; Q [L^3/T] the volumetric flow rate; q_{lin} [$L^3/T.L$]the lateral inflow rate; D_L [L^2/T] the longitudinal dispersion coefficient; α [T^{-1}] the mass-transfer coefficient; t the time [T]; x the distance [L]. Considering non-conservative solute, C_{sed} is the sorbate concentration on sediment; C'_s the background storage zone solute concentration; K_d [L^3/M] the partition coefficient; λ and λ_s [T^{-1}] the first-order decay in the main channel and the storage zone; λ' and λ'_s [T^{-1}] the sorption rate coefficient in the main channel and the storage zone; ρ [M/L^3] the mass of accessible sediment by volume water.

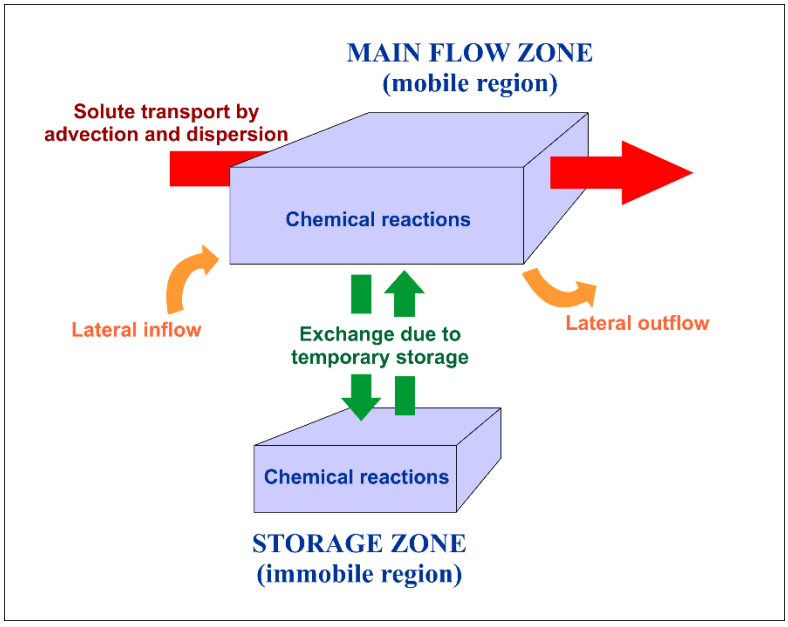

Figure 2. Main functioning principles in OTIS. Solute transport occurs in the main flow zone while an exchange with a storage zone exists (modified from Runkel, 1998).

However, the complexity encountered regarding the Furfooz BTCs modelling lies in the dual-peak appearance. In the previous chapter, we have proposed that the dual recoveries observed in the Furfooz system are the result of two different modes of transport in two different paths. The modelling of the double-peaked BTCs should then be performed in simulating solute transport in two conduits characterized by contrasted features. The use of OTIS to model double-peaked BTCs would imply to consider each peak separately and to apply the advection-dispersion equation to each one independently. That would mean that a

double-peaked BTC results from the superposition of two curves observed at the exit of two different paths that don't interact with each other. This concept is an important approximation of the reality, especially regarding the Furfooz case and the proposed hypothesis of a dual hydrodynamic that takes place within the lake. Field and Leij (Field and Leij, 2012) have developed a multi-dispersion model (DADE) and have demonstrated the relevance of using such a model instead of a weighted sum advection-dispersion model (WSADE) to simulate multi-peaked BTCs resulting from multiple path transport. The DADE does not, however, allow to discretize the flow system, nor to create an immobile water zone where the solute would be temporary stored.

For the Furfooz case, the use of OTIS in a weighted sum advection-dispersion approach is not accurate. The use of a multi- advection-dispersion model is clearly necessary. This model should furthermore offer the possibility to discretize the flow system and to propose the existence of immobile flow zones responsible for the strong tailing effect observed in some BTCs. As such a model wasn't available in the existing modelling tools, a new open-source model has been developed in the context of this thesis by A-J Tinet (University of Lorraine). This model is called OM-MADE (One-dimensional Model for Multiple Advection, Dispersion and storage in Exchanging zones). It has been successfully applied to the Furfooz BTCs in a submitted article named "OM-MADE: an open-source program to simulate one-dimensional solute transport in multiple exchanging conduits and storage zones" (Tinet et al., 2018). The submitted version of the paper, Appendix 4, describes the functioning of OM-MADE, validates the model against analytical solutions and other models (i.e. the DADE and OTIS). It finally proposes an application to the Furfooz case. The tracer test used for this application is the tracer test 3 performed in September 2013 in Furfooz (injection at the CN swallow hole) and presented in chapter 4. As the first aim of this article was to prove the efficiency of OM-MADE, the system discretization proposed in the paper is simplified compared to what is described below in section 6.3.1.

6.2.1 A new model: OM-MADE

The present section describes the general principle and equations of the OM-MADE program. All details about the numerical resolution scheme, the software architecture and the model validation can be found in the article stored in Appendix 4.

Figure 3 depicts the conceptual model of an OM-MADE simulation. OM-MADE is designed to simulate advection-dispersion in multiple, parallel transport zones that can exchange solute with one another, and with storage zones (not necessarily unique). These parallel zones are divided into reaches along the flow. In each reach, the defined parameters are kept constant. The flow rate is defined as an input parameter and is steady all along the flow, though lateral solute inflows and outflows can be simulated. The flow rate is nil in the storage zone. Decay and adsorption processes can affect the solute concentration in both mobile and immobile zones. OM-MADE is a one-dimensional model, making thus the assumption that the solute concentration varies only in the longitudinal direction.

Given the model assumptions and considering mass conservation, the solute transport in a zone *p,* which exchanges with other zones q, can be described by the following general equation:

$$A\frac{\partial C}{\partial t} = -Q\frac{\partial C}{\partial x} + \frac{\partial}{\partial x}\left(AD\frac{\partial C}{\partial x}\right) + q_{lin}\,(C_{lin} - C) + \sum_{q \neq p}\alpha_{qp}\left(C_q - C\right) - \lambda AC \qquad (4)$$

where t [T] is the time; x [L] the distance; A [L^2] the cross-sectional area of zone *p*; C, C_{lin} and C_q are the solute concentrations [CU] in, respectively, zone *p*, lateral inflow, and zone *q*; Q [L^3/T] is the volumetric flow rate in zone *p*; D [L^2/T] is the longitudinal dispersion coefficient; q_{lin} [L^2/T] is the lateral inflow rate per unit of distance; α_{qp} [L^2/T] is the exchange coefficient between zones *p* and *q*, multiplied by the exchange surface area; λ [T^{-1}] is the first order degradation coefficient in zone *p*.

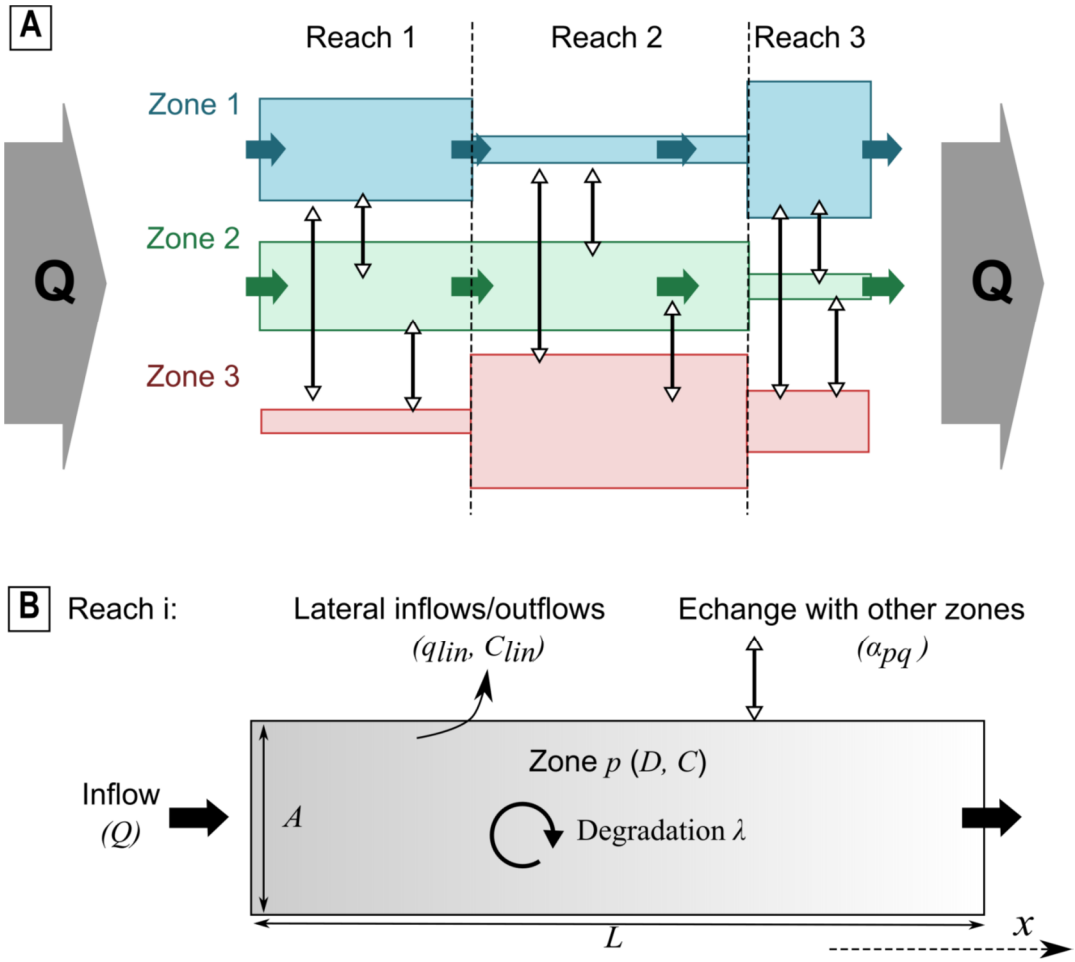

Figure 3. OM-MADE, functioning principles and characteristics. A) Three parallel zones are defined in this example. Two are transport zones with an imposed inflow at the entrance, the third zone is a storage zone in which the flowrate is nil. Solute exchanges occur between all the zones. The parallel zones are divided in reaches in which the transport parameters are kept constant along the reach. B) Details of a reach defined by its length (L), cross-sectional area (A), longitudinal dispersion coefficient (D), solute concentration (C). The solute concentration can be affected by degradation λ (sorption and/or decay), by the exchange(s) with other zones (α_{pq}), and by lateral inflows and outflows (from Tinet *et al.*, 2018).

In storage zone, Q is nil, as should be the mechanical dispersion. Molecular diffusion could, however, be considered in the value given to D. For example, the diffusion coefficient of fluorescein approximates 0.64E-9 m^2/s (Galambos and Forster, 1998), while this coefficient for sulforhodamine B is about 0.45E-9 m^2/s (Kapusta, 2010).

If adsorption affects a non-conservative solute, Equation (3) should be adapted with the following relations that describe sedimentation zones where Q is nil:

$$C = \frac{C_{sed}}{K_d} \quad (5)$$

$$\alpha_{qp} = \frac{M_{sed}}{L} \lambda' K_d \quad (6)$$

Where C_{sed} is the absorbed concentration on sediments; K_d [L^3/M] is the partition coefficient; λ' [T^{-1}] the adsorption coefficient on sediments; M_{sed} [M] the mass of available sediments; L [L] the total length of the sedimentation zone.

6.3 Modelling of the Furfooz conceptual system

Now that the modelling tool has been introduced, the present chapter aim to model the conceptual discretized system of Furfooz.

6.3.1 The Furfooz conceptual system

Before to start with the modelling of the system, it is important to first describe the conceptual system on which the discretization and the modelling will be based. This conception of the real system is based on the observations and investigations conducted on the field.

In this conceptual system, the tracer mixture enters the underground system through the CN swallow hole and flows through an unknown zone of 70 m before to enter the TQF cave. There, the water flows along a secluded and muddy river with a very small section (0.05 m^2 measured on the field at low flow conditions) on about 140 m. Flow-rate gauging has shown that there was actually more water at the TQF river than at the swallow hole. It is considered here that the complementary amount of water is added to the system from its start. It is also considered that the totality of the water that enters the system flows through the TQF river. Therefore, tracer losses have to be explained by degradation. After its flow along the TQF river, the tracer cloud arrives into the TQF lake and, further on, to the PDV lake. In these lakes, it is supposed that the tracer cloud is divided in two through a dual advection-dispersion process that starts as soon as the tracer enters the TQF lake. This dual advection-dispersion ceases when the tracer return to a “river type” flow section. The first point downstream the lake where this kind of section can be observed is the Sepulture cave, located 180 m downstream the visible part of the PDV lake. Furthermore, double-peaked BTCs, with the same features of those observed at the GDS, have been observed at the Sepulture. This indicates that the dual advection-dispersion stops before the fluorimeter of the Sepulture cave. From the Sepulture, the tracer flows to the GDS through a partially unknown river. The flow sections measured at the Sepulture are of about 0.7 to 1 m^2 in moderate discharge conditions, but from the end of the Sepulture to the GDS, the underground river cannot be followed. Finally, from the GDS, the river flows in direction of the TDL on about 400 m. Only the first 50 m of this section are known; the measured flow sections are of about 0.2 to 0.5 m^2 (so, smaller than the one observed at the Sepulture). At the TDL, the underground Lesse reappears in small basins and

conduits obstructed by boulders just before the final resurgence that is scattered through rocks.

6.3.1.1 Discretization of the conceptual system

The conceptual system of Furfooz has just been described. Some parts of this system are unknown. Therefore, the discretization in reaches of this conceptual system has to deal with some choices that are exposed hereafter. These choices have been made with the idea that the system should be kept simple.

Reach 1: from the CN swallow hole to the TQF lake – 210 m

It has been chosen to consider together the first unknown 70 m of the system and the TQF river portion of 140 m. Only one transport zone should be considered in this reach. Some storage is possible.

Reach 2: the lakes – 330 m

The two lakes represent big volumes of water, probably compartmentalized by rock boulders that create some kind of wall between the two lakes. However, giving their clear hydraulic connection and the similar role they should play on the solute transport, they will be gathered in a single reach. The downstream end of this reach is however unknown. It is chosen to define the end of this reach at the Sepulture cave, located about 180 m downstream the PDV site. In total, reach 2 approximates 330 m (150 m for the known part of the lakes + 180 m unknown). Two exchanging transport zones are effective within this reach.

Reach 3: the Sepulture to the GDS – 220 m

This segment constitutes the second meander crossing as the underground river crosses the surface River Lesse before to reach the GDS. Most of this segment is unknown. At the Sepulture however, the underground river can be followed along 20 m of a rather narrow but deep flow section (about 1 m deep in mid flow conditions). Only one transport zone is active in this reach, and potentially some exchange with a storage zone.

Reach 4: from the GDS to the TDL

This last segment, that measures about 400 m, can only be followed on 50 m at its beginning at the GDS. The flow section there is rather large but shallower than what's observed in reach 3. After that, several small pools succeed each other. The path of the river between these pools and the TDL is unknown. One transport zone, and a potential storage zone should be considered in this reach.

6.3.1.2 OM-MADE simulations

To operate to the modelling of the Furfooz conceptual system, one tracer test has to be chosen. This test should correspond to an injection at the CN swallow hole, resulting in a nice double-peaked BTC, made during steady flow conditions and with a maximum of observation points along the system to constrain the model. Tracer test 3 (chapter 4, p. 100-102) is the only test that corresponds to these characteristics. During this test, BTCs were sampled at the TQF river, the GDS cave (upstream GDSb), and at the TDL. No data could be sampled at the Sepulture, as this cave had not been discovered yet. The discharge conditions stayed steady during this test except around 200 h after the injection when a flood is recorded at the GDS. The discharge, measured on the day of the injection was 5.5 l/s at the TQF and 6l/s at the GDS. In the simulations, a steady discharge of 5.7 l/s is considered all along the system.

As explained in the OM-MADE paper (Tinet et al., 2018), if several flow zones have to be simulated along one reach of the system, all the other reaches must have the same number of flow zones. The exchange coefficient imposed between the zones will define if there is actually a multiple transport or if there is equilibrium between the zones. Indeed, setting a high exchange coefficient between two mobile zones is equivalent to consider a single conduit (as long as the flow velocities are the same in both zones). On the contrary, giving a small value to this exchange coefficient allows to simulate transport in two conduits that exchange solute. Eventually, setting this exchange coefficient to zero will simulate transport in two totally independent conduits. In the Furfooz case, the dual recovery should be simulated by means of two flow zones and one storage zone in reach 2. All the other reaches must then include the same number of zones. Therefore, in reaches 1, 3 and 4 the exchange coefficient between the two flow zones must be set to a very high value so the transport is actually secluded in one conduit. Regarding the discharge conditions, a mean value of 5.7 l/s is considered for this tracer test. It is chosen to distribute equally the discharge between the two flow zones, at the entrance of the discretized system. This equal partition remains therefore all along the discretized system. No lateral inflows are considered along the system. The totality of the tracer is injected in flow zone 1 only.

Figure 4 is a schematic representation of the simulations conducted with OM-MADE, in accordance with conceptual model described in section 6.3.1 and the discretization proposed in section 6.3.1.1. A very important fact to consider in this simulation is the absence of an observed BTC at the end of reach 2 (the lakes). Indeed, as explained in chapter 4, the BTC sampled at the surface of the PDV lake is not representative of the actual transport but illustrates mainly a diffusion and dispersion effect through the lake. Therefore, it cannot be used to calibrate reach 2. That implies the calibration of reach 2 and 3 together by fitting of the simulated curve on the BTC observed at the end of reach 3 (SEP-GDS). To do so, some hypothesis allow to somehow constrain the applied fitting parameters:

- The dual advection-dispersion transport is effective in reach 2 only. It is furthermore supposed that those two transport zones exchange tracer with one common storage zone ;
- From the curve observed at the Sepulture cave in tracer test 7 (chapter 4, p. 108), it appears that the main features of the two peaks (quick and narrow first peak, slow and wide second peak, strong tailing) are already well marked at the Sepulture. It can

therefore be supposed that similar characteristics observed at the GDS in other circumstances, are inherited from the transport through the lakes mainly. Furthermore, tracer test 8 (chapter 4, p. 109-111) has shown similar recovery rates at the Sepulture and at the GDS, showing that there is not much degradation between these two points. In other words, the influence of reach 3 on the BTC shape should be limited and impact mainly the time of transfer;

- Reach 3 acts as one transport zone that can exchange with a storage zone. This storage zone is kept limited, in accordance to what is observed on the field at the Sepulture cave;
- The flow section of reach 3 is kept in values close to 1 m^2, which corresponds to the section observed on the field. Of course, the downstream part of this reach is unknown; so the section could vary a bit but we supposed that it stays in the same order of magnitude.

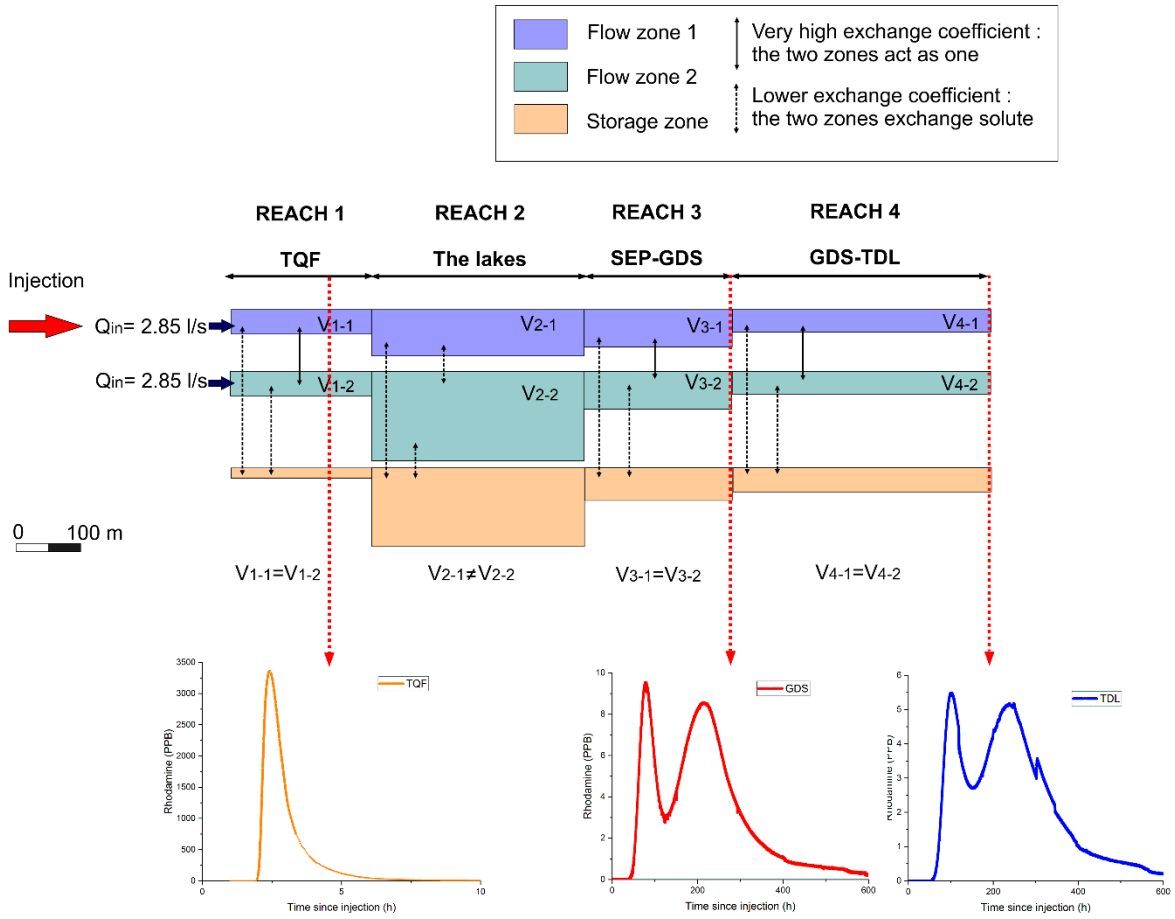

Figure 4. OM-MADE conceptual model for tracer test 3 (injection at the CN swallow hole in September 2013 – tracer test 3). Four reaches are defined along the flow. Each reach comprises three zones: two transport zones and one storage zone. However, the exchange coefficient between the two flow zones in one reach defines if there is actually a double transport or if the two zones act as one.

6.3.1.3 Calibration and final fitting

The OM-MADE simulation, based on the field BTCs and the hypothesis exposed earlier, proposes a global model that estimates the transport parameters for each reach. The simulation was performed with a chosen *dx* of 2.5 m and a *dt* of 360 s. The injection of 200 g of sulforhodamine B is performed in flow zone 1 only, as flow zone 1 and 2 act as one in reach 1. Considering a flow rate of 2.85 l/s, the input concentration corresponds to 194931 ppb during the first 360 s. The fitting was obtained by applying the following general methodology:

- The first arrival should be fitted at first, by accurately dimension the flow section;
- The rising limb is fitted. Its steepness is mainly defined by the dispersion coefficient of the concerned transport zone;
- The falling limb is fitted by adjusting the storage zone dimension and the exchange coefficient between the concerned transport zone and the storage zone.

This approach is, however, a bit complicated in the Furfooz case as the falling limb of the first peak and the rising limb of the second peak are, partially, unknown. Trial-error simulations remain the easiest way to assess the parameters, as they also permit to ensure their consistency with the field observations. The final result of the OM-MADE modelling by fitting of the simulated curves to the field ones is shown in Figure 5 and Table 1.

The fitting of the TQF and the GDS curves are very good, which is not the case for the BTC observed at the TDL, as explained hereafter. Solute transport in reach 1 leads to a narrow BTC with a small tail observed at the end of the recovery. Zone 1 and 2 of this reach act as a unique conduit of 0.334 m^2. With a constant flowrate of 5.7 l/s, the subsequent effective velocity (v) in this conduit is 0.017 m/s (62 m/h). The dispersivity (a), which corresponds to the division of D by the velocity, is limited to 0.6 m. Those parameters confirm the very advective behavior of the tracer to arrive at this first sampling site. It should also be said that these dispersivity and flow section values are a bit smaller, but similar, to the values estimated by QTRACER2 for the BTC observed at the TQF in tracer test 3 (chapter 4, section 4.2.3.3). Indeed, QTRACER2 proposed a dispersivity of 1.2 m and a cross-section of 0.43 m^2 for the flow section. A small storage zone is simulated to produce the small tail observed on the BTC. A strong degradation rate is applied to fit to the low tracer recovery in this reach.

In reach 2, the lowering of the exchange coefficient to 2e-7 allows the separation of the tracer in two exchanging transport zones which determines downstream the appearance of the double peak. The first flow zone generates the first peak, and the second zone generates the second peak, with strong interactions between the two zones. The two flow zones of reach 2 contrast by their dimensions: 2.05 m^2 for zone 1 and a voluminous zone 2 of 6.68 m^2, implying slower velocities in zone 2 (1.4e-3 m/s in zone 1 vs. 4.3e-4 m/s in zone 2). Both zones interacts with a large storage zone of 3.8 m^2, which explains the important tail observed at the GDS. The dispersivity is similar in both zones (10 m in zone 1, 9 m in zone 2). High degradation have to be considered in the transport zones and in the storage zone to reproduce the low observed recovery rates.

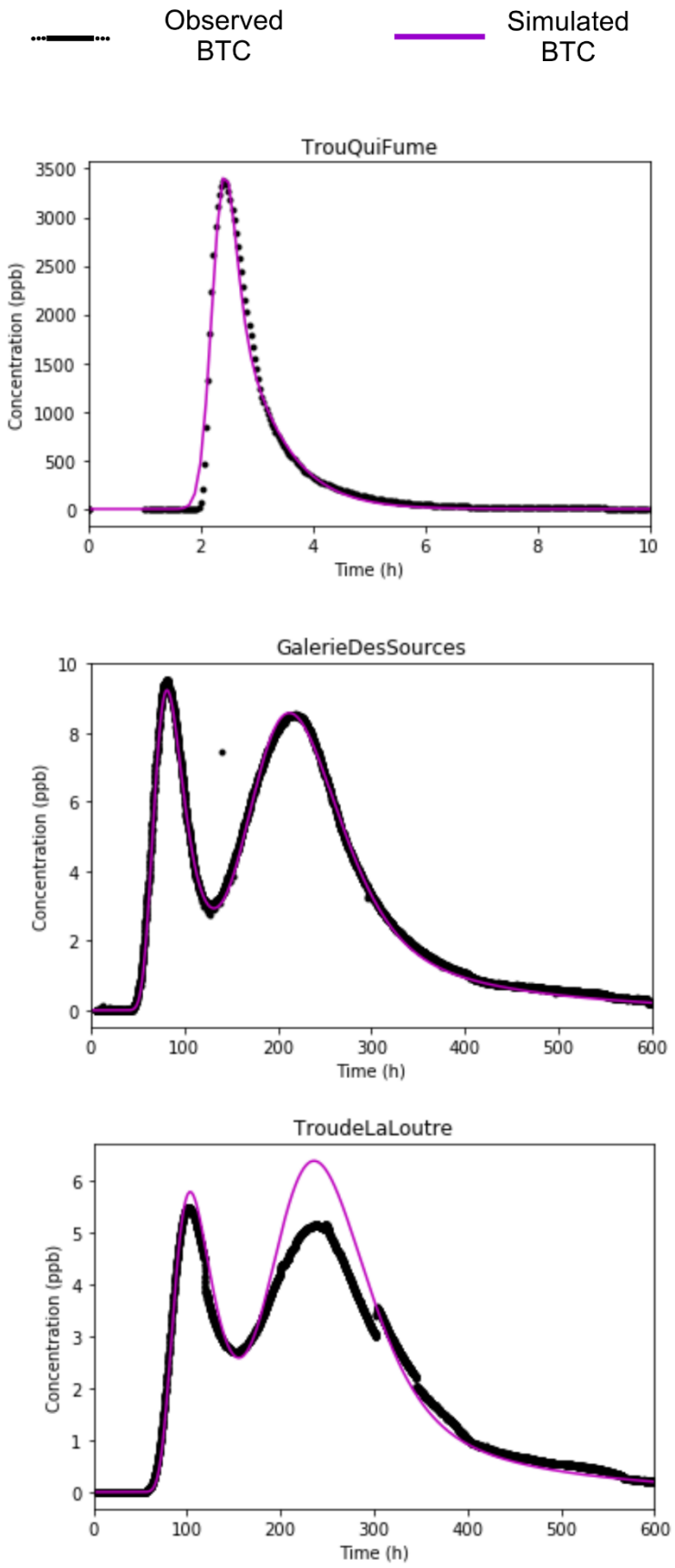

Figure 5. Fitting of the OM-MADE BTCs to the field BTCs. Three BTCs, observed respectively at the TQF river, the GDS and the TDL, are used for the fitting in order to calibrate each reach of the discretized system.

	REACH 1 – 210 m						
	A (m^2)	D_L (m^2/s)	a (m)	λ (1/s)	α_{ij} (m^2/s) Zone 1	Zone 2	Zone3
ZONE 1 (Q = 2.85 l/s)	**0.167**	**0.010**	**0.6**	**1.25e-4**	**0**	**1e-2**	**2.2e-5**
ZONE 2 (Q= 2.85 l/s)	**0.167**	**0.010**	**0.6**	**1.25e-4**	**1e-2**	**0**	**2.2e-5**
ZONE 3 (storage: Q= 0)	**0.063**	**0.45e-9**	**-**	**0**	**2.2e-5**	**2.2e-5**	**0**
	REACH 2 – 330 m						
	A (m^2)	D_L (m^2/s)	a (m)	λ (1/s)	α_{ij} (m^2/s) Zone 1	Zone 2	Zone3
ZONE 1 (Q = 2.85 l/s)	**2.05**	**0.015**	**10.7**	**1.0e-6**	**0**	**2e-7**	**8.2e-6**
ZONE 2 (Q= 2.85 l/s)	**6.68**	**0.004**	**9.4**	**2.6e-7**	**2e-7**	**0**	**1.8e-6**
ZONE 3 (storage: Q= 0)	**3.8**	**0.45e-9**	**-**	**4e-9**	**8.2e-6**	**1.8e-6**	**0**
	REACH 3 – 230 m						
	A (m^2)	D_L (m^2/s)	a (m)	λ (1/s)	α_{ij} (m^2/s) Zone 1	Zone 2	Zone3
ZONE 1 (Q = 2.85 l/s)	**0.77**	**0.011**	**3.0**	**0.8e-7**	**0**	**1e-2**	**1.8e-6**
ZONE 2 (Q= 2.85 l/s)	**0.77**	**0.011**	**3.0**	**0.8e-7**	**1e-2**	**0**	**1.8e-6**
ZONE 3 (storage: Q= 0)	**0.2**	**0.45e-9**	**-**	**0**	**1.8e-6**	**1.8e-6**	**0**
	REACH 4 – 400 m						
	A (m^2)	D_L (m^2/s)	a (m)	λ (1/s)	α_{ij} (m^2/s) Zone 1	Zone 2	Zone3
ZONE 1 (Q = 2.85 l/s)	**0.36**	**0.015**	**1.9**	**5.6e-6**	**0**	**1e-2**	**8.0e-6**
ZONE 2 (Q= 2.85 l/s)	**0.36**	**0.015**	**1.9**	**5.6e-6**	**1e-2**	**0**	**8.0e-6**
ZONE 3 (storage: Q= 0)	**0.2**	**0.45e-9**	**-**	**0**	**8.0e-6**	**8.0e-6**	**0**

Table 1. Transport parameters calibrated through the OM-MADE simulation for each reach of the discretized system. Note that the exchange coefficients between each zones are presented in the form of a matrix α_{ij} (with α_{ii} =0). The calculated dispersivity (a) is also displayed on the table.

Regarding reach 3, the applied parameters are, of course, very dependent of the choices made in reach 2. The parameters of reach 3 are however in accord with the hypothesis proposed in section 6.3.1.2: the degradation rate and the storage zone volume are kept limited; the total section of this reach is 1.57 m^2, which seems reasonable regarding the field knowledge. With these chosen parameters, reach 3 impacts mainly the travel time of the tracer as illustrated by Figure 6. This figure exposes the curve simulated at x = 540 m (end of reach 2) with the chosen set of parameters. When comparing this simulated curve with the curve observed at the GDS, it can be seen that the chosen set of parameters of reach 3 implies mainly a shift in time of the curve at x= 540 m.

Finally, the fitting of reach 4, on basis of the curve observed at the TDL, shows that the transport along this reach is made through a small conduit (0.72 m^2) with limited storage (0.2 m^2) and dispersivity (2 m). Some degradation (5.6e-7 in each transport zone) is necessary for the fitting. However, the fitting of the second peak at the TDL is not good, in the conditions defined by the conceptual model at least. The simulated second peak reaches higher concentration than the field one. This is perhaps due to the flood event that starts around 200 h after the injection (see chapter 4, Figure 11, p. 101). This rise of the discharge dilutes probably the second peak, at the TDL mainly. As the flow rate is kept constant, this dilution cannot be simulated.

It is very difficult to compare properly the fitted parameters with values described in the literature, because it is, of course, very dependent of the study context. Dispersivity values in karst conduit settings range usually from a meter to several tens of meters (Hauns, 1999; Massei et al., 2006; Morales et al., 2010). The minimum value obtained for Furfooz is 0.6 m in reach 1, and the maximum value is 10 m in reach 2, which is so consistent with literature values. Regarding the exchange coefficient, the comparison with literature would necessitate an extensive study that should first compare the definition of this exchange coefficient in different studies. Indeed, the mathematical expression of this coefficient varies with the model used for the BTC fitting. This comparison would therefore be very complicated and was not made in the context of this thesis.

As a short conclusion, it can be stated that the OM-MADE simulation has allowed to test the conceptual ideas proposed for the Furfooz system, and which relies on field observations. The simulation has succeeded to reproduce the BTCs observed in different sites of the Furfooz system during tracer test 3. It should be kept in mind that the modelling of the BTCs presented before depends of the choice of a set of parameters, but the solution is not unique. However, the hypotheses that have been formulated constrain the model. Taking into account these constraints and the chosen set of parameters that result from it, the simulation with OM-MADE has shown that the conceptual model is able to produce the double-peaked BTCs observed on the field and that the dual advection-dispersion transport is a relevant model for this issue. The proposed dimensioning is consistent with the field observations.

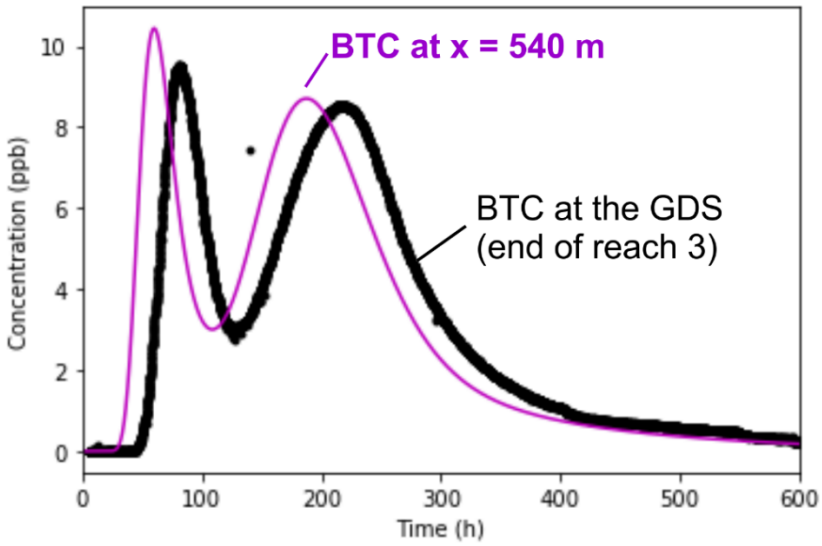

Figure 6. OM-MADE simulated BTC observed at x = 540 m, i.e. at the exit of reach 2 (the lakes). Given the parameters chosen in reach 3, the BTC observed at the exit of reach 2 is very similar to the BTC observed at the exit of reach 3, with a shift in time.

6.3.1.4 Sensitivity tests

Considering the conceptual system of Furfooz, reach 2 is the segment that determines the general shape of the two peaks of the BTC observed at the GDS. To evaluate the accuracy of the chosen set of parameters in reach 2 and to increase the confidence that can be given to the simulation, sensitivity tests are proposed. They consist in varying one parameter at a time, the other staying constant. These tests are run on reach 2 only, and the effect of the change of parameters is estimated at the GDS, in comparison with the initial fitted curve. The sensitivity of each zone is treated separately, and concerns three parameters: (i) the cross-sectional area of the storage zone (As), (ii) the dispersion coefficient (D) that concerns the transport zones only, and (iii) the exchange coefficient. The results of these tests are shown in Figure 7 (sensitivity of As), Figure 8 (sensitivity of D) and Figure 9 (for sensitivity of α_{ij}). The sensitivity of A in transport zones 1 and 2 is not considered as A is not really a fitted parameters but is imposed by the flow-rate - that is here imposed as equal in the two transport zones - and the length of transport.

Through Figure 7, it appears that the sensitivity of As is limited. The changes in the BTC shape is only noticeable for an increase or decrease of 50 % of the initial storage section. The changes impact mainly the junction between the two peaks and the tailing observed in the decreasing branch of the second peak. Of course, these observations are valid for the chosen set of exchange coefficient between the flow zones and the transport zones.

Regarding the sensitivity of the dispersion coefficient (Figure 8), clear reaction appears in zone 1 for changes of + or – 50 % of the initial dispersion value in zone 1. As the two zones are not independent, these changes of D in zone 1 have effects on both peaks. In transport zone 2, D is more sensitive: the decrease or increase of 10 % of the initial value has manifest effects on the second peak of the BTC. The increase of D moves the second peak earlier in time (because the simulated tracer cloud is more spread out), and, as a consequence the junction between

the two peaks happens at a higher concentration. The width and the tailing of the second peak are greater when D increases. Again, as the two zones are exchanging solute, the first peak is also influenced by the changes of D in zone 2, but only from – or + 50 %.

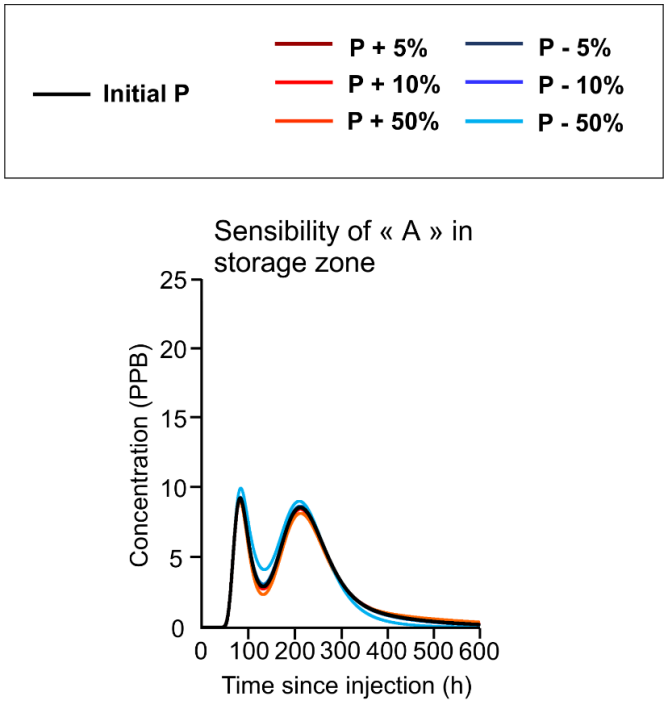

Figure 7. Sensitivity tests of the parameter "A" in the storage zone. The initial OM-MADE simulation [Initial P] is drawn. All the other curves are obtained by changing the concerned parameter [P] to a defined value.

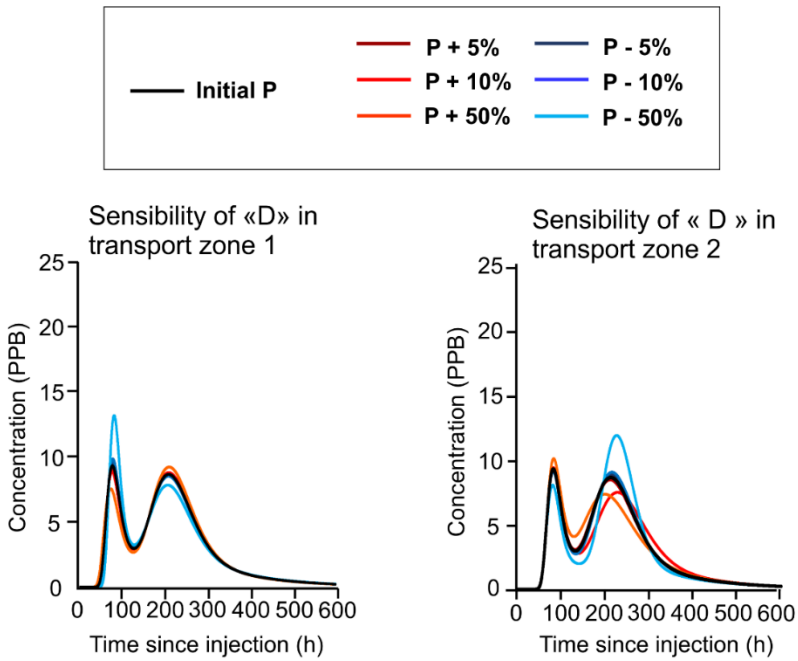

Figure 8. Sensitivity tests of the parameter "D" for transport zone 1 and transport zone 2.

Figure 9 depicts the sensitivity tests for the exchange coefficient parameters between each zone. Again, the observations that are given hereafter are valid only for the chosen values of the other parameters.

The exchange between the two transport zones (α_{12}) is poorly sensitive because, in this context, the minimum value of α_{12} that is necessary to produce two separated peaks is very low. The 50 % changes are barely visible on the graphs. Therefore, it was chosen to set α values that differs from the initial value (2.0E-7 m^2/s) with several order of magnitude. When α_{12} is set at 2.0E-8 m^2/s, the effect on the BTC nearly nil. This indicates that the initial value of 2.0E-7 m^2/s is the minimum exchange value needed to obtain two peaks that junction accordingly with the field data, for this set of parameters. When increasing the exchange to 2.0E-6 m^2/s, the influence of the exchange is clearly visible. The increasing of the exchange tends to moves the second peak earlier in time - which raises the level of the junction between the peaks - and to lower the C_{peak} of the first peak. At a value of 2.0E-5 m^2/s, there is only one peak with high concentration and a wide shape that appears.

The exchange between the flow zone 1 and the storage zone (α_{13}) is much more sensitive. The increase of the initial value has for effect to decrease the concentration of the first peak and to increase the concentration of the second peak; meaning that more solute of the first flow zone is transferred to the storage zone, which can, in turn, give more solute to the second flow zone. That depends of course of the exchange coefficients given to the two other zones, and to the size of the storage zone. The decrease of the α_{13} initial value acts in the opposite way and has a (small) effect on the tailing observed in the second peak.

Finally, the exchange between transport zone 2 and the storage zone (α_{23}) is determinant for the shape and time of arrival of the second peak. The effects of the change of – or + 50 % of the initial value are visible but rather limited. They impact only the concentration of the second peak but do not influence the first peak. The effect on the tailing is limited for these changes. When changing the order of magnitude of the initial value, the influence of α_{23} is clearer; especially for the increasing of the value to 1.8E-5 m^2/s. It can be seen that the tailing effect is more important supposing a greater transfer of the solute from the flow zone 2 to the storage zone, and in consequence the C_{peak} of the second peak is lower.

The sensitivity tests show that the simulation proposed in section 6.3.1.3 is accurate: for most of the parameters, the BTC shows significant deviation for changes applied to the parameters within 5 or 10 % of their initial value – the other parameters staying constant. The exchange parameter is less sensitive but it is, however, determinant for the separation of the tracer in two peaks and for the importance of the tailing observed in the descending branch of the second peak. The tests have also shown the strong dependency of the two transport zones that are due to the fitted exchange coefficients, the parameter variations in one flow zone having most of the time consequences on transport in the other flow zone.

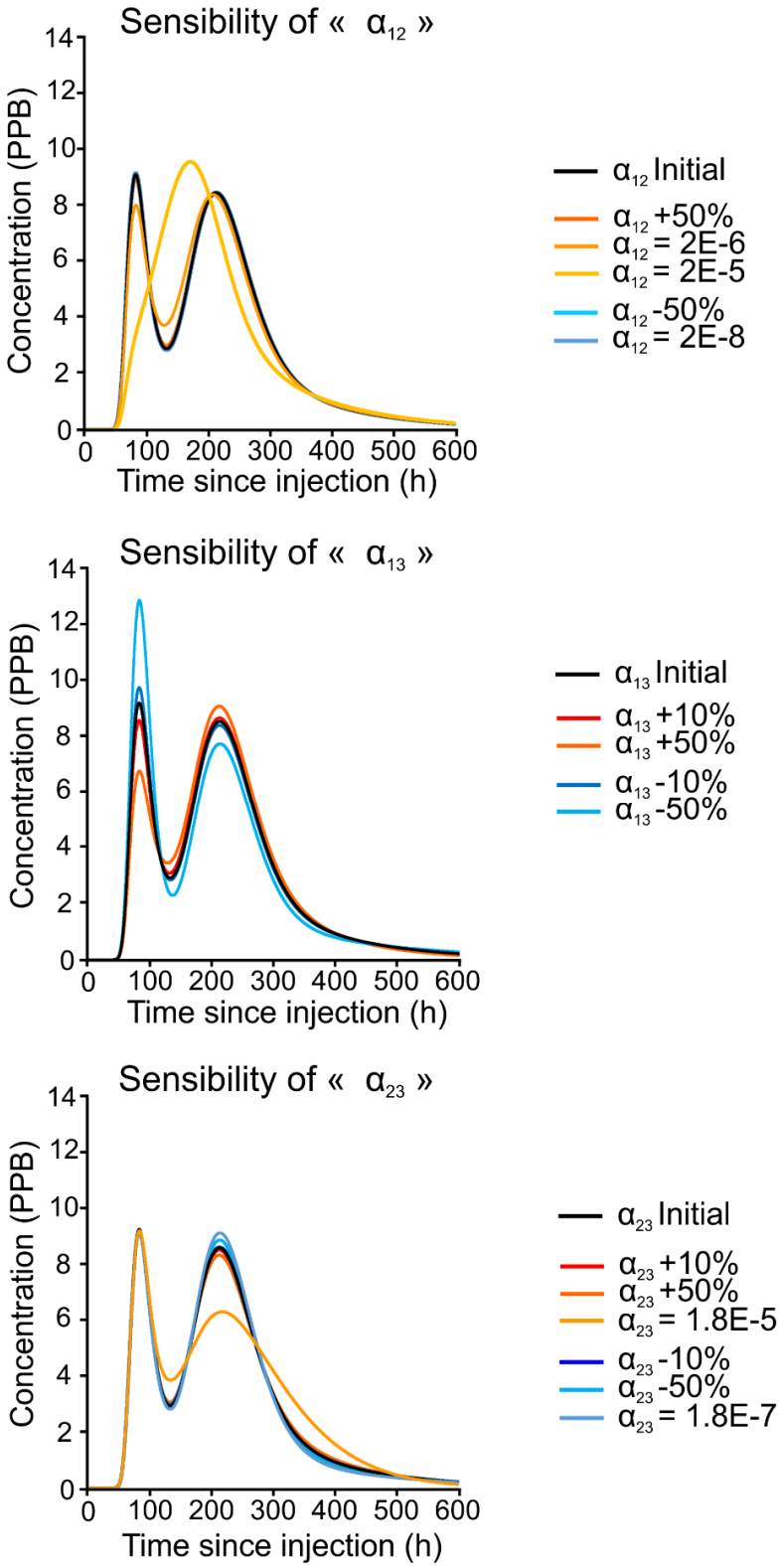

Figure 9. Sensitivity tests for the parameter α_{ij}, which defines the solute exchange between the zones ij. α_{12} corresponds to the exchange between transport zone 1 and transport zone 2, α_{13} is the exchange between transport zone 1 and zone 3 that is the storage zone, α_{23} determines the exchange between transport zone 2 and the storage zone.

6.3.2 The Furfooz conceptual model at very low discharge conditions

The simulation proposed in section 6.3.1.3 has shown that the hypothesis of the dual advection-dispersion transport in the lakes is relevant for the simulation of the double-peaked BTC in the conceptual system. In chapter 4, it has however been shown that the appearance of the double recovery is not systematic and depends mainly on the discharge. At very low flow conditions, an injection at the CN swallow hole results, at the GDS, in a single-peak BTC displaying a very strong tailing (tracer tests 5 and 6, chapter 4, p. 108-111). It has been proposed that the single peak corresponds to the first peak observed in the other double-peaked BTCs, while the second peak could be either absent (inactivation of the second flow zone), or hidden in the very strong tailing of the BTC.

To evaluate the possibility of these two proposals, it was chosen to perform simulations with OM-MADE on basis of tracer test 5. These simulations are based on the conceptual model of Furfooz described in section 6.3.1. However, some changes have to be applied, as the aim of the present simulations are to test the hypothesis exposed in the conclusion of chapter 4, that are:

- First hypothesis: the absence of the second peak is due to the inactivation of the second flow zone. Therefore, the dual advection-dispersion in reach 2 does not occur and the single-peak observed at the GDS is the result of only one flow path into the lake that interacts strongly with an important immobile zone to generate the very long tailing. The corresponding discretized model consists thus in one transport zone and one storage zone, discretized into three reaches (between the CN swallow hole and the GDS).

- Second hypothesis: this scenario proposes that the dual advection-dispersion occurs within the lake but that the second peak is not visible on the BTC observed at the GDS, because it is concealed in the tailing. It supposes a very slow and dispersive transport in transport zone 2, with potentially an important retardation, producing a wide, flared and asymmetric second peak.

Tracer test 5 constitutes the base of the simulations presented hereafter. It was realized at very low flow conditions (estimated Q_{mean} of 3l/s) and consisted in an injection of 200 g of fluorescein at the CN swallow hole. For the simulation purpose and according to the conceptual system, the system CN swallow hole-GDS is discretized in three reaches: (i) Reach 1 as the TQF river segment of 210 m; (ii) Reach 2 as the lakes segment of 330 m; (iii) Reach 3 as the Sépulture-GDS segment of 230 m. However, the BTC observed at the GDS is the only BTC available for the fitting of the parameters. This can therefore bring an important uncertainty on the model. Still, the aim of this simulation is not the calibration of the whole system but it is to test the two hypothesis exposed just before, with the assumed configuration of the Furfooz conceptual model.

Some postulates are made to constrain the simulation possibilities. The parameters of reach 1 and 3, in the present simulations, were indeed chosen taking into account the parameters fitted in tracer test 3 (section 6.3.1.3). Considering that, for tracer test 3, the flow section of reach 1 is fitted at 0.334 m^2, it is approximated (on basis of a simple rule of three) that the

flow section at 3l/s is about 0.176 m^2. The degradation rates are kept similar to those of tracer test 3. The same calculation is made for reach 3, so that a section of 0.8 m^2 is considered.

The simulations were realized with the same characteristics that the one used for the modelling of tracer test 3 in section 6.3.1.3: dt of 360s, dx of 2.5 m, discharge equally divided in the two flow zones, all the tracer injected in the first flow zone of reach 1 (185185 ppb during the first 360 s at 3l/s).

The result of hypothesis 1 is displayed in Figure 10, and the parameters calibrated with OM-MADE are shown in Table 2. In this simulation, only one transport zone exists in reach 2, and it exchanges with a storage zone. The total cross-sectional area of the only transport zone in reach 2 is 3.3 m^2, implying effective velocities of 9.10E-4 m/s. To simulate the very strong tailing, this flow zone has to interact with a voluminous storage zone (7.5 m^2 in section) with high exchange coefficients (1.3E-5). The total area section (transport zone + storage zones) is 10.8 m^2, which is smaller than the total section (transport zone 1 and 2 + transport zone) of 12.5 m^2 in tracer test 3. This observation is concordant with lower the flow conditions of tracer test 5.

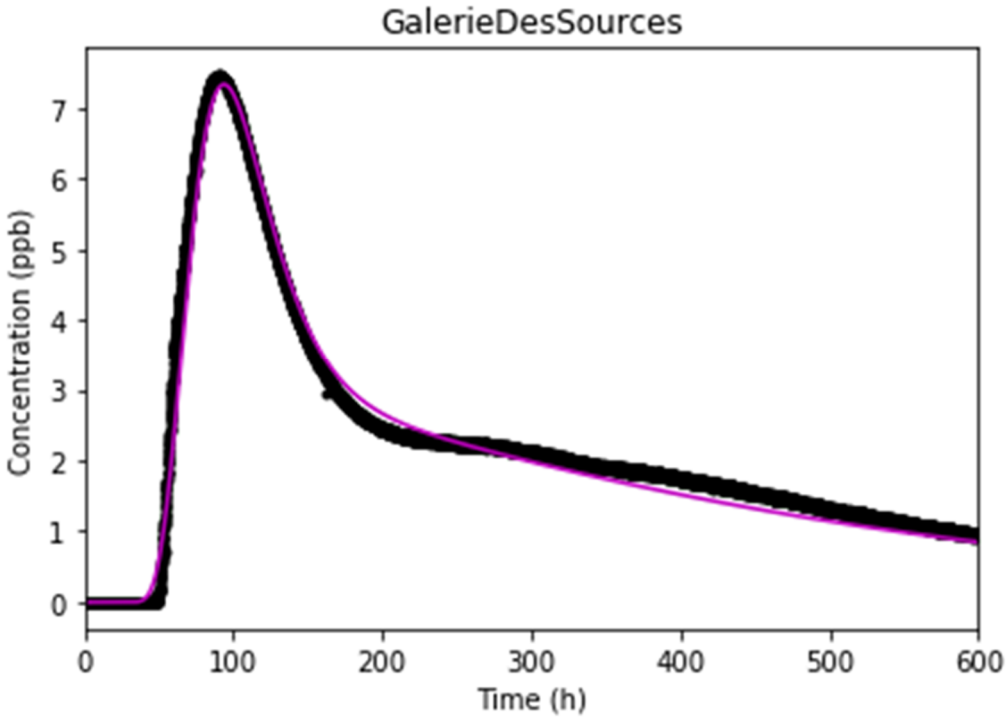

Figure 10. Fitting of the simulated curve to the BTC observed at the GDS. Only one effective transport zone is simulated in reach 2.

REACH 1 – 210 m					
	A (m^2)	**D_L (m^2/s)**	**λ (1/s)**	**α_{ij} (m^2/s)** Zone 1	Zone 2
ZONE 1 (Q = 3 l/s)	**0.176**	**0.009**	**2.1e-4**	**0**	**2.2e-5**
ZONE 2 (storage: Q= 0)	**0.01**	**0.6e-9**	**0**	**2.2e-5**	**0**
REACH 2 – 330 m					
	A (m^2)	**D_L (m^2/s)**	**λ (1/s)**	**α_{ij} (m^2/s)** Zone 1	Zone 2
ZONE 1 (Q = 3 l/s)	**3.30**	**0.030**	**1.0e-7**	**0**	**1.3e-5**
ZONE 2 (storage: Q= 0)	**7.5**	**0.6e-9**	**5.0e-8**	**1.3e-5**	**0**
REACH 3 – 230 m					
	A (m^2)	**D_L (m^2/s)**	**λ (1/s)**	**α_{ij} (m^2/s)** Zone 1	Zone 2
ZONE 1 (Q = 3 l/s)	**0.8**	**0.020**	**1.0e-7**	**0**	**7.0e-6**
ZONE 2 (storage: Q= 0)	**0.10**	**0.6e-9**	**0**	**7.0e-6**	**0**

Table 2. OM-MADE parameters used for the fitting of the simulated BTC on the field one, using one effective transport zone all along the system.

The second scenario succeeded also to reproduce the single-peaked BTC observed at the GDS (Figure 11). Table 3 presents the transport parameters used for the OM-MADE simulation. Reach 1 and 3 keep the same parameters than in the previous simulation of hypothesis 1. Reach 2 simulates two parallel flow zones exchanging solute with a rate of 2.0E-7 m^2/s. The two zones have very contrasted geometries as the cross-sectional area estimated for the first zone is 1.78 m^2 vs. 5.26 m^2 for zone2. Compared to the modelling of tracer test 3, the two zones are slightly smaller (2.05 m^2 for zone 1 and 6.68 m^2 for zone 2 in test 3). The effective velocities are respectively of 8.4E-4 m/s in transport zone 1, and 2.8E-4 m/s in transport zone 2. Both zones exchange with a very voluminous storage zone (11.5 m^2 in section) with rather high exchange coefficients (α_{13} = 6.9e-6 m^2/s, α_{23} = 2.2e-5 m^2/s). These exchanges with a big storage area are determinant in the appearance of the very strong tailing. The total area section (flow zone 1 and flow zone 2 + storage zone) is 18.54 m^2, so it is much higher than the total section of 12.5 m^2 in tracer test 3.

For a better understanding of the contribution of each zones to the BTC, the BTC at x=540 m, i.e. the exit of the lakes, was also simulated. The signal could be decomposed thanks to the numerical results of the simulation that allow to extract the contribution of each exchanging transport zones to the total BTC (Figure 12). This figure shows how the second peak is hidden in the tailing of the resulting BTC. The very flared shape of the second peak is mainly due to its strong interaction with the voluminous storage zone.

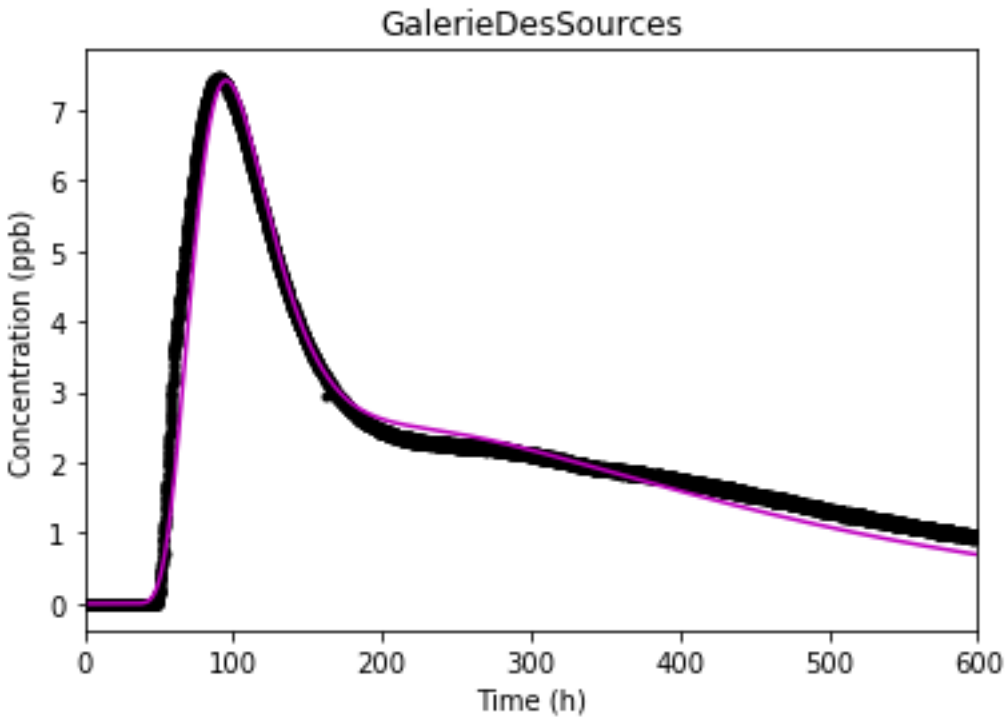

Figure 11. Fitting of the simulated curve to the BTC observed at the GDS. Two effective transport zones are simulated in reach 2.

Both scenarios have succeeded to reproduce with accuracy the field BTC. They do suppose a strong interaction of the flow zones with a voluminous volume of immobile water. However, in the second scenario, the dimensioning obtained to fit the simulated BTC to the field one supposes a total section (flow zone 1 + flow zone 2 + storage zone) of 18.54 m2. This value is much higher than the total section estimated in tracer test 3 (12.5 m^2). It is unlikely that the volume of water implied in the solute transport increases at lower flow conditions. Nevertheless, it should not be forgotten that a different dimensioning could have been achieved with different simulation choices. A more reliable dimensioning could maybe have been possible with, for example, another distribution of the flow-rate in both transport zones. Indeed, nothing justify, in case of two locally divergent conduits, that both discharge should be identical.

Scenario 1 (inactivation of the second flow zone) seems more reliable, once again on basis of the simulation choices. It proposes a total section of 10.8 m^2 that corresponds to 3.3 m^2 for the flow zone and 7.5 m^2 for the storage zone. The exchange rate between these two zones is high 1.3e-5 m^2/s. Therefore, it could be proposed that at very low discharge, the second flow zone is so slow that it becomes an immobile water zone. The storage zone area is therefore bigger at 3l/s (7.5 m^2) than at 5.7 l/s (3.8 m^2). Furthermore, due to the slower velocities in the unique flow zone, the residence time of the tracer in the flow zone is longer, offering more time for the tracer exchanges with this bigger storage zone. The exchange rates are, therefore, higher at 3 l/s (1.3e-5) than at 5.7 l/s (8.2e-6).

REACH 1 – 210 m						
	A (m^2)	D_L (m^2/s)	λ (1/s)	α_{ij} (m^2/s)		
				Zone 1	Zone 2	Zone3
ZONE 1 (Q = 1.5 l/s)	**0.088**	**0.009**	**1.75e-4**	**0**	**1e-2**	**2.2e-5**
ZONE 2 (Q= 1.5 l/s)	**0.088**	**0.009**	**1.75e-4**	**1e-2**	**0**	**2.2e-5**
ZONE 3 (storage: Q= 0)	**0.010**	**0.6e-9**	**0**	**2.2e-5**	**2.2e-5**	**0**
REACH 2 – 330 m						
	A (m^2)	D_L (m^2/s)	λ (1/s)	α_{ij} (m^2/s)		
				Zone 1	Zone 2	Zone3
ZONE 1 (Q = 1.5 l/s)	**1.78**	**0.026**	**1.6e-7**	**0**	**2e-7**	**6.9e-6**
ZONE 2 (Q= 1.5 l/s)	**5.26**	**0.0032**	**1.5e-6**	**2e-7**	**0**	**2.2e-5**
ZONE 3 (storage: Q= 0)	**11.5**	**0.6e-9**	**8.9e-7**	**6.9e-6**	**2.2e-5**	**0**
REACH 3 – 230 m						
	A (m^2)	D_L (m^2/s)	λ (1/s)	α_{ij} (m^2/s)		
				Zone 1	Zone 2	Zone3
ZONE 1 (Q = 1.5 l/s)	**0.4**	**0.022**	**1.4e-7**	**0**	**1e-2**	**9.0e-6**
ZONE 2 (Q= 1.5 l/s)	**0.4**	**0.022**	**1.4e-7**	**1e-2**	**0**	**9.0e-6**
ZONE 3 (storage: Q= 0)	**0.1**	**0.6e-9**	**0**	**9.0e-6**	**9.0e-6**	**0**

Table 3. Transport parameters calibrated through the OM-MADE simulation for each reach of the discretized system. Dimensionning proposed in the second scenario of the single-peaked BTC explanation (two flow zones and one storage zone).

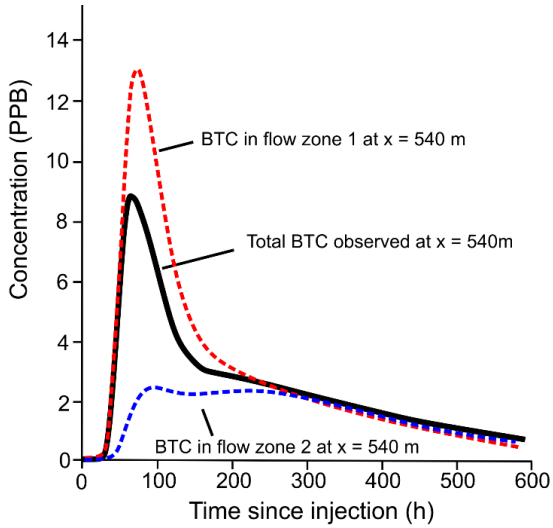

Figure 12. The BTC that would be observed at the exit of the lakes area (x=540 m) and the contribution of each transport zone in this BTC.

6.4 Conclusion

This chapter has shown the efficiency of a new modelling tool on the Furfooz BTCs. This tool has been specially designed for the modelling of solute transport in exchanging multiple flow and storage areas. The modelling of the double-peaked BTCs observed in the Furfooz system needs such an approach to be accurate. It demonstrates that a dual advection-dispersion in two zones with strong dependence could explain the double-peaked BTC observed in Furfooz. This dual advection-dispersion has been modeled in the lakes area only, in accordance with the field observations exposed in chapter 5 and the resulting conceptual model exposed in section 6.3.1. At this point, the modelling does not allow further interpretation: the dual-advective exchanging zones could be an effect of the lakes or an expression of a local auxiliary conduit that diverts the solute transport and then transports it back to the main conduit (Tinet *et al.,* 2018).

The observation of single-peaked BTC at the GDS at very low discharge conditions was explained in chapter 4 by two possible scenarios: the inactivation of the second flow zone on the one hand; the presence of the second peak in the strong tailing of the single-peak on the other hand. The modelling, based on these two scenarios has shown that both scenarios are possible from a numerical point of view. However, the dimensioning proposed for the second scenario seems unrealistic. Considering the postulates made in the conceptual model, it seems that, at very low discharge conditions, the second flow zone in the lakes is acting as immobile water. In consequence, the total volume of immobile water is bigger at very low discharge and the exchange rates are higher, which explains the very long tailing observed in the single-peaked BTC. It should not be excluded that a different conclusion could have been proposed with different simulation choices, especially regarding the flow-rate distribution between the two flow zones.

The various modelling made in the present chapter have been efficient and they highlight interesting facts and behaviors that can be related to field realities. It should always, however,

be kept in mind that the proposed simulations simplify a complex reality and rely on chosen conceptual ideas. Other fits could probably be achieved with other simulation choices, as, for example, the distribution of the flow-rate between the flow zones (equally distributed in our simulations), or the length of the reaches. Nevertheless, a global behavior implying the existence of two advection-dispersion exchanging zones within the lakes was simulated through numerical modelling and its relevance has been shown. To improve the reliability of this model, some complementary field information should be added. Particularly, a tracer test, made in steady discharge conditions, and that would gather BTCs at each sampling site including the Sepulture cave, would be precious.

Chapter key points:

- A new modelling tool (OM-MADE) has been developed to fit to the features required for the modelling of the Furfooz system: discretization and multiple exchanging advection-dispersion flows with storage zones;
- A conceptual system of Furfooz, based on field observations, is defined;
- Discretization of this system supposes some choices, as part of the system is unknown;
- Once all the postulates are defined, numerical simulation with OM-MADE is performed. The field BTCs could be successfully reproduced. It demonstrates that a dual advection-dispersion in two exchanging flow zones that interact with a storage zone, can explain the double-peaked BTC observed in Furfooz;
- The modelling with OM-MADE could explain the single-peaked BTCs observed at very low discharge by a possible inactivation of the second flow zone that is, actually, converted in storage zone.

6.5 References

Bonniver, I. (2011). *Etude hydrogéologique et dimensionnement par modélisation du « système-traçage » du réseau karstique de Han-sur-Lesse (Massif de Boine – Belgique)*. PhD thesis, University of Namur, Belgium, 350 p.

De Marsily, G. (1986). *Quantitative hydrogeology. Groundwater Hydrology for engineers*. New-York: Academic Press. 464 p

Dewaide, L., Bonniver, I., Rochez, G., & Hallet, V. (2016). Solute transport in heterogeneous karst systems: Dimensioning and estimation of the transport parameters via multi-sampling tracer-tests modelling using the OTIS (One-dimensional Transport with Inflow and Storage) program. *Journal of Hydrology*, *534*, 567–578. https://doi.org/10.1016/j.jhydrol.2016.01.049

Field, M. S., & Leij, F. J. (2012). Solute transport in solution conduits exhibiting multi-peaked breakthrough curves. *Journal of Hydrology*, *440–441*, 26–35. https://doi.org/10.1016/j.jhydrol.2012.03.018

Field, M. S., & Pinsky, P. F. (2000). A two-region nonequilibrium model for solute transport in solution conduits in karstic aquifers. *Journal of Contaminant Hydrology*, *44*(3–4), 329–351. https://doi.org/10.1016/S0169-7722(00)00099-1

Galambos, P., & Forster, F. K. (1998). Micro-fluidic diffusion coefficient measurement. In J. Harrison & A. Van den Berg (Eds.), *Micro Total Analysis Systems '98* (pp. 189–191). Baff, Canada: Kluwer Academic Publishers.

Hauns, M., Jeannin, P.-Y., & Atteia, O. (2001). Dispersion, retardation and scale effect in tracer breakthrough curves in karst conduits. *Journal of Hydrology*, *241*(3–4), 177–193.

Hubbard, E. F., Kilpatrick, F. A., Martens, L. A., & Wilson, J. F. (1982). Measurements of time of travel and dispersion in streams by dye tracing. In *Techniques of Water Resources Management - Book 3*. Washington, DC.: US Geological Survey.

Kapusta, P. (2010). *Absolute Diffusion Coefficients: Compilation of Reference Data for FCS Calibration*. PicoQuant GmBh. https://doi.org/10.1209/0295-5075/83/46001

Kreft, A., & Zuber, A. (1978). On the physical meaning of the dispersion equation and its solutions for different initial and boundary conditions. *Chemical Engineering Science*, *33*(11), 1471–1480. https://doi.org/10.1016/0009-2509(78)85196-3

Maloszewski, P., Harum, T., & Benischke, R. (1992). Mathematical modelling of tracer experiments in the karst of lurbach system. *Steirische Beiträge Zur Hydrogeologie*, *43*, 116–136.

Maloszewski, P., & Zuber, A. (1989). Mathematical models for interpreting tracer experiments in fissured aquifers. In *The Application of Isotope Techniques in the Study of the Hydrogeology of Fractured and Fissured Rocks* (pp. 287–301). IAEA.

Martin, J. L., & McCutcheon, S. C. (1998). *Hydrodynamics and Transport for Water Quality Modeling*. London, UK: Lewis. 816 p.

Rossier, Y., & Kiraly, L. (1992). Effet de la dilution sur la détermination des dispersivités par interprétation des essais de traçage dans les aquifères karstiques. *Bulletin Du Centre d'Hydrogéologie de l'Université de Neuchâtel*, *11*, 1–15.

Runkel, R. L. (1998). One-dimensional transport with inflow and storage (otis): a solute transport model for streams and rivers. *Water-Resources Investigations Report 98-4018*, *98*(4018), 0–80. https://doi.org/Cited By (since 1996) 47\nExport Date 4 April 2012

Tinet, A., Collon, P., Philippe, C., Dewaide, L., & Hallet, V. (2018). OM-MADE : an open-source program to simulate one-dimensional solute transport in multiple exchanging conduits and storage zones. *Computer and Geosciences*. Submitted

Werner, A., Höltz, H., & Maloszewski, P. (1997). Interpretation of tracer tests in karst systems with unsteady flow conditions. In C. Leibundgut, J. Gunn, & A. Dassargues (Eds.), *Proceedings of an international workshop held at Rabat, Morocco during the fifth scientific assembly of the IAHS (23 April to 3 May 1997)* (pp. 15–26). IAHS Publication.

Chapter 7

Conclusions and Perspectives

Chapter 7 Conclusions and Perspectives

The work developed in this thesis tackles karst aquifer issues from two points of view that are the karstogenesis – or karst development – through the massif of Furfooz, and the hydrodynamic of solute transport in conduits.

7.1 Summary and main outcomes

7.1.1 Karstification

The massif of Furfooz mainly originates from Waulsortian sediments of Tournaisian-Visean age (Waulsort Formation and lateral equivalents) that were deposited in the form of a mud-mound characterized by a length of several kilometers and a thickness of at least 300 m (Lees, Hallet, and Hibo, 1985; Lees, 1982). A pervasive and heterogeneous dolomitization affected these deposits, leaving today a limestone massif punctuated with dolomite patches.

Today‘s observations have highlighted a privileged development of karst within the dolomite patches. The investigations conducted in this doctoral research led to the proposal of a karstogenesis model mainly based on cathodoluminescence interpretations. In this model, we suggested that the porosity development in the studied dolomitized zones of the Furfooz massif is closely related to dedolomitization and calcitization processes. Part of the interpretation relies namely on the revealing of a petrographic gradient in which dolomite is replaced by calcite (dedolomite) when approaching the porosity network that can be partially or totally filled by calcite cement. In this context of study, the cathodoluminescence alone does not allow to infer with accuracy the paleo-environment conditions in which the various geochemical changes took place. Complementary analyses point out the meteoric signal that characterizes the isotopic composition and the fluid inclusions content of some samples. The Laser-Induced Breakdown Spectroscopy (LIBS) technique has allowed to give some geochemical references to the petrographic gradient observed at the sample scale. It has brought to light the variability of some chemical elements within the petrographic gradient and gives therefore some clues about the environmental changes that could have occured. The results, pending confirmation on other samples and insurance of their repetitiveness, are in accordance with oxidizing conditions that could prevail in an open system where karstification under meteoric influence could have taken place. In addition to the geochemical gradient, the LIBS images have also revealed a textural gradient in the dolomite that consists in a porosity increase towards the dedolomite zone.

This porosity development and the accompanying geochemical processes could have initiated the karstification process of the massif that leads to the existence of interconnected flow paths allowing groundwater flow.

7.1.2 The karst conduit system of Furfooz

In this thesis, the study of the groundwater flow has been limited to the behavior of the underground river in karst conduits.

Amongst the numerous karst development of the Furfooz massif, some correspond today to hydraulically interconnected conduit networks hosting an underground river. This river is due to the partial infiltration of the surface River *Lesse* in a swallow hole (CN swallow hole). The river flows underground on about 1.2 km before the diffuse resurgence ("Trou de la Loutre" - TDL). On its path, the underground river crosses two lakes: the "Trou Qui Fume" (TQF) lake and the "Puits des Vaux" (PDV) lake. Two other karst networks guarantee the access to the underground *Lesse*: the "Sépulture" (SEP) and the "Galerie des Sources" (GDS).

7.1.2.1 Monitoring

A monitoring of the Furfooz conduit system was realized during the last 6 years. It has allowed to characterize the hydrologic behavior and functioning of the system. It consisted in the continuous follow-up (through probes) of the water-level and physico-chemical data of the underground river in the various cave networks, as well as punctual flow-rate gaugings in various sites of the system. The compilation of these data have highlighted a behavior of the underground system that is coherent with – and sensitive to – the changes in surface run-off. A hydrograph could be built for the discharges evolution at the GDS, which is the only site where regular gauging can be made. The data have shown that the discharges seem to remain steady along the system, in low to moderate flow conditions at least. Finally, the chronicles reveal a singular behavior of the PDV lake which has a higher mean electric conductivity and shows some delay in its reaction to floods, compared to the downstream site of the GDS.

7.1.2.2 Tracer tests

Fifteen tracer tests were performed in the Furfooz underground system, in different discharge conditions and from different points of injection. A multi-sampling sites strategy was considered for each test in order to characterize solute transport in the different parts of the system. The tracer tests have brought to light a complex functioning of the Furfooz system, mainly due to the contrasted geometry of its conduits. This complexity appears in the double-peaked breakthrough curves (BTC) that were sampled downstream from the lakes, i.e. at the Sepulture cave, the GDS and the TDL. On the basis of field information (tracer tests, gauging, flow section measurements, etc.), it could be proposed that the separation of the tracer cloud, and the consequent double recovery, must happen in the area of the system that corresponds to the lakes. The two peaks display a different shape, which illustrate a different hydrodynamic behind each peak. The first and narrow peak results from a quick and rather advective

transport, while the second wide peak exhibits a slow and dispersive behavior. Given these strong differences, the two peaks must result from (at least) two different transport mode of transport.

A conceptual model, based on the field information, is proposed. It suggests that the separation of the tracer cloud is linked to the strong heterogeneity of the tracer flow distribution within the lakes due to the existence of an advective flow that crosses the lakes in depth. This advective flow would quickly transport the cloud of tracer downstream from the lakes, giving the first peak of the BTC. During its transport, the cloud of tracer would be exchanged with a big volume of slower water within the lake, and dispersed through it. The exit of the PDV lake could be made through two different conceptual ways. In the first hypothesis, the dispersed tracer could get out of the lake through a bifurcated conduit that would be located at the surface of the lake. The second scenario supposes no bifurcation but the exit of the dispersed tracer through the same path as the advective flow. In any case, the conceptual model proposes the existence of two zones of transport within the lake.

The performed tests have also shown the strong influence of the discharge on the BTC and on the relative shape of the two peaks. The second peak seems more flow-rate dependant, in term of transport time and BTC shape. The influence of the discharge appears also clearly at very low flow conditions. In these conditions (under 5 l/s), the BTCs observed at the GDS exhibit only the first peak with a very strong tailing. This could be linked to the inactivation of the bifurcated exit at the surface of the lake, or the effect of a very slow second zone of transport that exports the tracer in a very flat and wide curve, actually hidden in the very long tail.

7.1.2.3 Modelling

Both physical and numerical modellings were performed in this research. They both rely on a conceptual vision of the Furfooz karst system. Their aim is mainly to test the hypotheses on which is based the conceptual model of Furfooz. The modelling is therefore very much constrained by these strong hypotheses.

The physical modelling was performed through the use of a scale model of the conceptual Furfooz system. Some conditions were imposed in order to respect some dynamic and geometric similarities with the field observations. The scale model has demonstrated that it is possible to produce a double-peaked BTC when considering two exchanging transport zones within an important volume of water that have both a common exit to a single conduit. The scale model has also shown the strong influence of the imposed flow-rate on the BTCs.

The numerical modelling was made thanks to a new modelling tool called OM-MADE (Tinet et al., 2018). With this software, it is possible to simulate advection-dispersion transport in multiple exchanging zones that can also exchange with one or several storage zones. The conduits can be discretized in reaches. The conceptual system of Furfooz was tested and a dimensioning could be proposed. Taking into account the constraints imposed to the model,

the dimensioning of the system achieved thanks to the fitting of the simulated curve to the field one shows that the cloud of tracer is separated within the lakes area between two partially dependent zones of transport that exchange with a voluminous storage zone. The two transport zones contrast by their section sizes (2.05 m^2 vs 6.68 m^2), and, given the imposed equal distribution of the flow-rate between the zones, contrasted effective velocities (1.4e-3 m/s in zone 1 vs. 4.3e-4 m/s in zone 2). The dispersivities calculated in both zones are however very similar (about 10 m). This dimensioning of the system should be relativized as other fits could be achieved with other choices or postulates, in particular regarding the distribution of the discharge between the transport zones. However, the simulation with OM-MADE shows that the conceptual model is able to produce the double-peaked BTCs observed on the field and that the dual advection-dispersion transport is a relevant model for this issue.

7.2 Perspectives

7.2.1 Karstogenesis

The karstogenesis approach of this work has revealed very specific and interesting processes (porosity creation, dedolomitization, calcite cementation) that are somehow related to the overall and still ongoing karstification of the Furfooz massif. These processes imply geochemical and textural changes that should be linked to the geological and structural history of the massif. The timing of these changes should be defined through the establishment of a precise paragenesis of the different events that have impacted the waulsortian mud-mounds from their origin to their present status of karst reservoir.

The analyses performed in this doctoral research have pointed out some directions of reflection regarding namely the paleo-environmental conditions that lead to variations in some geochemical markers. These results were however established on observations made on a very limited numbers of sample. A first step would be, of course, to define if the established results can be generalized to the entire massif of Furfooz and the surrounding waulsortian mudmounds (Pont-à-Lesse, Freyr, Waulsort, Moniat,…). The connectivity of the “dolostone cavity type” bodies could also be investigated. This approach could indeed be relevant to tackle the question of the permeability development within the massif and the structuration of the karst conduits.

Finally, a comparison with other Waulsortian massifs that could have experienced other environmental and hydrogeological evolution should be envisaged. This comparison could also be made with other carbonates showing similar processes, but from different ages and different settings, in order to define common features or major dissimilarities that are determinant in the karstogenesis evolution.

7.2.2 Solute transport issue

In this thesis dissertation, the solute transport issue has been tackled under the experimental angle, i.e. by basing the reflections on field facts. The number of field information that could feed this problematic are potentially endless. More chronicles, more flow-rates measurements, more tracer-tests, etc. could always be added to precise some behaviors of the underground system. The present outlooks concentrate, however, on information that could constitute a real gain to this experimental approach.

About the double-peak BTC issue, it is clear that more data could be gathered on the lakes, namely regarding the heterogeneous distribution of the tracer. A very concrete and reasonable experiment that could be set up is the positioning of several fluorimeters, at different depth and during the same tracer test, at the PDV lake. This could help to characterize the advective flow supposed in the conceptual model of the lakes. The experiment could even be repeated in different discharge conditions (including at very low discharge) to evaluate its influence on the advective flow. These experiments should furthermore be done with a precise and continuous monitoring of the water-level both at the PDV lake and at the TQF lake. In a more global approach, these kinds of investigation could be exported to other case studies where contrasted geometries would be encountered. Would such case studies be illustrated by double-peaked BTCs or not? A general promising topic that arises from the present research is the characterization of the tracer distribution, in three dimensions, with regard to the flow section. The development of cost-effective flow-through fluorimeters (Poulain et al., 2017) opens to new perspectives, notably in this topic.

Another possible progress in the understanding of the Furfooz system relates to the double meander crossing. This feature of the system was a bit overlooked in the present research because the study possibility was limited. However, the recent discovery (February 2017) of the Sepulture cave, located just upstream of the second meander crossing, constitutes a real opportunity to investigate this problem. It could, furthermore, highlight interesting outcomes about the global issue of surface-underground water exchanges.

Finally, some perspectives can be proposed regarding the numerical modelling with OM-MADE. Although the tool has been useful to test the hypotheses put forward in the conceptual model of Furfooz, the dimensioning of the system remains questionable. A clear improvement could be achieved by constraining the model with a BTC sampled at the Sepulture cave, in addition to samplings at the TQF, the GDS and the TDL sites. It would also be interesting to test the sensitivity of the model regarding the discharge distribution between the two flow zones. In addition, the model could be tested with a more precise discretization of the system, notably in separating reach 1 in two reaches; i.e. a first one corresponding to the first 70 m of the system that remains unknown, and a second reach that would be the 140 m of the TQF secluded river where the flow section is measurable. Another improvement, related to the tool itself, would be the possibility to perform simulations at variable discharges. The total transit time of the BTCs in Furfooz being several hundreds of hours, it is indeed unlikely that the discharge stays steady for the entire duration of the test. Finally, the creation of OM-MADE

has been initiated thanks to this research, and it gives new modelling opportunities to other sites where multiple advection-dispersion paths are supposed.

7.3 Final comment: karstogenesis vs. solute transport

Seven years of doctoral research were devoted to the study of the karst of the Furfooz Waulsortian massif. The same object was studied under two different angles that are developed in this manuscript in different chapters. The question of the link between these two problematics is, however, a real scientific challenge. This issue should be part of a more global approach where the dynamic of the Furfooz sedimentological basin is taken into account for the understanding of the karst evolution within the massif. It has been defined that the “dolostone cavity types” were developed along structural discontinuities that have mainly the direction of the regional bedding and diaclases. The karst conduit networks, where flows the underground river, have the same development orientations. The structural approach is therefore a key point that would necessitate an extended study focusing on the basin dynamics. Furthermore, focus is given in this thesis to the impact of the contrasted geometries of the flow sections on the solute transport. But what is the origin of these contrasted geometries? The specific karstogenesis highlighted in the dolomitized sections of the mudmounds could have influenced the geometries of the conduits. More specifically, the presence of the large volumes of the lake could be questioned. The karstogenesis model, presented in chapter 2, proposes that the karst development initiates with an extensive dolomite dissolution that should, at one point, have created a highly porous material (“ghost rock” theory). Could the lakes be the result of the evacuation of this material? All these questions of possible links lead to more general perspectives of research that concerns the development of porosity within a massif and its structuration into a pervious and heterogeneous aquifer.

Karst aquifers are complex objects of study. This complexity, due to their spatial heterogeneity and temporal variability, is also a source of vulnerability. Yet, karst aquifers are essential groundwater resources all over the world, Belgium being no exception as most of the drinking water comes from karstified aquifers. The protection of this resource should be based on a better understanding of the karst aquifer functioning. The research conducted in this thesis is an example of a concrete and quantitative study, based on an experimental approach, and that should be taken into account into the vulnerability assessment of karst aquifers. It has been a real pleasure to work in this world of wonder that has, more than once, questioned my common sense and scientific *prior conceptions*. I hope that the achievements of this doctorate will bring new insights to the vast field of karst research.

7.4 References

Lees, A. (1982). The paleoenvironmental setting and distribution of the Waulsortian facies of Belgium and southern Britain. In K. Bolton, H. R. Lane, & D. V. LeMone (Eds.), *Symposium on the Environmental Setting and Distribution of the Waulsortian Facies* (pp. 1–16). El Paso Geological Society and University of Texas at El Paso.

Lees, A., Hallet, V., & Hibo, D. (1985). Facies variation in Waulsortian buildups. Part 1. A model from Belgium. *Geological Journal*, *20*, 133–158.

Poulain, A., Rochez, G., Van Roy, J.-P., Dewaide, L., Hallet, V., & De Sadelaer, G. (2017). A compact field fluorometer and its application to dye tracing in karst environments. *Hydrogeology Journal*, *25*(5). https://doi.org/10.1007/s10040-017-1577-1

Tinet, A., Collon, P., Philippe, C., Dewaide, L., & Hallet, V. (2018). OM-MADE : an open-source program to simulate one-dimensional solute transport in multiple exchanging conduits and storage zones. *Computer and Geosciences*. Submitted

Appendices

Appendix I

Water chemical analyses

Faculté des Sciences Appliquées - Département Argenco
Secteur GEO3 - Unité Hydrogéologie et Géologie de l'Environnement

Joël OTTEN
Ingénieur Chimiste
Tél : 04/366.20.41
Mail : J.Otten@ulg.ac.be

Université de Liège

A L'ATTENTION DE : Lorraine Dewaide	PROJET : FURFOOZ	JOB782	DATE : 30/09/2013

Référence ordinateur			D7847	D7848	D7849	D7850	D7851	D7852	D7853	D7854	D7855	D7856
Nom de l'échantillon			Lesse aval	Trou des Nutons	Trou qui fume	Puits des Vaux	Sebia	GDS1	GDS2	Loutre	Ri des Vesses	Ri des Vesses
Remarques											perte	résurgence
Conductivité à 25°c	µS/cm	POT	352,8	350,8	358,6	429,9	731,9	426,6	387,8	422,5	506,0	515,1
Résistivité à 25°c	Ω.cm		2834,5	2850,6	2788,6	2326,1	1366,3	2344,1	2578,6	2366,9	1976,3	1941,4
Température	°C		14,0	14,2	14,4	14,7	15,0	15,4	15,7	15,9	16,2	16,7
pH		POT	8,26	8,02	7,92	7,75	8,39	7,73	7,74	7,79	8,36	7,93
pHs (de saturation)		CAL	7,74	7,76	7,72	7,54	7,08	7,54	7,61	7,54	7,35	7,23
Indice de LANGELIER		CAL	0,52	0,26	0,20	0,21	1,31	0,19	0,13	0,25	1,01	0,70
Caractère			Incrustant	Incrustant	Incrustant	Incrustant	Incrustant	Incrustant	Incrustant	Incrustant	Incrustant	Incrustant
Dureté totale	°f	CAL	14,8	14,7	15,3	18,8	35,1	18,8	17,1	18,6	24,7	25,1
Dureté permanente	°f	CAL	2,9	3,1	3,1	3,5	8,0	3,6	2,9	3,4	8,2	8,1
Dureté temporaire	°f	CAL	11,9	11,6	12,2	15,3	27,1	15,2	14,2	15,2	16,5	17
TA	°f	CAL	0,1	0,1	0,1	0,1	0,4	0,0	0,0	0,1	0,2	0,1
TAC	°f	TIT	11,9	11,6	12,2	15,3	27,1	15,2	14,2	15,2	16,5	17,0
CATIONS												
Ca^{2+}	mg/L	TIT	48,44	47,85	49,36	60,41	121,81	60,42	55,15	59,93	85,96	86,99
	méq/L		2,42	2,39	2,46	3,01	6,08	3,01	2,75	2,99	4,29	4,34
Fe^{3+} soluble	mg/L	AA	<= 0.01	<= 0.01	<= 0.01	<= 0.01	<= 0.01	<= 0.01	<= 0.01	<= 0.01	<= 0.01	<= 0.01
	méq/L		0,00	0,00	0,00	0,00	0,00	0,00	0,00	0,00	0,00	0,00
Fer total	mg/L	AA	0,09	0,19	0,37	0,02	0,19	0,07	1,19	<= 0.01	0,23	0,11
K^+	mg/L	CIA	2,34	2,37	2,28	2,14	3,41	2,18	2,34	2,19	1,02	1,03
	méq/L		0,06	0,06	0,06	0,05	0,09	0,06	0,06	0,06	0,03	0,03
Mg^{2+}	mg/L	CIA	6,65	6,72	7,27	8,96	11,53	9,17	8,10	8,99	8,05	8,20
	méq/L		0,55	0,55	0,60	0,74	0,95	0,76	0,67	0,74	0,66	0,67
Mn^{2+} soluble	mg/L	AA	0,01	0,01	<= 0.01	<= 0.01	<= 0.01	0,01	0,01	0,01	<= 0.01	<= 0.01
	méq/L		0,00	0,00	0,00	0,00	0,00	0,00	0,00	0,00	0,00	0,00
Mn total	mg/L	AA	0,03	0,03	0,06	<= 0.01	0,04	0,02	0,02	0,01	0,03	0,01
Na^+	mg/L	CIA	13,68	13,23	12,57	14,20	19,79	13,13	12,58	13,97	7,71	7,45
	méq/L		0,59	0,58	0,55	0,62	0,86	0,57	0,55	0,61	0,34	0,32
NH_4^+	mg/L	CIA	0,70	0,62	0,65	0,66	1,27	1,97	0,54	0,66	0,99	1,45
	méq/L		0,04	0,03	0,04	0,04	0,07	0,11	0,03	0,04	0,06	0,08
ANIONS												
Br^-	mg/L	CIA	<= 0.3	<= 0.3	<= 0.3	<= 0.3	<= 0.3	<= 0.3	<= 0.3	<= 0.3	<= 0.3	<= 0.3
	méq/L		0,00	0,00	0,00	0,00	0,00	0,00	0,00	0,00	0,00	0,00
Cl^-	mg/L	CIA	23,93	24,08	22,90	28,02	41,33	28,35	23,37	24,43	23,59	26,82
	méq/L		0,67	0,68	0,65	0,79	1,16	0,80	0,66	0,69	0,66	0,76
F^-	mg/L	CIA	<= 0.2	<= 0.2	<= 0.2	0,11	0,41	0,29	<= 0.2	<= 0.2	<= 0.2	<= 0.2
	méq/L		0,00	0,00	0,00	0,01	0,02	0,02	0,00	0,00	0,00	0,00
$H_2PO_4^-$	mg/L	CIA	<= 0.2	<= 0.2	<= 0.2	<= 0.2	1,05	<= 0.2	<= 0.2	<= 0.2	<= 0.2	<= 0.2
	méq/L		0,00	0,00	0,00	0,00	0,01	0,00	0,00	0,00	0,00	0,00
NO_2^-	mg/L	CIA	<= 0.2	<= 0.2	<= 0.2	<= 0.2	<= 0.2	<= 0.2	<= 0.2	<= 0.2	<= 0.2	<= 0.2
	méq/L		0,00	0,00	0,00	0,00	0,00	0,00	0,00	0,00	0,00	0,00
NO_3^-	mg/L	CIA	15,02	13,38	13,19	12,91	46,79	13,27	11,19	11,71	43,70	43,38
	méq/L		0,24	0,22	0,21	0,21	0,75	0,21	0,18	0,19	0,70	0,70
SO_4^{2-}	mg/L	CIA	16,75	15,56	16,13	17,02	25,22	17,53	15,90	15,95	27,61	27,43
	méq/L		0,35	0,32	0,34	0,35	0,52	0,36	0,33	0,33	0,57	0,57
↔ carbonates												
OH-	mg/L	CAL	0,03	0,02	0,01	0,01	0,04	0,01	0,01	0,01	0,04	0,01
CO_3^{2-}	mg/L	CAL	1,43	0,81	0,68	0,58	4,36	0,55	0,52	0,63	2,48	0,96
	méq/L		0,05	0,03	0,02	0,02	0,15	0,02	0,02	0,02	0,08	0,03
HCO_3^-	mg/L	CAL	142,17	139,81	147,41	185,46	321,61	184,30	172,15	184,13	196,12	205,39
	méq/L		2,33	2,29	2,42	3,04	5,27	3,02	2,82	3,02	3,22	3,37
CO_2 libre	mg/L	CAL	0,55	0,93	1,24	2,31	0,92	2,40	2,19	2,09	0,60	1,69
SiO_2	mg/L	AA	2,80	2,76	3,53	6,08	9,54	6,27	6,63	6,44	10,91	10,48
Cations total	méq/L		3,66	3,61	3,70	4,46	8,04	4,50	4,05	4,43	5,37	5,44
Anions total	méq/L		3,64	3,54	3,63	4,42	7,90	4,43	4,01	4,25	5,24	5,43

Figure 1 presents the Piper diagram for different samples taken along the Furfooz system and from the Sebia and the Ri des Vesses. It shows that the Sebia and the Ri des Vesses have a different chemical signature than the waters flowing along the Furfooz system, with a higher content in dissolved calcium and sodium. All the samples coming from the Furfooz system show a very similar anions and cations content, although a slight enrichment in Ca^{2+} downward the system (from the CN to the TDL) can be highlighted.

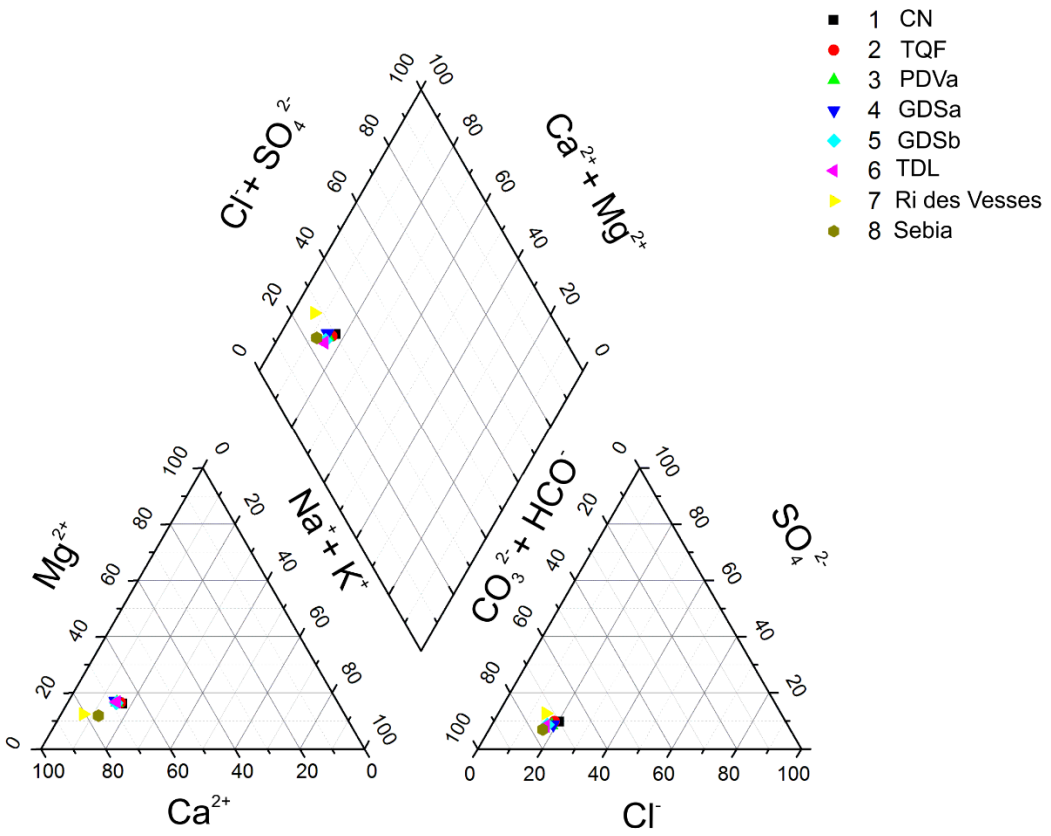

Figure 1. Piper diagram plotting different samples from the Furfooz system, the Ri des Vesses and the Sebia.

The Schoeller diagram (Figure 2) displays the concentration in mg/l of different anions and cations for different samples in a semi-logarithmic graph. This figure confirms the individual signatures of the Sebia and the Ri des Vesses that are richer in almost all the chemical components shown on the diagram. Regarding the Furfooz system, the downward enrichment of the waters in Ca^{2+} and Mg^{2+} is clearly visible, although the TDL sample keeps steady values compared to the GDSa. GDSa and GDSb show some differences in their content despite their very close location indicating some possible difference in their origin or path upstream their sampling point.

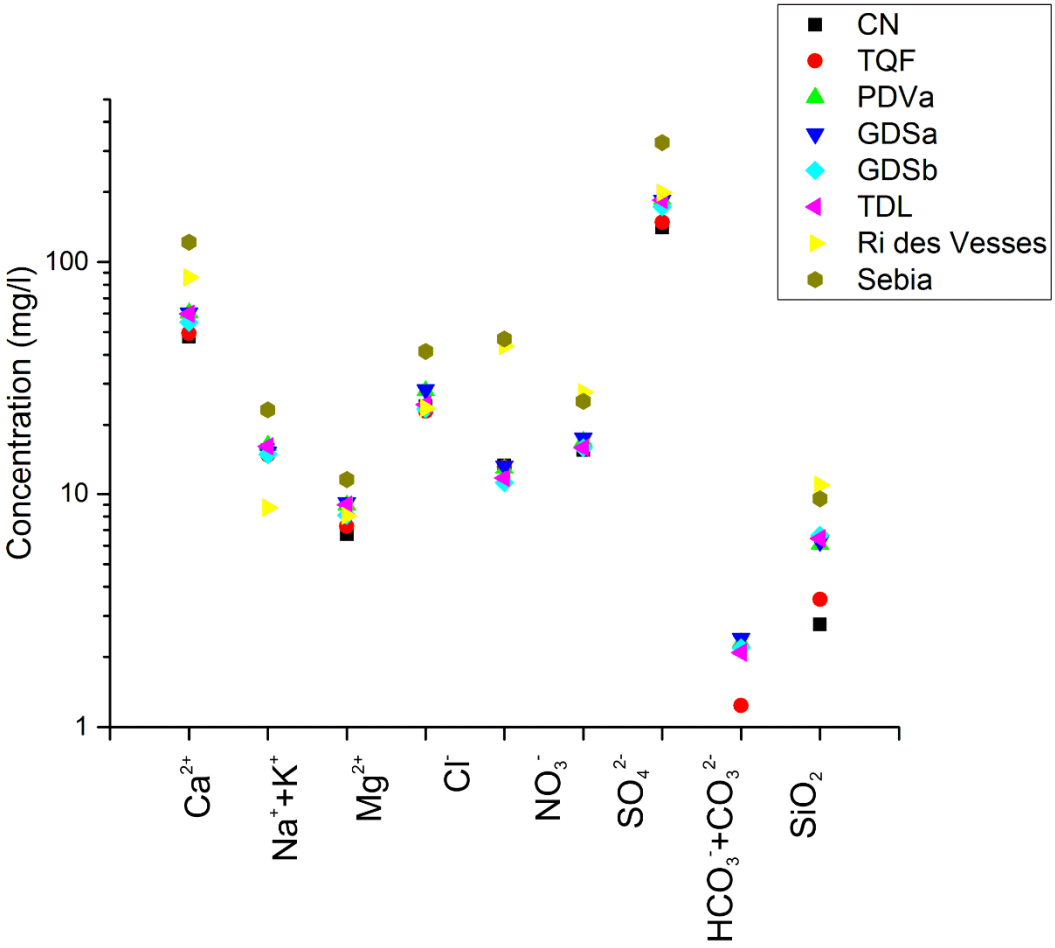

Figure 2. The Schoeller diagram representation of the water samples analyses.

Appendix II

Published Article

“Double-peaked breakthrough curves as a consequence of solute transport through underground lakes. The case study of the Furfooz karst system, Belgium”

Double-peaked breakthrough curves as a consequence of solute transport through underground lakes: a case study of the Furfooz karst system, Belgium

Lorraine Dewaide[1*], Pauline Collon[2], Amaël Poulain[1], Gaëtan Rochez[1], Vincent Hallet[1]

1. Department of Geology, University of Namur, 61 Rue de Bruxelles, 5000 Namur, Belgium email: lorraine.dewaide@unamur.be
2. Georessources, University of Lorraine, CNRS, CREGU, ENSG, 2 Rue du Doyen Marcel Roubault, BP 10162, 54505 Vandoeuvre-Lès-Nancy Cedex, France

*corresponding author

Abstract

The existence of double-peaked breakthrough curves (BTC) is reported, which are the result of the transport of a dye tracer through underground lakes. Investigations were undertaken on the Furfooz karst system in southern Belgium. In this system, the River Lesse sinks partially into a swallow hole. The water follows a solitary conduit leading to an underground lake that is directly connected to a second underground lake. Double-peaked BTCs were detected in the resurgent water, downstream of this second lake. The paper first describes field data (tracer tests in various hydrologic conditions) which point towards the double peak being linked to a non-linear process that originates within the lakes. Complementary investigations within the lakes show a complex behavior of the dye tracer related to a specific hydrodynamic feature that leads to the separation of the solute plume. A conceptual model of the solute transport within the lakes is proposed. This model emphasizes the physical effect of the lakes on the dye flow-through process.

Keywords: Karst, Tracer tests, double-peaked breakthrough curve, underground lake, Belgium

1. Introduction

The existence of double-peaked breakthrough curves (BTCs) in karst systems is documented but often poorly understood. The modelling of multi-peaked recovery curves is an issue that has been considered in several studies. The multi-dispersion model of Maloszewski et al. (1992) has been successfully applied to multi-peaked BTCs by several researchers, such as Werner et al. (1997) and Käss (1998, pp. 377-381). Field and Leij (2012) proposed a new model, the Dual-Advection Dispersion Equation (DADE), able to model dual-peaked BTCs due to solute transport in two conduits that are connected and that can exchange solutes between them. Few studies have considered the physical origin of those double curves. Goldscheider et al. (2008) recorded double peaks in a tracer test at Mammoth Cave, USA, for which they

explained the double-peaked curves by the possible presence of an unknown bifurcated flow path. Several sampling sites were settled for the Mammoth Cave system, from the injection point to the main resurgence, so that the researchers could identify the likely location at which subsurface flow conditions resulted in double-peaked recovery curves. Sometimes, double-peaked BTCs are also attributed to the injection mode (Brouyère and Rentier, 1997). Indeed, tracer tests in karst environments are, most of the time, performed through impulse injections (Dirac type). This usually involves injection of a supplementary volume of water to chase the tracer as quickly as possible. The repeatability of the results with respect to distinct double peaks depends on the injection mode or factors linked to the specific subsurface flow conditions. Two studies have established a link between those double peaks and the existence of a lake or a pool on the tracer path. Hauns and Jeannin (1998) showed that a secondary peak can appear when important changes in a section of the conduit system are observed, which could potentially be linked to the presence of a pool in the flow path. The authors attribute secondary peaks to the trapping of the tracer in eddies. They produced double-peaked BTCs through physical and numerical modelling. Field and Leij (2012) realized laboratory analogs to produce experimental double-peaked BTCs. One of those analogs simulated a pool where water flows in and out via small pipes simulating solitary conduits. In both cited studies, the authors have highlighted the strong control of conduit geometries on the resulting BTCs, as also shown in other studies (Hauns et al., 2001; Massei et al., 2006; Morales et al., 2010). The work reported in this article shows field evidence of a real karst system characterized by the presence of underground lakes that produce double-peaked BTCs. These observations could thus constitute reference data for future works that make use of numerical modeling.

The tracer tests presented here are used in a qualitative and quantitative approach. The resulting BTCs are analyzed in order to characterize solute transport in karst conduits, as usually done in karst hydrogeology (Käss, 1998; Schudel et al., 2003; Jeannin et al., 2007; Dewaide et al., 2016). It is first shown that the double-peaked BTCs should be explained by a process taking place in the lakes. Then, through the estimation of the transport and hydrodynamic parameters, the other features of the two BTC peaks are demonstrated to be inherited from different dynamics in the first and second lakes. Finally, complementary investigations highlight the different behaviors of the dye tracer in the two lakes.

2. Study site: overview of the underground system

The karstic system of Furfooz, located near Dinant in southern Belgium, is developed in Carbonifereous Dinantian carbonates. The River Lesse partially sinks through a small swallow hole. It reappears about 1.2 km downstream via a diffuse resurgence, after travelling below two surface-river meanders (Fig. 1).

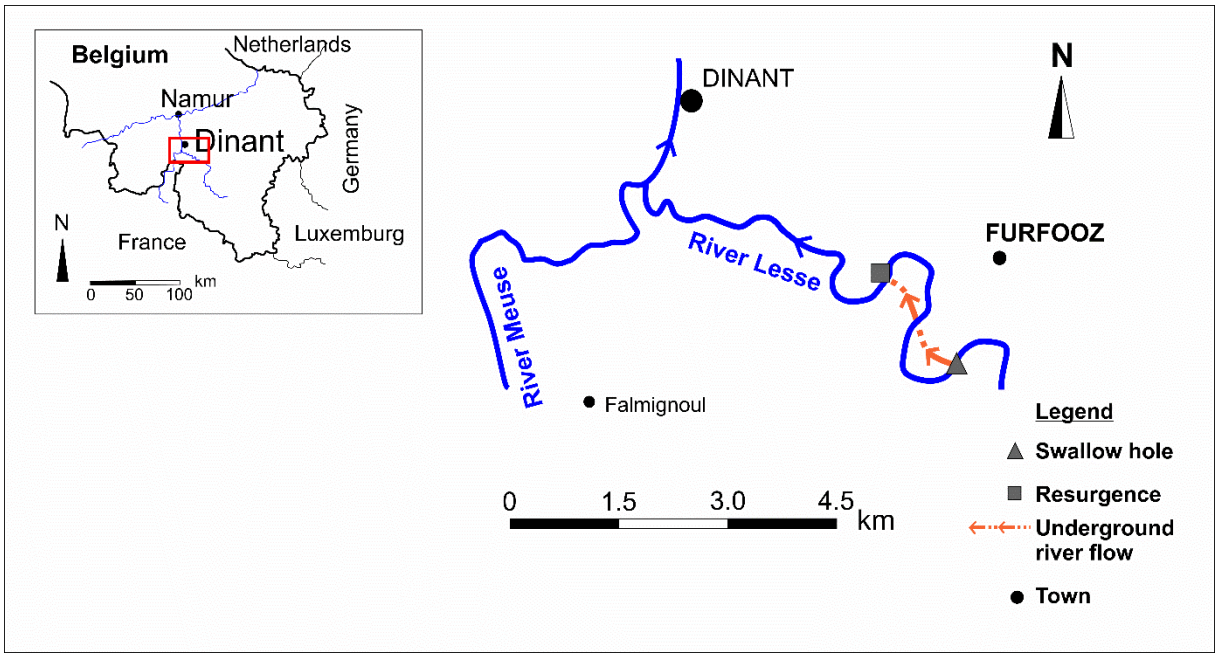

Fig. 1 Location of the karstic system of Furfooz. Note that the underground river crosses two surface-river meanders

Thanks to several speleological access points to the underground River Lesse (i.e. at sites 1, 2, 3, 4, and 5: Fig. 2), the system benefits from a good knowledge, except for the underground flow route between sites 3 and 4. The karstic river flows mainly through conduits with flooded cross sections of 1 to 2 m^2 in moderate flow conditions and crosses a major heterogeneity in the form of two successive underground lakes. The discharge cannot be measured at the exit of the system because the resurgence there is widely dispersed. For this reason, site 5 will not be mentioned any further in this paper and site 4 will be the most downstream point considered for the experiments described hereafter. Site 4 is the only location in the system where a continuous monitoring of the discharge could be done. This monitoring shows that the discharge at site 4 varies between 5 l/s and 70 l/s depending on the surface flow conditions. Occasional measurements have verified that the flows at sites 1 and 4 are similar.

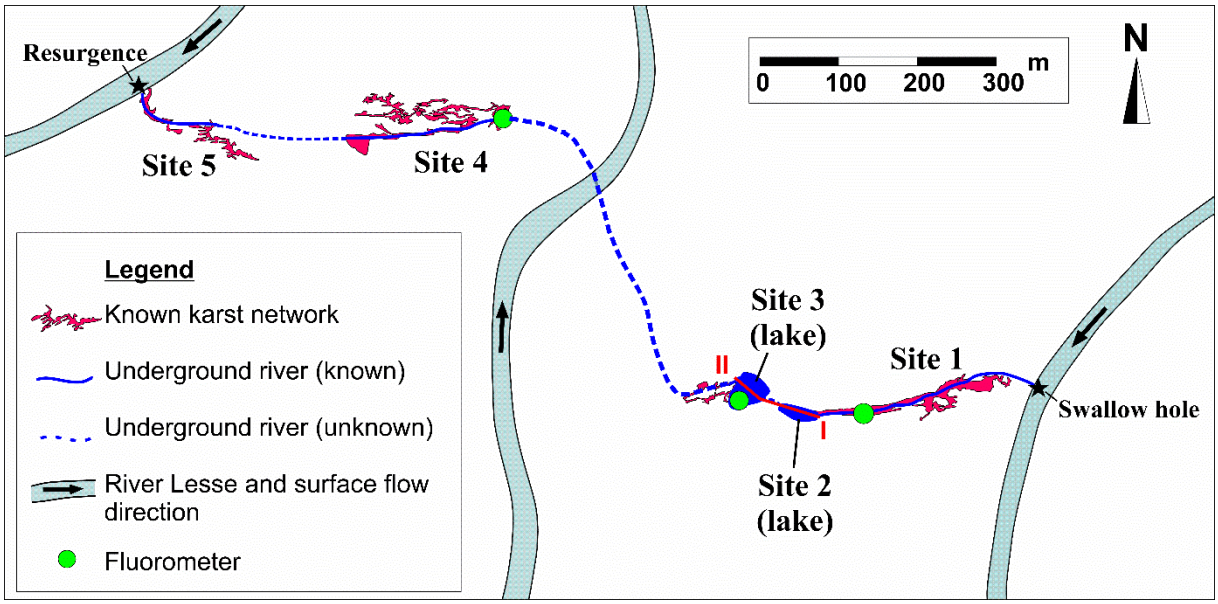

Fig. 2 Plan view of the River Lesse and the underground system with the speleological networks. The figure shows also the position of the fluorometers (*green circles*) used during the tracer tests. The *I-II line* locates the cross-section presented in Fig. 3.

Regarding the present study, particular attention must be accorded to sites 2 and 3. They both represent underground lakes that are connected but separated by a fractured rocky spur or by interconnected massive blocks of rock. The geometry of these lakes are not exactly known but the cave divers'reports have enabled a conceptual layout, as shown in Fig. 3. From site 1, the underground river can be easily followed until the mouth of the site 2 lake, which has a narrow shape and a supposed depth of 32 m. The speleological junction between site 2 and site 3 has never been found; therefore the site 3 lake has to be accessed via the ground surface above it. At site 3, the surface area of the lake is around 30 m^2 and the depth is at least 25 m. The lake's downstream water exit seems to be located at 15 m of depth.

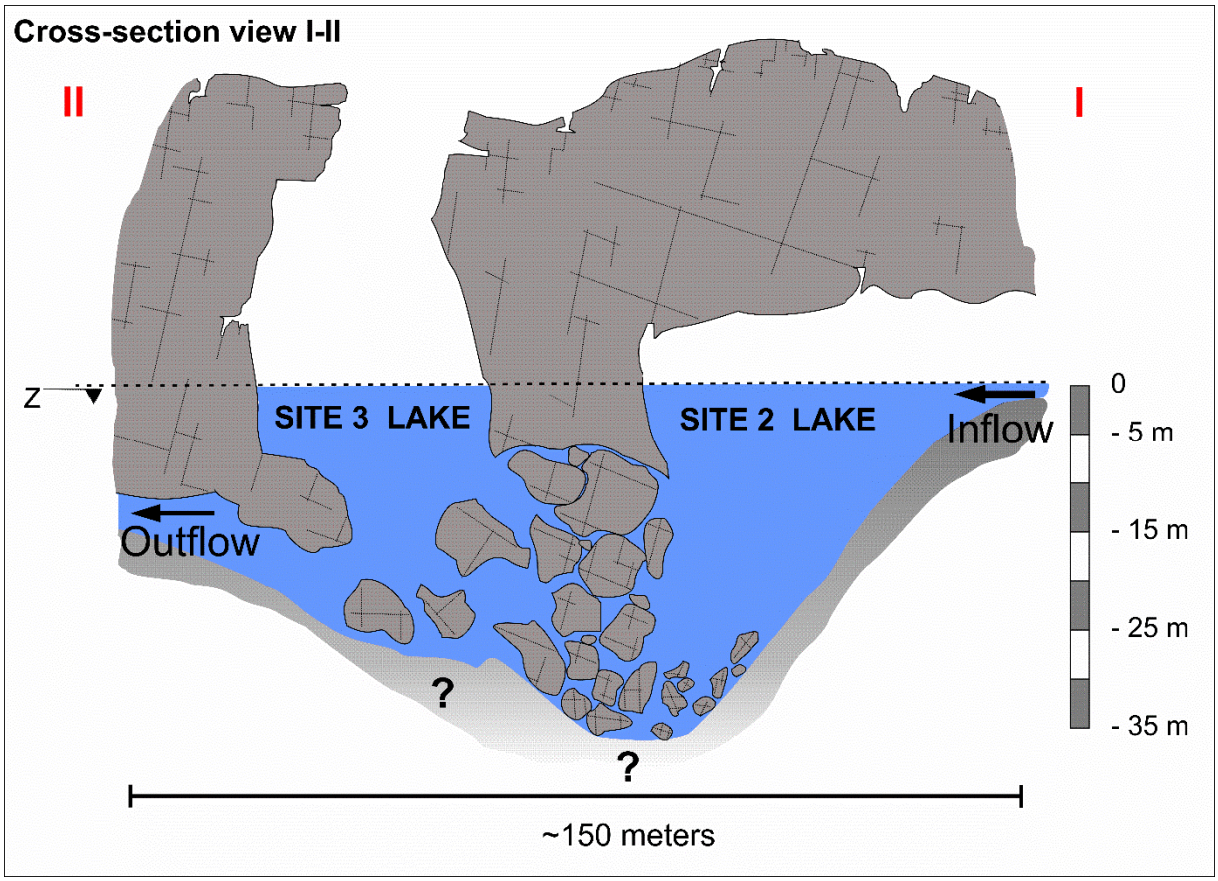

Fig. 3 Cross-section of the lake conceptual model based on diving descriptions. The position of the cross-section is shown in Fig. 2

3. Field tracer tests

In order to characterize solute transport through the Furfooz system, and more specifically to evaluate the influence of the lakes on the tracer recovery, several tracer tests were performed in 2013, under various flow conditions and from different injection points. To describe the dye tracer transport through the lakes, the nearest sampling station available downstream was used (site 4). Each test was undertaken in stable and moderate flow conditions and any false interpretations of the BTCs due to sudden floods or variable discharge can therefore be excluded. The dye tracers used during those tests were fluorescein or sulforhodamine B and the sampling devices were the automatic fluorometers GGUN-FL30 (Schnegg and Doerfliger, 1997) and the FLUO-G, developed recently by Poulain *et al*. (2017). Injections were performed at the swallow hole and at site 3. The fluorometers were therefore placed at sites 1, 3, and 4. There was no possibility at this time to place a fluorometer into the lake at site 2. Recovery rates at sites 1 and 4 are based on the discharge measurements done at each site. Recovery is not calculated for site 3 as the fluorometer was located at the surface of the lake where a real discharge cannot be measured.

3.1 Injections at the swallow hole

Injections (200 g of sulforhodamine B or fluorescein) were performed at the swallow hole and fluorometers were placed at sites 1, 3, and 4 (Fig. 2). Three injections were performed in different but stable flow conditions (mean discharge of 20 l/s, 11 l/s and 7 l/s respectively) in order to ensure the reliability of the results.

The results are shown in Fig. 4. The main transport parameters were calculated from these curves and are shown in table 1. At site 1, where the fluorometer is located about 150 m downstream from the swallow hole, the dye tracer arrives very quickly and transits very fast. The entire mass of injected tracer flows through this point (recovery of 100 %). The solute is therefore entering the site 2 lake in a very advective way. This behavior is in contrast with the wide curve observed in site 3, located 310 m downstream from the swallow hole. The dye tracer arrives there 20 to 36 h after the injection depending of the flow conditions, implying a maximum velocity of 15 to 8 m/h. The mean transit time is about 150 h but the complete recovery time is at least of 400 h, implying some skewness in the BTCs especially in higher flow conditions. This shows that the solute arriving at the surface of the site 3 lake has been subjected to an important dispersion through a consequent volume of water. The skewness observed in the BTC could be related to the diffusion of the tracer to immobile water zones in the lakes where it is temporarily caught (Field and Pinsky, 2000). All in all, the most surprising result of these tests is the appearance of a double-peaked BTC at site 4. The two peaks seem to have a different shape, and so they could be the result of different processes. Therefore, the peaks were treated separately in order to characterize them properly. The first peak arrives rather quickly at site 4 (less than 60 h). Actually it arrives nearly at the same time at site 4 as at the surface of the site 3 lake and it has a short transit time (less than 100 h) compared to the second peak. The second peak at site 4 is detected only 60 to 150 h after the injection and has a total transit time of at least 500 h. The recovery rates at site 4 are rather weak (maximum of 41.7 % when considering the two peaks together). This implies some loss of the tracer during transport. The reduction in tracer signal could be linked to it being trapped in dead zones that would exist in the lakes. Furthermore, the masses of dye tracer implied in the two peaks are very different. The first peak represents 5, 20 and 30 % of the second peak restituted mass for the test at 20, 11, and 7 l/s, respectively. The discharge seems therefore to have some control on the distribution of the dye tracer between the two peaks.

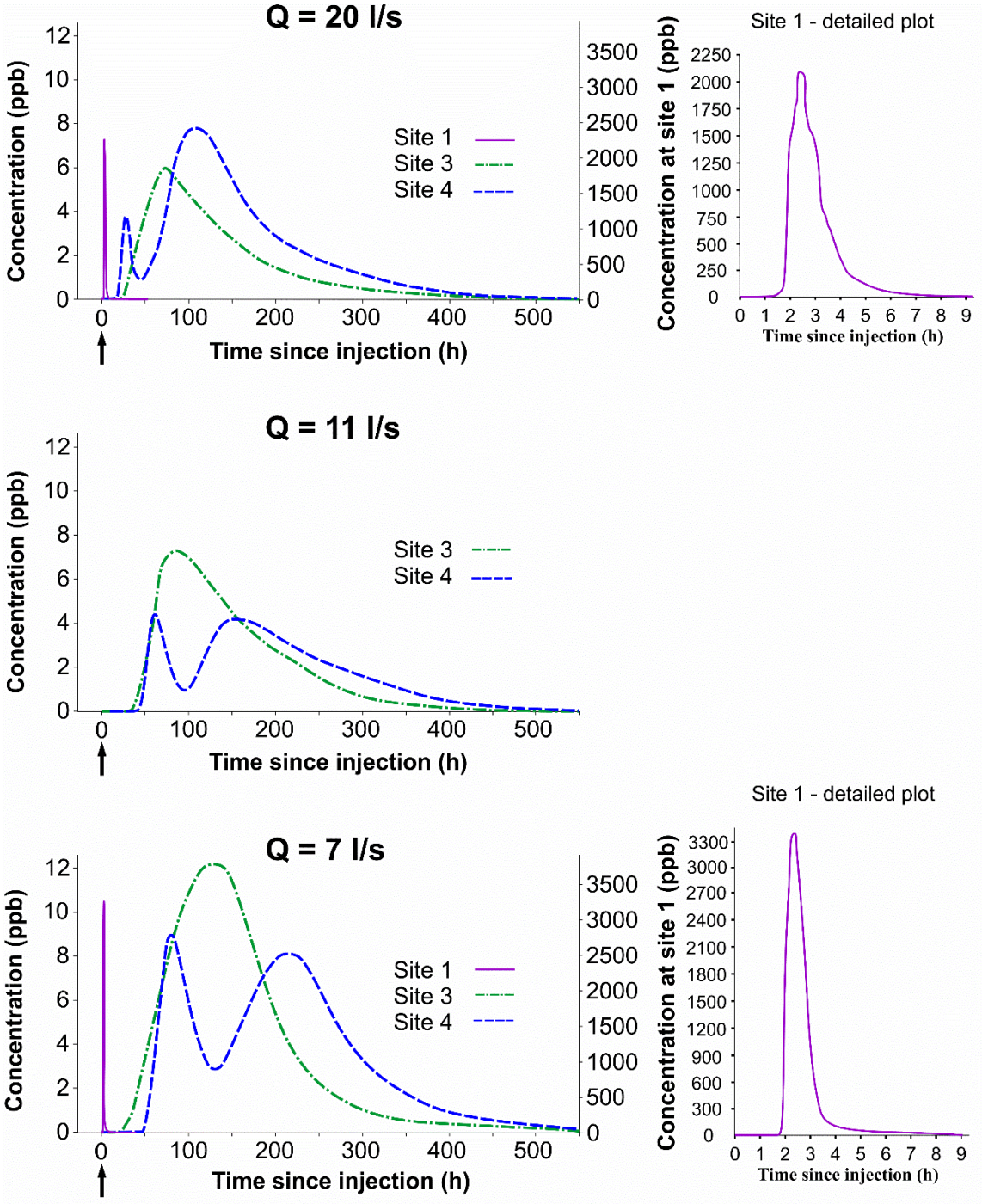

Fig. 4 Breakthrough curves of three tracer tests performed in different discharge (*Q*) conditions. The arrow below the X-axis shows the injection time. On the main plot (the left one), note the secondary Y-axis on the right that gives concentration at site 1 only. On the right, detailed plots of site 1 are also given.

Table 1 Main solute transport parameters from the BTCs analysis (injection at the swallow hole). *1st A.*: first arrival; T_{mean} : mean travel time; V_{max} : maximum velocity; V_{mean} : mean velocity; C_{peak} : maximum peak concentration (in parts per billion); T_{peak} : time to the maximum peak concentration; *R.R.*: recovery rate; /: no data

Tracer tests		1st A. (h)	T_{mean} (h)	V_{max} (m/h)	V_{mean} (m/h)	C_{peak} (ppb)	T_{peak} (h)	R.R. (%)
Tracer test 1 Q = 20 l/s	Site 1	1.5	3.1	100	45.5	2100	2.3	100
	Site 3	19.7	143.6	15.2	2.1	6.4	74.1	/
	Site 4 1st peak	22.0	34.5	32.7	20.9	4.0	33.0	1.8
	Site 4 2nd peak	48.2	174.9	14.9	4.1	8.0	112.0	39.9
Tracer test 2 Q= 11 l/s	Site 3	36.4	148.3	8.2	2.0	7.37	82.9	/
	Site 4 1st peak	38.7	68.2	19.9	11.3	4.40	61.0	2.4
	Site 4 2nd peak	85.0	219.1	8.4	3.5	4.20	153.7	12.9
Tracer test 3 Q = 7 l/s	Site 1	1.9	3.8	78.9	38.6	3367.8	2.4	100
	Site 3	30.0	157.8	10.3	2.0	12.7	125.8	/
	Site 4 1st peak	40.3	86.8	19.1	8.9	9.5	78.2	5.5
	Site 4 2nd peak	129.3	270.1	5.9	2.8	8.5	214.9	18.3

The QTracer2 program (Field, 2002) was used to estimate some hydrodynamic parameters: the longitudinal dispersion coefficient (D_L), the longitudinal dispersivity (a_L), the conduit cross-sectional area (Cs), and the Peclet (Pe) and Reynolds (Re) numbers (table 2). Pe gives an idea about the relative contribution of dispersion to transport, while Re represents the resistance to flow. Pe and Re are defined as (Grey and Pinder, 1976):

$$\mathrm{Pe} = \frac{v\, l}{D} \quad (1)$$

$$\mathrm{Re} = \frac{\rho\, v\, d}{\mu} \quad (2)$$

Where v is the solute mean velocity (m/s), l is the distance of transport (m), D the dispersion (m^2/s), ρ the density of the fluid (g/m^3), d the conduit diameter (m) and μ the fluid viscosity (g/m.s). It is usually considered that karst transport in conduits should be characterized by a Pe value that exceeds several times the value of 6 and by a Re value far greater than 2000, which reveals a turbulent flow (Landau and Lifshitz, 1987).

Table 2 Estimation of some hydrodynamic parameters from QTRACER2 (injections at the swallow hole). D_L: longitudinal dispersion coefficient; a_L: longitudinal dispersivity; *Cs*: conduit cross-section; *Pe*: Peclet Number; *Re*: Reynolds Number

Tracer tests		D_L (m^2/s)	a_L (m)	Cs (m^2)	Pe	Re
Tracer test 1 Q = 20 l/s	Site 1	0.016	1.63	1.91	67.5	13500
	Site 3	0.037	63.8	32.7	4.71	3287
	Site 4 1st peak	0.014	2.42	3.52	298	10658
	Site 4 2nd peak	0.070	60.9	17.5	11.8	4733
Tracer test 2 Q= 11 l/s	Site 3	0.023	41.4	18.7	7.25	2404
	Site 4 1st peak	0.019	6.17	3.33	126	5679
	Site 4 2nd peak	0.052	53.1	10.7	14.5	3169
Tracer test 3 Q = 7 l/s	Site 1	0.045	3.34	0.56	32.9	9630
	Site 3	0.021	39.1	12.9	7.92	1934
	Site 4 1st peak	0.044	17.8	2.81	43.2	4110
	Site 4 2nd peak	0.024	30.2	8.84	25.5	2330

The use of QTracer2 allows one to characterize in a quantitative way the hydrodynamic behavior shown by the different curves. The results confirm two contrasting behaviors at sites 1 and 3. BTCs at site 1 reveal a very advective transport with low dispersivity, and very high Pe and Re, while solute transport at site 3 is characterized by high dispersivity, and weak Pe and Re in large flow sections. A similar distinction is shown by the first and the second peaks of the double-peaked BTCs at site 4. The first peak reveals a classical behavior of transport in karst conduits with moderate dispersivity and high Pe and Re numbers, while the second peak, for which transport is much slower, is dominated by high dispersivity in large flow sections. Re and Pe are also weaker for the second peak. Given the contrasting Re and Pe values obtained in the different tests at each site, it was decided to plot the two parameters, see Fig. 5. From this graphic, and given what has just been discussed, two groups of plots are distinguished, that correspond to two different hydrodynamics. The first group, with high Re and Pe,

represents more turbulent and less dispersive transport, as is usual in karst transport mode. This group corresponds also to the peaks illustrating the quick and advective transport observed on the BTCs, i.e. the curves at site 1 and the first peaks at site 4. The second group gathers the slow and dispersive transport that is illustrated by BTCs at site 3 and the second peaks at site 4. This group is characterized by rather low Re and low Pe, and so by low turbulence and high dispersion which is not so usual for a classic conduit transport. Fig. 5 shows also the influence of the discharge on the transport dynamic, but this influence is different between the two groups. In group 1, Pe and Re are greatly impacted by the flow conditions with higher values when the flow increases, and much smaller values for small discharge. When the flow is low, transport tends to be less turbulent and more dispersive. The orange triangle is, besides, very close to group 2 values because of this discharge influence. In group 2 the impact is, however, less obvious because the range of values is less wide but the decrease in Re is still obvious. However, the Pe values of the second group plots tend here to increase when the flow decreases. This would therefore suggest that the transport in group 2 is less turbulent but also less dispersive when the flow decreases.

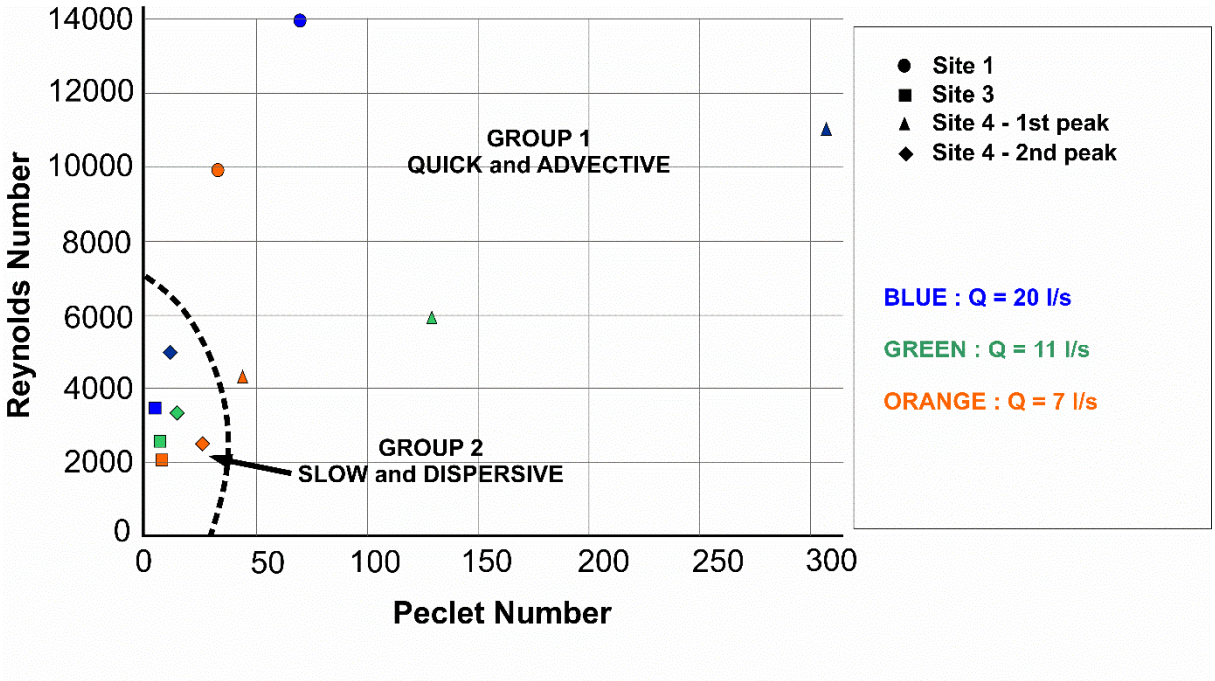

Fig. 5 A two-dimensional plot of Reynolds number and Peclet number evolution through the different sites in different flow conditions. The proposed *dashed line* delimits two groups of values that illustrate different hydrodynamic behaviors

3.2 Injection at site 3

An additional test was realized in order to have more information about the double peak appearance. An injection (200 g of fluorescein) was performed at the surface of the lake at site 3. The discharge (measured at site 4) was 6 l/s and remained steady during the test. The

resulting BTC obtained at site 4 is shown in Fig. 6. The main transport and hydrodynamic parameters are presented in table 3.

The injection within the site 3 lake does not produce a double-peaked BTC but a single-peaked one that expresses a dispersive behavior (α_L = 34.3 m). Transport is slow (*v* mean = 4.1 m/h) and values of Pe (12.5) and Re (2593) would enter in group 2 that is shown in Fig. 5. The calculated recovery rate is very low (7.48 %): it probably suggests that a great part of the tracer is lost into the site 3 lake. Long-term monitoring could probably not have recovered much more of the tracer, as natural decay and a wide dilution would make it pass under the detection limit (< 1 ppb).

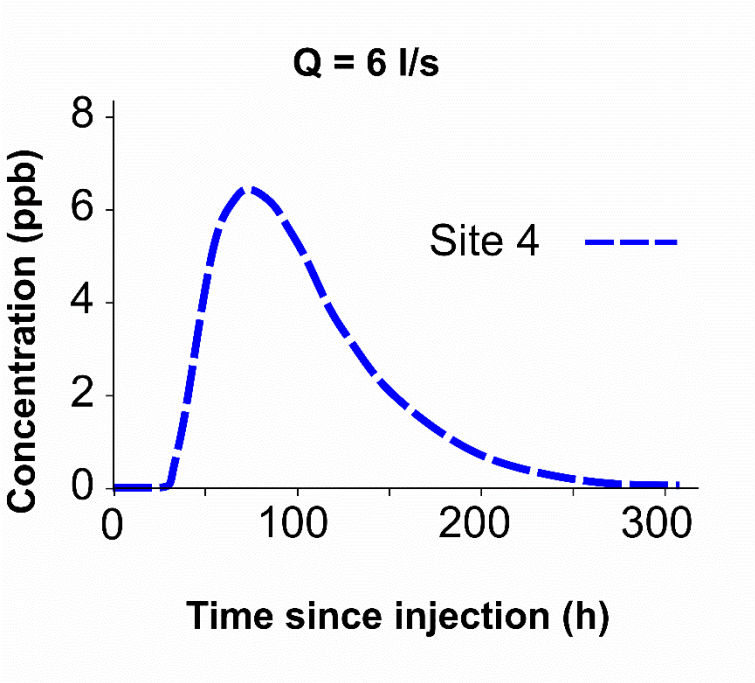

Fig. 6 The BTC observed at site 4 for an injection at site 3

Table 3 Estimation of the transport parameters for the BTC obtained at site 4 from injection (6 l/s) at site 3. *1st A.*: first arrival; T_{mean} : mean travel time; V_{max} : maximum velocity; V_{mean} : Mean velocity; C_{peak} : Maximum peak concentration; T_{peak} : time to the maximum peak concentration; *R.R.*: recovery rate; D_L: longitudinal dispersion coefficient; a_L: longitudinal dispersivity; *Cs*: conduit cross-section; *Pe*: Peclet Number; *Re*: Reynolds Number

Transport parameter:	**1st A. (h)**	**T_{mean} (h)**	**V_{max} (m/h)**	**V_{mean} (m/h)**	**C_{peak} (ppb)**	**T_{peak} (h)**	**R.R. (%)**	**D_L (m^2/s)**	**a_L (m)**	**Cs (m^2)**	**Pe**	**Re**
	33.5	104	12.8	4.12	6.53	76.3	7.48	0.039	34.3	6.25	12.5	2593

4. Complementary investigations within the lakes

More specific investigations were performed in the lakes at sites 2 and 3 to highlight heterogeneities that could be related to the behavior traits of the tracer. Different probe-systems were used to investigate the evolution of electrical conductivity, temperature and fluorescence related to depth within the lakes during a tracer test. Regarding the difficult access conditions at site 2 and site 3, different equipment strategies were applied to those two lakes.

4.1 Site 2 lake equipment and results

The site 2 lake can only be accessed after a long progression into a speleological cave (site 1) with narrow passages and muddy galleries. As a consequence, the supply of equipment to the lake is limited. The lake was explored once by diving but, given the dangerousness of this dive, the diver was not asked to intervene further for the equipment. The lake was equipped with three fluorometers (Fig. 7): one at the lake entrance (point A) and two in the center, about 30 m from the shore thanks to a boat. One of those two devices was placed 1 m below the water surface (point B) and the second 20 m deep (point C). A conductivity and temperature profile was also performed from the boat. It consisted of taking measurements every meter on a vertical profile from the surface to the bottom of the lake.

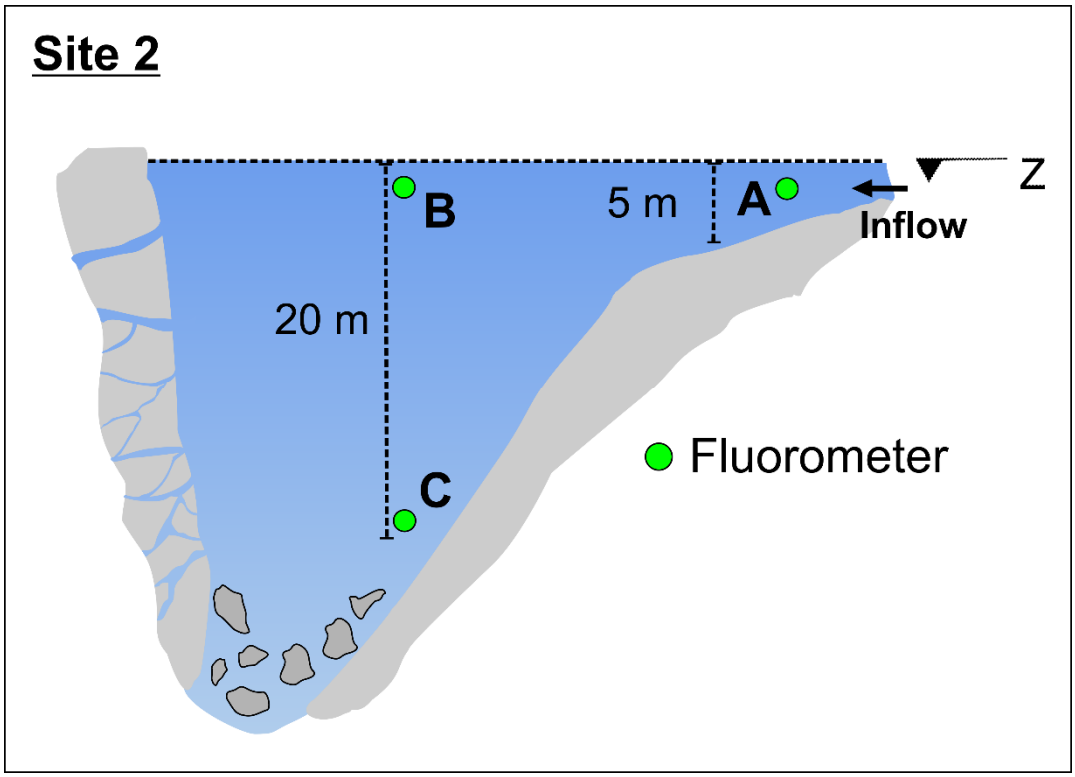

Fig. 7 The site 2 lake was equipped with three fluorometers (*A*, *B*, *C*) placed at different positions and different depths during complementary investigations

The conductivity and temperature profiles, made in spring time, showed very homogeneous results with no clear changes in temperature or conductivity with the depth. A small variation of less than 1°C was observed between the surface (12.1°C) and the bottom at 21 m (11.3°C). A conductivity value of 330 µS/m was constant along the profile except at the bottom where it reached 360 µS/m, but this is probably caused by sediment accumulation.

A dye tracer injection was made at the swallow hole. The discharge was estimated to be 9 l/s and stayed steady during the recovery. Results of this test show a clear difference in the tracer behavior between the surface and the bottom of the lake (Fig. 8). Indeed, the two fluorometers at the surface (points A and B) show a rapid arrival of highly concentrated tracer: the signal at point A shows a first arrival one hour after the injection and the concentration increases in a few minutes up to 600 ppb. At point B the tracer arrives 1.8 h after injection and reaches a concentration of 450 ppb. In those two BTCs, the concentration drops rapidly (within three hours) below 50 ppb. They both show a small queue of recovery and a total disappearance of the tracer within 35 h. At point C, the situation is very different. The tracer reaches the fluorometer at the bottom of the lake after nearly 4 h and the concentration there does not exceed 50 ppb. The BTC shows a rather wide and skewed shape indicating some dispersion compared to what happens at the surface. The solute leaves point C location after less than 80 h but the mean transit time is less than 20 h.

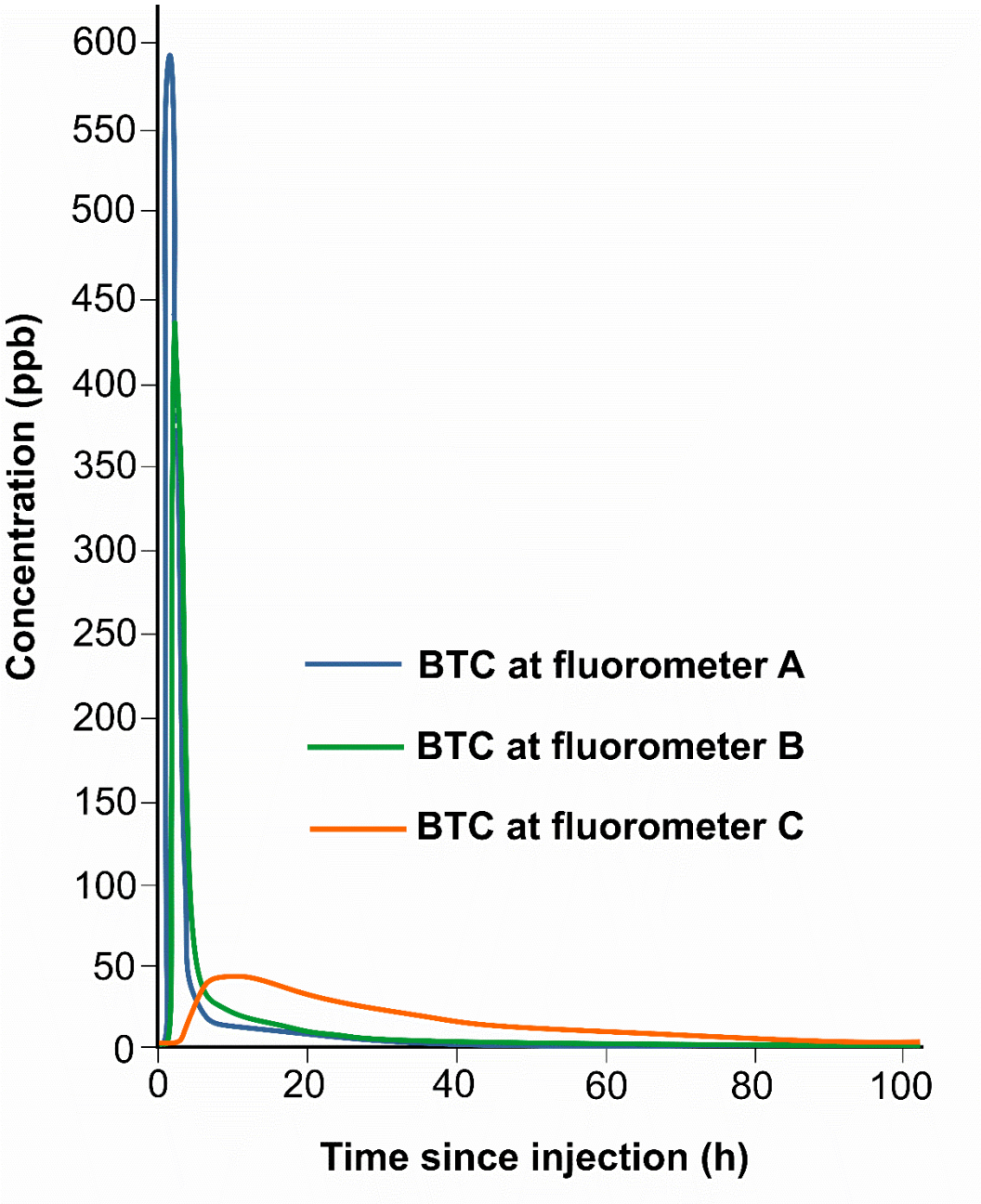

Fig. 8 The BTCs observed in the site 2 lake at each fluorometer for an injection at the swallow hole (*Q*: 9 l/s)

4.2 Site 3 lake equipment and results

At site 3, it was decided to equip the lake with a screened casing from the surface to the bottom (about 25 m deep). This was possible thanks to the help of a diver. The casing was chosen large enough so that a piezometric fluorometer could be inserted in it. The experiment consisted of making a concentration profile through the depth of the lake. An injection was performed at the swallow hole (200 g of fluorescein) and a sounding of the lake with the fluorometer through the casing was realized 120 hours after the injection. The results of this experiment are shown in Fig. 9. Two concentration profiles were realized: one in ascending

the fluorometer from the base of the casing to the top, and the other in descending the device. While fluorescein is observed in the whole profile, it shows clearly a higher concentration zone at a depth between 15 and 22 m. This would mean that the dye tracer coming from site 2 is entering site 3 at this depth.

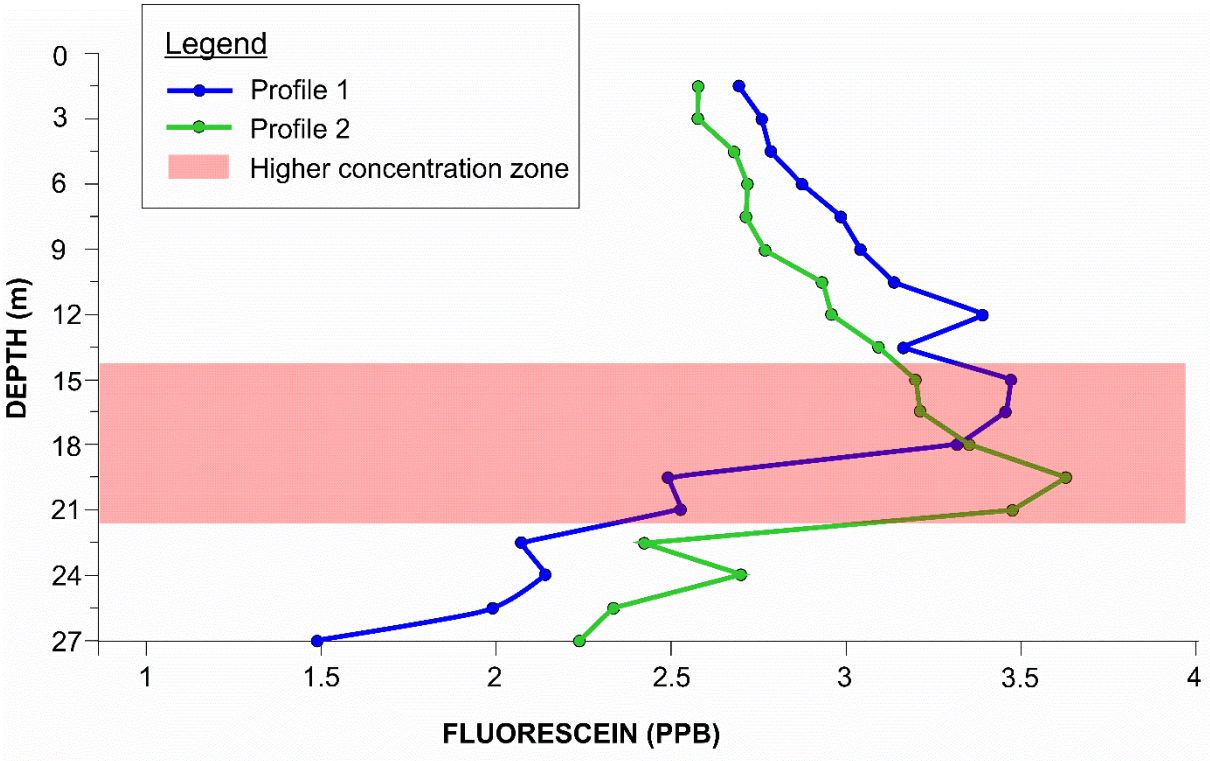

Fig. 9 Concentration profiles performed in site 3 lake. Two profiles were realized: profile 1 in ascending the fluorometer from the bottom to the surface; profile 2 in descending the fluorometer. Those two profiles show clearly a higher dye tracer concentration around 20 m of depth

5. Discussion

The performed experiments underline a complex functioning of the Furfooz system. This complexity seems linked to the existence of two consecutive underground lakes. The most remarkable feature of these experiments is the double-peaked BTC observed downstream of the lakes.

The double-peaked BTCs appear at site 4 if the injection is performed at the swallow hole. When the injection is made into the site 3 lake, however, the BTC at site 4 is single peaked. Therefore, the origin of the double recovery has to be upstream of site 3. Furthermore, recovery observed at site 1 is total (recovery rates of 100 %) which means that there is no bifurcated path upstream of site 1 sampling station. In consequence, there is reasonable proofs to locate the process responsible for the double recovery within the site 2 and site 3 lakes.

The BTCs analysis has shown that the two peaks are inherited from two different hydrodynamic behaviors. The behavior revealed by the first peak shows a rather quick transport dominated by advection while the second peak is characterized by a slow and dispersive transport. The complementary investigations within the lakes showed that the dye tracer has a very heterogeneous distribution into sites 2 and 3, highlighting some preferential route followed by the tracer.

Given all the field observations, and particularly the very heterogeneous behavior of the tracer into the site 2 and site 3 lakes, it is reasonable to propose that the double recovery is not linked to a bifurcated flow path but rather to a dual dynamic within the lakes. Fig. 10 is a new conceptual model that gathers all the field measurements. In this model, a dual dynamic is forced by an advective flow that takes place in the lakes. In site 2, this advective flow would follow a route located at the surface of the lake and at around 15 m of depth. There, this flow could enter a breach that ensures the connection with site 3. In the site 3 lake, the advective flow would exist at a depth between 15 to 22 m and it finally leaves the lake still around this depth. When an injection is performed at the swallow hole, a minor part of the solute arriving at site 2 will firstly follow this advective flow while the remaining tracer is dispersed into the lake. In this first step, the tracer that has followed the advective flow quickly leaves the lake in an advective way and gives the first peak at site 4. The fact that this first flow keeps a very small dipersion could be linked to a specific geometric feature that cannot be precisely defined as yet. In a second step, the remaining tracer that has spent time dispersing into the water is finally evacuated from the lakes by the same exit but in a slow and dispersive way. Regarding the BTCs recorded at the surface of the site 3 lake, they are single-peaked because the fluorometer there is not placed on the advective flow path and so it records only the dispersion of the tracer into the lake. As for the injection made in site 3, it cannot produce a double-peaked BTC because it takes time for the tracer to disperse in the lake before reaching the advective flow feature.

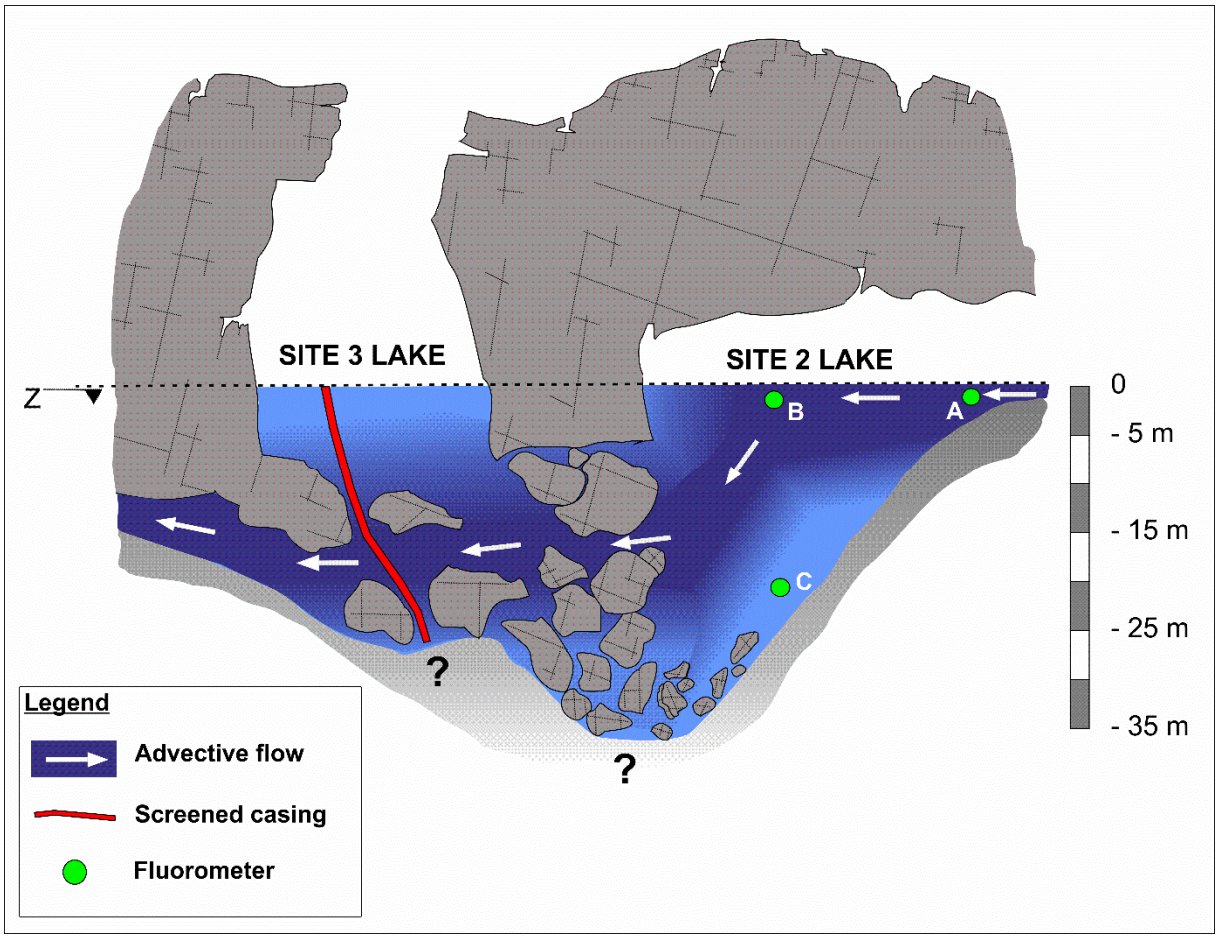

Fig. 10 New conceptual model showing the *advective flow* highlighted by the field investigations. The figure also displays *the screened casing* and *fluorometers* used in the investigations described in section *'Complementary investigations within the lakes'*. When the dye tracer enters the site 2 lake, some part of it follows this advective flow path and exits the lake quickly, while the remaining tracer is dispersing slowly into the volume of water that represents the lakes. After a while, the dispersed tracer also leaves the lake and produces the second peak visible at site 4

6. Conclusion

This paper reports surprising results brought about by field experiments. The existence of double-peaked BTCs due to solute transport through underground lakes is an exceptional fact that has been here observed. Numerous multi-sampling site tracer tests were performed to highlight this phenomenon. Original investigations, like a concentration profile and a depth-related tracer test within the lakes, led to an insight of the solute behavior. It appears that the dye tracer flows through the lakes in a non-linear way. These observations lead to the proposition of a conceptual model in which the presence of an advective flow responsible for the separation of the tracer plume is suggested.

A few studies have reported double-peaked BTCs as the result of solute transport through lakes or pools but this was brought out by physical laboratory experiments only (Hauns and Jeannin, 1998; Field and Leij, 2012). The present study is, for its part, based on field observations and ends in a conceptual model which is an attempt to give a physical explanation to a remarkable natural phenomenon. In this sense, a few new perspectives can be expected from this work. Firstly, the conceptual model could be re-enforced by additional field investigations. In particular, the screened casing at site 3 lake could be equipped with several fluorometers that would be placed at different depths during the entire recovery of an injection made at the swallow hole. Secondly, the conceptual model could be concretized in the form of a scaled physical model whose purpose would be to test the hypothesis of the advective flow and the resultant double peak. Finally, in order to quantify and add dimension to the physical processes that take place in the lakes, numerical modelling should be considered.

Acknowledgements

The authors would like to thank the “Ardennes et Gaume” NPO for giving us access to the Furfooz Natural Reserve. A special thank-you goes to Michel Pauwels, an experienced diver, whose precious information helped us to build the conceptual model and who was brave enough to take the casing to the bottom of the lake. The authors are grateful to the reviewers, in particular to Malcolm Field, whose remarks improved the quality of this report.

References

Brouyère S, Rentier C (1997) About the influence of the injection mode on tracer test results. In: Kranjc, A. (Ed.), Tracer Hydrology 97, Proceedings of the 7th International Symposium on Water Tracing. International Association of Tracer Hydrology (ATH) and Karst Research Institute ZRC SAZU, A.A. Balkema, Rotterdam, Netherlands, 11-17.

Dewaide L, Bonniver I, Rochez G, Hallet V (2016) Solute Transport in heterogeneous karst systems: dimensioning and estimation of transport parameters via multi-sampling tracer tests modelling using the OTIS (One-dimensional Transport with Inflow and Storage) program. J. Hydrol. 534, 567-578.

Field MS, Pinsky PF (2000) A two-region non equilibrium model for solute transport in solution conduits in karstic aquifers. J. Contam. Hydrol. 44 (3/4), 329–351.

Field MS (2002) The Qtracer2 Program for Tracer-Breakthrough Curve Analysis for Tracer Tests in Karstic Aquifers and Other Hydrologic Systems. U.S. Environmental Protection Agency, Office of Research and Development, National Center for Environmental Assessment, Washington Office, Washington, DC, EPA/600/R-02/001, 2002.

Field MS, Leij F (2012) Solute transport in solution conduits exhibiting multi-peaked breakthrough curves. J. Hydrol. 440-441, 26-35.

Goldscheider N, Meiman J, Pronk M, Smart C (2008) Tracer tests in karst hydrogeology and speleology. Int. J. Speleol. 37 (1), 27–40.

Grey WG, Pinder GF (1976) An analysis of the numerical solution of the transport equation. Water Resour. Res., 12 (3), 547-555.

Hauns M, Jeannin P-Y, Atteia O (2001) Dispersion, retardation and scale effect in tracer breakthrough curves in karst conduits. J. Hydrol. 241 (3-4), 177-193.

Hauns M, Jeannin P-Y (1998) Tracer transport in underground rivers in karst: tailing effects and channel geometry. Bull. d'Hydrogéol. 16, 123-142.

Jeannin P-Y, Groves C, Häuselmann P (2007) Speleological investigations. In : Goldscheider N and Drew D (Eds.) : Methods in Karst Hydrogeology. International Contributions to Hydrogeology. Taylor and Francis, London, UK , 25-44.

Käss W (1998) Tracing Technique in Geohydrology. Balkema, Rotterdam, 600 p.

Landau LD, Lifshitz EM (1987) Fluid mechanics. Pergamon Press; Addison-Wesley, London: Reading, Mass., second edition, 558 p.

Maloszewski P, Harum T, Benischke R (1992) Mathematical modelling of tracer experiments in the karst of lurbach system. In: Himmelsbach T, Hötzl H, Käss W, Leibundgut C, Maloszewski P, Meyer T, Moser H, Rajner V, Rank D, Stichler W, Trimborn P, Veulliet E (Eds.) Application of Tracer Models, Steirische Beiträge zur Hydrogeologie, 6th International Symposium on Water Tracing, Transport Phenomena in Different Aquifers (Investigations 1987– 1992), vol. 43. Joanneum Research, Graz, Austria, 116–158.

Massei N, Wang HQ, Field MS, Dupont JP, Bakalowicz M, Rodet J (2006) Interpreting tracer breakthrough tailing in a conduit-dominated karst aquifer. Hydrogeol. J. 14 (6), 849–858.

Morales T, Uriarte JA, Olazar M, Antigüedad I, Angulo B (2010) Solute transport modelling in karst conduits with slow zones during different hydrologic conditions. J. Hydrol. 390 (2010), 182-189.

Poulain A, Rochez G, Van Roy JP, Dewaide L, Hallet V, De Sadelear G (2017) A compact field fluorometer and its application for dye tracing in karst environments. Hydrogeol. J. doi : 10.1007/s10040-017-1577-1

Schnegg PA, Doerfliger N (1997) An inexpensive flow-through field fluorometer. Proceedings of the 6th Conference on Limestone Hydrology and Fissured Media, La Chaux-de-Fonds. Centre of Hydrogeology, University of Neuchatel, Vol. 2, 47-50.

Schudel B, Biaggi D, Dervey T, Kozel R, Müller I, Ross JH, Schindler U (2003) Application of artificial tracers in hydrogeology- Guideline. Centre of Hydrogeology, University of Neuchatel Bull. d'Hydrogéol, Special Issue, N°20, 91 p.

Werner A, Hötlz H, Maloszewski P, Käss W (1997) Interpretation of tracer tests in karst systems with unsteady flow conditions. In : Leibundgut C, Gunn J, Dassargues A (Eds) Karst hydrology : Proceedings of an international workshop held at Rabat, Morocco during the fifth scientific assembly of the IAHS (23 April to 3 May 1997), IAHS Publication n° 247, 15-26.

Appendix III

Published Article

"Solute transport in heterogeneous karst systems: Dimensioning and estimation of the transport parameters via multi-sampling tracer-tests modelling using the OTIS (One-dimensional Transport with Inflow and Storage) program"

Title

Solute transport in heterogeneous karst systems: dimensioning and estimation of the transport parameters via multi-sampling tracer-tests modelling using the OTIS (One-dimensional Transport with Inflow and Storage) program

Dewaide Lorraine[a] , Bonniver Isabelle[b 1], Rochez Gaëtan[c], Hallet Vincent[d]

a Affiliation : University of Namur, Geology Departement, Rue de Bruxelles, 61, 5000 Namur, Belgium

Corresponding author : lorraine.dewaide@unamur.be ; +3281724475

b Affiliation : University of Namur, Geology Departement, Rue de Bruxelles, 61, 5000 Namur, Belgium

1 Present address: SPW, DGO 3, Avenue Prince de Liège, 15, 5100 Namur, Belgium

c Affiliation : University of Namur, Geology Departement, Rue de Bruxelles, 61, 5000 Namur, Belgium

d Affiliation : University of Namur, Geology Departement, Rue de Bruxelles, 61, 5000 Namur, Belgium

Vincent.hallet@unamur.be

Abstract

This paper presents the modelling results of several tracer-tests performed in the cave system of Han-sur-Lesse (South Belgium). In Han-sur-Lesse, solute flows along accessible underground river stretches and through flooded areas that are rather unknown in terms of geometry. This paper focus on the impact of those flooded areas on solute transport and their dimensioning. The program used (One-dimensional Transport with Inflow and Storage: OTIS) is based on the two-region non equilibrium model that supposes the existence of an immobile water zone along the main flow zone in which solute can be caught. The simulations aim to replicate experimental breakthrough curves (BTCs) by adapting the main transport and geometric parameters that govern solute transport in karst conduits. Furthermore, OTIS allows a discretization of the investigated system, which is particularly interesting in systems presenting heterogeneous geometries. Simulation results show that transient storage is a major process in flooded areas and that the crossing of these has a major effect on the BTCs shape. This influence is however rather complex and very dependent of the flooded areas geometry and transport parameters. Sensibility tests performed in this paper aim to validate the model and show the impact of the parametrization on the BTCs shape. Those tests demonstrate that transient storage is not necessarily transformed in retardation. Indeed, significant tailing effect is only observed in specific conditions (depending on the system geometry and/or the flow) that allow residence time in the storage area to be longer than restitution time. This study ends with a comparison of solute transport in river stretches and in flooded areas.

Keywords: solute transport; karst conduit dimensioning; tracer-test; transport parameters; transient storage; tailing effect

1. Introduction

Tracer tests can be a powerful tool when they are used in a quantitative approach in order to characterize solute transport in karst conduits. They provide direct information about groundwater trajectories and hydraulic connections inside a complex karstic network and give breakthrough curves (BTCs) from which some major transport parameters can be easily assessed (first arrival, travel time, tracer velocity, tracer recovery,…).

Modelling of solute transport in karst conduits consists in fitting a modeled BTC with the one obtained in field experiment. Modelling of BTCs allows to define transport parameters, notably the advection and dispersion effects, to evaluate the active conduit geometry and to predict the behavior of a karstic system in different flow conditions.

The karstic site of Han-sur-Lesse is a major system in Belgium that offers interesting features in a modelling purpose. Indeed, the system corresponds to an entire stream sinking into a hole that can swallow up to 25 m^3/s and flooding a large heterogeneous karstic network made of flooded areas that are interconnected by conduit stretches. Flooded areas are saturated zones of unknown geometry, probably intensely karstified but with limited physical access. The assumption is that the transport dynamic is different in those flooded areas and in the river

stretches. Therefore the objectives of this study are firstly to observe and to characterize the solute transport in both the flooded zones and the river stretches; secondly to dimension the active system.

In this aim, the OTIS program (One-dimensional Transport with Inflow and Storage), developed by Runkel (1998), was chosen partly because it offers the possibility to build a discrete system and therefore to test the effect of geometry on solute transport. Furthermore the Han-sur-Lesse BTCs show an asymmetry, a tailing that is commonly observed in field BTCs in general. This persistent skewness is often associated to retardation in the literature. The process recognized as the main cause of retardation is the existence of immobile flow regions along the tracer path (Hubbard et al. 1982; Martin and McCutcheon, 1998). As OTIS allows the simulation of discrete immobile water zones, this study will also test the effect of transient storage on the BTCs. Finally, sensibility tests will show the efficiency of OTIS as a modelling program for solute transport parametrization and karst conduits dimensioning.

2. The OTIS program: theoretical background

Ground-water flow and solute transport in karst conduits are characterized by turbulent flow in a non-constant permeability media. Classical advection-dispersion equation (1) can explain solute transport in karst conduits only in the case of equilibrium model, i.e. in dynamic processes. In equilibrium model, evolution of the solute concentration (C) with time (t) is only dependent on the longitudinal flow velocity (v_L) and their longitudinal dispersion (D_L). Equation 1 supposes a decay coefficient (μ) that can affect the restitution rate and a retardation factor (R_f) that is here only linked to solute sorption on solid particles.

$$R_f \frac{\partial C}{\partial t} = D_L \frac{\partial^2 C}{\partial x^2} - v_L \frac{\partial C}{\partial x} - \mu C \quad (1)$$

Eq. (1) is however not sufficient to explain transport in karstic systems. Indeed, it can't explain the asymmetry generally observed in field BTCs. This persistent skewness and tailing has been widely discussed and considered as the results of complementary processes as adsorption-diffusion, molecular diffusion, dilution effects, multiple conduits effects, but the main process responsible for BTCs skewness is the interaction with immobile water (Hubbard et al. 1982; De Marsily, 1986; Maloszewski and Zuber, 1989; Rossier and Kiraly, 1992; Maloszewski *et al*., 1992; Werner *et al*., 1997). Therefore, transient storage has to be taken into account in eq (1). It exists in regular or irregular conduits due to the velocity gradient between the main flow zone and the conduits walls that causes turbulent flow (Martin and McCutcheon, 1998; Hauns and Jeannin, 1998; Hauns *et al.*, 2001). Field and Pinsky (2000) proposed the "two-region non-equilibrium model" that supposes the existence of immobile water zones along the solute transport path. An exchange exists between mobile and immobile zones but transport is only effective in the mobile, dynamic zone. Runkel (1998) developed a program called OTIS (One-dimensional Transport with Inflow and Storage) based on the two-region non-equilibrium approach. OTIS was initially created to solve solute transport problematic in surface streams implying concentration variation in longitudinal direction only and free elevation of the water

level, features that are relevant for karst conduit flows. As shown in figure 1, OTIS supposes a main dynamic flow in mobile zone in which solute is transported by advection and affected by dispersion and, possibly, adsorption and decay. Next to the main channel, immobile zones equally distributed along the main flow zone exist. They act as transient storage zones for the solute that can be affected by chemical reactions but where there is no transport by advection and dispersion. To permit storage in stagnant zones, an exchange between mobile and immobile water zones has to take place. Finally, lateral flow can be added and/or retract from the main flow.

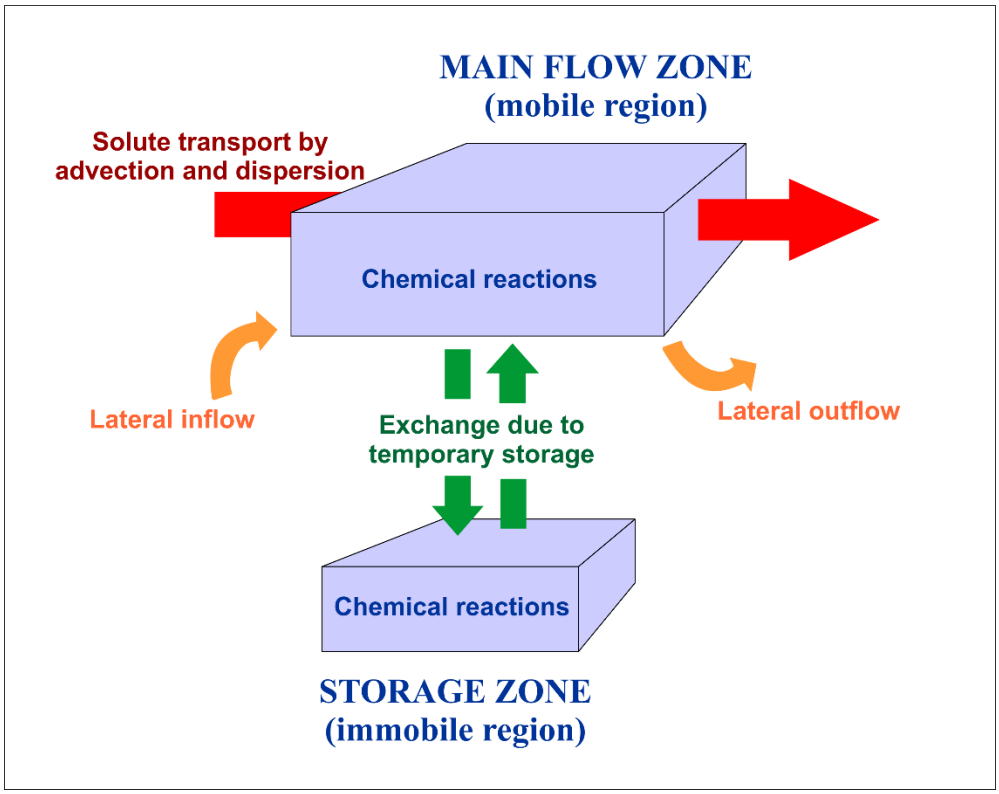

Figure 1. Main functioning principles in OTIS. Solute transport occurs in the main flow zone while an exchange with a storage zone exists (modified from Runkel, 1998).

In accord with all these features, the OTIS program is guided by the following equations for conservative and non-conservative solutes (terms in square brackets):

$$\frac{\partial C}{\partial t} = -\frac{Q}{A}\frac{\partial C}{\partial x} + \frac{1}{A}\frac{\partial}{\partial x}\left(AD_L\frac{\partial C}{\partial x}\right) + \frac{qlin}{A}(C_{lin} - C) + \alpha(C_s - C) + [\rho\lambda'(C_{sed} - K_d C) - \lambda C] \quad (2)$$

and,

$$\frac{\partial C_s}{\partial t} = \alpha\frac{A}{A_s}(C - C_s) + [\lambda'_s(C'_s - C_s) - \lambda_s C_s] \quad (3)$$

where C, C_{lin} and C_s [M/L^3][1] are solute concentrations in, respectively, the main channel, the lateral inflow and the storage zone; A and A_s [L^2]the cross-sectional areas in the main channel and storage zone; Q [L^3/T] the volumetric flow rate; q_{lin} [$L^3/T.L$]the lateral inflow rate; D_L [L^2/T] the longitudinal dispersion coefficient; α [T^{-1}] the storage zone exchange coefficient; t

[1] The fundamental units of Mass [M], Length [L] and Time [T] are used throughout this chapter.

the time [T]; x the distance [L]. Considering non-conservative solute, C_{sed} is the sorbate concentration on sediment; C'_s the background storage zone solute concentration; K_d [L^3/M] the distribution coefficient; λ and λ_s [T^{-1}] the first-order decay in the main channel and the storage zone; λ' and λ'_s [T^{-1}] the sorption rate coefficient in the main channel and the storage zone; ρ [M/L^3] the mass of accessible sediment by volume water.

The major advantage in OTIS is the possibility of discretization of the system which is a very interesting feature in heterogeneous environments. A system needs therefore to be conceptualized in order to be cut in "reaches" that can be modeled separately, and so being characterized by different dimensions and transport parameters. Each reach is subdivided in a number of discrete segments that represent control volumes within which mass is conserved. Equations (2) and (3) apply then in each segment and numerical solutions have to be found.
To implement a numerical solution scheme, OTIS uses the implicit Crank-Nicolson method (for details on the solutions, see Runkel, 1998 and Runkel and Broshears, 1991). The solution has to be constrained by conditions at the upstream and downstream boundary of the system. The upstream boundary condition (USBC) is the solute concentration injected in the system. This concentration can vary in time regarding to the injection mode (concentration-step, flux-step, concentration-continuous). The downstream boundary condition (DSBC) is not a concentration but a dispersive flux. This flux is defined at the interface between the last segment in the modeled system and an additional fictitious segment. Eventually, to solve the equations that governed the model, it should be precise if the solute is conservative or not (equations (2) and (3) without or with square brackets) and if the transport occurred in steady or unsteady flow.

3. Methodology

Quantitative tracer-tests are powerful tools to assess the main features of an active karst system. Indeed, the resulting BTCs parameters inform on the solute transport dynamics within the system. The system investigated in the context of this paper shows very distinct geometric features along the tracer path in the form of river stretches and flooded areas. Therefore, as the OTIS program gives the possibility to subdivide the system in reaches, each heterogeneity in the system can be associated to one different reach characterized by specific dimensions and transport parameters. In order to simulate solute transport in each reach, sampling points must be settled at the upstream and downstream boundaries of those reaches. In practice, each reach is first calibrated independently on basis of the intermediate sampling points; which means that each intermediate BTC is used as USBC. Secondly, the calibrated reaches are assembled in a unique discrete but continuous system in which are considered only one solute introduction at the entrance and an exclusive BTC at the exit (fig. 2). It is important to precise that the simulations presented below make the assumption that decay and sorption are non-existent along the path (conservative tracer). Consequently, retardation observed in BTCs will not be considered as the result of sorption-desorption effects and, taking into account equation (2), the only parameters that intervene in the simulations are the main flow section (A), the storage zone section (A_s), the mass exchange coefficient (α) and the longitudinal dispersion coefficient (D_L).

Calibration of the dimension and transport parameters is the result of trial and error tests (direct method). Once the fitting between the simulated curve and the field data is graphically accurate, a final step of optimization is realized thanks to OTIS-P which is a complementary version of OTIS. The OTIS-P model couples the mathematical framework of OTIS with the Nonlinear Least Square algorithms of STARPAC (for details see Runkel, 1998 and Donaldson and Tryon, 1990). This leads to an automated parameter estimation (inverse method). However, one should understand that this inverse determination of parameters comes after the trial-error tests. Indeed, to run OTIS-P, a first parameter estimation is needed. Therefore, this optimization process is rather constrained by the direct estimation which takes into account the observations made on the field.

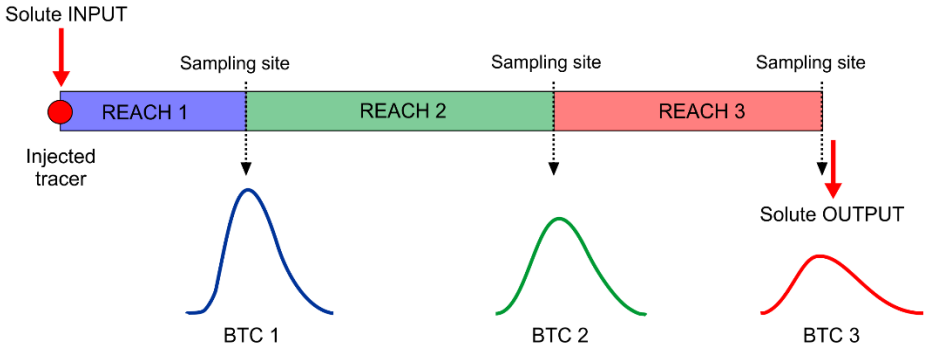

①

Calibration	USBC	DSBC
Reach 1	injected tracer	BTC 1
Reach 2	BTC 1	BTC 2
Reach 3	BTC 2	BTC 3

②

Discretization	USBC	DSBC
Whole system (reaches 1, 2,3)	Solute INPUT Injected tracer	Solute OUTPUT BTC3

Figure 2. Modelling principle. First, calibration is realized on each reach individually; then the final discretization simulate solute transport on the whole system. Optimization is a complementary process not shown in this figure.

Sensibility tests are systematically realized to evaluate the reliability of the modeled parameters values. They consist in varying one parameter at a time, the others staying constant. Furthermore, the numerical stability of the model can be verified by two parameters: the numerical Current (C_r) and Peclet (P_e). They are defined as follow (Gray and Pinder, 1976; Kinzelbach, 1986):

$$C_r = \frac{v.\Delta t}{\Delta l}, \text{ and, } P_e = \frac{v.\Delta l}{D_L}$$

Where v is the particle effective velocity, Δt the integration time-step, Δl the length of the discrete element and D_L the longitudinal dispersion. C_r should be inferior to 1 to ensure that the advection transport length is smaller than the discrete element length, so that the concentration variation due to advection is visible within this element. P_e expresses the equilibrium between advection and dispersion within the discrete element. It shouldn't exceed the value of 2 for a stable model.

A complete OTIS model can then finally be proposed and the results analyzed and criticized. At last, the accuracy of the model can be validated in applying this model to other tracer-tests realized in different flow conditions.

As stated in the introduction, the following chapters will show applications of the OTIS model in the case of the Han-sur-Lesse cave system. Next chapters will give a brief geological and karstic setting, the main results of the tracer-tests and the OTIS simulation assumption and optimized results.

4. Geologic and hydrogeologic settings

Han-sur-Lesse is a small village located in south Belgium, about 60 km south-west from the city of Namur. The Han-sur-Lesse karstic network is developed in the belgian Givetian limestones outcropping within a geomorphological unit called “La Calestienne” that forms a high relief in the landscape in contrast to the surrounding siltstones. More specifically, the cave appears in the “Boine Massif”, a 1.6 km^2 ridge of fractured limestones. This ridge corresponds to an anticlinal dome oriented E-W and with a westward plunge. Major faults and fractures follow either a NE-SW or a NNW-SSE direction. The complex structure of the Boine Massif is inherited from the variscan and meso-cenozoïcan tectonics and the cave network is follows mainly the intensely fractured fold axis (fig. 3). Given a strong relationship with the structural and lithological features, the sub-vertical stratification plans favor here a vertical development of the karst features (Havron *et al*., 2007).

The drainage of the massif is mainly supported by the 2 km long sinkhole-resurgence system between the Gouffre de Belvaux (GB) and the Trou de Han (TH). The active karst system is sustained by the surface Lesse river that drains a flow varying between 0,5 and 90 m^3/s. When the discharge of the river is less than 25 m^3/s, it sinks entirely into the swallow hole which is perched above the groundwater level. When the surface flow exceeds 25 m^3/s however, the sinkhole is saturated and overflows into the aerial waterway (Quinif, 1988) where downstream sinkholes can be activated. The system consists in subterraneous river stretches that connect flooded areas (fig. 4). While the river stretches are rather well known because of their speleological access, the flooded areas can only be explored by diving. Those areas can be described as permanently saturated zones, hundreds of meters long and that can reach at least 40 m below the resurgence level in deepness. They consist in interconnected heterogeneous flow sections that develop in highly fractured and karstified rock volumes (Bonniver, 2011). Due to the high degree of karstification, the regional piezometric gradient of the limestone aquifer is less than 0.1 %. The exact geometry of these flooded areas is unknown.

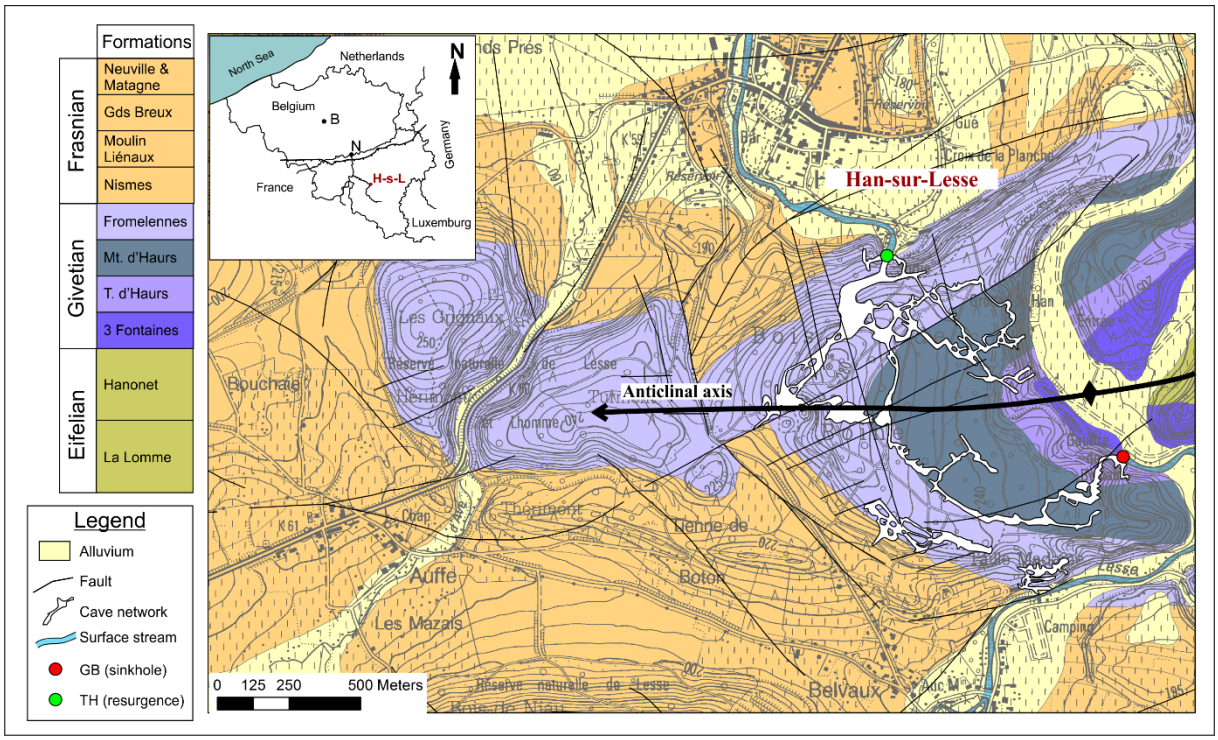

Figure 3. Location and geological setting of the Han-sur-Lesse karstic network. Karst is developed mainly along the intensely fractured fold axis in the Givetian limestones. [B] : Brussels, [N] : Namur, [H-s-L]: Han-sur-Lesse (modified from Blockmans and Demoulin, *in press*).

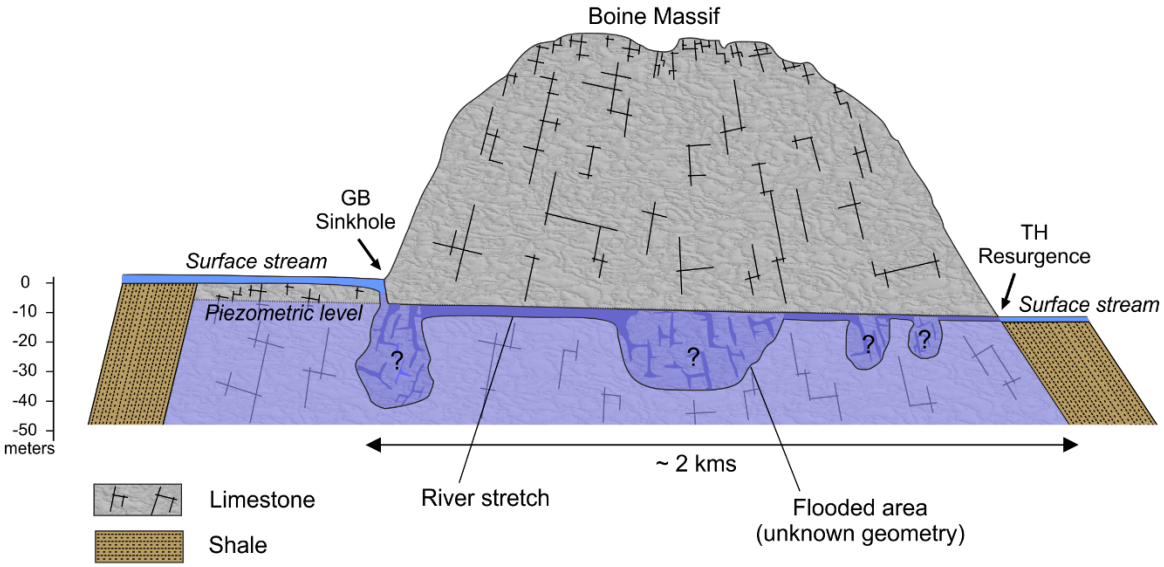

Figure 4. Cross section in the Boine Massif. The Han-sur-Lesse karstic system is a succession of flooded areas linked by underground river stretches. [GB]: *Gouffre de Belvaux*, [TH]: *Trou de Han*. Dimensions of the flooded zones are hypothetic (modified from Bonniver, 2011).

5. Solute transport features

5.2 Multi-sampling site tracer-test: first model building

As explained above, the karstic network in Han-sur-Lesse is very well known and precise topographic data are available. However, the flooded areas remain a question mark regarding their dimensions and their influence on solute transport. They can be described as irregular saturated zones embedded in fracturated stones and rocks of various volumes. Due to intense karstification, the top of these areas is at the atmospheric pressure. Given this erratic geometry, they should involve immobile water zones in which the solute is temporarily caught and can be exchange with the main flow zone. In contrast, river stretches are usual karst conduit where an actual river flows and where, according to field observation, transient storage in immobile water zones is either a minor or non-existent process. Therefore, in order to find how the transport parameters behave in flooded areas and in river stretches, modelling of those sections and their associate parameters is needed.

To address to this issue, a tracer-test was performed in low flow conditions in order to characterize solute transport between the Gouffre de Belvaux (GB) and the Trou de Han (TH). However, for practical reasons not developed here, the system considered for dimensioning is limited between GB and location C. The total length of this system (GB-C) is about 1.5 kilometers. The measured discharge was of 0.7 m^3/s. The flow was stable along the tracer path (no lateral inflow) and the discharges stayed steady during all the restitution period. 200 g of fluorescein was injected 260 m upstream the GB to assure a good homogenization of the tracer cloud before its entry in the system. Four automatic sampling and measuring devices (fluorometers GGUN-FL30, Schnegg and Doerfliger, 1997) were placed along the system and define three sub-systems of different length. Sub-systems GB-A and B-C correspond to flooded areas that are connected by the river stretch sub-system A-B (fig. 5).

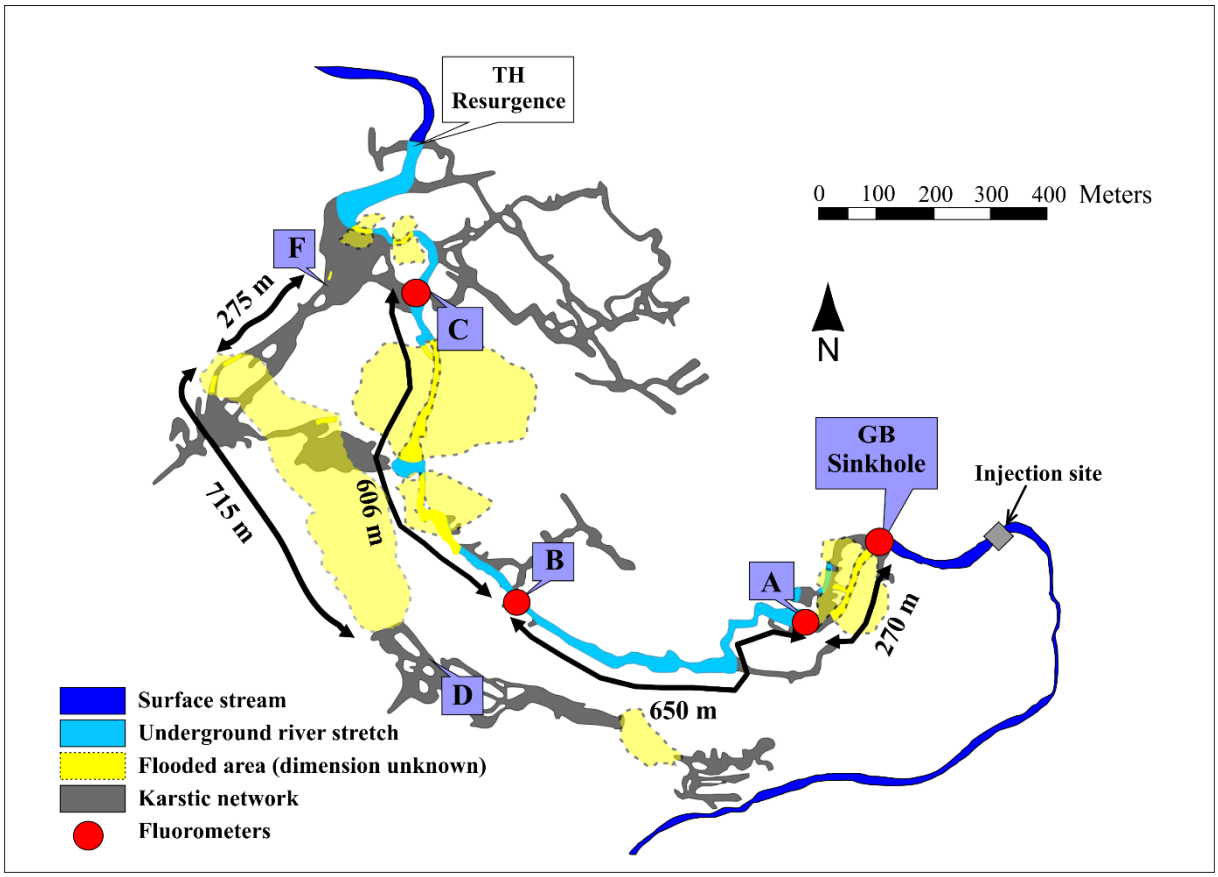

Figure 5. Tracer-test system divided in subsystems. Sections GB-A and B-C are mainly flooded areas while A-B corresponds to a river stretch. Locations D and F are involved in another test (section 4.3.2) (modified from Bonniver, 2011).

Restitution rate at the output was of 85 %, meaning that the losses are very poor. Given the modelling objective based on this tracer-test, BTCs obtained at each sampling site were corrected for a tracer recovery set at 100 % (fig. 6). Therefore, it is supposed that there is no loss of the tracer along the system; that the chemical reactions of sorption and decay are non-existent; and that location C is the only output of the system (which is confirmed by the observations of the geological environment). A qualitative analysis of the BTCs indicates that transport seems dominated by advection (closed and rather symmetric curves) and that the maximum concentration is decreasing along the path while the curves are widening. The growing asymmetry and flattering of the curves are related to retardation and dispersion effects. However, looking at the experimental BTCs shape, there is no clear difference in the behavior of the solute when it crosses the river stretch or the flooded area. The influence of the flooded area will therefore be evaluated through the modelling of the transport parameters. OTIS, allowing a discretization of the system, is a valuable and adequate tool in this purpose.

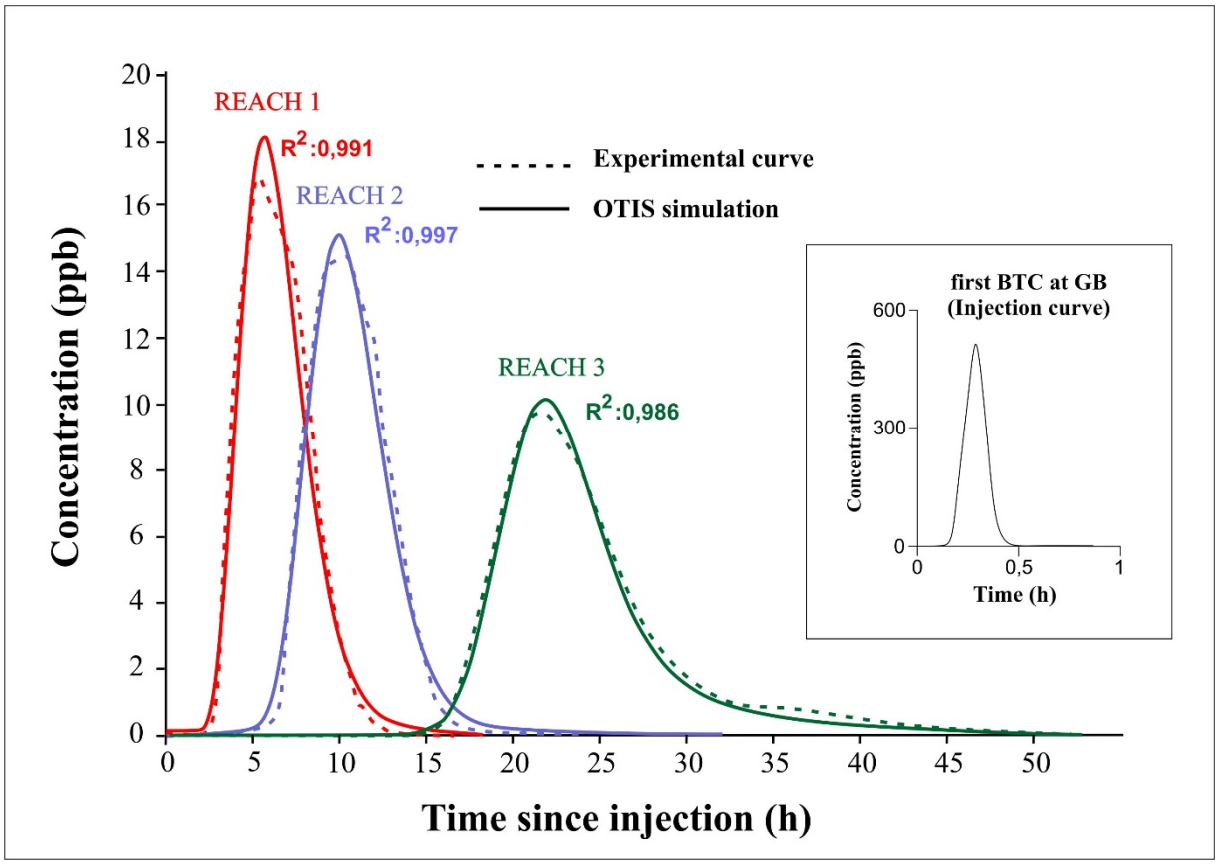

Figure 6. Tracer-test 1 results. Comparison between experimental BTCs and the curves obtained by calibration of each reach.

The conceptual model used to perform transport simulations in the Han-sur-Lesse cave is presented in figure 7. Each sub-system of the conceptual model corresponds to one "Reach" in OTIS. Each Reach is divided in segments of 0.5 meters length (L_{seg}) in which are performed equations (4) and (5) at an integration time of 8.10^{-4} h (ΔT). No lateral inflow (q_{lin}) or outflow (q_{lout}) is taken into account as none is known and furthermore there is no discharge variation between the upstream and the downstream flows of the system (steady flow). As the restitution rate considered in the BTCs is 100% (see above), chemical reactions are supposed non-existent (conservative tracer). Storage zone and exchange coefficient are simulated only in reaches corresponding to flooded areas.

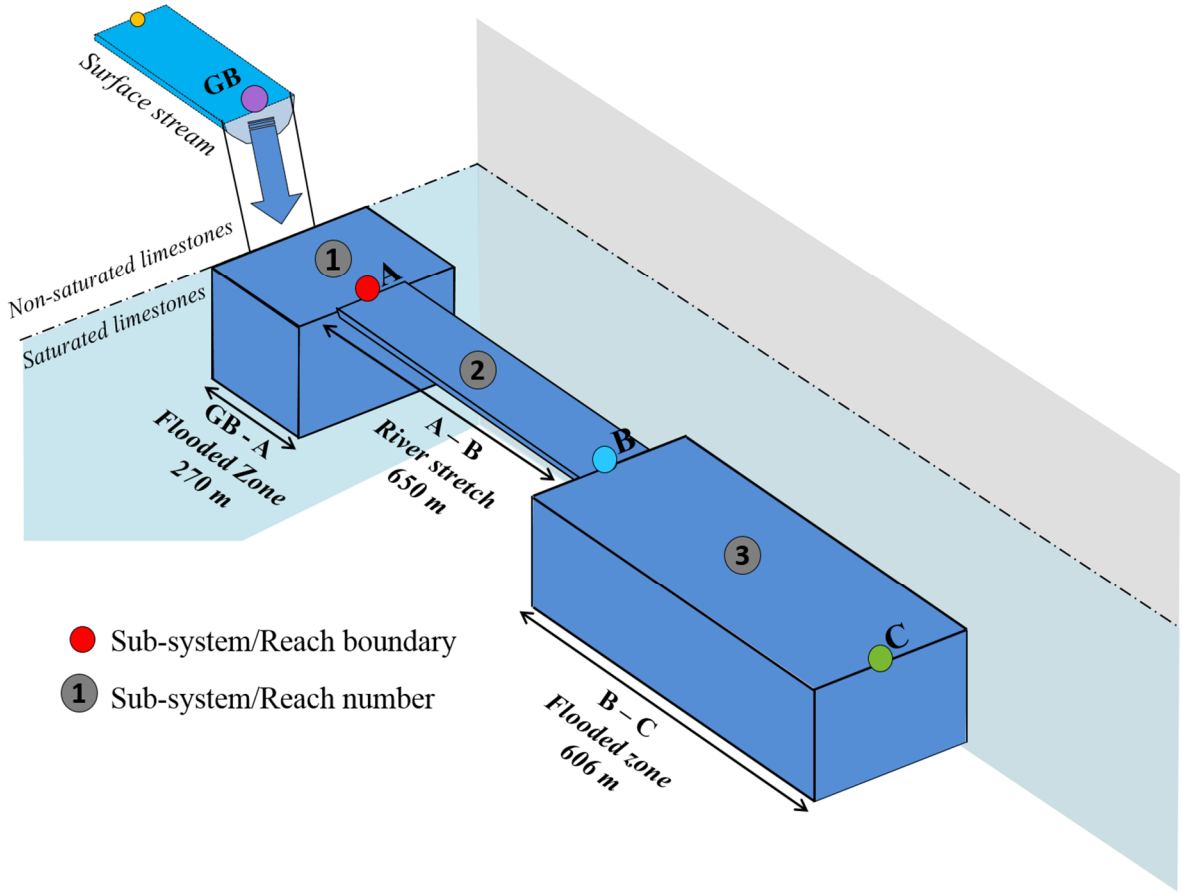

Figure 7. Conceptual model of the investigated system. Three sub-systems, defined as flooded zone or river stretch, are considered as reaches for the OTIS simulation. Note that the GB sinkhole site is considered as perched in contrast to the subterraneous system (modified from Bonniver, 2011).

Precise calibration of each reach was realized using the upstream BTC as the input and the downstream BTC as the output. Each experimental BTC was therefore simulated via OTIS in fitting the simulated curve to the experimental one, and this fitting was optimized with OTIS-P (fig. 6) The coefficients of determination have a value of 0.991; 0.997 and 0.986 for reach 1, 2 and 3 respectively. In addition to the conduits dimensioning, the transport parameters are also estimated (table 1 – tracer-test 1: Q = 0.7 m^3/s). Results are discussed in detail in the following chapter but it can already be said that dimensioning values from table 1 seem realistic. Indeed, the model estimates the river stretch main flow section at 17 m^2 which is consistent with field observations. A validation of the built model is proposed in the next chapter.

		Optimized parameters				Calculated from the parameters				Model stability	
Q (m^3/s)	**Reach**	**A** (m^2)	**A_s** (m^2)	**D_L** (m^2/s)	**α** (s^{-1})	**Vol** (m^3)	**Vol_s** (m^3)	**V_e** (m/s)	**a_L** (m)	**C_r**	**P_e**
0.7	**1** Flooded area	34.2	22.0	0.102	3.9E-04	9180	5940	0.020	4.5	0.02	0.07
	2 River stretch	17.0	/	0.683	/	11050	/	0.041	16.6	0.03	0.01
	3 Flooded area	43.3	7.5	0.174	1.6E-05	26240	4545	0.016	10.8	0.01	0.02
0.9	**1** Flooded area	36.6	23.5	0.085	1.0E-04	9880	6345	0.024	3.5	0.02	0.07
	2 River stretch	20.0	/	0.51	/	13000	/	0.045	11.3	0.03	0.03
	3 Flooded area	45.4	8.9	0.108	1.3E-04	27270	5340	0.019	5.7	0.01	0.04
1.4	**1** Flooded area	37.0	26.0	0.13	7.2E-05	9990	7020	0.038	3.4	0.02	0.07
	2 River stretch	22.2	/	0.72	/	14440	/	0.063	11.4	0.02	0.01
	3 Flooded area	45.0	10.3	0.12	6.8E-05	27270	6242	0.030	4	0.01	0.01

Table 1. Modelization of the traced system in different flow conditions (tracer-tests 1, 2 and 3): dimensioning and transport parameters estimation.

5.2 Model validation and discussion on the parameters

To validate the model, two complementary tracer tests were performed in various hydrological conditions: the second one was conducted for a river discharge of 0.9 m³/s and the third one for a discharge of 1.4 m³/s. The conceptual model of the investigated system remains the same, the parameters were adapted to each tracer test. Figure 8 shows the output BTCs (obtained at the system exit C) from tracer-test 1, 2 and 3 and the optimized fitted curves corresponding.

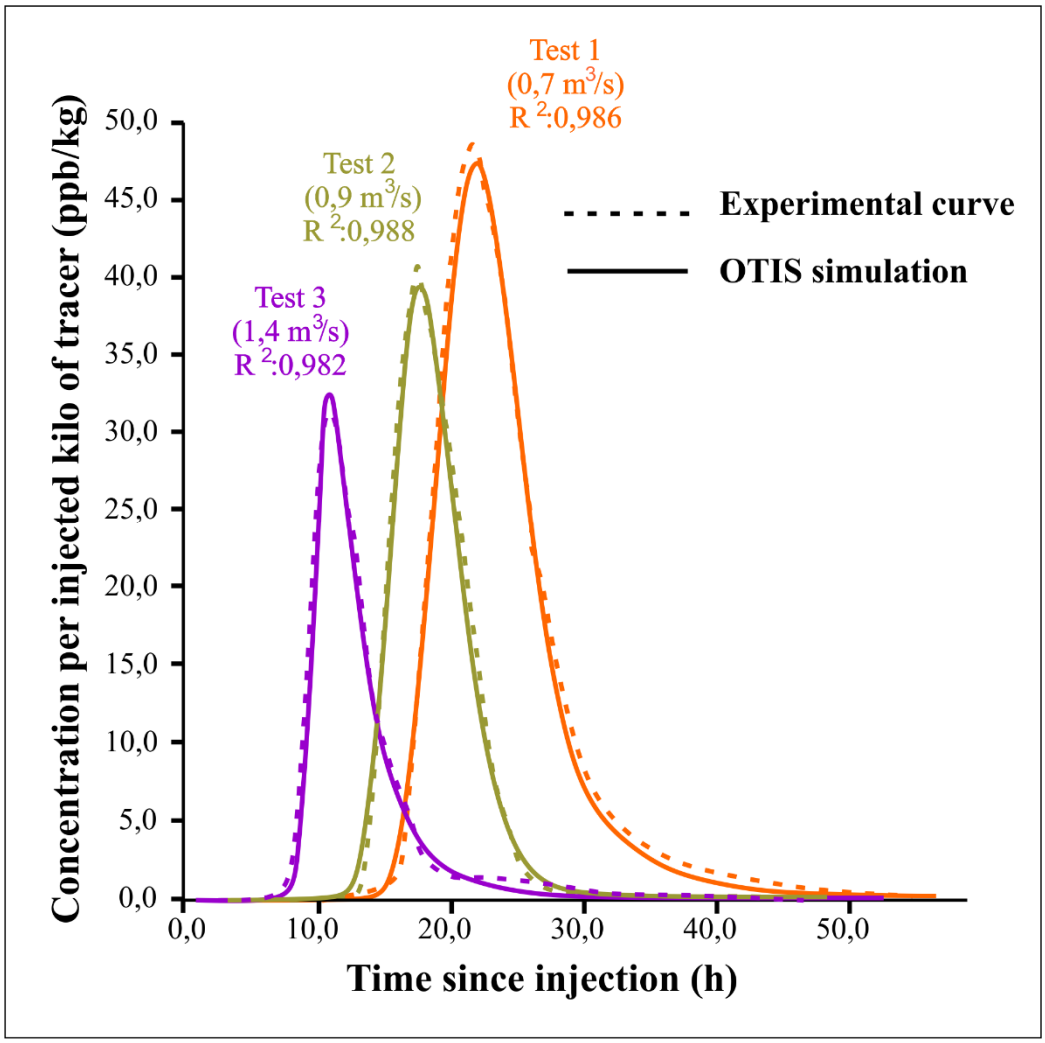

Figure 8. Comparison of the experimental output BTCs and the OTIS simulated curves for each tracer-test. Note that the concentration is expressed in ppb per injected kilo of tracer. The modeled system is the GB – C system that is discretized in three reaches.

Parameters values estimation are summarized in table 1. In each case, C_r and P_e numbers have values inferior to 1, which attests that the simulations are stable. On the transport parameters, a few first conclusions can be drawn:

Main flow section (A): The modeled dimensions seem reliable, all the more since the active river stretch section between locations B and C (reach 2) was evaluated on the field showing that in situ measures are similar to the OTIS values. Furthermore, as it could be expected, *A* values are much bigger for the flooded areas than for the active river. In consequence, effective velocity (V_e) is at least two times higher in the river section. Moreover, *A* in flooded areas does not vary in a significant way whatever the flow conditions while in the river stretches it increases with flow.

Storage zone section (A_s): OTIS confirms that the modelling of solute transport in flooded areas needs to suppose the existence of a storage zone (immobile water) in which solute can be caught. On the contrary, immobile water in the river stretch is considered as non-exist in the

model. A_s, and so the volume of the storage zone, is smaller than the main flow volume in both reach 1 and 3. However, considering the total volume of water affected by the tracer cloud; i.e. Vol + Vol_s, the immobile water constitutes 35 to 41 % of this total volume in reach 1 but only 12 to 15 % in reach 3. So the volume of immobile water is not influenced by the volume of the flow section.

Finally, unlike the main flow section, A_s is apparently dependent of the flow conditions as shown by the As value difference between tracer-test 1 and 3. Therefore, flooded areas have to be thought as fracturated rock volume in which the main flow section is constrained whatever the flow but where the volume of immobile water can increase with a growing discharge. Figure 9 proposes a conceptualization of flooded areas in Han-sur-Lesse.

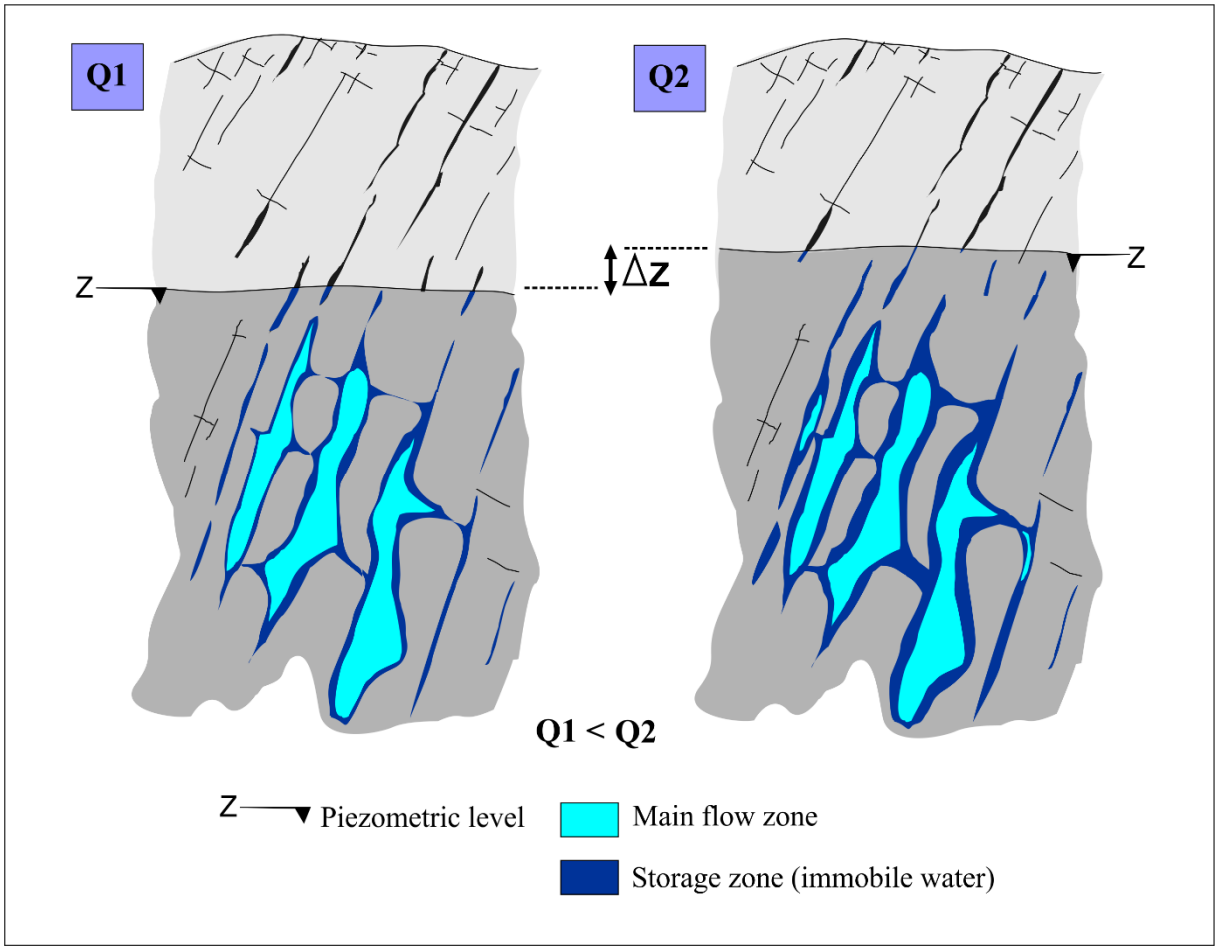

Figure 9. Flooded area conceptualization deduced from the modelling results. Main flow zone in flooded area is confined while the storage volume grows with the discharge (modified from Bonniver, 2011). The sketch is without scale.

Exchange coefficient (α): In OTIS, α is described as the fraction of the main channel volume that is exchanged with the storage zone, per unit time. So α constrains the mass of solute that will be exchange between mobile and immobile zone. The α values modeled by OTIS in the Han-sur-Lesse case vary between 1.6×10^{-5} and 3.9×10^{-4} s^{-1}. Comparing to α values found by Field and Pinsky (2000), i.e. 1.0×10^{-5} to 5.0×10^{-5}, or Geyer et al. (2007); i.e. 2.5×10^{-6} s^{-1}, α

in the Han-sur-Lesse system is slightly higher. There is no clear evolution tendency in the α values in regard to the discharge changes, and α stays rather stable in the different reach. It seems therefore that the exchange coefficient is not very dependent to the storage volume or flow conditions, at least in the range of discharge considered in this study.

Dispersion coefficient (D_L): Simulated D_L values vary between 0.085 and 0.72 m^2/s. There is no clear trend in the D_L values evolution between the tests. Theoretically, the dispersion coefficient should increase when the flow increases. Indeed, several authors (Hauns *et al*., 2001; Massei *et al*., 2006, Morales *et al*., 2010) have shown that the relation $D_L = a_L.V_e$ is verified in karst conduits. In our case, this relation is not so evident but one should keep in mind that the range of discharge in which the tests were performed is rather small. Actually, in the low flow conditions that characterized our field experiment, D_L seems more inherent to the type of environment than to the general flow conditions. Indeed, the river stretch has, in each case, a more dispersive behavior than the flooded areas. This fact can be easily understood, considering that velocity is much higher in the river given that the section is smaller. Turbulence effects along the walls are then presumably more important in the river stretches than in the flooded areas, giving way to higher dispersion. Furthermore, the absence of immobile water in the river stretches, which was stated from the field observation and confirmed by the modelling, should also explain the higher dispersion. Indeed, immobile water being logically concentrated along the rock walls, the storage section could be seen as a buffer zone that mitigates turbidity and thus dispersion. This immobile water being absent of the river stretches, there is no buffering action that could decrease turbidity.

4.3 Transport characterization in flooded areas

4.3.1 Sensibility tests

As the BTC's characterizing solute transport through the system GB-C are quite symmetric, the effect of immobile water present in flooded area is not easy to distinguish on the curves. Indeed, if the flaring and the asymmetry of the BTCs increase along the path, the tailing effect generally linked to retardation is not very clear. This is probably due to the equilibrium between residence time in storage zone and restitution time. In fact, when transport in the main flow zone is too quick or that the travel distance is too short, storage is not really effective because the contact time between mobile and immobile water is too short for it to develop (Brouyère, 2001; Zhang *et al*., 1998; Wang, 1987). Hauns *et al.* (2001) showed that retardation and dispersion are much more important in systems where dispersive structures (pool, rapids) exist, and that those processes are the expression of a transient storage. Nevertheless, the effect on BTCs is rather complex because of the "scale effect" which implies that retardation is dominant at a local scale but that it will decrease for the benefit of dispersion with growing length scale (Jeannin and Maréchal, 1997). This is explained by the fact that storage time becomes smaller than restitution time when distance increases. To resume, breakthrough time has to be long enough to allow the development of transient storage but not too long at the risk of becoming longer than the residence time in storage zone.

In the attempt to understand the hydrodynamic of the transport parameters in flooded areas particularly, sensibility tests were performed on reach 1 and 3. As they both showed similar responses to the sensibility tests, results presented here (fig. 10) are those of the tests leaded on reach 1 only. They consist in varying one parameter at a time, the three others staying constant. Figure 10 shows for each parameter the initial OTIS fitted curve and the resulting curve obtained from the parameter variation. The deviation of the new curve from the initial model can be assessed visually and mathematically thanks to the determination coefficient. Given the really good result of our initial modelling (R^2 superior to 0.991), it will be considered that a R^2 inferior to 0.980 corresponds to a significant deviation. Figure 10 indicates a strong control of the main flow section on the result (fig. 10 A). Indeed a change of + 10 % or – 10% of the A initial value is enough to lower R^2 to 0.961 and 0.957 respectively. In varying the A value, the first arrival and the peak concentration are greatly impacted. It can therefore be considered that the initial A value is accurately estimated within an error margin of less than 10% of its value. The storage zone section estimation seems also to have a major influence on the BTC shape but it is a bit less sensible than A as a change of at least 20% of its initial value is needed to lower R^2 to less than 0.980. (fig. 10 C). The BTC changes are seen mainly in the first arrival and the peak concentration as well. Variation of D_L (fig. 10 B and α (fig. 10 D) values has an impact on the peak concentration mainly. They are however much less sensible as in the D_L case, a change of more than ± 50 % of the value is necessary to see a significant deviation (R^2 under 0.980) from the fitted curve.

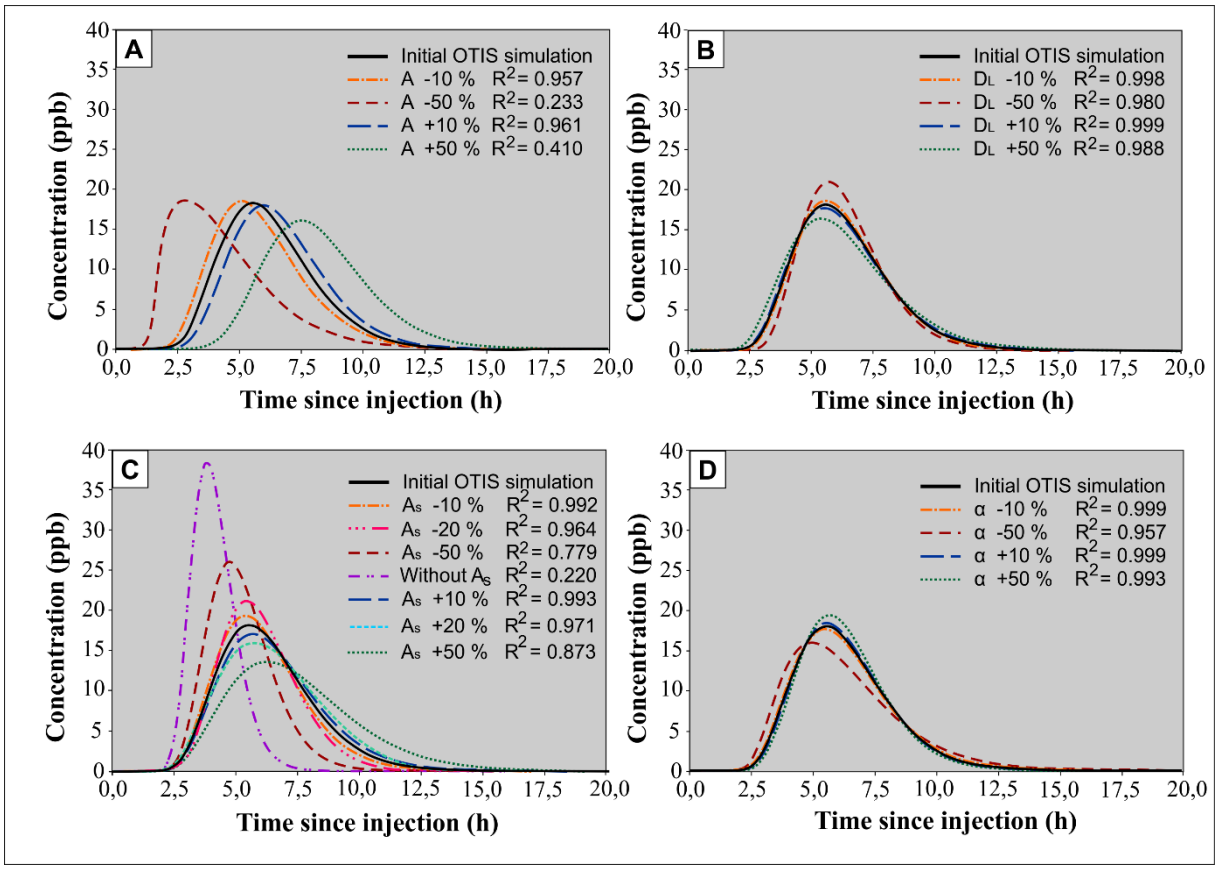

Figure 10. Parameters sensibility tests for reach 1 modeled in tracer-test 1. Each graph corresponds to one different parameter: A) flow zone section; B) dispersion coefficient; C) storage zone section; D) transient storage coefficient.

In addition to assessing the sensibility of the different parameters, those tests show also interesting things in regard to the BTC shape, especially concerning the tailing effect. Equation (3) governing the evolution of concentration in the storage zone should be kept in mind during the following analysis. In this equation, we will suppose an initial situation where solute concentration in the main flow zone is superior to the concentration in the storage zone, therefore the gradient considered implies an accumulation of solute in the storage zone. Solute restitution from the storage zone to the main flow zone happens when $C_s > C$. Looking at figure 10 A, strong asymmetry and important retardation appear on the curve when A comes down to half of its initial value, which means in case of reach 1 that A is set to 17.1 m^2. Reaching this value, A becomes even smaller than A_s (22 m^2). Eq. (3) involves that a diminution of A slows down the accumulation rate in the storage zone, delaying the moment where Cs > C and then prolonging the solute residence time in the storage zone. In these conditions, transient storage in immobile water is translated in tailing effect due to a breakthrough time that has become shorter than the residence time in storage zone, and, on the other hand, first arrival comes earlier. On the contrary, on the "A + 50%" curve, retardation tends to disappear probably in the benefit of dispersion (flattering and widening of the curve).

When looking at the sensibility test on D_L, it seems clear that changing the dispersion coefficient has no real impact on the tail of the curve but only on the widening of this one and on the peak concentration. More or less dispersion contributes to having a more or less concentrated cloud of tracer in the main flow zone but would not impact the transient storage.

The behavior of the BTC in relation to A_s and α has to be examined. It is clear through figure 10 that the presence of a storage zone is necessary to fit the simulated curve to the experimental one. Adding transient storage increases retardation as tailing is clearly growing with A_s. Retardation becomes evidently a major process of the transport on the "A_s + 50 %" curve. This evolution is in accord with equation (3) which states that evolution of concentration slows when A_s increases and therefore breakthrough time becomes shorter than the residence time in storage zone. One could propose that a bigger volume of immobile water dilutes solute concentration and delays the restitution of the solute to the main flow. However, when looking at the last graphic that concerned α sensibility, it can be seen that rising α with A_s stable has no impact on the tailing but has a small effect on the peak concentration of the BTC which is slightly higher. That could be explained in thinking that the storage zone becomes saturated in solute more quickly when α increases which favor the setting of a gradient releasing solute from the storage zone to the main flow. Solute trapping in the storage area is not long enough to cause real retardation. The fact that the global shape of the BTC is not really affected by a growing α is probably linked to a maximum storage capacity in the defined volume of immobile water; i.e. the mass released in the main flow zone will be limited to an upper value that could not change much the peak concentration in the main channel. In contrast, a significant decrease (-50%) of α modifies the restitution by growing the BTC asymmetry and the tailing effect. Indeed, storage zone will take more time to release the caught solute in the flow channel allowing retardation to affect the solute transport.

4.3.2. Application to an another case study

In order to compare the simulation results and to confirm the role of flooded areas, an additional tracer-test was performed on a small tributary network in Han-sur-Lesse where the tracer will flow mainly through a flooded area. The system traced, that we will call the D-F system (fig. 11), starts with an accessible underground river stretch whose section could be measured and evaluated at 0.018 m^2. Then, this streamlet flows into a huge flooded zone whose features are unknown. Tracer sampling was performed in a conduit (measured section of 0.117 m^2) 275 meters downstream the flooded area. A discharge difference was observed between the injection point (0.02 m^3/s) and the sampling point (0.034 m^3/s). The additional 0.014 m^3/s have been attributed to natural aquifer drainage by the karstic system (Bonniver, 2011).

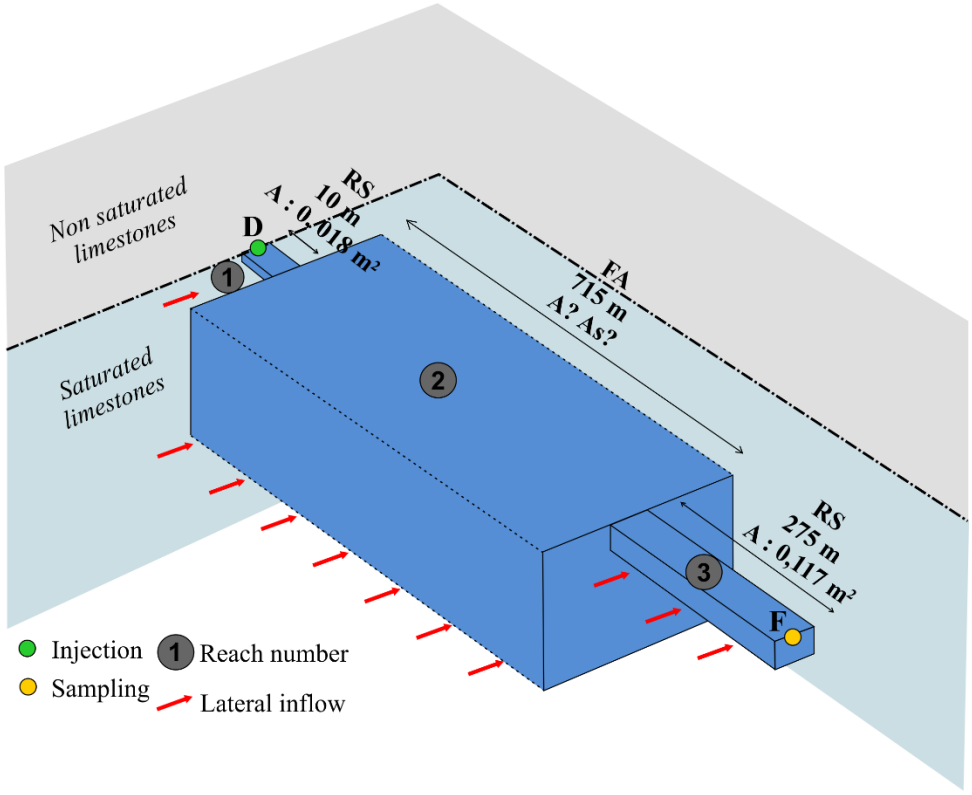

Figure 11. Conceptual model of the D-F system. Reaches 1 and 3 are river stretches (RS) whose section are known while reach 2 is a big flooded area (FA) of unknown geometry.

The experimental BTC (fig. 12), set at a restitution rate of 100 %, shows a strong asymmetry and tailing. This suggests an important retardation that could be due to the flooded area crossing. An OTIS simulation was therefore performed to dimension the traced system, especially the flooded area. However, for technical reasons, there is only one sampling point at the exit of the system. Therefore, there was no intermediate curve available for a first calibration and the modelling was performed directly on the system as a whole. This is possible with OTIS as long as the system is not too complex. Furthermore, in this case, dimensions of the two river stretches sections were measured on the field. Heterogeneity of the D-F system allows representing it in a conceptual model made of three reaches (fig. 11): a river stretch of 10 m length followed by a flooded area long of 715 m and finally a river stretch long of 275 m. A

steady flow of 0.02 m^3/s is set at the upstream boundary while a lateral inflow of 0.000014 $m^3/s*m$ is spread on the total system length (1000 m). Modelling results are shown in table 2 and figure 12.

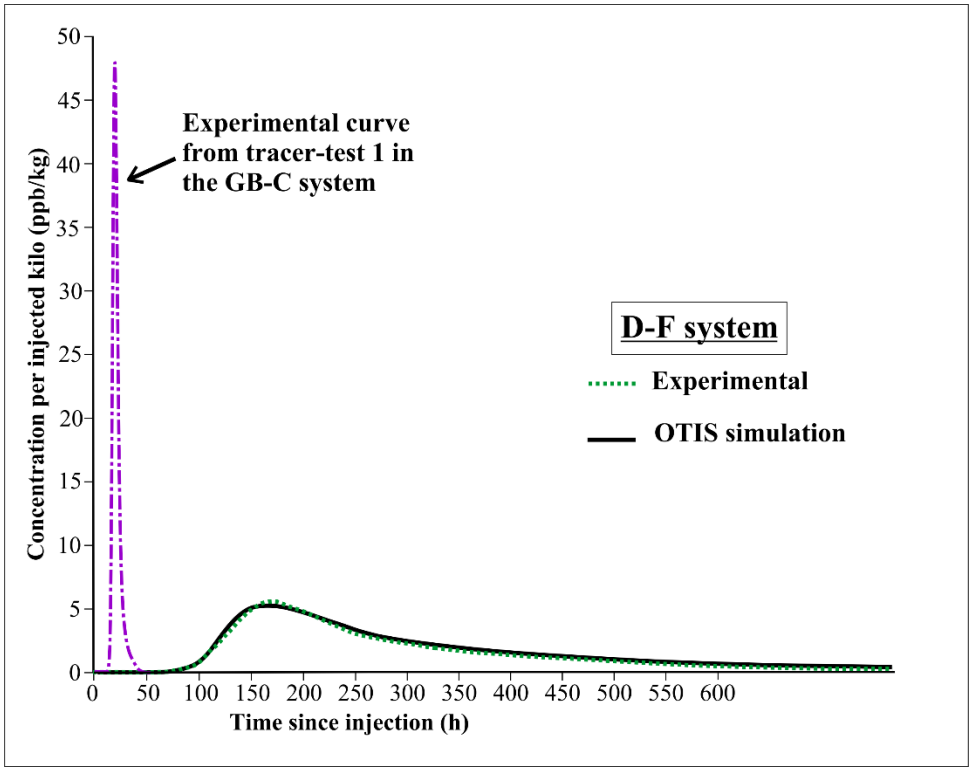

Figure 12. Experimental and simulated BTC from the tracer-test performed on the D-F network. In comparison, the exit BTC from tracer-test 1 is also present on the graph.

	Optimized parameters				Calculated from the parameters				Model stability	
Reach	**A (m^2)**	**A_s (m^2)**	**D_L (m^2/s)**	**α (s^{-1})**	**Vol (m^3)**	**Vol_s (m^3)**	**V_e (m/s)**	**a_L (m)**	**C_r**	**P_e**
1 River stretch	0.018	/	5.43	/	0.18	/	1.11	4.89	0.04	0.10
2 Flooded area	23.0	40.0	0.05	1.8E-06	16445	28600	0.0013	38.5	0.001	0.01
3 River stretch	0.117	/	4.36	/	32.2	/	0.29	15	0.01	0.03

Table 2. Parameters value estimation from the OTIS simulation on the D-F system.

As in the GB-C system, a storage zone needs to be simulated in OTIS to fit the modelled BTC to the experimental one. In the D-F system case, OTIS evaluates a main flow section of 23 m^2 for a storage zone section of 40 m^2. The flooded area has then a storage zone whose volume is 40 % bigger than the main flow zone volume. The coefficient that regulates exchanges between the main conduit and the storage area has a fitted value of $1.8x10^{-6}$ s^{-1}. The combination of a huge storage zone and a small exchange coefficient explain the important retardation observed on the BTC because it extends the residence time in the storage zone as shown by the sensibility tests above. In order to compare the two systems, the tracer-test 1 BTC from the GB-C system was added on figure 12. The flooded area modelled in the D-F system is much less transmissive than those existing in the GB-C system and show a significant tailing. Concerning the dispersion coefficient, this simulation confirms that the conduit river type is clearly a more dispersive environment than the flooded area. One should notice that the value scale of D_L in those river stretches is much higher than in the GB-C system. That is linked to a quicker effective velocity in the D-F system. This simulation is consistent with the field observations and leads to the same conclusions that could be made on the parameters estimation in the GB-C system. This case study shows also that in a same global system (the Han-Sur-Lesse system), flooded areas can act very differently on the solute transport and that the appearance of an important tailing effect is clearly linked to the system geometry.

Finally, in regard with the informations brought by this additional case study, and when summing up informations provided by the GB-C and the D-F simulations, a global scheme comparing flooded areas with underground river conduits can be proposed (fig. 13):

- River stretches are highly transmissive environments where advection and dispersion are the main processes. They are mainly dependent of the flow conditions,
- Flooded areas consist in low velocity transport zone where dispersion moderates for the benefit of solute exchange with immobile water. Immobile water areas are located along the walls and act as buffer zones that mitigates turbidity and so, dispersion. Transient storage will result in retardation if the residence time in the storage zone is long enough. This parameter is strongly dependent of the flooded area geometry.
- The residence time in the storage zone is not necessarily longer when the flow increases but the storage capacity will grow with the discharge, while the main flow zone volume is rather constrained and the exchange rate stays steady.

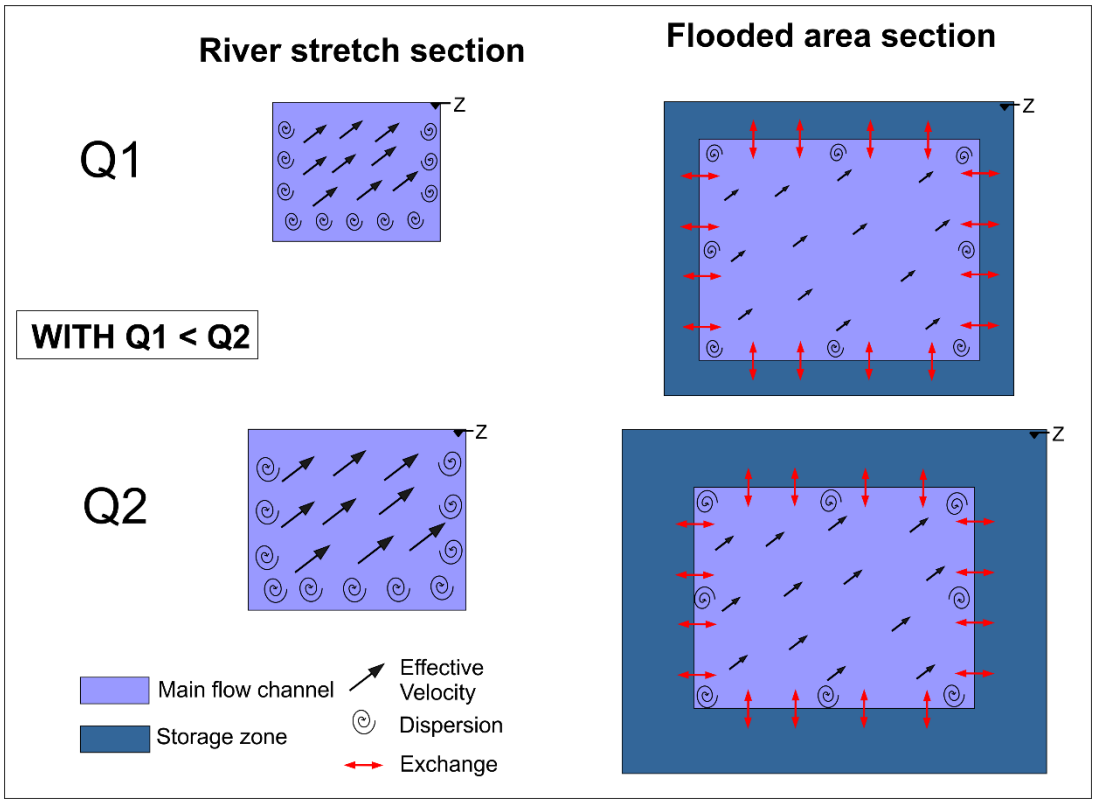

Figure 13. Comparison of the transport parameters evolution in river stretch and flooded area when discharge increases. The size of the symbols reveals the intensity of the different processes. The scheme is without scale.

6. Conclusion

The karstic system of Han-sur-Lesse is, as many other, very heterogeneous in its geometry. Indeed it combined transport in underground river stretches and in flooded areas. While the river stretches are usually accessible by speleologists, flooded areas are rather unknown given a limited physical access. This paper aim to define the geometry of those flooded zones and to characterize their effect on solute transport in comparison with the classical river stretches. In this purpose, multi-sampling sites tracer-tests were performed and the resulting BTCs were modelled via the OTIS program. The discrete system build with OTIS show a clear parametrization difference between the river stretches and the flooded zones. Indeed, flooded zones act as low transmissive environment where transport is dominated by the interaction with immobile water zones. The geometry of those zones, especially the ratio between the main flow section and the storage zone section is a major parameter that influences solute transport. Furthermore, the simulations and the sensibility tests demonstrate that the crossing of a flooded zone will give way to an important tailing only if the geometry and the exchange coefficient (α) allow the retardation to be longer than the restitution time. Actually, the direct effect of the storage on the tracer restitution is not systematic and seems clearly dependent on additional factors linked to the whole system functioning and geometry (presence of flooded areas and their geometry, flow conditions, system length,…). Finally, it can be said that conceptual models proposed by OTIS are, firstly, accurate and realistic and, secondly, strongly constrained

by the BTCs which reflect the reality. Sensibility tests show that the OTIS model is stable because the fitting of the simulated curve to the real ones depends on an evaluation of parameters that is made in a narrow window of values. Equations that governed OTIS maintain the stability of the model and their resolution is highly dependent of the features of the investigated network. OTIS simulation gives informations on the system geometry which help to understand hydrodynamic processes that control solute transport in a specific network.

Acknowledgements

The authors would like to thank the limited company “Les Grottes de Han” and its members for the free access to the site and their interest in our work. A special thanks to Professor Yves Quinif who shared his knowledge of the Han-sur-Lesse karst with us. The writers are grateful to the University of Namur for supporting this research.

References

Blockmans, S., Dumoulin, V., *in press*. Houyet-Han-sur-Lesse 59/1-2. Carte Géologique de Wallonie. Service public de Wallonie, DGO3 (Direction Générale Opérationnelle Agriculture, Ressources Naturelles et Environnement).

Bonniver, I., 2011. Etude hydrogéologique et dimensionnement par modélisation du « système-traçage » du réseau karstique de Han-sur-Lesse (Massif de Boine – Belgique). PhD Thesis, Département de Géologie, Facultés Universitaires Notre-Dame de la Paix (FUNDP), Université de Namur, Belgique, 349 p.

Brouyère, S., 2001. Etude et modélisation du transport et du piégeage des solutés en milieu souterrain variablement saturé : Evaluation des paramètres hydrodispersifs par la réalisation et l’interprétation d’essais de traçage in situ. PhD Thesis, Laboratoires de Géologie de l’Ingénieur, d’Hydrogéologie et de Prospection Géophysique, Faculté des Sciences Appliquées, Université de Liège (Ulg), Belgique, 572 p.

De Marsily, G., 1986. Quantitative hydrogeology. Groundwater Hydrology for engineers. Academic Press, New York, 440 p.

Donaldson, J.R., Tryon, P.V., 1990. User’s guide to STARPAC—The standards, time series, and regression package: National Institute of Standards and Technology Internal Report NBSIR 86-3448.

Field, M.S., Pinsky, P.F., 2000. A two-region non equilibrium model for solute transport in solution conduits in karstic aquifers. J. Contam. Hydrol. 44 (3/4), 329–351.

Geyer, T., Birk, S., Licha, T., Liedl, R., Sauter, M., 2007. Multitracer test approach to characterize reactive transport in karst aquifers. Ground Water 45 (1), 36–45.

Gray, W.G., Pinder, G.F., 1976. An analysis of the numerical solution of the transport equation. Water Resour. Res., 12 (3), 547-555.

Hauns, M., Jeannin, P.-Y., Atteia, O., 2001. Dispersion, retardation and scale effect in tracer breakthrough curves in karst conduits. J. Hydrol. 241 (3-4), 177-193.

Hauns, M., Jeannin, P.-Y., 1998. Tracer transport in underground rivers in karst: tailing effects and channel geometry. Bull. d'Hydrogéol. 16, 123-142.

Havron, C., Vandycke, S., Quinif, Y., 2007. Interactivité entre tectonique méso-cénozoïque et dynamique karstique au sein des calcaires dévoniens de la région de Han-sur-Lesse (Ardennes,Belgique). Geologica Belgica, 10 (1-2), 93-108.

Hubbard, E.F., Kilpatrick, F.A., Martens, L.A., Wilson, J.F. Jr., 1982. Measurements of time of travel and dispersion in streams by dye tracing. Techniques of Water-Resources Investigations, Book 3, Applications of Hydraulics, chapter A9, US Geological Survey, Washington, DC.

Jeannin, P.Y., Maréchal, J.C, 1997. Dispersion and tailing of tracer plumes in a karstic system (Milandre, JU, Switzerland). Proceedings of the 12th International Congress of Speleology, La Chaux-de-Fonds, Switzerland, vol.2, 149-152.

Kinzelbach, W., 1986. Groundwater modeling: An introduction with Sample Programs in BASIC. Elsevier, Amsterdam, 333 p.

Maloszewski, P., Zuber, A., 1989. Mathematical models for interpreting tracer experiments in fissured aquifers. The Application of Isotope Techniques in the Study of the Hydrogeology of Fractured and Fissured Rocks, IAEA, 287-301.

Maloszewski, P., Harum, T., Benischke, R., 1992. Mathematical modelling of tracer experiments in the karst of Lurbach system. Steirische Beiträge zur Hydrogeologie 43, 116–136.

Martin, J.L., McCutcheon, S.C., 1998. Hydrodynamics and Transport for Water Quality Modeling. Lewis, London, 794 pp.

Massei, N., Wang, H.Q., Field, M.S., Dupont, J.P., Bakalowicz, M., Rodet, J., 2006. Interpreting tracer breakthrough tailing in a conduit-dominated karst aquifer. Hydrogeol. J. 14 (6), 849–858.

Morales, T., Uriarte, J.A., Olazar, M., Antigüedad, I., Angulo, B., 2010. Solute transport modelling in karst conduits with slow zones during different hydrologic conditions. J. Hydrol. 390 (2010), 182-189.

Quinif, Y., 1988. Structure hydrogéologique du Massif de Boine. Lapiaz, Han special number, 11-14.

Rossier, Y., Kiraly, L., 1992. Effet de la dilution sur la détermination des dispersivités par interprétation des essais de traçage dans les aquifères karstiques. Bull. Centre Hydrogéol. Univ. Neuchâtel 11, 1–15.

Runkel, R.L., 1998. One-dimensional Transport with Inflow and Storage (OTIS): A solute transport model for streams and rivers. USGS, Water-Resources Investigations Report, 98-4018, 73 p.

Runkel, R.L., Broshears R.L., 1991. One-dimensional Transport with Inflow and Storage (OTIS): A solute transport model for small streams. Boulder, Colo., University of Colorado, CADSWES Technical Report 91-01, 85 p.

Schnegg, P.A., Doerfliger, N., 1997. An inexpensive flow-through field fluorometer. Proceedings of the 6th Confernece on Limestone Hydrology and Fissured Media, La Chaux-de-Fonds, August 1997. Centre of Hydrogeology, University of Neuchatel, Vol. 2, 47-50.

Wang, H., 1987. Modélisation des transferts de masse en milieu saturé à double porosité ; application aux écoulements convergents en craie fissurée et multicouche. PhD Thesis, University of Paris XI, Paris.

Werner, A., Hoetzl, H., Käss, W., Maloszewski, P., 1997. Interpretation of tracer experiments in the Danube-Aach-System (Western Swabian Alb, Germany) with analytical models. In: Günay, Johnson (Eds.). Karst Waters Environmental Impacts. Balkema, Rotterdam, 153-160.

Zhang, H., Schwartz, F.W., Wood, W.W., Garabedian, S.P., LeBlanc, D.R., 1998. Simulation of variable-density flow and transport of reactive and nonreactive solutes during a tracer test at Cape Cod, Massachusetts, Water Resour. Res., 34 (1), 67-82.

Appendix IV

Submitted Article

“OM-MADE: an open-source program to simulate one-dimensional solute transport in multiple exchanging conduits and storage zones.”

OM-MADE: an open-source program to simulate one-dimensional solute transport in multiple exchanging conduits and storage zones.

Anne-Julie Tinet[a], Pauline Collon[a,*], Camille Philippe[a], Lorraine Dewaide[b], Vincent Hallet[b]

[a] *Université de Lorraine, CNRS, GeoRessources, F-54000 Nancy, France*
[b] *University of Namur, Geology Department, Rue de Bruxelles,61, 5000 Namur, Belgium*

Abstract

OM-MADE (One-dimensional Model for Multiple Advection, Dispersion, and storage in Exchanging zones) is an open-source python code for simulating one-dimensional solute transport in multiple exchanging conduits and storage zones. It aims at helping the interpretation of multi-peaked skewed breakthrough curves (BTCs) that can be observed in tracer tests conducted in karstic systems. OM-MADE is based on the resolution of classical mass conservation equations. In OM-MADE, all parallel and exchanging flow zones are divided along the direction of flow into reaches, in which all model parameters are kept constant. The total flowrate is preserved all along the flow, but lateral solute inflows or outflows can be simulated. The solute may also been affected by adsorption / decay processes either in mobile or immobile zones. Each reach is subdivided into discrete segments of equal length. The partial differential equations are solved with a fractional approach: a temporal explicit resolution scheme and a spatial Lax-Wendroff scheme are used to solve advection, while dispersion is solved with an implicit approach. A validation is proposed against analytical solutions, OTIS software (Runkel, 1998), and the Dual-Advection-Dispersion Equation (DADE) proposed by Field and Leij (2012). An application to a tracer test carried out in the karstic area of Furfooz (Belgium) is then performed to reproduce the double-peaked positively skewed BTC that has been observed. It constitutes a demonstration of the software capacities in the case of two reaches and three exchanging zones, among which two are mobile ones and one represents a storage zone. It thus permits to verify numerically the consistency of the conceptual interpretation of the observed BTC.

Keywords: Multi-peaked breakthrough curves; Solution conduits; Karsts; Storage zone; Degradation; Adsorption; Lateral flow

Highlights:

- An open-source python code to simulate one-dimensional solute transport in conduits.

*Corresponding author: Tel.: +333 83 72 74 45 23
Email addresses: anne-julie.tinet@univ-lorraine.fr (Anne-Julie Tinet), pauline.collon@univ-lorraine.fr (Pauline Collon), camille.philippe14@outlook.fr (Camille Philippe), lorraine.dewaide@unamur.be (Lorraine Dewaide), vincent.hallet@unamur.be (Vincent Hallet)

- Simulate multiple exchanging flow and storage zones.
- Help the interpretation of multi-peaked breakthrough curves observed in karstic system tracer tests.

Author Contributions

AJT wrote the numerical code, with a small contribution of PC for the structure and interface. PC initiated the collaboration, made the application to Furfooz (with contribution of AJT) and wrote the paper (with contributions of AJT, LD and VH). A first code version was developed and tested during CP master's project, advised by AJT and PC. LD and VH initiated the Furfooz study and provided the field data.

1. Introduction

The specific geometries of karstic systems have a huge impact on the underground fluid circulations. In such media, hydraulic connections are difficult to predict with the classical laws describing porous media transport: a more or less porous matrix co-exists with fractures and large open drains of various topologies and sizes. Tracer tests are a common and powerful tool to assess groundwater trajectories and get a first-order understanding of a hydrogeological system (e.g., Goldscheider et al., 2003; Perrin and Luetscher, 2008; Goldscheider et al., 2008; Field and Leij, 2012; Mudarra et al., 2014; Dewaide et al., 2016). Used in karstic settings, they provide direct information on two major points: (i) the existence of a hydraulic connection between two points - generally a sink or swallow hole and a spring - (e.g., Knöll and Scheytt, 2017), and (ii) the time needed for the fluid to travel between these two points (e.g., Morales et al., 2007).

A careful analysis of breakthrough curves (BTCs) provides additional information on the major, and potentially secondary, flows between inlets and outlets (e.g., Smart, 1988; Perrin and Luetscher, 2008). In particular, asymmetric BTCs with long tail are commonly observed. Several processes could be proposed to explain such retardation of tracer arrival: adsorption-desorption (De Marsily, 1986), large molecular diffusion (Seiler et al., 1989), dilution effect (Rossier and Kiraly, 1992), hydrodynamic conditions (Massei et al., 2006), multiple conduit configurations, or interactions with pools or immobile water zones. This last assumption has been numerically demonstrated (Hauns et al., 2001), and is largely promoted in several case studies (e.g., Hubbard et al., 1982; Bencala, 1983; Martin and McCutcheon, 1998; Goldscheider et al., 2003; Bonniver, 2011; Dewaide et al., 2016). Multi-peaked BTC is a second specific feature that has been reported in some tracer tests carried out in karstic systems (Goldscheider et al., 2008; Dewaide et al., 2017). It has been often interpreted as an effect of the presence of auxiliary conduits that divert the solute and then transport it back to the main one (Smart, 1988; Goldscheider et al., 2008; Perrin and Luetscher, 2008). This configuration is indeed largely observed in anastomotic sytems (Smart and Ford, 1982). More recently, Brouyère et al. (2005) demonstrated that multi-peaked BTCs could also been obtained by a specific injection

mode, when an impulse injection of the tracer in a well is directly followed by a supplementary injection of water to chase the tracer. A third explanation has also been proposed: double-peaked BTCs could also be due to the presence of a large pool in the flow path, allowing part of the solute to be temporary trapped in eddies (Hauns et al., 1998). This process has been numerically and experimentally reproduced by Field and Leij (2012). Recently, Dewaide et al. (2017) have provided field measurements in the Furfooz karst system (Belgium) that show a double-peaked BTC. This specific system is characterized by the presence of a large underground lake, partly segmented into two zones by a vertical wall. The authors have thus proposed a conceptual model of solute transport that would imply a dual-advective transport within the lakes combined with a strong dispersive effect of this storage zone.

If further field investigations should help to check these hypotheses, numerical tools could also be used for that purpose. The OTIS program (One-dimensional Transport with Inflow and Storage) has already been used by Dewaide et al. (2016) to model tracer tests carried out in the Han-sur-Lesse karstic system and help their interpretation in term of corresponding conduit geometries. But the conceptual model here implies two advective flow zones, while OTIS only allows to model one. To model multi-peaked BTCs, Field and Leij (2012) have proposed a dual-advection dispersion equation (DADE) that revealed to efficiently reproduce such BTCs. But this model does not allow to discretize the conduits along the flow, nor to combine two exchanging advective zones with a storage area.

This paper presents OM-MADE, an open-source python code for simulating one-dimensional solute transport in multiple exchanging flow and/or storage zones. After presenting the principles and funding equations of OM-MADE (Section 2), we briefly describe the software design (Section 3). In Section 4, we validate OM-MADE against analytical solutions, OTIS, and DADE models. Finally, we show an example of application of OM-MADE to model one tracer test realized in the Furfooz area (Section 5).

2. OM-MADE: One-dimensional Model for Multiple Advection, Dispersion, and storage in Exchanging zones

2.1. General equations

OM-MADE is an open-source software that simulates one-dimensional solute transport. Its specificity is to allow multiple advective-dispersive parallel flow zones, or channels, that can exchange with each others, as well as storage, or immobile, zones (Fig. 1). All zones are identically described, the difference between mobile and immobile regions is done through the input flowrate Q, which is nil for immobile - storage - zones. All parallel channels are divided along the direction of flow into *reaches*, in which all model parameters are kept constant. Flowrate is preserved all along the flow (steady flow regime), but lateral solute inflows (or outflows) can be simulated similarly to what is done in OTIS software (Runkel, 1998). The solute may also been affected by adsorption / decay processes either in mobile or immobile zones.

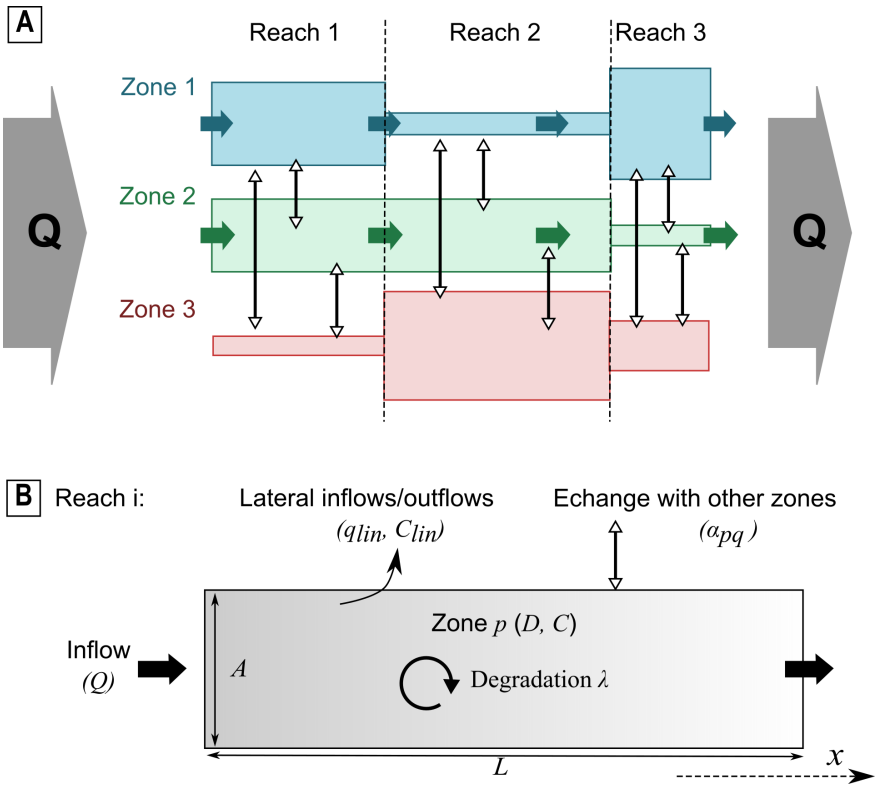

Fig. 1. Schematic representation of an OM-MADE model: (a) In this example, two mobile zones (zone 1 and 2) are interconnected with one storage zone (zone 3). The total flowrate Q is preserved all along the flow (steady flow regime). Three reaches are defined to allow longitudinal variations of the system geometrical characteristics. (b) Detailed representation of one reach of a zone p: a reach is defined by a given length L, a cross-sectional area A, a dispersion coefficient D, a solute concentration C, linear lateral inflows or outflows (flowrate and concentration q_{lin}, C_{lin}), internal decay or sorption (coefficient λ) and exchange(s) with other(s) zone(s) (coefficient(s) α_{qp}).

Considering mass conservation, the general equation of a solute transport in a one-dimensional uniform flow in a zone p that can exchange with other zones q can be written:

$$A\frac{\partial C}{\partial t} = -Q\frac{\partial C}{\partial x} + \frac{\partial}{\partial x}\left(AD\frac{\partial C}{\partial x}\right) + q_{lin}\left(C_{lin} - C\right) + \sum_{q \neq p} \alpha_{qp}\left(C_q - C\right) - \lambda AC \tag{1}$$

where t (T) designates the time and x (L) the distance, A (L^2) is the stream channel cross-sectional area of the zone p, C (CU) is the solute concentration in zone p, Q (L^3/T) is the volumetric flowrate across p, D (L^2/T) is the dispersion coefficient, q_{lin} (L^2/T) is the lateral inflow rate per unit of distance, C_{lin} (CU) is the solute concentration in lateral inflow, α_{qp} (L^2/T) is the exchange coefficient between the zones p and q multiplied by the exchange surface area, λ (T^{-1}) is the first order decay (or adsorption) coefficient in p.

In an immobile - storage - zone, the inflow rate Q is nil. Physically, dispersion is also nil but molecular diffusion can be considered by setting an adapted value of D, for example in the case of fluoresceine tracing tests: $D \approx 0.64 \times 10^{-9} m^2/s$ (Galambos and Forster, 1998).

This global formulation can also be adapted to describe sedimentation zones ($Q = q_{lin} = 0$) with the following relations:

$$C = \frac{C_{sed}}{K_d} \tag{2}$$

$$\alpha_{qp} = \frac{M_{sed}}{L}\widehat{\lambda}K_d \tag{3}$$

where K_d (volume/mass unit) is the coefficient of partition, $\widehat{\lambda}$ the adsorption coefficient on sediments, M_{sed} the mass of available sediments, C_{sed} the adsorbed concentration on sediments and L the total length of the zone.

2.2. Numerical resolution schemes

The partial differential equation 1 that had to be solved for each zone p, requires temporal and spatial discretization schemes. Each reach is thus subdivided into discrete segments of length dx, referred to with the index i.

We do not use the same numerical resolution schemes than OTIS, we chose to use a fractional approach. The fractional approach consists in separating the advective and dispersive parts of the equation, to solve them separately in two successive time-steps. With t the temporal index, we get:

$$A\frac{\partial C}{\partial t} \approx A\frac{C^{[t+1]} - C^{[t]}}{dt} = A\frac{C^{[t+1]} - C^{[t']}}{dt} + A\frac{C^{[t']} - C^{[t]}}{dt} \tag{4}$$

For the advective part, a temporal explicit resolution scheme is chosen (Eq. 5). Indeed, explicit resolution avoids to perform a matrix inversion, which can be computationally expensive for non-symmetric matrices.

$$A\frac{C^{[t']} - C^{[t]}}{dt} = -Q\frac{\partial C^{[t]}}{\partial x} \tag{5}$$

The spatial resolution is done with a Lax-Wendroff scheme (centred scheme, Eq. 6), which has a precision of order 2.

$$\frac{C^{[t',i]} - C^{[t,i]}}{dt} = -\frac{Q}{A_i}\left(\frac{C^{[t,i+1]} - C^{[t,i-1]}}{dx}\right) + \frac{dt}{2}\frac{Q}{A_i}^2\left(\frac{C^{[t,i+1]} - 2C^{[t,i]} + C^{[t,i-1]}}{dx^2}\right) \tag{6}$$

This choice has a consequence: it requires Courant-Friedrichs-Lewy (CFL) condition to be stable:

$$|\frac{Udt}{dx}| \leq 1 \tag{7}$$

with U the fluid velocity. It defines so a CFL time step, noted dt_{CFL}, as follows:

$$dt_{CFL} = \frac{dx}{U} = dx\frac{Q}{A} \tag{8}$$

For the dispersive part, the equation is solved with an implicit approach (Eq. 9). This allows higher level of freedom for choosing the time-step, as this resolution scheme is unconditionally stable. Implying a matrix inversion, this resolution scheme has a higher computational cost than an explicit one.

$$A\frac{C^{[t+1]} - C^{[t']}}{dt} = \frac{\partial}{\partial x}\left(AD\frac{\partial C^{[t+1]}}{\partial x}\right) + q_{lin}\left(C_{lin} - C^{[t+1]}\right) + \sum_{q\neq p}\alpha_{qp}\left(C_q^{[t+1]} - C^{[t+1]}\right) - \lambda AC^{[t+1]} \tag{9}$$

Solving the spatial terms leads to the following equation:

$$\begin{aligned}\frac{C^{[t+1,i]} - C^{[t',i]}}{dt} = &\frac{(AD)_{i+\frac{1}{2}}\left(C^{[t+1,i+1]} - C^{[t+1,i]}\right) - (AD)_{i-\frac{1}{2}}\left(C^{[t+1,i]} - C^{[t+1,i-1]}\right)}{(A)_i dx^2} \\ &+ \left(\frac{q_{lin}}{A}\right)_i\left((C_{lin})_i - C^{[t+1,i]}\right) + \sum_{q\neq p}\left(\frac{\alpha_{qp}}{A}\right)_i\left(C_q^{[t+1,i]} - C^{[t+1,i]}\right) - (\lambda)_i AC^{[t+1,i]}\end{aligned} \tag{10}$$

Note that these equations are solved for each time-step and each segment of each zone. An average concentration C_{av} can be computed, if wanted, for each location x and each time-step t as a weighted sum of each zone :

$$C_{av}(x,t) = \frac{\sum_p C_p Q_p}{\sum_p Q_p} \tag{11}$$

But it is only meaningful in locations where all zones are considered to be mixed.

Solving the partial differential equations 1 describing the concentration evolution in each zone requires to specify initial and boundary conditions. At the inlet, a time-dependent imposed concentration conditions each zone. Therefore, both continuous or step-wise tracer injection can be simulated. A Dirac injection can be approximated by imposing concentration at one time step only. Boundary condition at the outlet corresponds to a zero diffusive flux condition. At initial step, a constant concentration is imposed in all reaches for each zone.

3. Description of the software architecture

OM-MADE is written in Python v3. Python is a high-level interpreted language that allows rapid developments and is easy to pick up by non-programmers. It lacks runtime performance, but one-dimensional solute transport simulation has no strong computing requirements. Python is open-source, multi-platform and allows functional and object-oriented programming. Several powerful libraries have been developed that allow to directly use optimised and verified algorithms for matrix manipulations, scientific computation or result visualisation. In OM-MADE, we use *numpy* (http://numpy.scipy.org) to invert matrices, and *matplotlib* (Hunter, 2007) is used in some examples of main programs to directly visualize the results of a simulation.

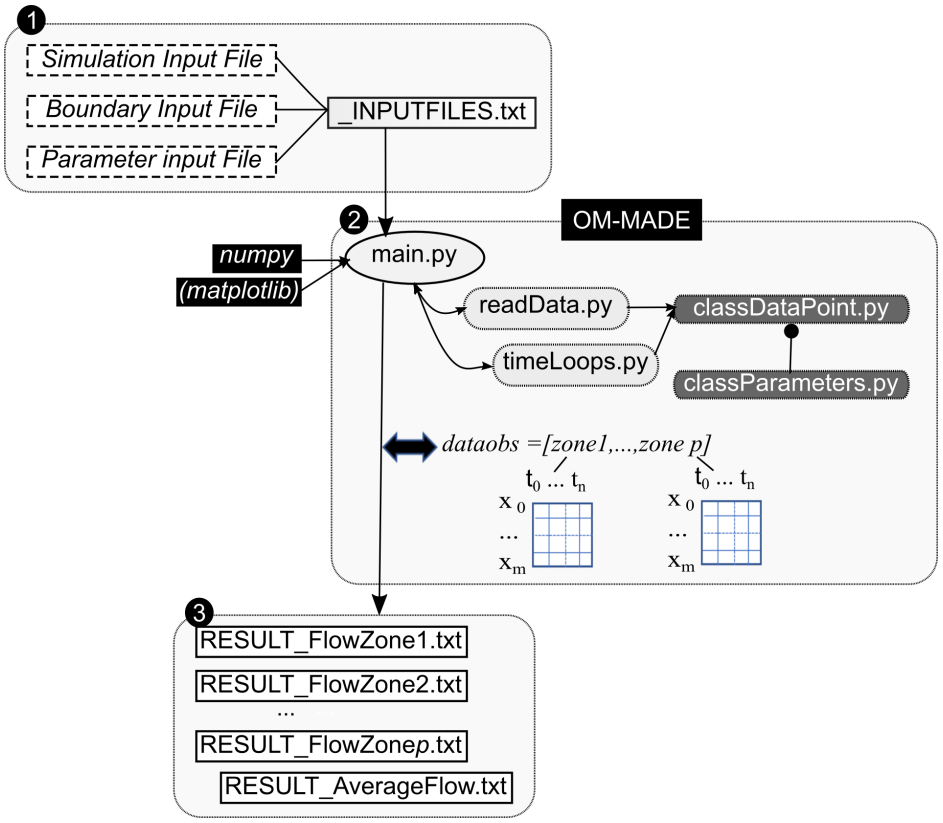

Fig. 2. OM-MADE architecture: Three text input files are required by the _INPUTFILES.txt file (1). They contain all information to run a specific simulation. OM-MADE (2) should be launched by running the main program (several examples are provided), which calls four python modules. The result of a simulation is stored in the *dataobs* variable, which is a list of arrays containing, for each zone, the concentration for each printed time and distance. This variable can be used to generate several text files containing the result of the simulation (3)).

The program is divided into four modules - all reusable in any other Python program - that are called by an independent file containing the main program (Fig. 2). In the package, different specific examples of main programs are given, which exploit directly the possibilities of a direct result visualization thanks to

matplotlib, as well as a generic main program. The generic main program reads an *_INPUTFILES.txt* text file, which should contain the path and names of the different input parameter files. Three input parameter files are required: (i) one describing the simulation parameters (spatial step, time step, initial concentration, printing locations, and printing times), (ii) one for boundary conditions (input concentration through time for each zone), and (iii) one describing zone and reach characteristics (length, area, dispersion coefficient, degradation rate, lateral flow, lateral concentration, and exchange coefficients). As output of the simulation, it produces one file per flow zone containing the concentration through time at the printing locations, and the corresponding time steps in the first column. An additional output file *RESULT_AverageFlow.txt* contains also the corresponding average concentration for all mobile zones (Eq. 11) at each printing locations.

Two class are defined in two modules : (i) the class *Parameters* defines all physical parameters for one zone and reach of the domain; (ii) the class *DataPoint* contains the physical data required for computation on one point (flow type and location) of the domain. It defines, punctually, the calculation of advection, dispersion, mass exchange between two flow types co-located points and mass exchange through either degradation or lateral flow.

These classes are used by the functions implemented in the *readData* and *timeLoops* modules. The first module gathers functions that permit the reading and storage of the simulation parameters from the input text files. The second one initialises the concentration and does the overall loop (advection, and then dispersion) for each time step, until reaching the total simulation time. It returns a matrix containing the concentration for each printing location at each printing time step. As the advection is solved with an explicit schema, it is constrained by the Courant-Friedrich-Lewy (CFL) stability condition. Thus, if the input time step, dt, is greater than the required CFL time step, dt_{CFL}, the advection is solved iteratively with time steps equal to dt_{CFL} until the time $t + dt$ is reached (function *advectionLoop*). If $dt \leq dt_{CFL}$, the used time step is dt.

The OM-MADE package is freely available on GitHub as a Python library (`https://github.com/OM-MADE/OM-MADE`). It is provided with examples of applications on the following validation case studies (Section 4), as well as an application on the Furfooz karstic area (Section 5).

4. Validation

The model is tested on classical configurations with analytical solutions for validation.

4.1. Pure advection

A pure advective flow is simulated in a single conduit of 1500 m length, 1 m^2 cross-sectional area, with a flowrate of 0.01 m^3/s. Initial concentration is nil, and a concentration of 350 g/m^3 is injected during 3 h. The total simulation time is 40 h. Space step is 1 m and time step is 300 s. Fig. 3 plots the concentration

profiles observed along the conduit each 5 h. The model reproduces the analytical solution, despite the oscillations, which are characteristic of a Lax-Wendroff scheme (Lax and Wendroff, 1960).

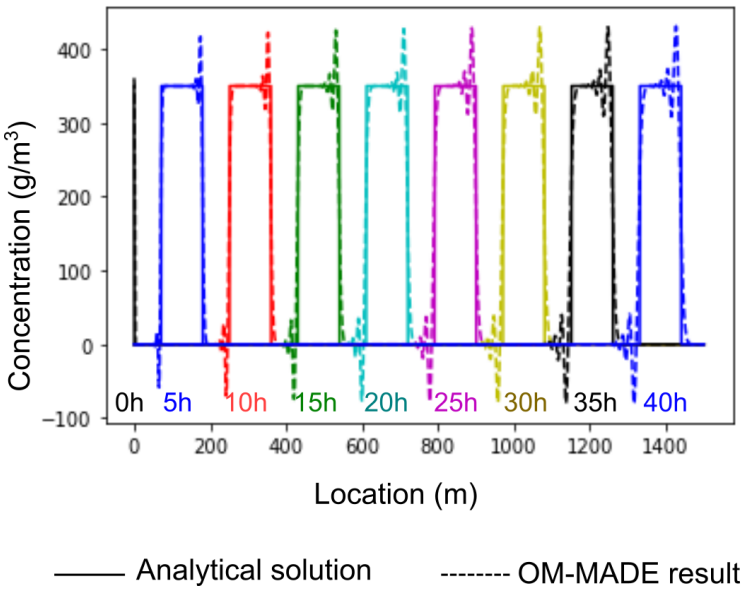

Fig. 3. Comparison of OM-MADE result with an analytical solution in the case of a pure advective flow. Oscillations are characteristic of a Lax-Wendroff resolution scheme.

4.2. Pure dispersion

A similar configuration is used to test the model for pure dispersion: no flowrate (it is an immobile flow zone) in a single conduit of 1500 m length, 1 m^2 cross-sectional area. The dispersion coefficient is set to 0.05 m^2/s. Initial concentration is nil, and a constant concentration of 350 g/m^3 is injected continuously. The total simulation time is 40 h, space step is 1 m and time step is 9000 s. Fig. 4 plots the concentration profiles observed along the conduit each 150 h. It is compared to the analytical solution in case of a semi-infinite wall:

$$C(t) = C_0 erf\left(\frac{x}{2\sqrt{Dt}}\right) \tag{12}$$

with C_0 the injected concentration and D the dispersion. Considering that the outlet boundary conditions of the numerical model and of the analytical solution are different, a comparison between the two is only valid when the outlet boundary impact on the solution is negligible, i.e. at short-times. This explains the small differences observed at $x = 1500m$, when the tracer arrives at the output location at $t = 1200h$.

4.3. Advection - Dispersion

A solute transport by advection-dispersion is simulated in the same conduit of 1500 m length and 1 m^2 cross-sectional area, with a flowrate $Q = 0.01\ m^3/s$ and a dispersion coefficient $D = 0.05\ m^2/s$. Initial

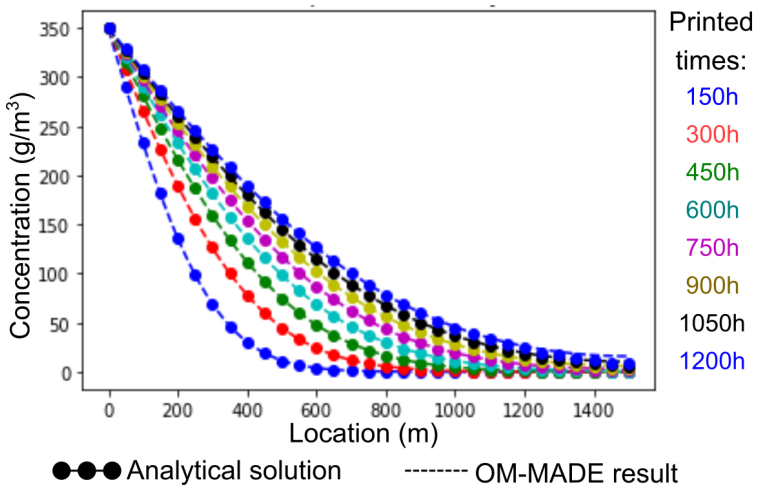

Fig. 4. Comparison of OM-MADE result with an analytical solution in the case of a pure dispersive flow. At $t = 1200h$, the tracer arrives at the output location, thus the semi-infinite wall condition is no more valuable and explain the small differences that can be observed with the analytical solution.

concentration is nil, and we consider an instantaneous solute pike corresponding to the injection of $M = 900\ g$ of tracer. The total simulation time is 40 h, space step is 1 m and time step is 300 s. For the simulation, instantaneous injection is not possible to model: the tracer is injected during one time step $dt = 300\ s$. Thus, it corresponds to a concentration $C_0 = M/(Q * dt) = 300\ g/m^3$. Fig. 5 plots the concentration profiles observed along the conduit each 5 h, compared to its corresponding analytical solution in a semi-infinite media:

$$C(t) = \frac{M}{A\sqrt{4\pi Dt}} exp\left(-\frac{(x-Ut)^2}{4Dt}\right) \tag{13}$$

with U the velocity of the fluids, and A the cross-sectional area.

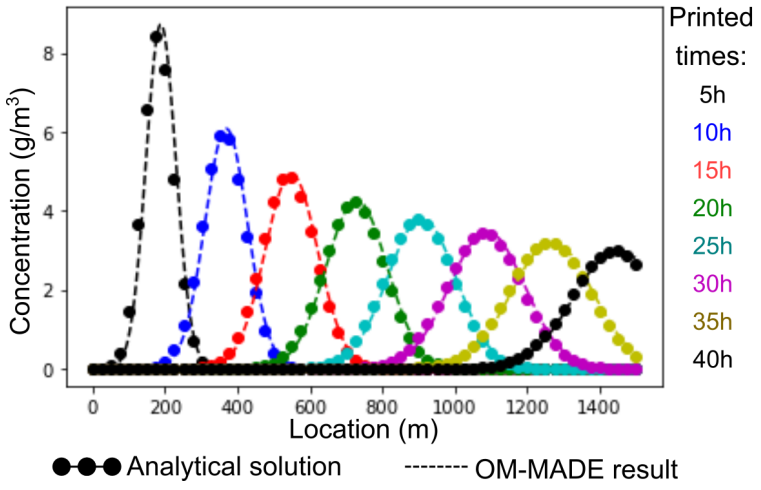

Fig. 5. Comparison of OM-MADE result with an analytical solution in the case of advective-dispersive flow.

4.4. Dual advection and dispersion: verification against WSADE and DADE solutions

To validate the model for multiple mobile flow zones we used two examples published in Field and Leij (2012).

The first one considers two mobile flow zones with no exchange. The channels are 200 cm long, and the concentrations are observed at 10 cm, 25 cm and 40 cm. Flowrates in conduits[1] are $Q_1 = 10\ cm^3/d$ and $Q_2 = 5\ cm^3/d$, both cross-sectional area equal to 1 cm^2, and the respective dispersion coefficients are $D_1 = 2.5\ cm^2/d$ and $D_2 = 1.25\ cm^2/d$. The total simulation time is 10 s, space step is 0.2 cm and time step is 0.01 s. An instantaneous solute pike of 12 mg is injected in each channel. In the simulation, we inject during one time step $dt = 0.01\ s$. The corresponding input concentration $C_{0,k}$ for each zone k, is deduced by the following relation: $C_{0,k} = M_k/(Q_k * dt)$ with M_k the mass injected in each zone and Q_k the flowrate in each zone. For each zone, it corresponds to $C_{0,1} = 120\ mg/cm^3$ and $C_{0,2} = 240\ mg/cm^3$.

As shown in Fig. 6a, OM-MADE gives similar results than the Weighted-Sum Advection Dispersion Equation (WSADE) solution given by Field and Leij (2012) from the subsolution by Leij and Toride (1995).

The second example is the same than the first one, except that an exchange is effective between both mobile zones. The exchange coefficient applied in Field and Leij (2012) is equal to 0.05 d^{-1}, which corresponds in OM-MADE to $\alpha_{1-2} = 0.1\ cm^2/d$. Fig. 6b shows that OM-MADE gives similar results than the DADE approach for two exchanging mobile zones.

4.5. Multi-reaches single flow with storage zone or degradation rate: verification against OTIS

To test the capacity of our software to model single mobile zones discretized into several reaches and exchanging with storage zones, we compare it to the results obtained with OTIS to simulate a conservative transport in a stream with immobile zones (Application 1 in Runkel (1998)). This simulation has been itself validated against field measurements of a chloride tracer test in Uvas Creek, a small pool-and-riffle stream in northern California (US) (Bencala and Walters, 1983). The main stream is represented by a mobile zone with a constant flowrate of $Q = 0.0125\ m^3/s$. Pools are modelled by exchanging mobile zones. The stream is characterized by an initial concentration equals to 3.7 mg/l. The experiment consisted in the injection during 3 h of chloride at a constant rate of 11.4 mg/l starting from 8.25 h for the reference experiment. In our simulation, this initial period is skipped, and the injection is started at 540 s, and thus ends at 11340 s. The total simulation time is 24 h, which corresponds in our simulation to 56700 s. The time step is 180 s (= 0.05 h), the space step is 1 m, and the concentrations are printed at 5 locations: 38, 105, 281, 433, and 619 m from the injection point, corresponding to the five sampling points and the exact limit of the reaches.

[1] It seems to be some inconsistencies in the reference paper where q_1 and q_2 are referred to as "volumetric flow rate in conduit i per total cross-sectional area" (in cm/d) but also considered as additive values. We have corrected the published values to ensure unit and physical consistencies. In particular, a correction seems to be necessary to reason globally as everything is presented relatively to the contribution of each areas, and thus divided by 2.

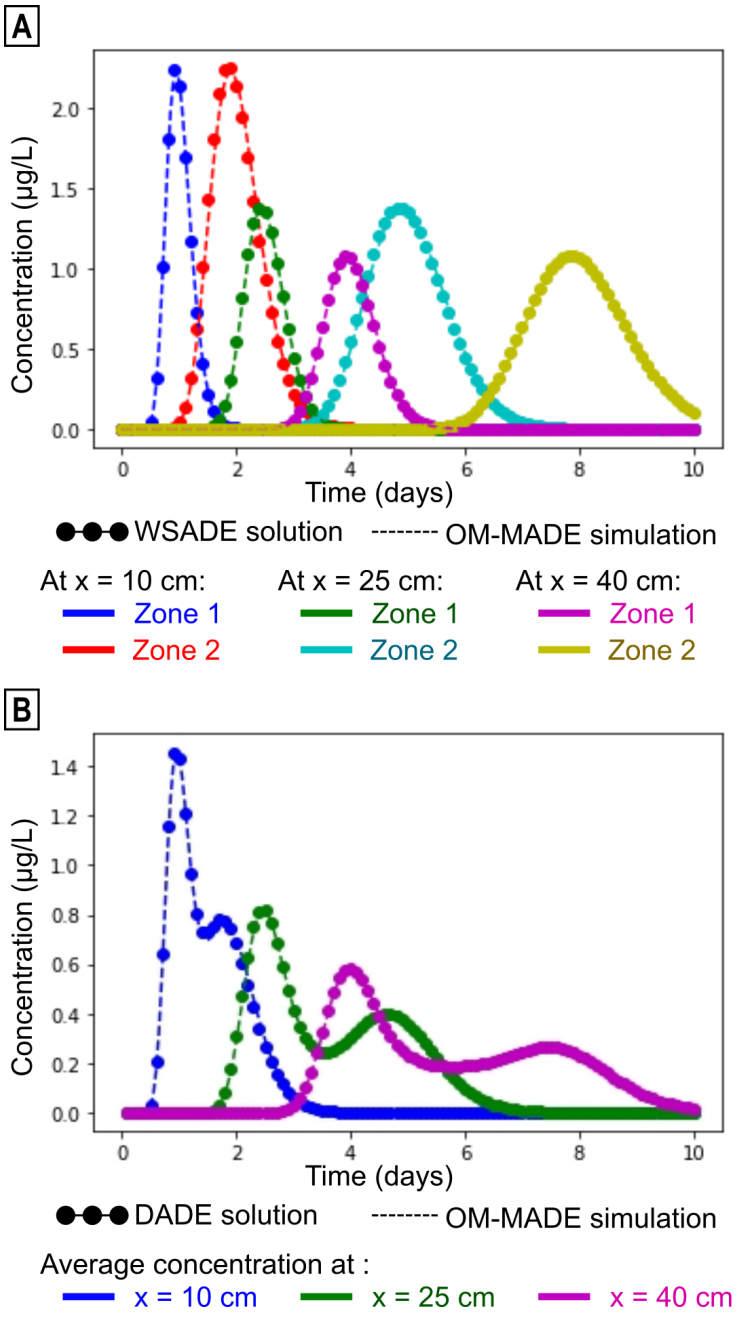

Fig. 6. Simulation of two mobile zones and comparison with solutions of Field and Leij (2012) at three positions: (A) in the case where no exchange between the two zones (WSADE solution); (B) in the case where exchanges are taken into account between both zones (DADE solution)

Table 1

Parameters of the OM-MADE simulation for multi-reache single flow with storage. These are based on the ones realized with OTIS by Runkel (1998) for the tracer tests by Bencala and Walters (1983) in Uvas Creek.

	Exchange	**Mobile zone (Main Stream)**				**Storage Zone (Pools)**			
	$\alpha_{1,2}$ (m^2/s)	A (m^2)	D (m^2/s)	Q_{LIN} $(m^3/s/m)$	C_{LIN} (mg/l)	A (m^2)	D (m^2/s)	Q_{LIN} $(m^3/s/m)$	C_{LIN} (mg/l)
Reach 1	0	0.30	0.12	0	3.7	0.05	0	0	0
Reach 2	0	0.42	0.15	0	3.7	0.05	0	0	0
Reach 3	1.08e-5	0.36	0.24	4.545e-6	3.7	0.36	0	0	0
Reach 4	4.10e-6	0.41	0.31	1.974e-6	3.7	0.41	0	0	0
Reach 5	2.34e-5	0.52	0.40	2.151e-6	3.7	1.56	0	0	0

The domain is divided into 5 reaches whose characteristics are given in Table 1. The reaches 3, 4, and 5 are characterized by the presence of pools. To reproduce the increasing flow in the downstream direction, positive lateral inflows are introduced in reaches 3, 4, and 5. All parameters are the same in OM-MADE and OTIS, except for the exchange coefficients which are not defined the same way (Table 1). For homogeneity purposes (Eq. 10), we defined indeed the exchange coefficient between two zones as a value expressed in $[m^2/d]$. In OTIS, the exchange coefficient is expressed in d^{-1} and defined as: $\alpha_{OTIS} = \alpha_{OM-MADE}/A$, where A is the cross-sectional area of the mobile zone. Results show a very good fitting with observation at the five observation locations in the flow zone (Fig. 7(A)). In the storage zone differences are observed (Fig. 7(B)). It is explained by the location of observation points which corresponds, each time, to the junction between successive reaches. In OTIS, the code affects, indeed, the properties of the previous point to the following location, while OM-MADE computes an average between previous and following points. This is particularly visible for the location at the location $x = 433m$: the values calculated with OTIS do not fit the one calculated with OM-MADE at $x = 433m$ but at $x = 432m$. This, observation underlines that the simulation domain should be preferentially discretized so that observation points would not be located at the exact junction between two reaches. In this example, this was not possible without distorting the comparison with the OTIS reference simulation.

A second comparison with OTIS was performed to validate the simulation of transport with first-order degradation rate (Application 3 in Runkel (1998)). It illustrates a hypothetical problem of a single reach - single flow zone transport of a decaying substance, which has been analytically solved in Runkel (1996). The simulation is thus characterized by one mobile zone of 2200 m long and 1 m^2 cross-sectional area, with an initial null concentration and a constant flowrate $Q = 0.1\ m^3/s$. Its dispersion coefficient is $D = 5\ m^2/s$. The unique reach is discretized in 10 m cells, and the concentrations are observed at 100 m and 2000 m. The simulation lasts 12 h (= 43200 s) with a time step $dt = 144\ s$. The decaying substance is injected during 2 hours starting at $t = 3600\ s$ with a constant input concentration $C_0 = 100\ g/m^3$. The degradation rate

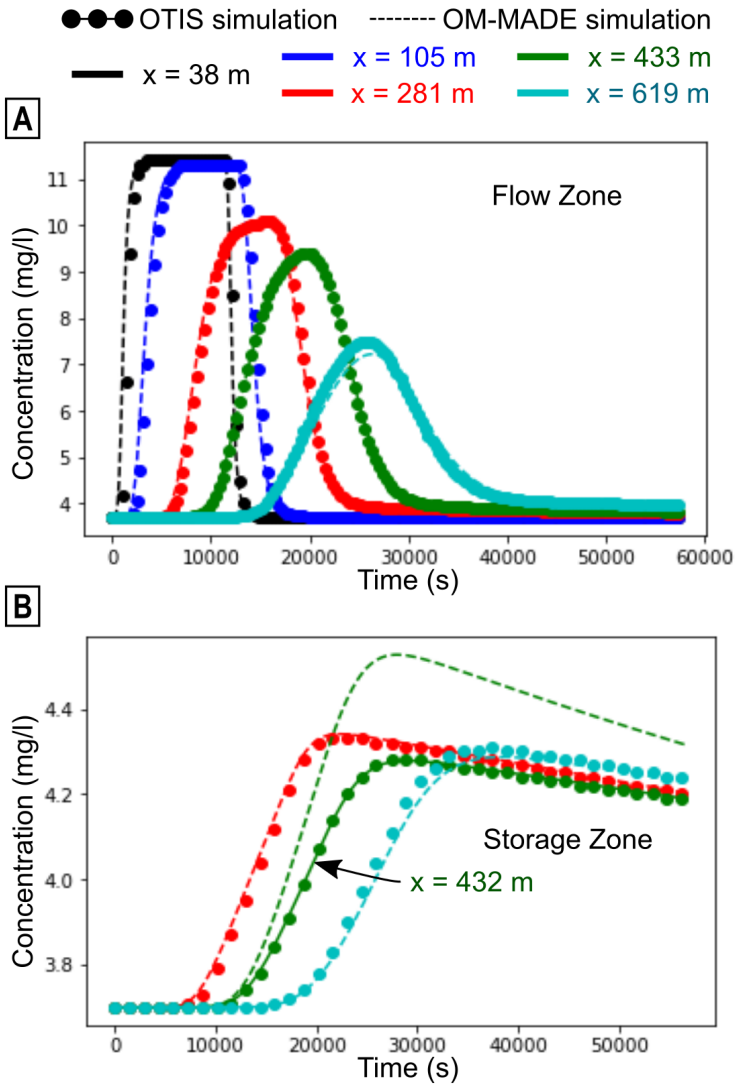

Fig. 7. Simulation of BTCs in the case of multi-reache single flow with storage: the domain is divided in 5 reaches, one mobile zone exchanges with storage zones in the reaches 3, 4, and 5. Simulated concentrations with OTIS and OM-MADE: (A) in the flow zone and (B) in the storage zones.

is $\lambda = 1.10^{-4}\ s^{-1}$. The results obtained with OM-MADE are, again, similar to those obtained with OTIS and validated against analytical solution by Runkel (1998) (Fig. 8).

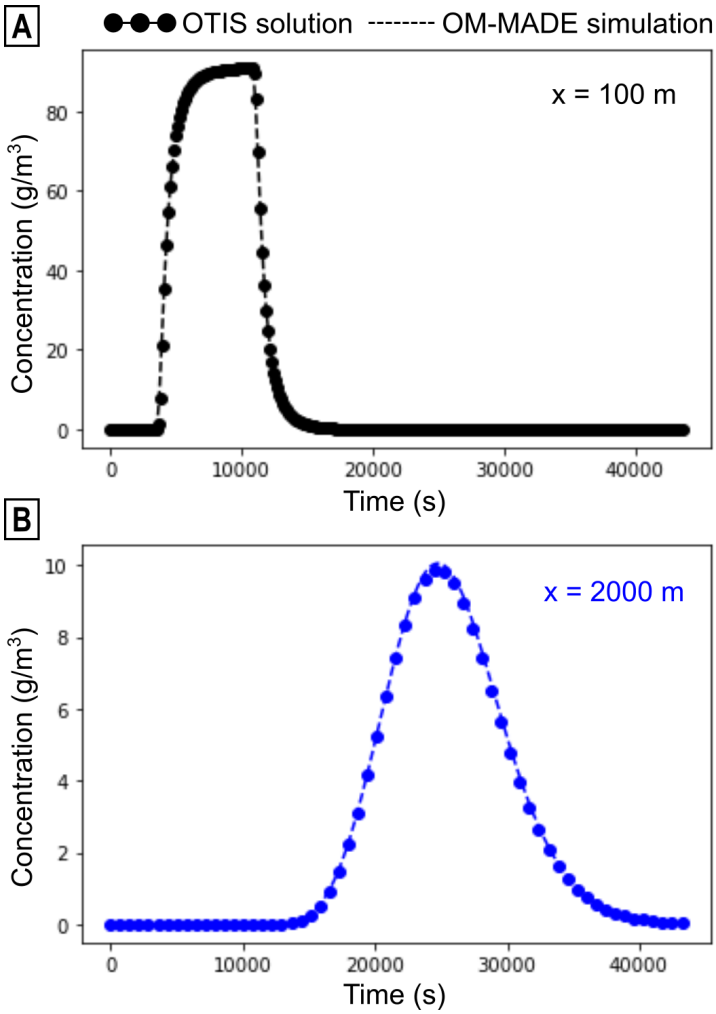

Fig. 8. OM-MADE results compared to OTIS solution in the case of transport with first-order decay.

5. Application on the Furfooz karstic system

The karstic system of Furfooz is located in the South of Belgium, near Dinant. The Furfooz karst has developed in the limestones of Carboniferous Dinantian, more specially in the Waulsortian mudmounds (Dewaide et al., 2014). The network mainly consists in conduits with flooded cross-sections of 1-2 m^2 in moderate flow conditions, and has the specificity to cross two successive underground lakes (Fig. 9). It thus constitutes an underground system of approximately 1.2 km length, which catches partially the Lesse River and returns the water back to surface through a diffusive resurgence. While a large part of the system has

been explored, the downstream part of the lakes remains unknown, as well as the first 70 m downstream the swallow hole.

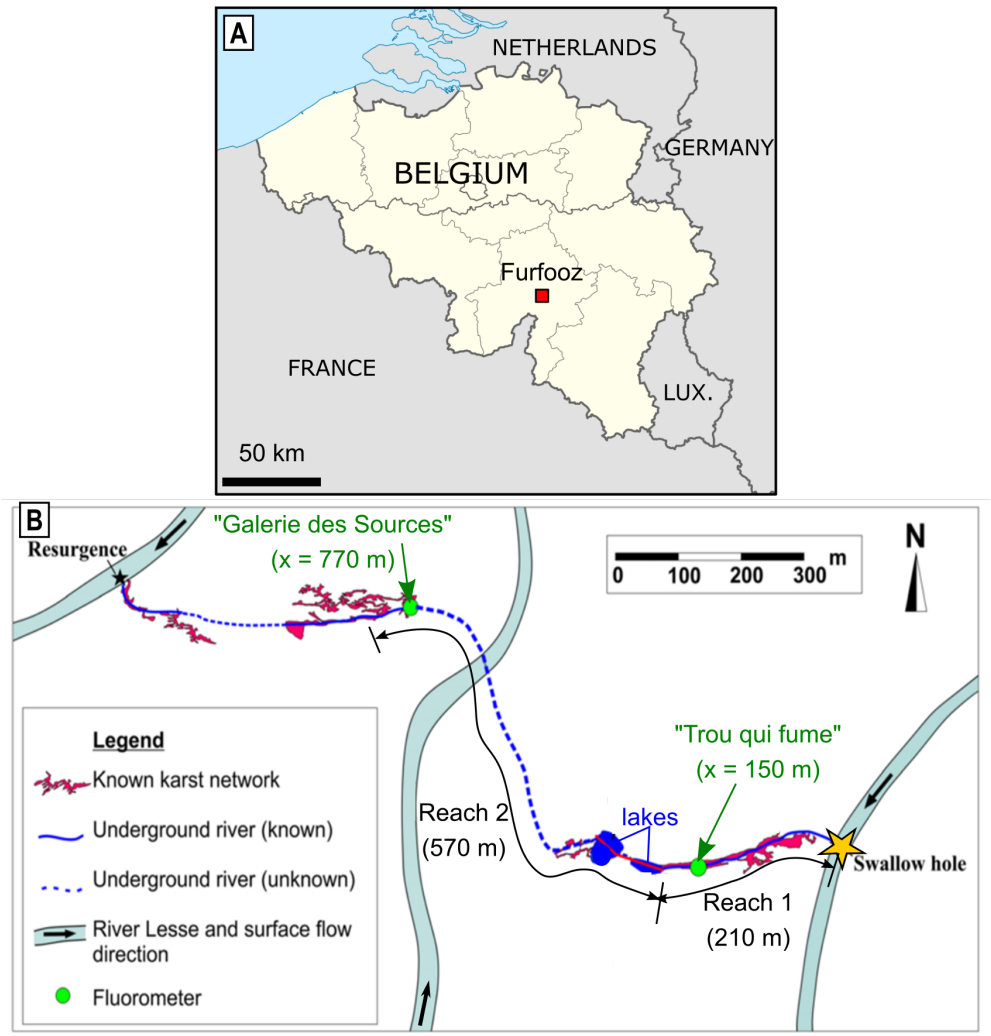

Fig. 9. The Furfooz karstic system and its numerical representation. Two sampling locations are considered : the *Trou qui fume* and the *Galerie des Sources*. The system is approximated by two reaches: (i) the first one represents a first mainly advective part ; (ii) the second reach represents the ensemble made by the lakes and their unexplored downstream part.

A tracer test has been performed, consisting in the injection of 200 g of sulforhodamine B at the swallow hole, located 210 m upstream the lakes, during stable low flow conditions. Several flow measurements were performed during the tracer test at several locations and times, and provide integrated values that vary in the underground network between 5.5 l/s to 5.97 l/s from the *Trou qui fume* to the *Galerie des Sources*[2].

[2]These values have been recently recalculated from the raw field data, showing that the first published discharge of 7 l/s measured further (Dewaide et al., 2017) corresponded to a slight over-estimation of the mean discharge in the upstream network

But at the swallow hole, the flowrate was estimated around 3.5-3.8 l/s, suggesting that around 2 l/s are penetrating the karstic system through diffuse entries before the main karstic conduit of the *Trou qui fume*. Water samples were analysed on site using field fluorometers at two locations: in the *Trou qui fume*, and in the *Galerie des Sources* (Fig. 9). The *Trou qui fume* is the first explorable part of the Furfooz karstic system. It is preceded by an impenetrable zone, probably tortuous and highly fractured, right after the swallow hole, that hydrogeologists and speleologists consider to represent a flow path of approximately 70 m long. Then, in the *Trou qui fume*, the water is mainly confined in a single conduit of approximately 140 m long, only partly flooded and easy of access, that ends in the first lake. Located in the middle of this single conduit, the first sampling point is estimated to be 150 m downstream the swallow hole. The water flows a minimum distance of 120 m through the lakes before penetrating an unexplored conduit part to the *Galerie des Sources*. Inside the *Galerie des Sources*, the second sampling point is considered by hydrogeologists and speleologists to be located approximately 410 m downstream the lakes.

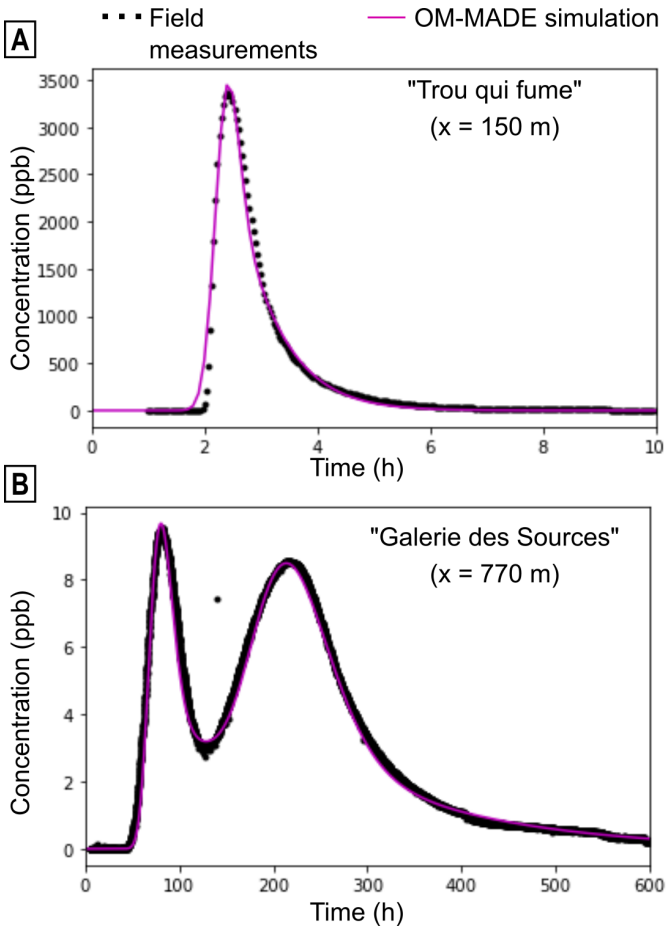

Fig. 10. OM-MADE simulated BTC fit to a tracer test conducted in Furfooz. The first site, named "Trou qui fume" is located 150 m downstream the swallow hole while the second site, the "Galerie des Sources" is located 770 m downstream the injection point.

At the first sampling point, the tracer recovery results in a classical single peaked BTC with a slight asymmetry. On the contrary, downstream the lakes at the *Galerie des Sources*, tracer recovery results in a skewed dual-peaked BTC. Further investigations have conducted Dewaide et al. (2017) to propose a conceptual model of the system that explains this BTC by a combination of a storage zone effect and a dual-advective flow zone. Thus, analysing this BTC with OM-MADE seems appropriate.

Fig. 10 depicts the OM-MADE fit to the BTC observed at the *Trou qui fume* and the *Galerie des Sources*. The system is represented by a succession of 2 reaches, corresponding to both monitored zones: (i) the first one represents the first part of 210 m long, which is observed at the *Trou qui fume*, 150 m downstream the injection point; (ii) the second reach corresponds to a transport distance of 570 m downstream the lakes and illustrates the combined effect of the lakes and of their downstream part until the *Galerie des sources*, located at a supposed distance of 770 m downstream the injection point. Note that to avoid eventual boundary effects, the reach terminates further than the observation point location. In this application, we decided to ignore the intermediary sampling sites (sites 2 and 3 in Dewaide et al. (2017)) as, located at the surface of the lakes, they did not seem to be representative of the tracer test average behaviour (strong effects of diffusion through the lakes).

Compared to the second one, the first BTC expresses a quick (in less than 3 hours) and mainly advective transport of the tracer. Thus, to avoid numerical dispersion while keeping reasonable computational times to simulate a tracer test of 600 h (= 2160000 s), we use a space step of 2.5 m and a time step of 360 s. With those numerical parameters, the simulation takes 4 mn 30s on a standard laptop with 8 Go RAM and a 2.60 GHz Intel(R) Core(TM) Processor. In this model, which largely approximates the natural behaviour and uses a steady flow regime, we consider a total mean discharge of $Q = 5.7\ l/s$. Given the observations at the swallow hole, we decided to distribute this discharge between the two mobile zones as followed: 3.7 l/s is considered to penetrate in the first mobile zone, while zone 2 is characterized by an input discharge of 2 l/s. The initial concentration of the water is nil, and at $t = 0$ an injection of 200 g of the tracer is performed in zone 1 only, which, applied to our time step and with an input flowrate of 3.7 l/s, corresponds to an input concentration of $C_1 = 150150\ ppb$ during the first 360 s. The input concentration is nil in zone 2.

To illustrate the fact that all water is drained by a single conduit in the main part of the first reach, and especially where the sampling is performed, we use two knacks : (i) we have chosen an important exchange coefficient that mimics an almost instantaneous equilibrium between both mobile zones; (ii) we have decided to impose almost the same flowrate v_i in both mobile zones by an adapted choice of the corresponding cross-sectional areas A_i ($A_2 \simeq Q_2/Q_1 \times A_1$). Due to this equilibrium between both zones, their respective values of degradation coefficients and of exchange coefficients with the storage zone act similarly on the resulting global BTC at the *Trou qui fume*. Thus, we chose to distribute the coefficient effects easily by using equal values in both zones. The degradation coefficients express the limited tracer recovery observed at both sites: a quick integration of the BTCs indicates, when considering a mean discharge of 5.7 l/s, a restitution of

around 35% at the *Trou qui fume*[3] and 19% at the *Galerie des sources*. Introducing a small storage zone is necessary to reproduce the BTC asymmetry. This could be related to the unknown part, in the first 70 m of the system, probably combined with an effect of the small pools and of the variations of the underground stream geometry all along the karstic system, as it has been demonstrated on other karstic sites (Hauns et al., 2001). In the second reach, a partial independence of both mobile zones is set thanks to a lowest exchange coefficient, and the cross-sectional areas of both mobile zones are not linked any more.

With these input constraints, the different parameter values were manually tuned to fit the two measured BTCs. The resulting set of parameters, presented in Table 2, do not represent a field reality: they are the values that correspond to an average behaviour of two parts of the system, with a given conceptual scenario. To reproduce a double-peaked BTC, it is necessary to impose different relative cross-sectional areas, and thus flow rates, in both mobile zones. Here, we have enlarged the second mobile zone, but it has not to be linked with the boundary conditions of each zone: at the end of the first reach, the water has mixed between both conduits, thus, even if the tracer was injected in zone 1, the concentration in zone 2 is similar at the beginning of the reach. As a consequence, another fit could probably be done by accelerating the flow in the second zone rather than in the first one. In this simulation, the long tail observed at the *Galerie des Sources* is the effect of a large storage zone that interacts with both mobile zones.

This application shows that the observed dual-peaked skewed BTC could be explained by two mobile zones exchanging with a storage zone in the part of the karst between the lakes and the *Galerie des Sources*. This global behaviour does not imply a more precise interpretation : the dual-advective exchanging zones could be an effect of the lakes or an expression of a local auxiliary conduit that diverts the solute transport and then transports it back to the main conduit. At that point, OM-MADE has mainly showed its capacity to simulate one dimensional solute transport in multiple exchanging conduits and storage zones. But, more field investigations should now be performed to precise the exact functioning of the Furfooz system. A recent discovery of a conduit between the lakes and the *Galerie des Sources* will certainly help in that purpose.

6. Discussion and Conclusion

OM-MADE is a simple flexible code that allows to simulate one-dimensional transport in the case of multiple exchanging mobile and immobile flow zones. Such configurations are indeed often suggested to explain multi-peaked BTCs observed when performing tracer tests in karstic systems. It also allows to segment the domain of interest into several reaches of constant model parameters, which is useful to represent the different parts of a karst network that field investigation can reveal.

[3] In Dewaide et al. (2017) an error appears in the table 1 for the tracer test 3: even when considering a men discharge of 7 l/s, the integration of the BTC observed at site 1 gives a restitution rate around 43%.

Table 2

Parameters of the OM-MADE simulation for modelling one tracing test carried out in the Furfooz karstic system : the system is described by a model with multi-reaches dual-mobile zones with storage. Lateral inflows (q_{lin} and C_{lin}) are nil. The simulation is performed with a spatial step $dx = 2.5m$ and a time step $dt = 360s$. A total mass of 200 g of sulforhodamine B is injected at $t = 0$ in zone 1.

	Reach 1: 0 - 210 m					
	A	D	λ	Exchange coefficients α_{ij} (m^2/s)		
	(m^2)	(m^2/s)	$(1/s)$	zone 1	zone 2	zone 3
Zone 1 ($Q = 3.7L/s$)	0.217	0.011	1.25e-4	0	1e-2	2.2e-5
Zone 2 ($Q = 2L/s$)	0.116	0.009	1.25e-4	1e-2	0	2.2e-5
Zone 3 (Storage)	0.063	0.6e-9	0	2.2e-5	2.2e-5	0
	Reach 2: 210 - 780 m					
	A	D	λ	Exchange coefficients α_{ij} (m^2/s)		
	(m^2)	(m^2/s)	$(1/s)$	zone 1	zone 2	zone 3
Zone 1 ($Q = 3.7L/s$)	1.90	0.015	8.7e-7	0	1e-7	9.8e-6
Zone 2 ($Q = 2L/s$)	2.88	0.007	4e-8	1e-7	0	8.5e-7
Zone 3 (Storage)	4	0.6e-9	2e-7	9.8e-6	8.5e-7	0

OM-MADE has been tested to simulate a real tracer test realised in Furfooz, allowing to demonstrate its potential and also its limits. By modelling a one-dimensional transport, OM-MADE simplifies a complex reality and, as other models, OM-MADE is parametrised by different variables that can not all be measured on the field (*e.g.*, the exchange coefficients, or even the average cross-sectional area of each reach). Thus, defining the values of the various parameters by a try-and-error approach can become a long and difficult task as the number of reaches increase. An obvious improvement should be to implement an automated parameter estimation process, for example by minimizing the squared differences between the simulated and observed concentrations. Nevertheless, such functionality should also allow to fix some of these parameters which, depending on the field case that is studied, can be already known (e.g. cross-sectional areas of some conduits, nil exchanging coefficients, ...), or stacked by the field knowledge. Moreover, only uniform flow is now considered in OM-MADE. Future improvements could also consist in integrating turbulent flow.

If Python programming language is flexible, and easy to pick up by non-programmers, open-source and multi-platform, Python is also known to lack of running performance. If complex case studies should be simulated (*e.g.*, with numerous flow zones or high resolution time/space steps), combining python with another language (like C++) could be interesting to gain in simulation time.

Despite these limitations, OM-MADE proposes an open-source solution to help a first analysis and simulation of multi-peaked BTCs observed in karstic systems, which can be now used in any institution and location, and improved by everyone to fit his requirements.

Acknowledgements

The authors acknowledge USGS and its developers for providing the inspiring OTIS software, as well as M. Field and F. Leij for providing the DADE. The authors are grateful to both the University of Lorraine (France) and the University of Namur (Belgium) for supporting this research. In particular, a part of this work has been financially supported by the program *Widen Horizons* of Lorraine Université d'Excellence (LUE).

References

Bencala, K. E., 1983. Simulation of solute transport in a mountain pool-and-riffle stream with a kinetic mass transfer model for sorption. Water Resources Research 19 (3), 732–738.

Bencala, K. E., Walters, R. A., jun 1983. Simulation of solute transport in a mountain pool-and-riffle stream: A transient storage model. Water Resources Research 19 (3), 718–724.

Bonniver, I., 2011. Etude hydrogéologique et dimensionnement par modélisation du "Système-Traçage" du réseau karstique de Han-sur-Lesse (Massif de Boine - Belgique). Ph.D. thesis, FUNDP Namur.

Brouyère, S., Carabìn, G., Dassargues, A., 2005. Influence of injection conditions on field tracer experiments. Ground Water 43 (3), 389–400.

De Marsily, G., 1986. Quantitative hydrogeology. Elsevier Science Publishing Co Inc.

Dewaide, L., Baele, J.-M., Collon-Drouaillet, P., Quinif, Y., Rochez, G., Vandycke, S., Hallet, V., oct 2014. Karstification in dolomitized Waulsortian mudmounds (Belgium). Geologica Belgica 17 (1), 43–51.

Dewaide, L., Bonniver, I., Rochez, G., Hallet, V., 2016. Solute transport in heterogeneous karst systems: Dimensioning and estimation of the transport parameters via multi-sampling tracer-tests modelling using the OTIS (One-dimensional Transport with Inflow and Storage) program. Journal of Hydrology 534, 567–578.

Dewaide, L., Collon, P., Poulain, A., Rochez, G., Hallet, V., sep 2017. Double-peaked breakthrough curves as a consequence of solute transport through underground lakes: a case study of the Furfooz karst system, Belgium. Hydrogeology Journal.

Field, M. S., Leij, F. J., 2012. Solute transport in solution conduits exhibiting multi-peaked breakthrough curves. Journal of Hydrology 440-441, 26–35.

Galambos, P., Forster, F. K., 1998. Micro-Fluidic Diffusion Coefficient Measurement. Springer Netherlands, Dordrecht.

Goldscheider, N., Hötzl, H., Käss, W., Ufrecht, W., apr 2003. Combined tracer tests in the karst aquifer of the artesian mineral springs of Stuttgart, Germany. Environmental Geology 43 (8), 922–929.

Goldscheider, N., Meiman, J., Pronk, M., Smart, C., 2008. Tracer tests in karst hydrogeology and speleology. International Journal of Speleology 37 (1), 27–40.

Hauns, M., Jeannin, P.-Y., Atteia, O., jan 2001. Dispersion, retardation and scale effect in tracer breakthrough curves in karst conduits. Journal of Hydrology 241 (3-4), 177–193.

Hauns, M., Jeannin, P. Y., Hermann, F., 1998. Tracer transport in karst underground rivers : tailing effect from channel geometry. Bulletin d'Hydrogéologie 16, 123–142.

Hubbard, E., Kilpatrick, F., Martens, L., Wilson, J. J., 1982. Measurments of time of travel and dispersion in streams by dye tracing. In: USGS (Ed.), Techniques of Water-Resources Investigations, Book 3, Applications of Hydraulics. USGS, Washington, DC, Ch. A9, p. 44.

Hunter, J. D., 2007. Matplotlib: A 2D Graphics Environment. Computing in Science & Engineering 9 (3), 90–95.

Knöll, P., Scheytt, T., nov 2017. A tracer test to determine a hydraulic connection between the Lauchert and Danube karst catchments (Swabian Alb, Germany). Hydrogeology Journal.

Lax, P., Wendroff, B., 1960. Systems of conservation laws. Communications on Pure and Applied mathematics 13 (2), 217–237.

Leij, F. J., Toride, N., jul 1995. Discrete Time- and Length-Averaged Solutions of the Advection-Dispersion Equation. Water Resources Research 31 (7), 1713–1724.

Martin, J. L., McCutcheon, S. C., 1998. Hydrodynamics and transport for water quality modeling. CRC press.

Massei, N., Wang, H. Q., Field, M. S., Dupont, J. P., Bakalowicz, M., Rodet, J., oct 2006. Interpreting tracer breakthrough tailing in a conduit-dominated karstic aquifer. Hydrogeology Journal 14 (6), 849–858.

Morales, T., Fdez. de Valderrama, I., Uriarte, J. A., Antigüedad, I., Olazar, M., feb 2007. Predicting travel times and transport characterization in karst conduits by analyzing tracer-breakthrough curves. Journal of Hydrology 334 (1-2), 183–198.

Mudarra, M., Andreo, B., Marín, A. I., Vadillo, I., Barberá, J. A., aug 2014. Combined use of natural and artificial tracers to determine the hydrogeological functioning of a karst aquifer: the Villanueva del Rosario system (Andalusia, southern Spain). Hydrogeology Journal 22 (5), 1027–1039.

Perrin, J., Luetscher, M., aug 2008. Inference of the structure of karst conduits using quantitative tracer tests and geological information: example of the Swiss Jura. Hydrogeology Journal 16 (5), 951–967.

Rossier, Y., Kiraly, L., 1992. Effet de la dilution sur la détermination des dispersivités par interprétation des essais de traçage dans les aquifères karstiques [Role of dilution on the estimation of dispersivities based on the interpretation of tracer tests carried out in karst aquif. Bull Centre Hydrogéol Neuchâtel 11, 1–15.

Runkel, R. L., sep 1996. Solution of the Advection-Dispersion Equation: Continuous Load of Finite Duration. Journal of Environmental Engineering 122 (9), 830–832.

Runkel, R. L., 1998. One-dimensional transport with inflow and storage (OTIS): a solute transport model for streams and rivers. Tech. rep., USGS.

Seiler, K.-P., Maloszewski, P., Behrens, H., jan 1989. Hydrodynamic dispersion in karstified limestones and dolomites in the Upper Jurassic of the Franconian Alb, F.R.G. Journal of Hydrology 108, 235–247.

Smart, C., Ford, D., 1982. Quantitative dye tracing in a glacierised alpine karst. Beit. Geol. Schweiz. Hydrol. 28 28 (1), 191–200.

Smart, C. C., jul 1988. Artificial Tracer Techniques for the Determination of the Structure of Conduit Aquifers. Ground Water 26 (4), 445–453.

Appendix V

Photographs

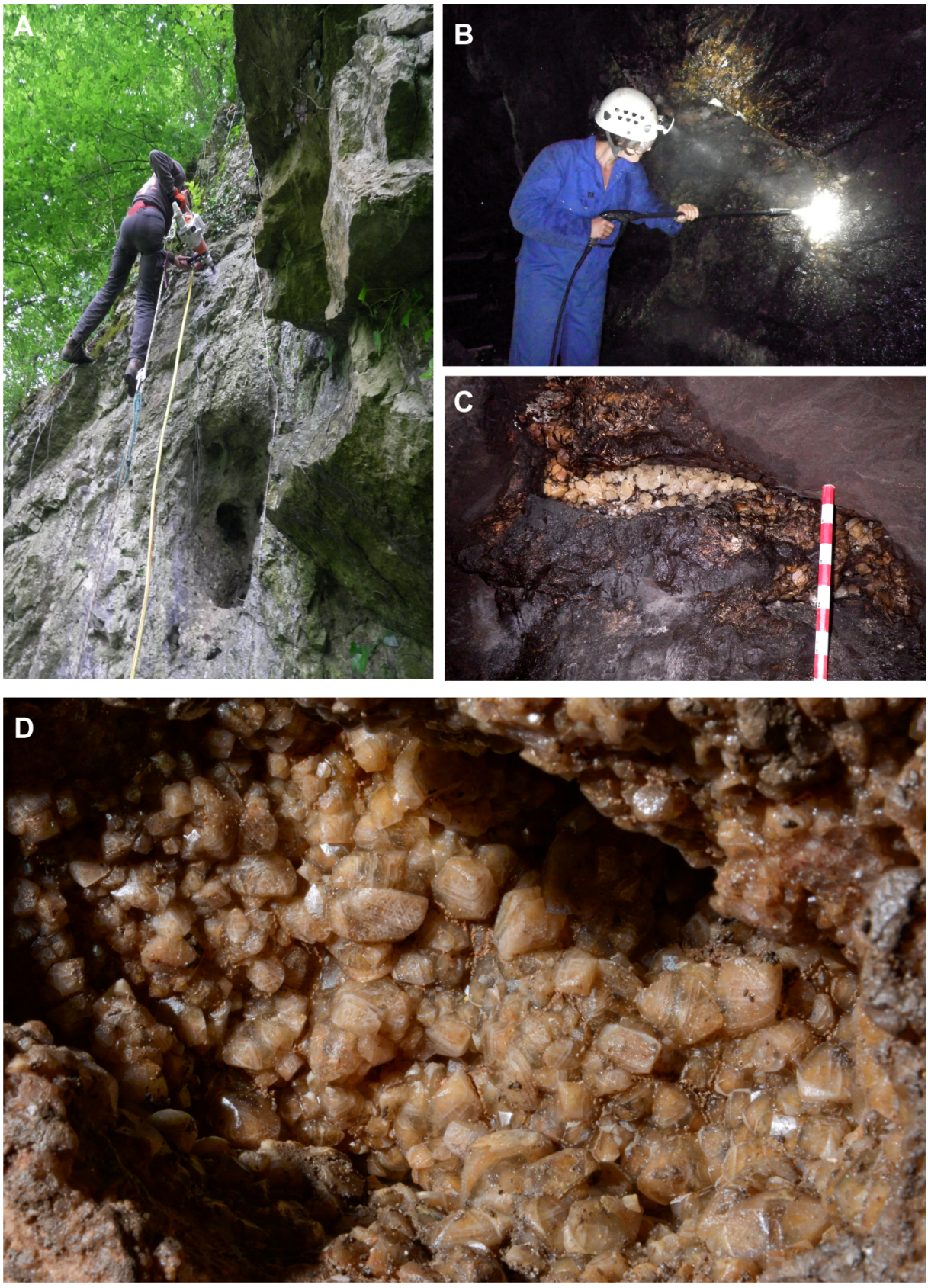

Karst - Field observations: [A] : core sampling; [B]: washing of a rock wall before sampling; [C] and [D] calcite cementation in a cavity. Photos: G. Rochez, L. Dewaide.

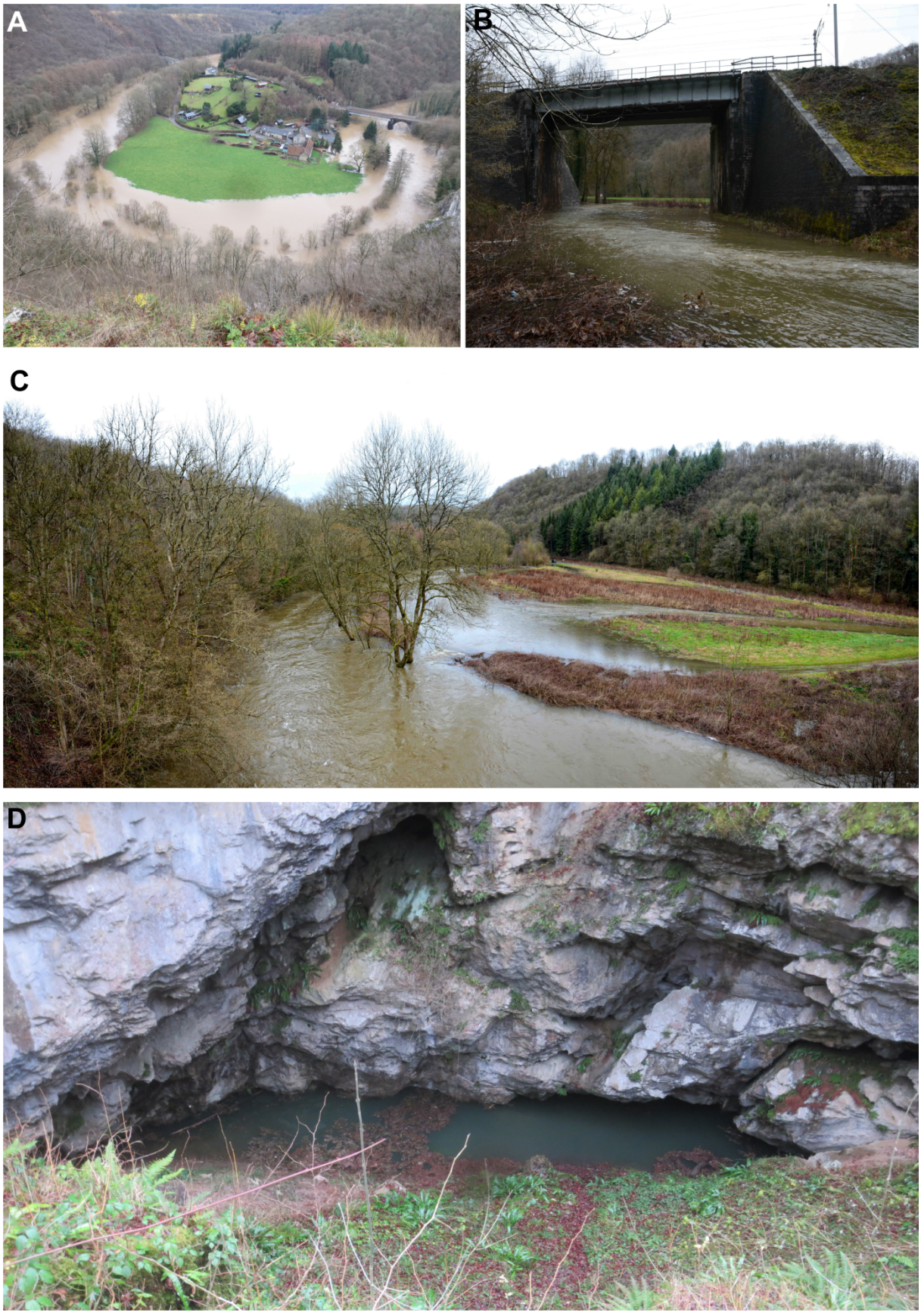

Flood in Furfooz: [A], [B], [C]: Overflow of the Lesse River; [D] : The PDV lake during a flood. Photos: G. Rochez, Bibiche.

Field monitoring: [A]: Gauging at the GDS cave; [B], [C]: data recording; [D]: section measurement at the TQF. Photos: G. Rochez, A. Poulain.

Dye-tracing: [A]: rhodamine injection in the Sebia (November 2013); Fluorimeter (GGUN-FL13) at the GDS; [C] coloring of the TQF river (March 2013); [D]: screened casing placement at the PDV. Photos: G. Rochez.

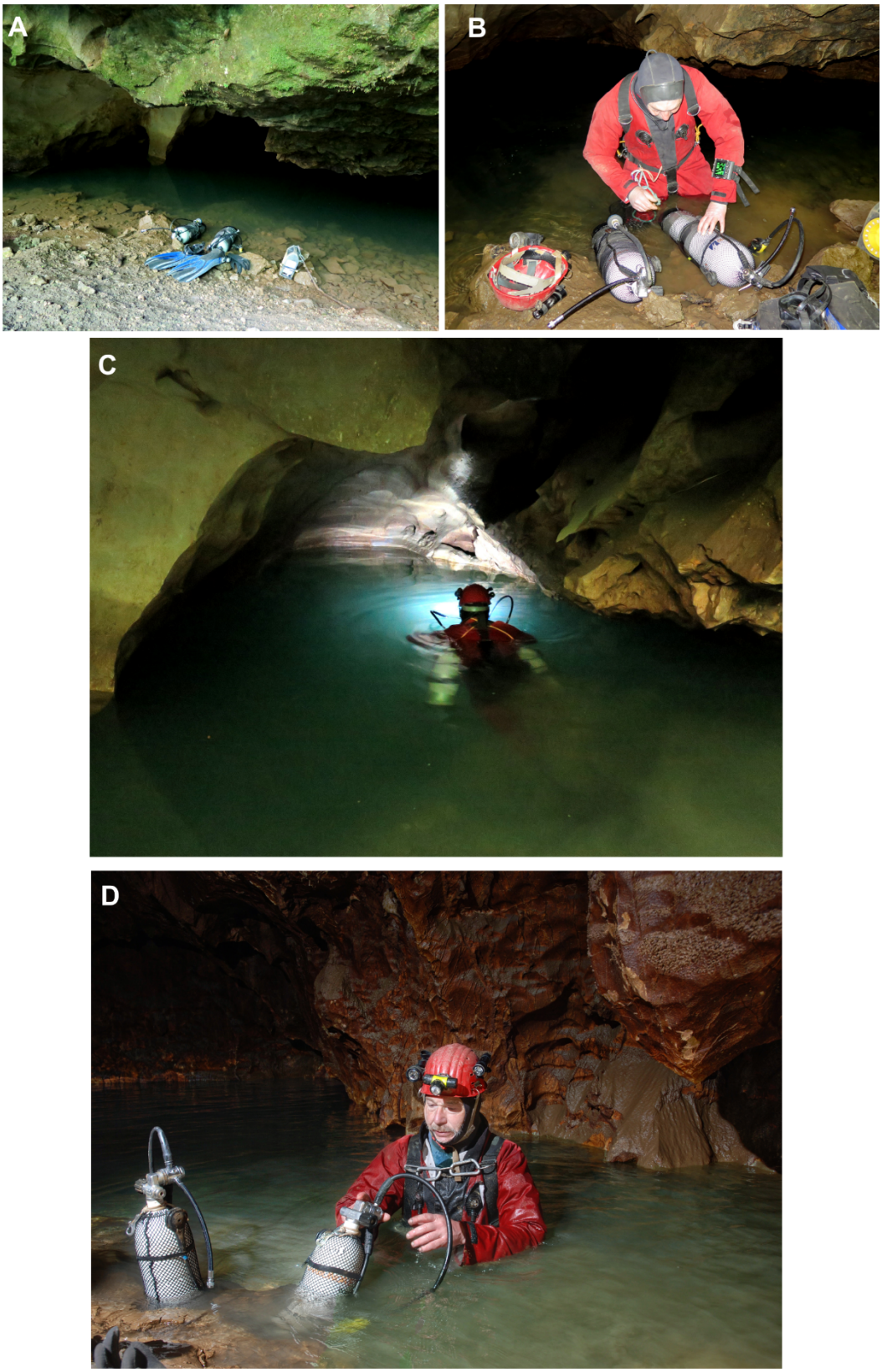

Michel Pauwels diving in the PDV lake ([A], [B], [C]) and at the Sepulture cave [D].

Photos: G. Rochez.

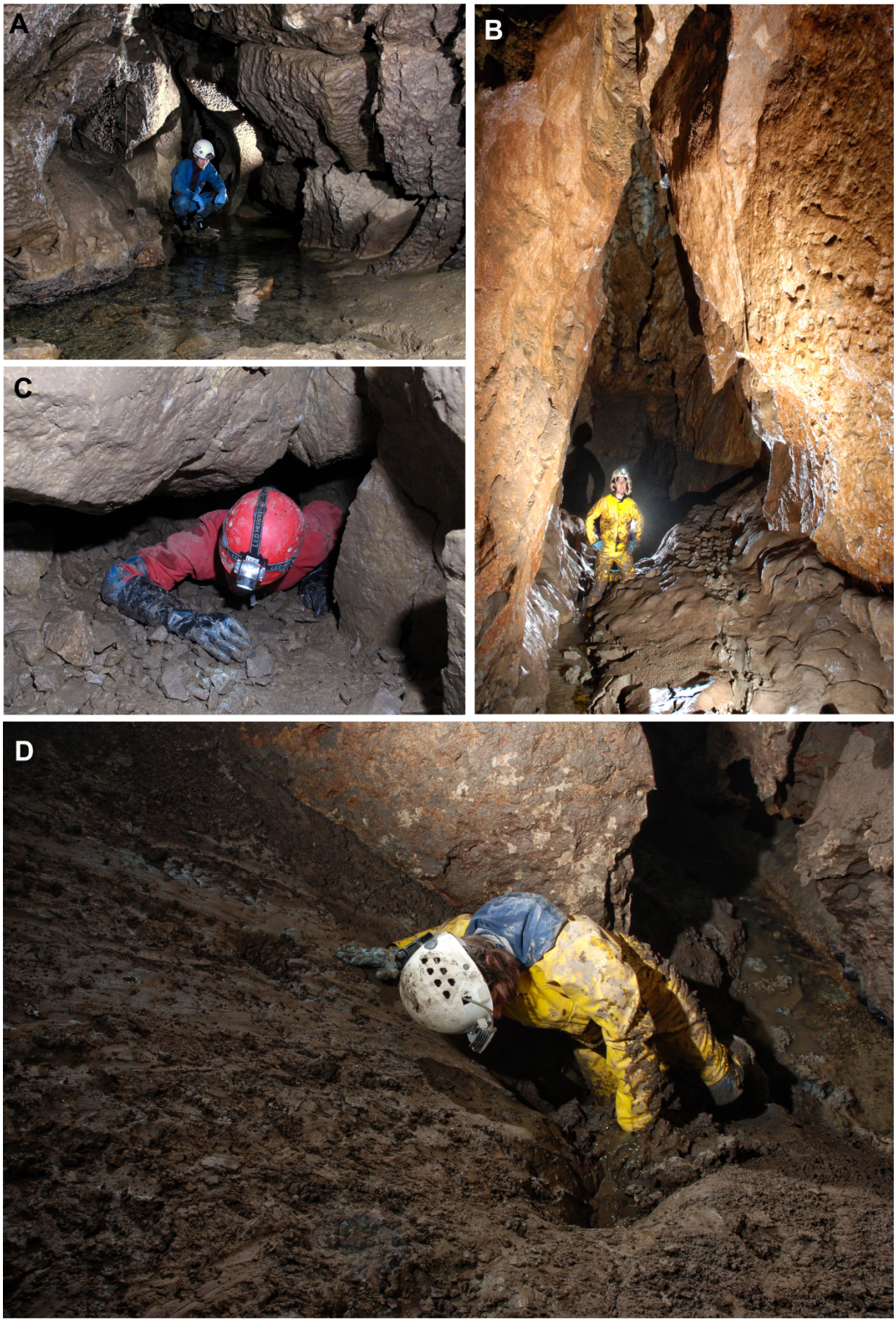

Cave exploration. [A]: Galerie Des Sources; [B], [C], [D] : Trou Qui Fume. Photos: G. Rochez.